Linear and non-linear statistics of the cosmic density field in modified gravity cosmologies

Author: Suhani Gupta

Advisors: dr. hab. Wojciech A. Hellwing, prof. CFT PAN

dr. hab. Maciej A. Bilicki, prof. CFT PAN

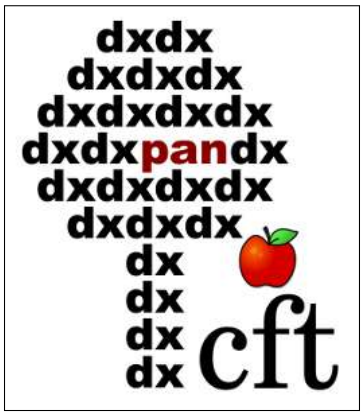

Centrum Fizyki Teoretycznej Polskiej Akademii Nauk

Thesis submitted in partial fulfillment of the requirements for the degree of Doctor of Philosophy in Physics

November 2023

Dedicated to my parents

for everything

Looking at the universe as a whole; cosmology, the birth, life and death of the whole universe, we used to have a nice simple model. Then we had to add things like dark energy, and our nice simple picture is getting messier and messier and messier.

-Jocelyn Bell Burnell

Abstract

Einstein's theory of General Relativity forms the basis of modern cosmology. According to this framework, approximately 96% of our Universe is made of Dark Matter and Dark Energy. The important role of these dominant components in influencing the dynamics of our Universe is well-understood. Dark Matter explains the stability of large-scale structures, whereas Dark Energy accounts for the accelerated expansion of the Universe. Hence, one of the most important goals of modern cosmology is to understand the nature of these two cosmic entities.

According to the standard ΛCDM (Λ-Cold Dark Matter) cosmological model, Λ (or the cosmological constant) is the leading Dark Energy candidate, and explains the cosmic speed-up. However, Λ faces notable theoretical and observational challenges. As a result, there are a wide variety of beyond-ΛCDM theories that seek to explain the apparent accelerated expansion by assuming modifications to the standard gravity theory on cosmological scales. In this thesis, we work with two such modified gravity (MG) models: namely $f(R)$ and nDGP gravity. These MG theories offer a very good test-bed to explore the freedom of modifying Einstein's gravity theory, in order to produce a physical mechanism which effectively mimics the action of the cosmological constant, resulting in the cosmic acceleration. The effect of these MG models is incorporated in the gravitational dynamics of large-scale structures, and can potentially impact the formation and evolution of Dark Matter halos. Thus, the statistical properties of halos, that form the building blocks of cosmological observables associated with large-scale structures in the Universe, offer opportunities for testing modifications to the gravitational forces. Studying the cosmological implications of these MG theories, and constraining them using observations is an active research topic in cosmology.

Owing to the non-linear character of these beyond-ΛCDM theories, numerical simulations are the most reliable tools to study these MG models, which are, however, computationally expensive. The greater computational cost of MG simulations makes it difficult to achieve the resolution and volume that we have attained for the state-of-the-art ΛCDM simulations. This further limits the scope of accurately testing gravity on cosmological scales using precise observational data. Therefore, in order to make the best use of the wealth of data for MG tests from our current and future surveys, it is important to prepare accurate theoretical predictions. These theoretical templates can be safely combined with observations to make precise and unbiased constraints on cosmological observables. The first part of this thesis addresses this need for reliable analytical modelling of the cosmological properties in MG.

In the second part of the thesis, we quantify the impact of additional attributes on the large-scale statistics, and how these properties further influence the impact of MG. Particularly, we study additional dependencies induced by the internal halo properties, and the cosmic environments. These factors introduce additional systematics in the study of large-scale clustering and should be properly accounted for to obtain unbiased

and accurate constraints in cosmological parameter analysis. Achieving the percent-level accuracy we aim for in our present and future cosmological surveys demands this attention.

Abstract in Polish

Ogólna teoria względności Einsteina stanowi podstawę współczesnej kosmologii. Zgodnie z tą teorią, około 96% naszego Wszechświata składa się z Ciemnej Materii i Ciemnej Energii. Rola tych dominujących składników we wpływaniu na dynamikę naszego Wszechświata jest dobrze rozumiana. Ciemna Materia wyjaśnia stabilność struktur wielkoskalowych, podczas gdy Ciemna Energia odpowiada za przyspieszoną ekspansję Wszechświata. Dlatego jednym z najważniejszych celów współczesnej kosmologii jest zrozumienie natury tych dwóch kosmicznych bytów.

Zgodnie ze standardowym modelem kosmologicznym ΛCDM (Λ-Cold Dark Matter), Λ (lub stała kosmologiczna) jest głównym kandydatem na Ciemną Energię i wyjaśnia przyspieszoną ekspansję Wszechświata. Jednak Λ stoi w obliczu znaczących wyzwań teoretycznych i obserwacyjnych. W rezultacie istnieje wiele różnych teorii wykraczających poza ΛCDM, które starają się wyjaśnić obserwowaną przyspieszoną ekspansję, zakładając modyfikacje standardowej teorii grawitacji na skalach kosmologicznych. W niniejszej rozprawie pracujemy z dwoma takimi modelami zmodyfikowanej grawitacji (MG): mianowicie z grawitacją f(R) i nDGP. Powyższe teorie MG oferują bardzo dobry poligon doświadczalny do badania swobody modyfikacji teorii grawitacji Einsteina w celu wytworzenia mechanizmu fizycznego, który skutecznie naśladuje działanie stałej kosmologicznej, powodując przyspieszoną ekspansję. Efekt tych modeli MG jest wpisany w dynamikę grawitacyjną struktur wielkoskalowych i może potencjalnie wpływać na powstawanie i ewolucję hal ciemnej materii. Tak więc statystyczne właściwości hal, które tworzą elementy składowe obserwabli kosmologicznych związanych z wielkoskalowymi strukturami we Wszechświecie, oferują możliwości testowania modyfikacji sił grawitacyjnych. Badanie kosmologicznych implikacji tych teorii MG i ograniczanie ich za pomocą obserwacji jest aktywnym tematem badawczym w kosmologii.

Ze względu na nieliniowy charakter tych teorii wykraczających poza ΛCDM, symulacje numeryczne są najbardziej wiarygodnymi narzędziami do badania tych modeli MG. Są one jednak kosztowne obliczeniowo. Większy koszt obliczeniowy symulacji MG utrudnia uzyskanie rozdzielczości i objętości, które osiągnęliśmy dla najnowszych symulacji ΛCDM. To dodatkowo ogranicza zakres dokładnego testowania grawitacji na skalach kosmologicznych przy użyciu precyzyjnych danych obserwacyjnych. Dlatego, aby jak najlepiej wykorzystać bogactwo danych do testów MG z naszych obecnych i przyszłych przeglądów nieba, ważne jest przygotowanie dokładnych przewidywań teoretycznych. Te teoretyczne szablony mogą być uważnie połączone z obserwacjami w celu uzyskania precyzyjnych i bezstronnych ograniczeń na obserwable kosmologiczne. Pierwsza część niniejszej rozprawy dotyczy potrzeby wiarygodnego analitycznego modelowania właściwości kosmologicznych w MG.

W drugiej części rozprawy określamy ilościowo wpływ dodatkowych atrybutów na statystyki wielkoskalowe oraz sposób, w jaki te właściwości dodatkowo wpływają na efekty związane z MG. W szczególności badamy dodatkowe zależności powodowane

przez wewnętrzne właściwości halo i środowiska kosmiczne. Czynniki te wprowadzają dodatkową systematykę w badaniu wielkoskalowego grupowania się i powinny być odpowiednio uwzględnione, aby uzyskać obiektywne i dokładne ograniczenia w analizie parametrów kosmologicznych. Osiągnięcie dokładności na poziomie procentowym, do której dążymy w naszych obecnych i przyszłych badaniach kosmologicznych, wymaga tej uwagi.

Acknowledgements

My PhD journey, like everyone else's, was filled with ups and downs. It was my first time living outside my home country, and Poland was a welcoming change in my life. I loved living here, and I learned so much during my stay here: about the beautiful and kind-hearted Polish people, the extremely difficult Polish language (still trying to learn it!), the delicious Polish cuisines, and the prettiest landscapes, ranging from mountains in the South, to sea in the North. This country has so much to offer and living here has been nothing but a delight. It was here where I really learned adulting: renting an apartment, learning to cook, taking care of my expenses, and facing emotional and mental challenges.

I would first like to thank my supervisors: **Wojciech (Wojtek) Hellwing and Maciej (Maciek) Bilicki** for giving me the opportunity to work with them. Throughout my PhD time, I never felt that I was alone, and I always had this assurance that I have their complete support in all domains. From both Wojtek and Maciek, I learned the importance of being inclusive, patient, having good work ethics, being open-minded, always being inquisitive, curious, and critical, and never to stop loving science. It was an amazing experience working with them, and I hope I can continue to appreciate the values they have taught me in my next ventures. I express my gratitude to them for not only supporting my research, but also actively encouraging me to participate in conferences and workshops. These opportunities allowed me to showcase my research to a broader audience, fostering connections with numerous professionals in my field. As a result, I had the privilege of establishing valuable collaborations that have proven to be immensely fruitful. Also, I would like to thank both Wojtek and Maciej for helping me improve my scientific writing, presentation skills, and assisting me throughout with the obligations necessary in the doctoral school. I extend my special gratitude to **Krishna Naidoo** for patiently assisting me with even the silliest of doubts. Your remarkable ability to present difficult problems with ease and clarity has been truly admirable. Engaging in discussions with you has consistently been a pleasure, and I really appreciate your unwavering support. I would also like to express my gratitude to my collaborators: **Sergio Contreras, Jońas Chaves-Montero, Punyakoti Ganeshaiah Veena, Simon Pfeifer, Jorge Enrique García-Farieta, and Mariana Jaber**. My collaboration with each of them was a source of immense learning and growth, and it is a privilege to work alongside these exceptionally talented individuals.

Having a supportive family is very important and I have been extremely blessed with one. **My parents** have always lent me solid support since I remember: they supported my decision to pursue science, to move abroad and to make a life for myself, without the need for me to compromise on anything. They always trusted in me more than I could ever trust myself, and I owe to them what I am today. My heartfelt appreciation to **Sanchit bhaiya and Reema bhabhi** for their constant, unwavering love and support. Your presence in my life brings me immense comfort, and I know I can always count

on you. Furthermore, I must give a special mention to our cherished little **Shaurya**, whose presence fills our lives with immeasurable joy and happiness. I want to express my gratitude to **Urvi didi**, my beloved elder sister and my dearest friend, for her unwavering support and profound understanding. Your guidance and companionship have imparted invaluable life lessons to me, and I am eternally thankful for that. I fondly miss our precious moments we shared during our younger years. I would also like to thank my entire family: **my grandparents, my aunts and uncles, my sisters, cousins, and nieces and nephews**. Each of you, in your unique ways, has played a role in my growth and development, contributing to the person I have become today. Your collective support and love have been instrumental in my journey, and for that, I am deeply appreciative.

After moving to Poland, I made an amazing group of friends, which made me feel so welcome and at home. Everyone says that we do not make special friends in adult life, I can say that I found an exception in **Ishika**. She has been an unwavering presence in my life since my very first day in Warsaw: as a guiding senior, a trusted friend, an elder sister, and so much more. Those initial two years with Ishika by my side were unquestionably the most cherished times of my life in Warsaw. From the evening teas to late-night strolls, from our deep midnight conversations to potlucks, and from our shared travel adventures to countless other moments, every experience felt extraordinarily precious with her. Life took an unexpectedly different turn after she moved away, but the bond we created is for a lifetime. I also want to give a special appreciation to **Rajeev** for being my personal therapist and a friend to whom I could pour out my thoughts and feelings without reservations. You made it so easy to share my concerns, and your willingness to listen whenever I needed support lightened the load of this journey. Thank you for making this adventure a little less daunting.

My gratitude to the incredible colleagues at CFT: **Michele, Grzegorz, Julius, Lorenzo, Rafael, Shubhayan, Bestin, Raj, Tae Hun, Priyanka, and Oliver,** each of you contributed to making my time at the office an unforgettable experience. Sharing the workspace with **Paweł, Anjitha, Feven, and Gursharanjit** later on added another layer of trust and friendship that I will dearly miss. The laughter, discussions, and the wonderful moments we shared have left an indelible mark on my heart.

I'd also like to express my deep appreciation to all my friends outside of work who played a pivotal role in making my PhD life more memorable: **Sara, Chandra, Ayush, Abinash, Ruchi, Saba, Satvik, Kuba, Apratim, Simran, Abhipsa, Ashutosh, Jarek, Tilak, Ganesh, Sumit, Ankan, Deepika di, Aashina, Aana, and Valentina**. Your friendship and support enriched my experiences here in countless ways, and I am profoundly thankful for the lasting memories we've created together.

Fortunate are those who share their lives with best friends, witnessing each other's transformation from quirky kids to even quirkier teenagers, and ultimately to the quirkiest of adults. In this regard, I consider myself immensely fortunate to have **Sunakshi** as my best friend. Throughout this journey (and even before), you've stood by me

through every thick and thin, offering support during my toughest moments and celebrating each of my victories. Your unwavering presence and care, especially during my most challenging times, mean the world to me. I wish nothing but the very best for you as you chase your dreams and live the life you've envisioned for yourself. I'd like to extend a special thanks to **Aatashi and Vedika** for being the pillars of strength I could lean on whenever I needed a shoulder to cry on, or someone to share laughter with. You both understand me more than I understand myself. I am so happy for the new professional journeys you two have started, and I am so proud of you for your achievements.

I wish to express my heartfelt appreciation to my **IISER family**, who have been a constant source of support: **Manish, Rhythm, Shailesh, Pranav, Amol, Samridhi di, Akhil, Alkit, and Sharon**. You've always been there when I needed assistance, and I cherish the incredible memories we created during our time at IISER, and after. I am so glad that even after the conclusion of our five years in college, we continue to make precious memories together. I am immensely proud of each one of you for your outstanding contributions in your respective fields.

My profound gratitude to **CFT PAN** for its invaluable support, which has been instrumental in facilitating my doctoral journey. I wish to thank the **entire CFT administration** for their unwavering assistance and their remarkable ability to streamline all of our requirements, making our academic pursuits exceptionally smooth.

I extend a special note of appreciation to our esteemed director, **Prof. Krzystof Pawłowski**, who has been a steadfast supporter, and very approachable from the very inception of my PhD. He, along with Maciek, provided invaluable guidance and assistance with the intricacies of doctoral school procedures, simplifying the often complex formalities. I would also like to thank **Prof. Remigiusz Augusiak** for his support with the help of the doctoral thesis procedures.

I acknowledge the financial backing I received from both the **National Science Center, Warsaw4PhD doctoral school, and CFT PAN**.

Declaration

The work described in this thesis has been done between 2019 and 2023, while I was a doctoral student under the supervision of dr. hab. Wojciech A. Hellwing, and dr. hab. Maciej A. Bilicki, at Center for Theoretical Physics of the Polish Academy of Sciences, in Warsaw, Poland. No part of this thesis has been submitted for any other degree.

The first two chapters of this work have appeared in the following published articles:

- **S. Gupta**, W. A. Hellwing, M. Bilicki, and J. García-Farieta, *"Halo mass function as a probe of gravity"*,
  Proceedings of the Polish Astronomical Society, vol. 12, 95-100 (2022).

- **S. Gupta**, W. A. Hellwing, M. Bilicki and J. E. García-Farieta, *"Universality of halo mass function in modified gravity cosmologies"*,
  doi: 10.1103/PhysRevD.105.043538, arXiv:2112.03699.

- **S. Gupta**, W. A. Hellwing, and M. Bilicki, *"Improved analytical modeling of the non-linear power spectrum in modified gravity cosmologies"*,
  doi: 10.1103/PhysRevD.107.083525, arxiv:2301.12016.

I performed all the numerical calculations and created all the figures, in both the published works and in the thesis, except for Fig. 3.3 and Fig. 5.1 which were taken from [86] and [261] respectively.

The abstract is translated to Polish by Paweł Drozda.

Other contributions

I contributed as a co-author in the following published works:

- J.E. García-Farieta, W. A. Hellwing, **S. Gupta**, and M. Bilicki, *"Probing gravity with redshift-space distortions: Effects of tracer bias and sample selection"*, doi: 10.1103/PhysRevD.103.103524, arXiv:2103.14019.

- J. E. García-Farieta, W. A. Hellwing, **S. Gupta**, and M. Bilicki, *"Relative clustering ratios in modified gravity cosmologies"*, Proceedings of the Polish Astronomical Society, vol. 12, 120-126 (2022).

The contents of the co-authored articles are not mentioned in the thesis.

Contents

List of Figures

Table 1: Abbreviations, Full Forms, and Units Key: A comprehensive table providing a quick reference for all acronyms, their corresponding full-forms, and units (if applicable) utilised in the thesis.

Abbreviation	Full-forms	Units
z	Redshift	
$a = \frac{1}{1+z}$	Scale factor	
H	Hubble parameter	km/s/Mpc
h	H/(100 km/s/Mpc)	
$\bar{\rho}$	Mean matter density of the universe	$h^2 M_\odot Mpc^{-3}$
ρ_{cric}	Critical density of the universe	$2.775 \times 10^{11} h^2 M_\odot Mpc^{-3}$
$\Omega_X = \frac{\rho_X}{\rho_{cric}}$	Fractional density parameter	
DM	Dark Matter	
DE	Dark Energy	
HMF	Halo Mass Function	$(Mpc/h)^{-3}$
$P(k)$ or PS	Matter Power Spectrum	$(Mpc/h)^{-3}$
LSS	Large-Scale Structure	
CW	Cosmic Web	
WL	Weak Lensing	
HAB	Halo Assembly Bias	

Chapter 1: Introduction

Each one of you can change the world, for you are made of star stuff.

-Vera Rubin

Chapter 1

Introduction

The most relevant force of nature on cosmological scales is **gravity**. As a result, the most important physical description of the Universe on large scales lies in the theory of gravity. For this, the best candidate we have so far is *Einstein's General Theory of Relativity* (GR). Proposed over a century ago, GR empowers us to formulate a captivating and a testable theory of the Universe. It further allows us to quantitatively probe the age old questions like: "How old is our Universe?" or "How did everything around us come into existence?". More remarkably, over the developments in both the theoretical and observational sectors, we have been able to probe the physics of our Universe across different length and time scales, with high level of accuracy and precision.

The standard cosmological paradigm, which is based on GR, is referred to as ΛCDM. Here Λ is the cosmological constant, and CDM is for the cold dark matter. ΛCDM has proven to be a very successful description of the evolution of the Universe. This standard model explains very well the abundance of light elements from the primordial nucleosynthesis, the temperature and polarisation anisotropies of the cosmic microwave background, the large-scale clustering of matter using multiple probes, as well as the late-time accelerated expansion of the Universe [78, 68, 10, 40, 269].

Despite its observational success, the standard cosmological model carries its own set of challenges. Within the ΛCDM model, the composition of the matter content in the Universe is dominated by *dark matter* (DM) that explains the stability of large-scale structures. To satisfy both theoretical and observational tests, DM is non-relativistic. Hence, it is referred to as *cold*. The observed cosmic acceleration is governed by a mysterious *dark energy* component, and the Λ here is the leading candidate to explain this cosmic speed-up. The nature of both these components, despite their dominant composition and years of dedicated research and experiments, remains a mystery. Furthermore, to explain the formation of small initial perturbations, that later formed structures in the Universe, the theory of *inflation* is invoked which is still far from being observationally tested. Consequently, it becomes imperative to subject GR (and, by extension, the ΛCDM cosmological model) to rigorous scrutiny, rather than regarding

these as definitive descriptions governing the fundamental physics of cosmology.

The phenomenological nature of ΛCDM, along with the theoretical and observational challenges it confronts [280, 224, 54, 186], have motivated searches for alternative scenarios or extensions to the concordance model. One particularly vibrant research theme in the last decade focused on attributing the accelerated late-time expansion to some beyond-GR extensions (usually scalar-tensor theories), rather than to the vanishingly small cosmological constant. Such models are commonly dubbed as **"Modified Gravity"(MG)**. These MG models are constructed in such a way that they have negligible consequences at early times and share the same expansion history and cosmological background as ΛCDM. As a result, the effect of these MG models is incorporated in the perturbation equations that govern the gravitational dynamics of LSS. Hence, we would expect that the observables and measures associated with large-scale structure formation are a promising probe to further investigate departures from the standard GR predictions. This is broadly the main theme of this thesis: *To study the impact of MG phenomenology on the large-scale structure formation, and in turn the associated measures and observables.*

Before delving into these beyond-GR models (from Section 1.4), we first introduce the key topics of the standard cosmological framework pertinent to this thesis (Section 1.1 to Section 1.3).

1.1 Fundamentals of General Relativity and cosmology

Cosmology was born as a science from the advent of GR, where the latter shows that the geometry of space-time is governed by the matter content of the Universe. The fundamental equation of the Einstein's GR is

$$G_{\mu\nu} \equiv R_{\mu\nu} - \frac{1}{2} g_{\mu\nu} R - \Lambda g_{\mu\nu} = \frac{8\pi G}{c^4} T_{\mu\nu}. \tag{1.1}$$

Here, $G_{\mu\nu}$ is the Einstein's tensor, and $R = g^{\mu\nu} R_{\mu\nu}$ is the Ricci scalar that describes the geometry of the Universe. Λ is the above-mentioned cosmological constant. $T_{\mu\nu}$ is the energy–momentum tensor that describes the matter and energy distribution. As evident from Eq. (1.1), a beautiful connection emerges between the geometry of the Universe (L.H.S.) and the distribution of matter (R.H.S.).

The Cosmological Principle is the assertion that, on sufficiently large scales (hundreds of Mpc), the Universe is both *homogeneous* and *isotropic*. Homogeneity is the property of being invariant to translations, while isotropy is the property of being invariant to rotations. The Universe is clearly not exactly homogeneous, so we define homogeneity in an average sense: the Universe is taken to be identical in different places when one looks at sufficiently large pieces. The Universe has been observed to be nearly isotropic from the studies of the cosmic microwave background radiation [257,

130, 68]. Isotropy, however, does not necessarily imply homogeneity without the additional assumption that the observer is not in a special place: the so-called *Copernican Principle*.

As mentioned, GR is a geometrical theory. Therefore, we must begin by investigating the geometrical properties of homogeneous and isotropic spaces. Let us suppose we can regard the Universe as a continuous fluid and assign to each fluid element the three spatial coordinates $x_\alpha(\alpha = 1,2,3)$. Thus, any point in the space-time can be labelled by the coordinates x_α, corresponding to the fluid element which is passing through the point, and a time parameter which we take to be the proper time t measured by a clock moving with the fluid element. The geometrical properties of space–time are described by a Friedmann–Lemaître–Robertson–Walker (FRLW) metric, and the most general space–time metric describing a Universe in which the Cosmological Principle is obeyed is of the form (*i.e.* synchronous gauge)

$$ds^2 = (cdt)^2 + a(t)^2\left[\frac{dr^2}{1-Kr^2} + r^2(d\theta^2 + sin^2\theta d\phi^2)\right], \tag{1.2}$$

where we have used spherical polar coordinates (r,θ,ϕ) and $a(t)$ is called the cosmic scale factor (elaborated in the next paragraph).

It is well-established that our Universe is expanding. This means that in the early history, the physical distances were much smaller compared to the present time. Also, the greater the distance from us to an object, the earlier we are seeing them in time. As we mentioned in the previous equation, we can describe the expansion by introducing a scale factor $a(t)$, whose present value is set to 1 today. At earlier times, $a(t)$ was smaller than 1. For an expanding Universe, the physical location of any observer, $\vec{r(t)}$ is given by

$$\vec{r}(t) = a(t)\vec{x}, \tag{1.3}$$

where $\vec{x}$ is the comoving position which is fixed for a fundamental observers *i.e.* for observers with no other component of motion other than the universal expansion.

GR gives prescription of how $a(t)$ evolves with cosmic time t. At early times, when Universe was dominated by *radiation*, $a \propto t^{1/2}$. As time evolved and Universe became *matter-dominated*, $a \propto t^{2/3}$. At present when the Universe is dominated by *Dark Energy*, $a \propto e^t$, showing exponential expansion of our Universe.

In particular, for a homogeneous and isotropic perfect fluid of the cosmological background, with rest-mass energy density ρc^2 and pressure p, the Einstein equation (Eq. (1.1)) reduce to the Friedmann cosmological equations, that describe the evolution of the scale-factor. These equations are given as

$$\begin{aligned} \frac{\ddot{a}}{a} &= -\frac{4}{3}\pi G\left[\rho + 3\frac{p}{c^2}\right] + \frac{\Lambda c^2}{3}, \\ \left(\frac{\dot{a}}{a}\right)^2 &= \frac{8\pi G}{3}\rho - \frac{Kc^2}{a^2} + \frac{\Lambda c^2}{3}. \end{aligned} \tag{1.4}$$

Here, the cosmological constant can be treated as a component with density $\rho_\Lambda = \frac{\Lambda c^2}{8\pi G}$, and pressure $p_\Lambda = -\rho_\Lambda c^2$.

The dot represents a derivative with respect to cosmological proper time t. To quantify the change in the scale factor, we define the Hubble rate

$$H(t) \equiv \frac{1}{a(t)}\frac{da(t)}{dt}. \tag{1.5}$$

For the present time, $H_0 \equiv H(t_0)$, is the *Hubble's constant*.

We usually define the density ρ in terms of the critical density, ρ_{cr} ($\rho_{cr} \approx 10^{-29}$ g/cm^3), given as the fractional density parameter, $\Omega_X = \frac{\rho_X}{\rho_{cr}}$. Here X can be the radiation (γ), matter (m), cosmological constant (Λ), or curvature (K) component. The current total density is given by $\rho_0 = \sum_{X,0} \rho_{X,0}$, and the total density parameter $\Omega_0 = \sum_{X,0} \Omega_{X,0} = 1$. As noted in Eq. (1.1), theory of GR connects geometry to energy. Accordingly, total energy density in the Universe, ρ_0 determines the geometry, given here by the curvature parameter K: if the density is higher than a critical density *i.e.* $\rho_0 > \rho_{cr}$, the Universe is closed ($K > 0$). If $\rho_0 < \rho_{cr}$, the Universe is open ($K < 0$). For $\rho_0 = \rho_{cr}$ or $\Omega_0 = 1$, the Universe is flat ($K = 0$). A plethora of observational evidences indicate that it is indeed the case, and our Universe is flat (*i.e.* $\Omega_K = 0$) [130, 68].

Also, a directly related effect to the expansion is that the physical wavelength of light emitted from a distant object is stretched out proportionally to $a(t)$, so that the observed wavelength is larger than the emitted wavelength. This stretching is described by redshift, z

$$1 + z \equiv \frac{\lambda_{obs}}{\lambda_{emit}} = \frac{a_{obs}}{a_{emit}} = \frac{1}{a_{emit}}. \tag{1.6}$$

The greater the redshift, the further we are looking in the past.

1.2 Dark matter density fields

In this work, we describe the matter density field in terms of the density contrast, $\delta(\vec{x},t) = \frac{\rho(\vec{x},t)}{\overline{\rho}} - 1$. Here, $\delta(\vec{x},t)$ quantifies local departure of the density field, $\rho(\vec{x},t)$ from the average uniform density field, $\overline{\rho}$ at a given position, $\vec{x}$, and for a specific time, t.

As large scale cosmic density field can be considered both statistically homogeneous and isotropic. For statistical homogenity, all the joint multi-point probability distribution functions $p(\delta_1, \delta_2, ..)$, or its *moments*, which are the ensemble averages of the local density products, remain the same under translation of the spatial coordinates x_i. In this case, the probability densities depend only on relative positions. On the other hand, a field is called as statistically isotropic if $p(\delta_1, \delta_2, ..)$ remains invariant under spatial rotations.

1.2.1 Two-point correlation function and Power spectrum

The most basic characteristic that describes large-scale matter distribution is the *two-point correlation function,* $\xi(r)$. This quantity defines the excess probability, δP of finding average density of matter in a given volume element, δV [223]

$$\delta P = [1 + \xi(r)]\delta V. \tag{1.7}$$

$\xi(r)$ depends on norm of r $(= |r|)$ due to statistical homogeneity and isotropy. Physically, $\xi(r)$ characterises the strength of clustering across length scales. Furthermore, this quantity also evolves with time, thereby making it an important cosmological observable as it depends strongly on the underlying gravitational physics that governs the large-scale clustering.

Fourier counterpart of $\delta(\vec{x})$ can be written as

$$\delta(\vec{x}) = \int d^3k \delta(k) \exp(-ik \cdot x). \tag{1.8}$$

As $\delta(\vec{x})$ is real

$$\delta(k) = \delta^*(-k). \tag{1.9}$$

Therefore, $\xi(r)$ in Fourier space is given as

$$\xi(r) = \frac{1}{(2\pi)^3} \int d^3k \langle |\delta_k|^2 \rangle e^{-ik \cdot r}. \tag{1.10}$$

Density power spectrum, $P(k)$ measures the contribution of each Fourier mode to the total variance of the density fluctuations *i.e.* $P(k) \equiv \langle |\delta_k|^2 \rangle$. This further gives

$$\xi(r) = \int d^3k P(k) \exp(-ik.r). \tag{1.11}$$

Hence, $\xi(r)$ and $P(k)$ are Fourier pairs. $P(k)$ is a well-defined quantity for δ, which is a homogeneous and isotropic random field.

The amplitude of the fluctuations in each Fourier component of the density fields is determined by the physical process that generates these fluctuations. Working with the power spectrum is advantageous as it quantifies these fluctuations in each Fourier mode. For the small linear fluctuations, the evolution of these Fourier components can be studied independently. As a result, using the linear $P(k)$, we can determine the physical processes that govern these fluctuations.

1.3 Theory of structure formation

The observed temperature anisotropies in the Cosmic Microwave Background (CMB) is the oldest available imprint we have of the initial density fluctuations in the Universe [257, 130, 68]. By the relentless action of gravity, these density perturbations

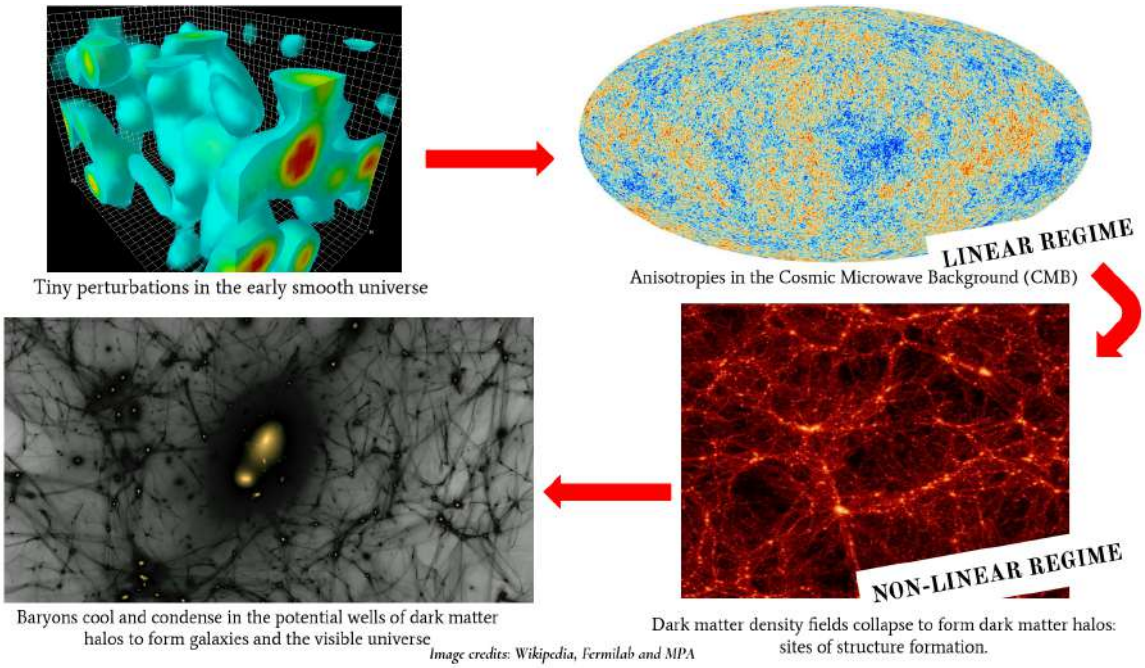

Figure 1.1: Schematic diagram showing how structures evolved from tiny perturbations in the smooth background early Universe.

amplified over time. When the amplitude of the perturbations reach a critical value, these overdensities decouple from the cosmic Hubble expansion, turn-around, and contract to form a stable structures after reaching virial equilibrium. This process led to the formation of structures called the *Dark Matter halos*. Within the potential wells of these halos, the gas cools and condenses to form stars, galaxies, clusters, and the visible Universe as we know it. In this section, we aim to elaborate on this timeline of structure formation. The significance of this process is visually depicted in Fig. 1.1, where we illustrate how all cosmic structures we currently observe can be traced back to initial perturbations within the otherwise smooth early Universe. The small density perturbations can be studied within the linear regime. As densities grow over time, the non-linear effects become more significant, and linear theory can no longer explain the evolution of the density perturbations at later times.

1.3.1 Linear perturbation theory

Small inhomogenities in the early times can be treated as tiny perturbations in the otherwise smooth background, and we can consider the perturbed quantities to their first order. The local velocity dispersion of CDM particles is sufficiently small compared to the mean free path of the perturbations, such that the particle diffusion can be neglected at relevant scales, and the matter distribution can, in-turn be treated as an ideal fluid. Within this scenario, the evolution of the inhomogenities can be studied using the Linear Perturbation Theory.

As highlighted, gravity is the driving force behind the formation of cosmic structures. Within the linear regime, the evolution of cosmological perturbations can be described

using Newtonian Perturbation Theory, which is a good approximation to GR for weak fields (*i.e.* the gravitational potential, $\phi/c^2 \ll 1$), and for the case when density contrast $\delta \ll 1$.

Assuming the cosmological background to be filled with a homogeneous, dissipationless ideal fluid with density $\rho(r,t)$, velocity field $v(r,t)$, pressure $p(r,t)$, and gravitational potential $\Phi(r,t)$ that further grow to form large structures, we can write fluid equations for expanding background in the Eulerian framework, that are based on the Newtonian theory as

1. Continuity Equation (mass-energy conservation)

$$\left(\frac{\partial \delta}{\partial t}\right)_{\vec{x}} + \frac{\nabla_{\vec{x}}}{a} \cdot [(1+\delta)\vec{v}] = 0. \tag{1.12}$$

2. Poisson Equation (equation of self-gravity)

$$\nabla^2_{\vec{x}} \Phi = 4\pi\rho G a^2 \delta. \tag{1.13}$$

3. Euler Equation (balance of energy and momentum)

$$\left(\frac{\partial \vec{v}}{\partial t}\right)_{\vec{x}} + \frac{\dot{a}}{a}\vec{v} + \frac{1}{a}(\vec{v}.\nabla_{\vec{x}})\,\vec{v} = -\frac{1}{a}\nabla_{\vec{x}}\Phi - \frac{1}{a}\frac{\nabla_{\vec{x}} p}{\overline{\rho}(1+\delta)}. \tag{1.14}$$

Here, $\nabla_{\vec{x}}$ is gradient *w.r.t.* comoving coordinate $\vec{x}$, and $\Phi = a\ddot{a}x^2/2$

Combining the fluid equations (Eqs. (1.12) to (1.14)), and the H we get an equation for the evolution of δ for the matter-dominated regime (*i.e.* for $a \propto t^{2/3}$)

$$\ddot{\delta} + 2\frac{\dot{a}}{a}\dot{\delta} - 4\pi G\overline{\rho}\delta - \frac{c_s^2}{a^2}\nabla^2\delta = 0. \tag{1.15}$$

Here, $\dot{\delta} = \left(\frac{\partial \delta}{\partial t}\right)_{\vec{x}}$. For a given density ρ, speed of sound, $c_s = \frac{\nabla_{\vec{x}} p}{\rho}$. $\frac{\dot{a}}{a}$ is the Hubble drag term, which suppresses the growth of perturbations due to the expansion of the Universe. The third term sources the growth of perturbations due to gravitational instability, and the fourth term is the pressure contributor due to spatial density variations. We consider the matter-dominated epoch since most of the structure formation took place during this regime.

In the linear regime, we can expand Eq. (1.15) in some suitable mode functions. For the flat Universe, or when scales under consideration are much smaller than the horizon size, the mode functions can be chosen to be plane waves and the perturbation fields can be represented by their Fourier transforms, $\delta(k)$ (Eq. (1.8)). Also, as we highlighted previously, it is convenient to work in k-space as each mode evolves independently in the linear regime, and hence can be studied separately.

In the Fourier space, ∇ in Eq. (1.15) can be replaced by ik, and ∇^2 by $-k^2$ to obtain

$$\ddot{\delta}_k + 2\frac{\dot{a}}{a}\dot{\delta}_k = 4\pi G\rho(1 - \frac{c_s^2 k^2}{4\pi G\rho a^2})\delta_k. \tag{1.16}$$

Expressing the density contrast as a function of both space and time, we get

$$\delta(k,t) = \delta_+(k)D_+(t) + \delta_-(k)D_-(t). \tag{1.17}$$

Here, $D_+(t)$ corresponds to the growing, and $D_-(t)$ to the decaying solutions.

Eq. (1.16) tells us about the growth of perturbation δ_k which is governed by gravitational potential ($4\pi G\rho_0(t) = \nabla^2\phi$) and pressure (speed of sound indicates the presence of pressure perturbations). Threshold condition, when both the gravitational potential and pressure perturbations are equal, gives the value of Jeans' length, k_J

$$k_J = \left(\frac{4\pi G\rho a^2}{c_s^2}\right)^{1/2}. \tag{1.18}$$

For the matter dominated era, $a(t) \propto t^{2/3}$, and the pressure perturbations are negligible. In this case, $k \ll k_J$, and we solve Eq. (1.16) using power series to get a solution of the form

$$\delta_k = A_k t^{2/3} + B_k t^{-1}.$$

The first term signifies the perturbation that grows with time, and the second that diminishes as the time passes.

The growing mode solution scales as the scale factor ($\propto t^{2/3}$). Thus matter perturbations scale as a power law during the matter dominated era, and the decaying mode scales like the Hubble term known as the Hubble drag, defined previously.

Significance of Linear Perturbation Theory

Study of linear evolution of perturbations is significant to analytically understand the evolution of small primordial fluctuations. The linear matter power spectrum, $P(k)$

$$P(k) \propto P_0(k)T^2(k). \tag{1.19}$$

Here, $P_0(k)$ refers to primordial power spectrum, and $T^2(k)$ refers to transfer function which is a factor by which linear fluctuations with wavenumber k are enhanced or suppressed relative to large-scale fluctuations

$$T^2(k,a) = \left(\frac{\delta_k(a)}{\delta_k(a=1)}\right)^2. \tag{1.20}$$

The linear power spectrum is also used to define the growth rate of structure for-

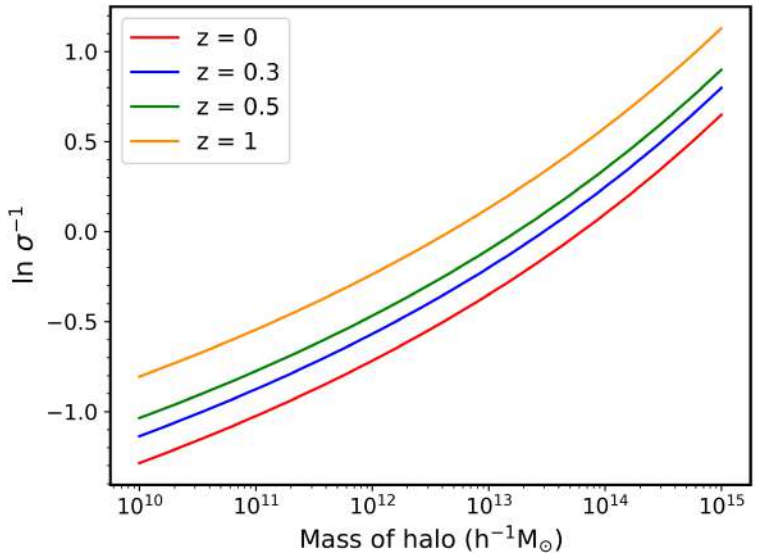

Figure 1.2: ΛCDM variance of density field, defined in Eq. (1.23) plotted as a function of halo mass, for $z = 0$ to $z = 1$.

mation, *i.e.*

$$f = \frac{d \ln D_+(a)}{d \ln a}. \tag{1.21}$$

Here, $D_+(a)$ is the growing mode solution from Eq. (1.17). From the linear power spectrum, it can be computed using the following equation

$$D_+(a) = \frac{\delta(k,a)}{\delta(k,a=1)} \equiv \sqrt{\frac{P(k)_a}{P(k)_{a=1}}}. \tag{1.22}$$

Variance of density field

Another standard quantity defined using the linear power spectrum is the linear variance of density fluctuations, $\sigma^2(M,z)$.

Halos can be considered as statistical fluctuations in the Gaussian random fields. For a spherical halo of mass M and background density $\rho_m(z)$, the linear variance of the density fluctuation field, smoothed on some comoving length scale, $R_L(M)$ is given by

$$\sigma^2(R_L(M),z) = \frac{1}{2\pi^2} \int_0^\infty k^2 W^2(kR_L) P(k,z) dk. \tag{1.23}$$

Here, W is the filter function smoothed at scale $R_L(M)$. $P(k,z)$ is the linear theory power spectrum. We smoothed the density field because we can not measure the $\delta(x)$ field with an *infinite* resolution. Thus, a smoothing is required for comparing theoretical analysis with observational/simulation results.

In Fig. 1.2, we plot Eq. (1.23), where we can see the monotonic relation between the halo mass and $\ln \sigma^{-1}$. This relation is both scale and redshift-dependent. Hence, instead of using a physical entity like halo mass, we can instead use $\sigma(M,z)$ to express

length and time-scales. This substitution fosters a more coherent and uniform study of the evolution of the density fields over length and time scales, and is invoked to define LSS properties in this thesis.

Also, one of the important cosmological parameter constrained using clustering and weak lensing surveys is the σ_8 (or $\sigma(R = 8\text{Mpc/h})$), which quantifies the linear variance at 8 Mpc/h. For the most viable cosmological models, the scale of 8 Mpc/h separates non-linear regime of density perturbations ($\delta \gg 1$), from the linear regimes ($\delta \ll 1$). This is a crucial parameter, and has important implications of the growth of fluctuations in the early universe.

In reality, this regime of 8 Mpc/h lies in the mildly non-linear regime, and has influence of mode-coupling in the non-linear evolution of the density fields. We will further show in Section 5.3.2 that the variance computed using directly the density fields from simulations is further influenced by the late-time non-linear evolution of the density fields. As a result, σ_8 measured from both simulations and observations is different than the linear theory predictions.

1.3.2 Beyond the linear perturbation theory

Zel'dovich Approximation

This theory is an extension of the Lagrangian perturbation theory, which concentrates on the trajectory of individual particles. In this case, the growth of perturbations is given by the displacement $\mathbf{x} - \mathbf{x}_i$. The peculiar velocity, $\mathbf{v}$ is the velocity of an object relative to the Hubble expansion, and is a result of local gravitational effects. This approach can be used to study the evolution of structures in regimes where the displacement is no longer small ($\delta \leq 1$) such that the linear theory fails. This is termed as the *Zel'dovich Approximation* (ZA). ZA provides an intuitive way into the emergence of LSS through the anisotropic collapse of matter.

The resultant density field is the Jacobian of the transformation $\mathbf{x}_i \rightarrow \mathbf{x}$, and can be written as

$$\rho(\mathbf{x}, t) = \frac{\bar{\rho}}{(1 - \lambda_1 D)(1 - \lambda_2 D)(1 - \lambda_3 D)}. \tag{1.24}$$

Here, $\lambda_1 > \lambda_2 > \lambda_3$ are eigenvalues for the deformation tensor $D_{ik} \equiv \partial_i \partial_k (\Phi_i / 4\pi G \bar{\rho_m} a^3)$, and determine the collapse condition of given cosmic masses in Eulerian space.

For the linear case, $\lambda_1 D \ll 1$, $\delta(\mathbf{x}) = D(a)\delta_i(\mathbf{x})$. For $\lambda_1 D(a) \approx 1$, $\rho \rightarrow \infty$, the density diverges for the first time and this gives a unilateral compression along eigenvalue corresponding to λ_1 axis, thus forming "pancake" along the same axis. ZA suggests that pancakes (or sheets) were the first structures to be formed by gravitational clustering. Filaments and knots from simultaneous contractions along the second and the third axes, respectively.

ZA fails after the collapse of the first axis *i.e.* after the formation of sheets, and when there is shell crossing. After this instance, ZA can no longer describe the trajectory of

particles. Within the Zel'dovich prescription, after a pancake forms, particles continue travelling in straight lines. However, we expect that the gravitational potential wells of collapsed structures should be able to retain and accrete particles, thereby perpetuating the process of structure formation.

Given its limitations, ZA is however still widely used to generate initial conditions for cosmological N-body simulations. This is because ZA gives a very robust estimate of the distribution of matter on the large-scales using only the initial density field. Further accurate initial conditions can be generated using higher orders of the Lagrangian Perturbation Theory [76].

Gravitational collapse models

Galaxies and clusters that we observe today have densities, $\mathcal{O}(\delta) \geq 10^2$, which are orders of magnitude higher than the average density of the Universe. These correspond to highly non-linear regimes, and thus their evolution cannot be described using the perturbation theory approaches. As a result, our best resort to fully understand the non-linear structure formations is through cosmological N-body simulations. However, there are analytical approaches to get valuable insight into this complicated process. In this section, we focus on two such widely studied analytical models of gravitational collapse that leads to the formation of virialised DM halos. Since non-linear growth couples different k-modes, these theories of non-linear evolution is studied effectively in the real space.

1. Spherical Collapse Model for structure formation

Spherical collapse model was developed by Gunn and Gott in 1972 [109]. It gives a simplified picture of the evolution of an over-dense spherically symmetric region isolated in a homogeneous and isotropic background Universe. The tidal effects of the neighbouring density perturbations are ignored, and the spherical collapse dynamics considers only non-relativistic matter.

The gravitational force within the overdense region slows down expansion *w.r.t.* the background, which further increases the overdensity of the region. The overdense region expands, reaches the maximum turn-around radius and starts to collapse. The solution of spherical collapse is cyclic in nature, where inner shells (with higher densities) collapse first, followed by the regions with increasing radii. As collapse to singularity is not possible for a collision-less fluid, the overdense region virialises, and forms a bound structure at the virial radius. The dynamics of spherical collapse model can be described within the Newtonian limit.

Assuming $\Omega_m = 1$ and $\Omega_\Lambda = 0$, we obtain the following numerical values for overdensities at various epochs from the spherical collapse model:

- **For the turn-around radius:** Solving for δ, we get $\delta_{ta} = 4.55$ at the time of maximum expansion. Linearly extrapolated value gives $\delta_{ta,L} = 1.062$.

- **For the virialisation epoch:** Here, the value of density contrast, $\delta_{vir} = 169$. This value would increase with the Ω_m parameter, and for $\Omega_m = 0.3$, $\delta_{vir} \approx 171$. Thus, in order to have a conservative and a cosmology-independent threshold, $\delta_{vir} = 200$ is adopted for defining halos in simulations.

  Linearly extrapolated $\delta_{vir,L}$ =1.686. This value is used in the analytical studies of structure formation (For instance, the Press-Schechter framework [231], defined in Chapter 2).

The results from the spherical collapse model suggest that the final density of the virialized objects does not depend upon the mass of the overdensity, and all objects after collapse will have the same overdensity compared to the background. However, this is a simplified picture as a real density perturbation is neither spherical nor homogeneous, and the collapse of overdensities to form virialised halos involves much more complicated dynamics.

2. Ellipsoidal Collapse model for structure formation

Spherical Collapse Model improves the theory of structure formation by introducing non-linear effects. However, the model still is an oversimplification as the density peaks, in reality are not spherically symmetric but are triaxial with initial shear field, and tidal effects play a key role in determining their evolution [27]. As a result, a more realistic analytical picture of overdensities in a Gaussian random field is generally ellipsoidal rather than spherical, in which the initial gravitational collapse is largely driven by the initial tidal field.

The collapse of a homogeneous ellipsoid can be characterized by its initial overdensity δ_s, and the parameters that define the asymmetry of the tidal field: the ellipticity e, and prolateness p of the tidal field, which are given as:

$$e \equiv \frac{(\lambda_1 - \lambda_3)}{2\delta_s}, \qquad \text{and} \qquad p \equiv \frac{(\lambda_1 - 2\lambda_2 + \lambda_3)}{2\delta_s}. \tag{1.25}$$

Here, we assume that $\lambda_1 \geq \lambda_2 \geq \lambda_3$. Also, $\delta_s = \lambda_1 + \lambda_2 + \lambda_3$. $e(\geq 0)$ measures the ellipticity in (λ_1, λ_3) plane, and p measures the oblateness $(0 \leq p \leq e)$ or prolateness $(0 \geq p \geq -e)$ of the ellipsoid. $p = e \neq 0$ for oblate spheroids, $p = -e$ for prolate spheriods, $p = e = 0$ for spheres.

For a range of e and p, the comparison of evolution of the density contrast values obtained from spherical collapse and the ellipsoidal collapse model is given by the fitting form [251]:

$$\frac{\delta_{ec}(e,p)}{\delta_{sc}} = 1 + \beta \left[5(e^2 \pm p^2) \frac{\delta_{ec}^2(e,p)}{\delta_{sc}^2} \right]^{\gamma} \tag{1.26}$$

Here, $\delta_{ec}(e,p)$ gives the final value of overdensities for the collapsed structures. $\beta = 0.47$ and $\gamma = 0.615$. Plus and minus are used for negative and positive p respectively. δ_{sc} is the overdensity for spherical collapse (*i.e.* when $e = p = 0$).

The deviation between δ_{ec} and δ_{sc} increases for increasing values of both e and p. In terms of variance, the above equation is given as:

$$\delta_{ec}(\sigma, z) = \delta_{sc}(z)\left(1 + \beta\left[\frac{\sigma^2}{\sigma_*^2(z)}\right]^{\gamma}\right). \tag{1.27}$$

Here, $\sigma*(z) \equiv \delta_{sc}(z)$. For massive objects, $\sigma/\sigma* \ll 1$ and solving Eq. (1.27) for this case gives $\delta_{ec}(\sigma, z) \approx \delta_{sc}(z)$. This implies that the massive objects are a special case of more general ellipsoidal collapse model where the collapse can be described using the spherical collapse dynamics.

Also, critical density, $\delta_{ec}(\sigma, z)$ increases with increase in $\sigma(m)$ where $\sigma(m)$ has a monotonically decreasing relation with M (see Fig. 1.2). This implies that δ_{ec} is greater for less massive objects, and low mass objects are influenced more by external tides compared to the high mass halos.

Eq. (1.27) further helps include the effects of ellipsoidal collapse in excursion set approach (defined in the next chapter) to compute the Halo Mass Function.

1.4 Going beyond standard cosmological model

The theory of GR, which forms the basis of the standard ΛCDM model of the Universe, was proposed more than 100 years ago, and since then, numerous tests have been conducted to confirm the validity of this theory. Remarkably, GR has withstood the rigours of time and scrutiny, emerging as a resolute theory of gravity. Through a series of experiments within our own Solar System, such as gravitational time-delay, gravitational lensing, and calculations elucidating the precession of Mercury's orbit [250, 285], GR was found to give accurate and precise estimations. The theory was further validated through the scrutiny of the cosmic microwave background (CMB) data from the early Universe, as demonstrated in missions like COBE, WMAP, PLANCK [257, 130, 68]. Moreover, results from Laser Interferometer Gravitational Wave Observatory (LIGO), and Event Horizon Telescope [1, 2] have not only confirmed some of the most fundamental predictions of GR (like gravitational waves and black holes), but also have led constraints on gravity in the *strong-field regime*. The exact timing of millisecond pulsars is allowing us to dramatically increase the precision with which we can measure a number of fundamental parameters that characterize deviations from GR in the transition from the weak-field to strong-field regime [265, 190]. Collectively, these and many more experiments serve to reinforce the versatility of General Relativity (GR) across a diverse spectrum of length, time, and field strength scales.

This success of GR (and hence the ΛCDM cosmological model) then raises a fundamental question: why should we devote significant efforts to testing the theory of GR? Many reasons attribute to this study. First, none of the present theories can incorporate both GR and the quantum theory. As a result, small- and large-scale physics

are currently described by different physical frameworks. Furthermore, as mentioned in the beginning, ΛCDM model of our Universe requires the addition of Dark Matter and Dark Energy to explain astrophysical and cosmological observations, and neither of these components have compelling explanation from any non-gravitational theories. This raises the possibility that these phenomena may be artefacts arising from the application of an incorrect (or incomplete) theory of gravity dominating the cosmological scales. And, thirdly, there is vast regime of space and time where GR is still not yet well-tested. GR is known to adequately describe the current observations of gravity at small and dense regions, due to the tight constraints from Solar-System and astrophysical tests. However, tests of gravity on the largest scales of our Universe are still not constraining enough. Instead of extrapolating the theory to these regimes, we can consider the possibility of a more general theory of gravity, of which GR could could be a special case in the tested regimes.

Building upon the aforementioned motivations, a plethora of literature has emerged, dedicated to addressing these cosmological discrepancies through the exploration of modifications to various facets within the current cosmological framework ([54, 235, 186] to cite a few). Parallel to theoretical models, there have been a number of proposals for testing deviations from GR predictions on the unexplored regimes on the experimental side ([238, 97, 153]). The resultant constraints would complement those obtained from the tested scales (for example, in the Solar System or in the strong-field regime, or the early universe). These experiments will test different aspects of GR in different gravitational environments, and seek further the validity of the theory.

The accurate data coming from the large cosmological surveys [4, 129, 163, 80, 10] further opens up the possibility of quantitatively probing the nature of DE: an exotic fluid of negative pressure, which is responsible for the current accelerated expansion of our Universe. In GR, the simplest solution to this fluid is to add a constant term in the Einstein field equations, the so-called Cosmological Constant, Λ (as we see in Eq. (1.1)). Nevertheless, this simple solution faces conceptual and observational problems [280], which, in turn, prompts us to look for alternatives to this DE candidate.

In these alternative theoretical frameworks, the late-time Universe's acceleration would not be due to a mysterious DE, but could be a manifestation of the breakdown of GR on cosmological scales. Such scenarios have received large attention in the literature over the past decades, and are commonly described as **Modified Gravity (MG)** theories. Here, viable theories are built by exploiting the freedom in the Einstein-Hilbert's action and introducing additional degrees of freedom (or the *fifth-force*). This fifth-force acts on top of the standard gravity on cosmological scales, and its solutions fuel the low-redshift acceleration of the space-time.

1.5 Modified Gravity models

As mentioned, in Modified Gravity (MG) theories, the additional force acts on cosmological scales on top of the standard gravity. In this thesis, we focus on families of two such MG models: namely $f(R)$ **and nDGP gravity models**. These MG theories offer a perfect test bed to explore the freedom of modifying the Einstein-Hilbert action to produce a physical mechanism effectively mimicking the action of Λ, that would result in cosmic acceleration. Here, we give a brief description of these MG models

1.5.1 $f(R)$ gravity model

In the $f(R)$ gravity model, we consider the possibility of extra non-linear function $f(R)$ of Ricci scalar R in the Einstein Hilbert action. This results through additional coupling between matter and scalar field φ. In this model, the accelerated expansion of the Universe is produced by this $f(R)$ term, thereby replacing Λ in the action integral. The resultant action is

$$S_{f(R)} = \frac{1}{2\kappa^2}\int d^4x\sqrt{-g}(R+f(R)) + \int d^4x\sqrt{-g}L_M[\psi_i, g_{\mu\nu}]. \tag{1.28}$$

Here, $\kappa^2 = 8\pi G$, g is the determinant of metric, ψ_i denotes all matter fields, and L_M is the corresponding Lagrangian density of the matter fields. Here, both matter and the scalar field source the curvature of space-time. Setting $f(R) = 0$ recovers the standard Einstein-Hilbert action.

The variation of action *w.r.t.* the metric field $g_{\mu\nu}$ gives the modified Einstein's field equation (Eq. (1.1))

$$G_{\mu\nu} + f_R R_{\mu\nu} - \left(\frac{1}{2}f(R) - \Box f_R\right) g_{\mu\nu} - \nabla_\mu\nabla_\nu f_R = \kappa^2 T_{\mu\nu}. \tag{1.29}$$

$f_R = df(R)/dR$ is scalaron which is the additional degree of freedom in $f(R)$. This quantity controls the range of the interaction of the scalar, and hence quantifies the deviation from GR. $\Box = \nabla^\mu\nabla_\mu$ is the d'Alambertain, $G_{\mu\nu}$ is the standard Einstein tensor, $R_{\mu\nu}$ is the Ricci tensor, and $T_{\mu\nu}$ is the Energy-momentum tensor.

Taking the trace of Eq. (1.29), we get the equation of motion of the scalaron

$$\nabla^2 f_R = \frac{1}{3}\left(R - f_R R + 2f(R) + 8\pi G\rho_m\right). \tag{1.30}$$

N-body simulation of the $f(R)$ gravity solve the above equation at every time-step to determine the fifth-force ($= \nabla^2 f_R$).

In our work, we have considered the functional form of $f(R)$ introduced in [133]

(referred to as the Hu-Sawicki (HS) $f(R)$ gravity) where

$$f(R) = -\tilde{m}^2 \frac{c_1(-R/\tilde{m}^2)^n}{c_2(-R/\tilde{m}^2)^n + 1}. \tag{1.31}$$

Here, $\tilde{m}^2 = H_0^2\Omega_m$ is the mass scale and c_1, c_2 and n are positive free parameters which control the $f(R)$ expansion history. Here the scalaron field has the form

$$f_R = -\frac{c_1}{c_2^2} \frac{n(-R/\tilde{m}^2)^{n-1}}{[(-R/\tilde{m}^2)^n + 1]^2}. \tag{1.32}$$

For this model, the background expansion history can be made similar to the standard ΛCDM, but without introducing a cosmological constant. This can be achieved by setting $c_1/c_2 = 6\Omega_\Lambda/\Omega_M$, and

$$R \approx 3m^2 \left[a^{-3} + \frac{2}{3}\frac{c_1}{c_2}\right], \tag{1.33}$$

which gives $|R| \gg m^2$ and

$$f_R \approx -n\frac{c_1}{c_2^2}\left(\frac{m^2}{-R}\right)^{n+1}. \tag{1.34}$$

This limit allows us to fully specify Hu-Sawicki $f(R)$ model for a particular choice of (n, f_{R0}). Here, f_{R0} is the present value of the f_R parameter, which is given by

$$\frac{c_1}{c_2^2} = -\frac{1}{n}\left[3\left(1 + 4\frac{\Omega_\Lambda}{\Omega_m}\right)\right]^{n+1} f_{R0} \tag{1.35}$$

In this thesis, we explore the $f(R)$ variants with $n = 1$, and $|f_{R0}| = 10^{-5}$ (F5), and $|f_{R0}| = 10^{-6}$ (F6).

1.5.2 nDGP gravity model

The normal branch of Dvali-Gabadadze-Porrati (nDGP) model introduced in [90, 79] is one of the simplest and most popular explanations of the accelerated expansion of the Universe through higher dimensional spacetime. In this gravity model, all standard forces, except gravity, are confined on a four-dimensional brane that is embedded in five-dimensional bulk spacetime, and gravity propagates in an additional fifth dimension. Here, the modified Einstein-Hilbert action is given by [155]

$$\begin{aligned} S = \int d^4x\sqrt{-g}\left[\frac{R}{16\pi G} - L_m(\psi, g_{\mu\nu})\right] + \\ \int d^5x\sqrt{-g^{(5)}}\left[\frac{R^{(5)}}{16\pi G^{(5)}}\right], \end{aligned} \tag{1.36}$$

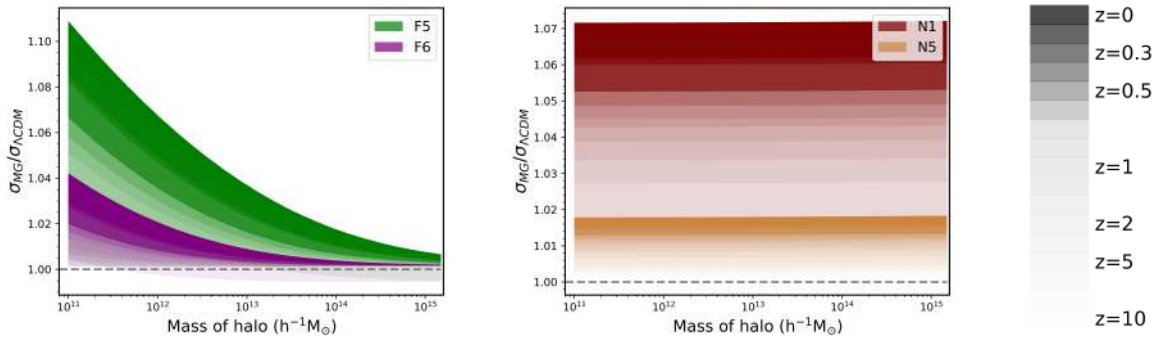

Figure 1.3: Linear growth enhancement, defined in terms of the $\sigma(M)$ relation (Eq. (1.23)) for the Modified Gravity (MG) models *w.r.t.* ΛCDM from $z = 0$ to $z = 10$, as a function of halo mass. The left plot shows the growth enhancement in variants of $f(R)$ gravity model, and right plot are the nDGP gravity variants.

Where g, R, G and L_m denote the determinant of the metric, Ricci scalar, Gravitational constant and Lagrangian density respectively on the 4D brane and their counterparts with superscripts $^{(5)}$ denote their equivalents on 5D bulk.

The ratio of the gravitational strengths defines a parameter for the model given by crossover scale, r_c, *i.e.*

$$r_c = \frac{1}{2}\frac{G^{(5)}}{G}. \tag{1.37}$$

This corresponds to the transition scale at which gravity changes from 5D on larger scales to 4D on small scales. For $r > r_c$, gravity leaks out of the 4D brane as the second term dominates over the first term in Eq. (1.36).

The variation in action changes the expansion rate of the Universe in nDGP cosmology which is given by

$$H(a) = H_0\sqrt{\Omega_{m0}a^{-3} + \Omega_{DE}(a) + \Omega_{rc}} - \sqrt{\Omega_{rc}}. \tag{1.38}$$

Here, $\Omega_{rc} = 1/(4H_0^2 r_c^2)$ is a single parameter which can uniquely define any nDGP model. Here we can infer that in the limit $H_0 r_c \to \infty$, we recover standard GR.

In the above eqn., we can see that this model requires addition of an explicit dark energy component ρ_{DE} (not necessarily Λ) with an appropriate equation of state on the four-dimensional brane. Ω_{DE} is an effective cosmological constant tuned to yield expansion history similar to ΛCDM i.e. $H(a) = H_{\Lambda CDM}(a)$. Also, equation of state $\omega_{DE}(a) \geq -1$, which reduces to -1 for the case of $r_c H_0 \to \infty$ [31].

1.6 Structure formation in Modified Gravity scenarios

Both $f(R)$ and nDGP gravity models are formulated in a way that, on large scales, the evolution of scalar metric and density perturbations must be compatible with the ΛCDM expansion history [68]. On small scales, in DM halos, such as our own galaxy,

modifications must be suppressed in order to satisfy stringent local tests of general relativity [250, 285] (more details in the Section 1.7). As a result, the main modifications that can be expected in these MG models are on the intergalactic scales. In this section, we define how the standard structure formation paradigm is altered in context of these two MG models.

The growing mode equation (Eqs. (1.16) and (1.17)) is modified in MG models to give

$$\ddot{D} + 2H\dot{D} - 4\pi G_{eff}\bar{\rho}_m D = 0. \tag{1.39}$$

Considering only scalar perturbations and assuming spatial flatness, perturbed FRLW metric can be written as [28]

$$ds^2 = (1+2\Psi)dt^2 - a(t)^2(1-2\Phi)dx^2, \tag{1.40}$$

where t is the cosmic time, $a(t)$ is the scale factor, and Ψ and Φ are the gravitational potentials due to density perturbations (also called as the Bardeen potentials [28]). On sub-Horizon scales, we can work in the quasi-static approximation, in which the time variation of the gravitational potentials is small compared to the Hubble time, and one can neglect the time derivatives of these potentials in the perturbation equations.

In nDGP, φ is the scalar degree of freedom associated with the brane bending mode which is due to the displacement on the brane, and the gravitational forces in nDGP are governed by

$$\nabla\Psi = \nabla\Psi_N + \frac{1}{2}\nabla\varphi. \tag{1.41}$$

We can see that φ here sources the fifth-force. The equation of motion of φ in quasi-static approximation for spherically symmetric FRLW spacetime is [155]

$$\nabla^2\varphi + \frac{r_c^2}{3\beta(a)a^2}[(\nabla^2\varphi)^2 - (\nabla_i\nabla_j\varphi)^2] = \frac{8\pi G}{3\beta(a)}a^2\delta\rho_m. \tag{1.42}$$

This equality arises on considering the weak-field limit i.e. Φ, Ψ, and the gravitational potential $\phi \ll 1$. $\delta\rho_m = \rho_m - \bar{\rho}_m$ is the matter density perturbation, and $\beta(a)$ governs the magnitude of the fifth-force given by [243]

$$\beta(a) = 1 + 2H(a)r_c\left(1 + \frac{\dot{H}(a)}{3H(a)^2}\right), \tag{1.43}$$

where the overdot denotes derivative with time.

Brane bending modes are always attractive in nDGP [242] and hence, $\beta(a)$ in Eq. (1.43) is always positive and decreases with time which results in always an enhancement of gravity and in-turn, structure formation with time.

In nDGP gravity, on scales much smaller than both the horizon ($\ll c/H$), the model is described as an effective scalar-tensor theory. We consider quasi-static approximation

and the modified Poisson equation governing structure formation can be expressed as

$$\nabla^2\Psi = 4\pi G a^2 \delta\rho_m + \frac{1}{2}\nabla^2\varphi. \tag{1.44}$$

For this, $G_{eff,\mathrm{nDGP}} = G\left[1+\frac{1}{3\beta(a)}\right]$ from Eq. (1.39) is the effective gravitational strength that quantifies enhancement of gravity due to the fifth-force, and is a function of only time (given here by the scale factor). As a result, *linear growth of structures is time-dependent but scale-independent in the nDGP gravity theory.* This can also be seen in the right plot of Fig. 1.3, where we plot the ratio of growth in nDGP *w.r.t.* ΛCDM (growth is given here in terms of the $\sigma(M)$ relation (Eq. (1.23)), as a function of halo mass (which also corresponds to the physical length scales). Here N1 and N5 denote different nDGP variants, with the nDGP parameter $\mathrm{r}_c\mathrm{H}_0 = 1$ and 5 respectively. This ratio is plotted across different epochs (from $z = 10$ to $z = 0$). Here we can see that the growth enhancement in nDGP increases with time, and is a constant across the length (or mass) scales.

For the case of $f(R)$ gravity, in the quasi-static and weak field limits, the modified Poisson equation is given by [49]

$$\nabla^2\Psi = 4\pi G a^2 \delta\rho_m - \frac{1}{2}\nabla^2 f_R, \tag{1.45}$$

where

$$\nabla^2 f_R = \frac{a^2}{3}(\delta R - 8\pi G\delta\rho_m). \tag{1.46}$$

Here, $\delta R = R(f_R) - \bar{R}$. This is approximated in the limit of $|f_R| \ll 1$ at all redshifts and $|f/R| \ll 1$.

In Fourier space, Eq. (1.45) can be written as

$$k^2\Psi(k) = 4\pi G\left(\frac{4}{3} - \frac{1}{3}\frac{\tilde{m}_{fR}^2 a^2}{k^2+\tilde{m}_{fR}^2 a^2}\right) a^2\delta\rho_m(k). \tag{1.47}$$

In the small-scale limit, $k \gg \tilde{m}_{fR}$, there is 1/3 enhancement of gravity compared to GR. This is the maximum enhancement in $f(R)$ models, independent of its functional form.

For the equation of linear growth of perturbations, Eq. (1.39), $G_{eff,f(R)} = G\left[\frac{4}{3} - \frac{1}{3}\frac{\tilde{m}_{fR}^2 a^2}{k^2+\tilde{m}_{fR}^2 a^2}\right]$. Contrary to the case of nDGP gravity, *the linear growth enhancement in $f(R)$ gravity is both scale and redshift dependent* which we also see in the left plot of Fig. 1.3, where the growth enhancement is a function of both scale (given here by halo mass) and time (redshift) for each $f(R)$ variant. The linear growth enhancement increases with time, and decreases with the length scale. Here, as previously highlighted, F5 and F6 denote different $f(R)$ variants.

1.7 Screening mechanism

We have previously highlighted that there are stringent precise tests of GR on small scales (like our Solar System), or strong field high density regimes (like black holes or neutron stars). Thus, any prospective MG theory needs to employ a theoretical mechanism that would allow it to recover standard GR behaviour on Solar System scales, and around dense bodies. Such an physical phenomenon is called a *screening mechanism*, which, as the name suggests, screens the fifth-force in these regimes. While the screening mechanisms allow a given theory to pass the small-scale and strong field regime observational tests, its introduction comes with a high price, as theories with screening exhibit much stronger non-linear behaviour, and as a result, have interesting implications on structure formation and associated observables.

There are a few different types of screening mechanisms. This complicates the program of extracting information from the screening-dominant regimes in a controlled manner, but at the same time offers the prospect of testing a greater range of MG theories by means of just a few screening mechanisms. We describe here the screening mechanisms implemented in our MG theories. Hu-Sawicki (HS) $f(R)$ implements *Chameleon screening*, whereas nDGP implements *Vainshtein screening* to suppress the fifth-force. Both these screening mechanisms have fundamental physical differences, which we describe in the following sub-sections.

1.7.1 Chameleon Screening Mechanism

Chameleon cosmology has been proposed in [146] that allows for the evolution of scalar fields with the possibility of minimal coupling to matter. This screening mechanism is employed to screen the fifth-force in the HS form of $f(R)$ gravity models to evade the Solar System constraints [133].

Scalar fields require a mass to propagate which depends on the local matter density, and its value is determined by the interplay of the field's self-interactions and conformal coupling of the scalar field to matter of the form $e^{\beta\phi/M_{pl}}$, where β is the coupling constant (different from Eq. (1.43)). Higher density corresponds to a massive field and, in turn a shorter range of the fifth-force.

For scalar field with heavy mass in high-density regions, thin-shell develops screening in high density regions. For a top-hat overdensity, screening develops when

$$\frac{\varphi_{out} - \varphi_{in}}{6\beta\phi_{in}} \ll 1.$$

Where φ_{out} and φ_{in} are the values of the scalar field outside and inside of the overdensity and ϕ_{in} is the Newtonian potential at the surface of the overdensity

Here the field outside the body is generated by the contribution from the thin shell and the bulk of the body contributes negligibly. The profile of the field outside the

body is given by

$$\varphi(r) = -\frac{\beta}{4\pi}\frac{M_C e^{-m_B(r-r_C)}}{r} + \varphi_{out},$$

where r_C and M_C the radius and mass of the top-hat overdensity, and the first term is the contribution from the thin-shell which is exponentially suppressed and depends on the mass of the body.

The gravitational force on a test particle of mass m outside the overdensity is given by

$$F = \frac{GM_C m}{r^2}\left(1 + \frac{1}{3}\frac{\Delta R}{R_C}\right), \tag{1.48}$$

and the screening factor is

$$\frac{\Delta R}{R_C} = min\left\{\frac{3|\varphi_{in} - \varphi_{out}|}{2\phi_C}, 1\right\}. \tag{1.49}$$

$\phi_C = \frac{GM_C}{R_C}$. For a massive overdensity (small value of $\frac{1}{\phi_C}$), or a high density regime (small value of $|\varphi_{in} - \varphi_{out}|$), $\frac{\Delta R}{R_C} \ll 1$, thereby screening the fifth-force in Eq. (1.48) and retrieving the standard Newtonian gravitational force.

1.7.2 Vainshtein Screening Mechanism

On very large scales, in the equation governing the gradient of φ (Eq. (1.42)), $|\nabla^2\varphi| \ll r_c^{-2}$, the linear term on the RHS dominates and the modified Poisson Equation (Eq. (1.44)) becomes

$$\nabla^2\Psi = \nabla^2\Psi_N + \nabla^2\varphi = 4\pi G a^2\left(1 + \frac{2}{3\beta(a)}\right)\delta\rho. \tag{1.50}$$

The above eqn. is valid on linear scales with small density fluctuations, and for regions far away from massive bodies.

On the contrary, in the regime $|\nabla^2\varphi| \gg r_c^{-2}$, non-linear terms in Eq. (1.42) dominate, thus implying $\nabla^2\varphi \ll \frac{8\pi G}{3\beta(a)}\delta\rho a^2$

$$\nabla^2\Psi = \nabla^2\Psi_N + \nabla^2\varphi \approx 4\pi G a^2\rho\delta \approx \nabla^2\Psi_N. \tag{1.51}$$

Here, we can see that the non-linearity of scalar fields suppresses the coupling between the scalar field and matter. This is referred to as the Vainshtein screening mechanism [271] which is employed in the nDGP formalism to recover GR in regions which are much denser *w.r.t.* the cosmic mean.

A simple illustration of Vainshtein screening can be done by considering a spherically symmetric solution [244, 243, 155, 184] in which case, Eq. (1.42) can be written as

$$\frac{d\varphi}{dr} = \frac{GM(r)}{r^2}\frac{w}{3\beta}g\left(\frac{r}{r_v}\right), g(x) = x^3\left(\sqrt{1+x^{-3}} - 1\right). \tag{1.52}$$

Here, $M(r)$ is the enclosed mass, and r_v is the Vainshtein radius given by

$$r_v^3 = \frac{16GM(r)r_c^2}{9\beta^2}. \tag{1.53}$$

As can be seen in the above equation, r_v depends on the mass considered, its configuration and the cross-over scale r_c. Vainshtein screening has little or no dependence on the environment, unlike chameleon screening [146], but from Eqs. (1.50) and (1.51), we can see that the dynamics of φ depends whether the object is inside an under-dense or an over-dense environment [214]. The resultant force enhancement in nDGP *w.r.t.* GR is given by

$$\Xi(r) \equiv \frac{d\phi/dr}{d\Psi_{GR}/dr}. \tag{1.54}$$

For a given Lagrangian radius $R_L(z)$, $\Xi(z)$ from Eq. (1.52) given by[93]

$$\Xi(R_L(z)) = \frac{2}{3\beta}\frac{R_L(z)^3}{r_v^3}\left(\sqrt{1+\left(\frac{r_v}{R_L(z)}\right)^3}-1\right). \tag{1.55}$$

For $R_L(z) \gg r_v$, $\Xi(r) \to \frac{1}{3\beta}$ which corresponds to linear enhancement of gravity and for small $R_L(z), \Xi(r) \to 0$ and the fifth-force is screened.

1.8 Growth parameterisation

When dealing with cosmological observations with the aim of constraining the gravity model, it is useful to adopt a phenomenological approach. Parameterised gravity frameworks are a potent and efficient method for testing gravity without bias towards a specific model.

For the MG models that we consider in this work, the lensing potential, which describes the propagation of relativistic particles, $(\Psi - \Phi)/2$ is unchanged. However, the dynamical potential, Ψ gets modified *w.r.t.* standard GR, giving rise to a fifth-force.

The first-order perturbed Einstein equations in Fourier space gives the evolution of Φ and Ψ

$$-k^2\Phi(a,k) = 4\pi G a^2 \mu(a,k)\rho(a)\Delta(a,k), \tag{1.56}$$

and

$$-k^2(\Phi+\Psi)(a,k) = 8\pi G a^2 \sum(a,k)\rho(a)\Delta(a,k). \tag{1.57}$$

Here $\rho(a)$ is the average density, and $\Delta(a,k) = \delta + 3aH\theta$ is the comoving density contrast, δ the fractional overdensity, and θ the expansion scalar $(= \frac{\nabla.\vec{v}}{aH})$. The ratio of the two gravitational potentials is denoted as η, and is called the gravitational anisotropic stress,

$$\eta \equiv \frac{\Psi(a,k)}{\Phi(a,k)}. \tag{1.58}$$

$\eta(a,k)$, $\mu(a,k)$ and $\Sigma(a,k)$ quantify all possible deviations of Einstein's gravity in these equations. The value of these parameters are equal to unity for the case of standard GR. These parameters are related by

$$\sum(a,k) = \frac{\mu(a,k)}{2}(1+\eta(a,k)). \tag{1.59}$$

The parameter μ quantifies the additional force, and therefore is given as

$$\frac{G_{eff}(a,k)}{G} = \mu(a,k). \tag{1.60}$$

Here, G is the standard Newton constant.

1.9 *N*-body simulations

DM halos cannot be directly probed in observations, and we can only study them indirectly through gravitational lensing surveys, or cluster studies. Moreover, DM structure formation takes place at length and time scales which are way beyond any imaginable experimental limits. Hence, the only direct way to study DM dynamics and evolution is through *numerical simulations*. Using computational powers, we can create many realizations of DM-only simulations (due to stochastic nature of initial conditions) in order to compute reliable statistics of the measured quantities, and we can have a full-time evolution of the matter distribution, in combination with a snapshot of today's distribution.

Initial density perturbations were of the order of $\sim \mathcal{O}(10^{-5})$ [68], and perturbations evolved to present day DM halos, with central densities over $\mathcal{O}(10^6)$. As we showed in the previous sections, the growth of structures in the former case of small perturbations can be described analytically using the Linear Perturbation Theory. This picture has shown to be accurate, and has been tested rigorously in the past, both for GR and non-GR theories. However, for the latter case of higher densities, most of the cosmological information concerns the non-linear regime of structure formation, which cannot be described using the analytical methods. As a result, the only way to probe and study the non-linear regime of gravitational instability is to use sophisticated algorithms in computer simulations. Here, simulations play a significant role of connecting the theoretical predictions with observations, by giving a reliable and quantitative insight into the growth of structures from primordial initial conditions to the present-day large-scale structures.

Furthermore, MG theories have additional computations involving the fifth-force, and hence have a large unconstrained parameter space. This makes their analytical study challenging. Also, the non-linear screening mechanisms implemented in these MG frameworks further add to the complexity of understanding the impact of these theories on large-scale structure formation. As a result, the evolution of our Universe

by invoking these MG models and screening physics can be properly understood, and the distinction in large-scale structure properties *w.r.t*. GR can be quantitatively measured only by the means of cosmological simulations. Also, simulations are the tools for building fast and efficient methods (like semi-analytical models, or emulators) that help explore the parameter space of these MG phenomenologies.

For the purpose of this thesis, we mainly focus on DM density fields and halo catalogs generated using ELEPHANT (Extended LEnsing PHysics using ANalaytic ray Tracing) cosmological simulations (discussed in [60, 214, 11]). For these simulations, we have the Hu-Sawicki (HS) form of $f(R)$ gravity [133], which implements Chameleon screening [146], and the normal branch of Dvali-Gabadadzi-Porrati (nDGP) model [90], which implements Vainshtein screening [271]. $f(R)$ simulations are run using ECOSMOG code [175, 50], and nDGP simulations are run using ECOMOG-V code [173, 29]. Both are parallelizable Adaptive-mesh-refinement (AMR) codes for MG, and are based on publicly available RAMSES code [266]. In the AMR approach [37], the grid cells in high-density regions are much finer than the cells in regions of low density. This approach is fundamentally needed in the case of MG theories in order to understand the dynamics of both the fifth-force, and the screening mechanisms, where latter is especially dominant in the high density regimes. In the AMR approach, a grid is refined whenever the number of particles within a grid cell exceeds some user-defined threshold, N_{th}. This ensures that the high-density regions are sufficiently well-resolved, while saving computational resources in regions where the density is lower. When the effective particle number in a grid cell exceeds N_{th}, the cell is split into eight daughter cells so that the code hierarchically achieves higher resolutions in dense environments.

Both ECOSMOG and ECOMOG-V implement new sub-routines to RAMSES for solving the additional dynamical degrees of freedom (*i.e.* the scalar fields) present in MG theories. These codes solve the equation of motion of the scalar field by performing Gauss-Seidel iterative relaxations on an adaptively refined grid. AMR technique in these force calculations are needed both to accurately trace the trajectories of the particles, and in-turn to ensure the accuracy of the fifth-force solutions.

The ELEPHANT simulations are run for 1024^3 collision-less and equal mass DM particles with the mass of each particle, $m_p = 7.798 \times 10^{10} \mathrm{M}_\odot/h$, and the comoving force resolution $\epsilon = 15\mathrm{kpc}/h$ in a box of $1024\mathrm{Mpc}/h$. The simulation are run from an initial redshift $z_{ini} = 49$, to a final redshift $z_{final} = 0$, with the initial conditions generated by MPGRapfic [232], using Zel'dovich Approximation [291]. A high value of initial redshift ensures long enough time for the evolution of the system to wipe out any transients that would affect the initial particle distribution, which could be a consequence of employing the first-order Lagrangian perturbation theory [76].

To reduce the effect of sample variance, each model has 5 independent realizations at four cosmic epochs: $z = 0$, 0.3, 0.5 and 1, which is achieved by selecting a different seed value. As both $f(R)$ and nDGP models deviate negligibly from ΛCDM at early times,

each realization is started using the same initial conditions which also helps us to avoid any anomalies that could arise due to differences in phases of the initial density fields. As a result, any difference in the clustering dynamics could be attributed specifically to the modifications in the underlying gravitational physics, as MG realizations have been evolved using the modified equations of motion.

The background cosmological parameters of the simulations are: Fractional matter density $\Omega_m = 0.281$, fractional baryonic density $\Omega_b = 0.046$, fractional density of CDM $\Omega_{CDM} = 0.235$, fractional density of cosmological constant $\Omega_\Lambda = 0.719$, fractional density of relativistic species $\Omega_\nu = 0$, Hubble constant in units of 100 km $s^{-1}Mpc^{-1}, h = 0.697$, slope of power spectrum of primordial density $n_s = 0.971$ and the value of variance of fluctuations normalized for a sphere at 8 Mpc h^{-1}, $\sigma_8 = 0.842$.

The ELEPHANT simulations consider ΛCDM, 2 variants of HS $f(R)$ gravity with the parameters of Eq. (1.35): $n = 1$ and $|f_{R0}| = 10^{-5}$ and 10^{-6} (decreasing order of variation from ΛCDM) which are here referred to as F5 and F6 respectively, and 2 variants of nDGP with $r_c H_0 = 1$, and 5 (again with decreasing order of variation from ΛCDM) written as N1 (or nDGP(1)) and N5 (or nDGP(5)) respectively.

Halos are identified using the Robust Overdensity Calculation using K-Space Topologically Adaptive Refinement (ROCKSTAR) halo finder [36], which evolves the DM particles in six-dimensional phase-space to identify halos, using information about both the velocity and position of particles. This halo finder is a massively parallel code [151], and is highly efficient in resolving halos for lower number count of DM particles [189]. We use the halo definition, M_{200} which is the mass contained in a region, within which the mean density of the Universe is 200 times the critical density $\rho_{crit}(z) \approx 2.775 \times 10^{11} h^2 M_\odot Mpc^{-3}$. We restrict our analysis to halos with mass equal to or greater than 100 times m_p to minimize the shot noise or resolution effects. In principle, the presence of the fifth-force would require a modification to ROCKSTAR (or in general to any standard halo-finding algorithm). Nonetheless, the authors in [174] found the effect of this modification to be quite small, and hence we use the standard ROCKSTAR algorithm on both GR and MG models.

In the first three plots of Fig. 1.4, we show a 10.24 Mpc/h slice of DM density field obtained from ELEPHANT simulations, for ΛCDM, F5, and N1 gravity models. The density fields are obtained for 1024^3 grid, using Triangular-Shape-Cloud (TSC) technique [260]. We see large-scale cosmic structure, with distinction in overdense (bright) and underdense (dark) regions across the density field. Here, we can clearly see that the overall distribution of large-scale structures are not altered from the GR paradigm. In the bottom two plots, we show how the density differs across these strong MG variants *w.r.t.* ΛCDM. On the contrary, here is a clear distinction in the density distribution between the standard and the non-standard cases.

For validity and sanity checks, we have also used simulations from MILLENNIUM[1]

[1] http://gavo.mpa-garching.mpg.de/Millennium/

and COSMOSIM[2] public databases. Furthermore, we augmented our analysis by incorporating simulations conducted within our research group. Throughout this thesis, unless explicitly specified, all the simulations discussed are derived from the analysis of the ELEPHANT simulations.

1.10 Dark Matter halos and the associated statistics

We emphasised in the previous sections that going beyond the smooth background Universe offers a multitude of additional observables that probe the evolution of structures in the Universe. Both the $f(R)$ and nDGP gravity models mimic the cosmological constant at the background level to satisfy the observational constraints. However, they have different evolution of perturbations, and hence these models can still give significantly different predictions of the growth rate of structures than what we expect from standard ΛCDM. As a result, in these models, we expect different values of the measures associated with the structure formation, which leaves the possibility to search for MG signatures in the properties of LSS. Therefore, the LSS of the Universe offers a promising testing ground to explore as to what extent one can detect departures from GR with present and upcoming cosmological data.

DM halos are the building blocks of the LSS, and their associated observations. As elaborated, these are the product of evolution of tiny perturbations from the early Universe to the present day, where they host galaxies and the observable Universe. Hence, the study of formation and evolution of halos is expected to be sensitive to the underlying structure formation theory, and the associated measures/observables form one of the key ingredients in the theoretical description of LSS, and to test different structure formation scenarios in beyond-GR models.

Taking this as the motivation, we build this thesis on the study of the properties of DM halos in both $f(R)$ and nDGP gravity models. These LSS properties form the basis of many cosmological observables and measures. Namely, we study *Halo Mass Function* (HMF) (Chapter 2 and Section 5.4.1), *halo bias* (Section 4.1), and *halo density profile* (Section 4.2.1) in these MG models, and how they differ from standard ΛCDM results across length and time scales. We further show how these LSS properties can further be used to propose analytical modelling to the study the properties of non-linear DM density fields, which further finds applications in the observational domains (Chapter 3). In later sections (Chapters 4 and 5) we show how these LSS properties in MG models are further impact by large-scale environments and other internal halo attributes.

[2] https://www.cosmosim.org/

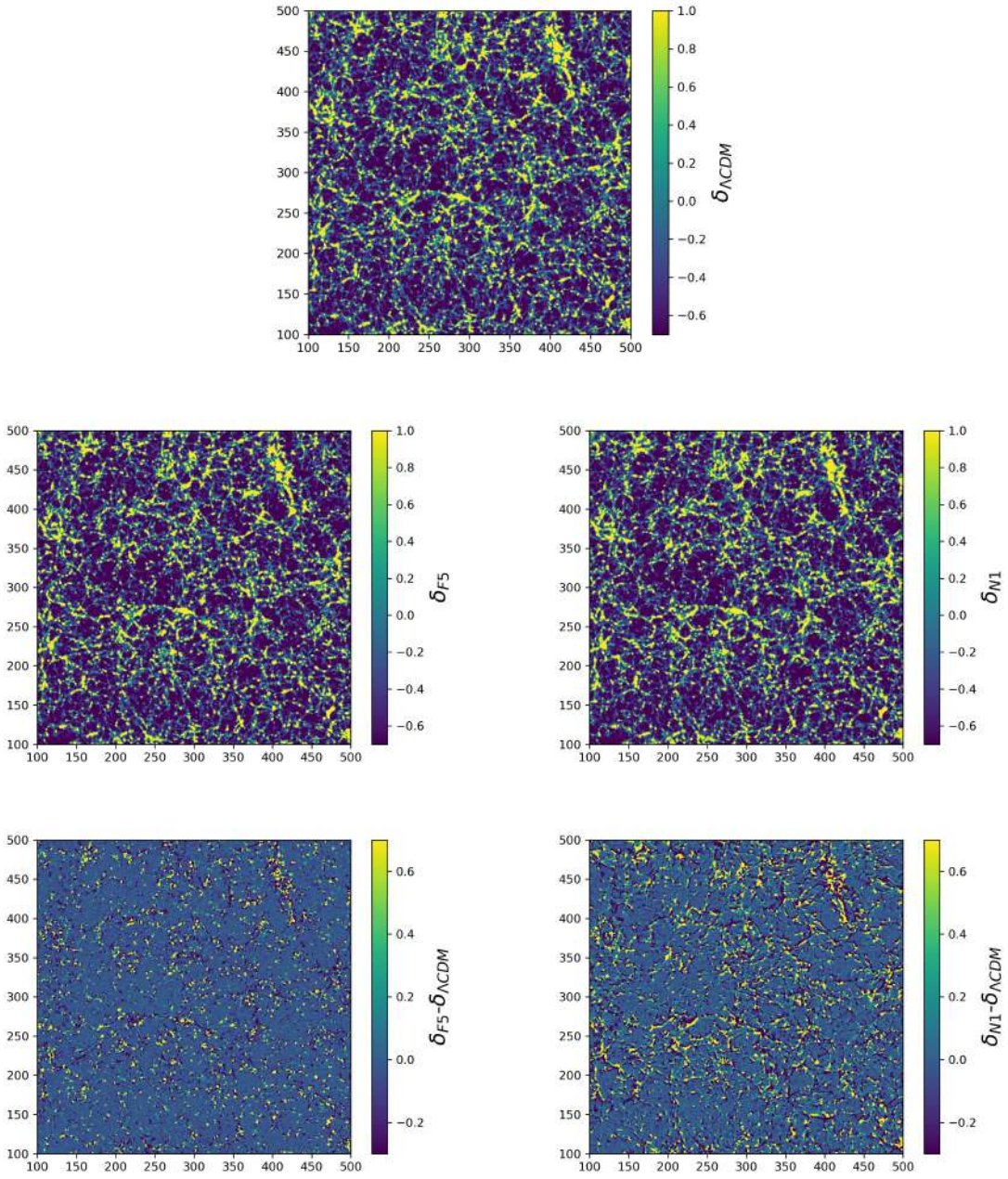

Figure 1.4: *First three plots:* A thin slice of DM density field of 10.24 Mpc/h from ELEPHANT simulations, for ΛCDM, F5 and N1, at $z = 0$. *Bottom plots:* A comparison of the density fields in F5 (left) and N1 (right) with ΛCDM. The colormap on the right of each plot represents the density contrast, with lighter colours representing higher density regions. The density field is obtained for 1024^3 grid, using the Triangular-Shape-Cloud (TSC) technique.

1.11 Thesis overview and our motivation

This thesis presents the results of a planned research that aimed at analysis, quantification and modeling of the simulated large-scale cosmic density fields both in standard ΛCDM and Modified Gravity (MG) models. We characterise this work into two broad topics:

1. **To build a semi-analytical framework for computing non-linear Dark matter and halo properties in Modified Gravity models. This part is discussed in Chapter 2 and Chapter 3.**

   Cosmological simulations are our best tools to understand the non-linearities associated with the large-scale structure formation, that occurs at large length and time-scales. Owing to the well-understood background physics, the fields of simulations and theoretical modelling in ΛCDM are very sophisticated and powerful. Furthermore, the parameter space of the standard model is strongly constrained by the influx of high-quality data from past and present surveys [128, 80, 3, 115, 10, 274].

   On the contrary, MG models lack strong physical constraints in their parameter space, resulting in a substantially large number of degrees of freedom. MG simulations are available, but are however limited and mostly model-specific. The additional calculations of the fifth-force, and the inherently non-linear screening mechanisms further increases the complexities in these MG computations. Consequently, MG simulations are characterized by their considerably higher costs and time requirements. All these factors make MG simulations orders of magnitude more expensive and time-consuming than the standard ΛCDM N-body runs. Considering the plethora of potentially viable MG theories, it is impractical to thoroughly investigate the parameter space of each model, both analytically or by using cosmological simulations. These simulations need to be run for a specific MG variant, and it becomes tricky to generalise the results from one model to another.

   Given the considerable computational and monetary expenses of MG simulations, it is worthwhile to develop alternative approaches to simulations, which capture the main MG effects, and simultaneously help enable reliable and quicker forecasts and constraints over cosmological parameters. In Chapters 2 and 3, we worked in this regard and built an analytical framework to compute non-linear measures associated with these MG frameworks, which are general enough to be, in principle, extended to other beyond-GR models.

   In Chapter 2, we study the Halo Mass Function, and its significance. We further probe this quantity in both Hu-Sawicki $f(R)$ and nDGP gravity models. The results of this chapter are published in [111, 112], in which we study the difference

in MG to ΛCDM HMF across different mass and time scales. In addition, we also propose different analytical expressions that can help us compute MG HMF, without requiring to run MG simulations. In Chapter 3, we further used our HMF modelling, along with the inputs of halo bias and halo concentration (from existing literature), to build an analytical framework for computing non-linear matter power spectrum in our MG models. We did this by extending the standard Halo Model framework [73, 22] to these MG models. Our complete analytical framework is presented in [110]. We summarise the findings of both these articles in the last section of the respective chapters, and these articles are attached after each chapter.

2. **To quantify the dependence of non-linear measures associated with large-scale cosmic density field on the environment, and halo properties in Modified Gravity scenarios. This part is discussed in Chapter 4 and Chapter 5.**

   Greater advancements in cosmological simulations have shown that the large-scale halo properties have an intricate relationship with other attributes: like their assembly histories and associated properties, or the environment that hosts them. These dependencies source further systematics in the studies of large-scale clustering, and should be accounted for properly in order to get unbiased and accurate constraints on cosmological parameter analysis. These additional dependencies have been well investigated for ΛCDM scenario, and we extend these investigations to our beyond-GR models. This venture is essential to break any degeneracies which would be an effect either of the MG, or the halo properties, or the hosting environment. This further helps quantify systematics that would be useful in order to achieve percent-level accuracy which we want from our present and future surveys [163, 182, 262].

   In Chapter 4, we study the Halo Assembly Bias (HAB), which quantifies the differences in large-scale halo clustering for same mass halos. HAB from different attributes has been thoroughly investigated for ΛCDM. However, such explorations are majorly lacking for beyond-GR scenarios. To circumvent this, we investigate the impact of our MG phenomenologies on the HAB amplitude, and how it differs from ΛCDM. In this chapter, we first define the large-scale clustering in terms of the halo bias relation. Later we describe the internal halo properties that we use to quantify the HAB effect in both ΛCDM and MG: halo concentration, and halo spin. We further investigate the role of these intrinsic halo properties on influencing the halo bias in both ΛCDM and MG models, and quantify the differences in the HAB amplitude. This is an important venture in order to understand any unknown systematic that could be due to the MG physics on large-scale clustering measurements.

   Building on similar grounds, we investigate the impact of MG on large-scale prop-

erties in the context of different cosmic web (CW) environments in Chapter 5. It has been shown in previous studies how CW impacts LSS properties, and we extend this analysis to see how these properties are further effected by modifying the underlying gravitational forces, and how environment impacts these modifications. In this chapter, we first investigate the impact of MG on the clustering amplitudes of the density fields in different CW environments. In the later half of this chapter, we consider the role of CW environment in influencing the impact of MG physics on halo properties, namely Halo Mass Function and Halo spin. For all the Dark matter density and halo properties investigated in this chapter, we find a non-trivial influence of the CW environment on MG. This highlights the importance of CW in providing valuable insights into comprehending the dynamics of the fifth-force and the screening mechanisms.

In Chapter 6, we summarise our findings, along with future implications of our results.

Chapter 2: Halo mass function in Modified Gravity cosmologies

All my life through, the new sights of Nature made me rejoice like a child.

-Maria Skłodowska-Curie

Chapter 2

Halo Mass Function in Modified Gravity cosmologies

One of the most fundamental predictions of the theory of structure formation is the number density of halos of a given mass, which is termed as the ***Halo Mass Function*, (HMF)**. This quantity can be directly measured in the simulations, and can be estimated observationally using tracers of underlying halos, which are galaxy clusters. This is possible as a cluster can be identified with a massive halo; and the number of member galaxies are observed to be correlated with the mass of the hosting halo [227, 157]. The HMF serves as the foundational element in many theoretical studies of late-time LSS and galaxy formation models [*e.g.* 144, 161, 252, 73, 157]. Considering the pivotal role of this cosmological statistic in the LSS studies, it becomes imperative to evaluate its deviations from ΛCDM in viable MG theories.

HMF is a crucial connecting point between cosmological models and observations as the number of halos or galaxy clusters across epochs are sensitive to the background cosmologies, and the underlying governing physics [245, 56, 108, 217]. Different N-body simulations with different initial conditions, background cosmology, and/or different DM physics lead to different HMF predictions. The authors in [24] showed that the HMF varies with the spectral index of the primordial power spectrum, while [74] showed that the shape of the HMF depends on the mass of neutrinos and matter density; the sensitivity of HMF to the underlying gravity theory was studies in numerous works, like [33, 32, 112, 203, 245, 242]. The work of [15] further illustrated that formation, evolution and hence abundance of halos is suppressed in Warm DM models, when compared to the CDM case. All these results (and many more) conclude that HMF is an important cosmological measure, and studying HMF can help us to constrain for the cosmological parameters from observational data-sets, and effectively test GR on cosmological scales. Any significant deviations in the HMF predicted from our ΛCDM model would create tensions in our current understanding of structure formation in the Universe. HMF is not only a sensitive measure of cosmological parameters by itself, but also a key ingredient in the analytical and semi-analytical modelling of DM distribution

and several aspects of the formation, evolution and distribution of galaxies [144, 161, 73, 248]. This latter application is a primary domain in which we extend the utility of our HMF modelling, that is described in detail in this and the subsequent chapter.

2.1 Theory of Halo Mass Function

2.1.1 Press-Schechter Framework

The first modern formalism for HMF was proposed in the seminal works of Press and Schechter (1974) [231] (Hereafter PS74), and Bond et al. (1991) [44], which gave the first quantitative insight into predicting the abundance of peaks that collapse to form halos. These works derived the following functional form for the HMF

$$n(M) \equiv \frac{dn}{dM} = \frac{\rho_m}{M^2} F(\sigma) \left| \frac{d\ln\sigma}{d\ln M} \right|. \tag{2.1}$$

Here, ρ_m is the average density of the Universe, M is the mass of halo, $F(\sigma)$ is the halo multiplicity function (elaborated further in Section 2.2), and σ is the variance of density fluctuations, defined in Eq. (1.23).

PS74 were the first to combine the statistics of the initial density field with the model of the evolution of perturbations, based on the spherical collapse of top-hat overdensity (for details o spherical collapse in Section 1.3.2). They proposed that the fraction of mass in halos, which are more massive than a given mass, M is related to the fraction of volume in which the smoothed initial density field is above some threshold δ_c ($= 1.69$ from Section 1.3.2). The density field is linearly extrapolated to the present time ($a(t_0) = 1$), given by $\delta = \delta_i / a_i$, where i denotes the initial time. PS74 argued that since the linear density field smoothed on comoving scale $R_L(M)$ follows a Gaussian, with mean $= 0$ and variance $\sigma^2(R,z)$, then the fraction of collapsed mass at any resolution $\sigma^2(R,z)$ can be given by the probability of δ_l being larger than δ_c, *i.e.*

$$F(M) = \int_{\delta_c}^{\infty} P_{\delta_l}(\delta_l, R) d\delta_l = \frac{1}{2} erfc\left[\frac{\nu}{\sqrt{2}}\right]. \tag{2.2}$$

Here $erfc(x)$ is the complementary error function, and $\nu = \delta_c/\sigma(M)$ is the peak-height, which is the height of the threshold in units of the standard deviation of the smoothed density distribution.

Here, for the top-hat filter, the mass variance M is related to the density variance $\sigma^2(R,z)$ by

$$M = 4\pi\bar{\rho}R^3(\sigma^2(R,z))/3. \tag{2.3}$$

$\sigma(R)$ becomes arbitrarily large when R becomes arbitrarily small. Thus, $F(0)$ gives the fraction of all mass in collapsed objects. For, $erfc(0) = 1$, in Eq. (2.2), $F(M) = 1/2$ *i.e.* only half of the mass density of the Universe is contained in virialized objects.

As a result, the factor of 2 was introduced by PS74 as an $ad-hoc$ factor to recover the correct normalisation, and have results consistent with simulations *i.e.* to obtain

$$\lim_{M\to 0} F_{coll,PS}(M,z) = 1. \tag{2.4}$$

They stated that the missing mass would accrete on the formed structure without any change in the mass function, but did not give any proper justification for the same. This turned out to be one of the major drawbacks of the PS74 approach. In the PS74, only the initial overdensities are considered to have collapsed, and the initial under-dense regions that have a finite probability of becoming over-dense are neglected. Also, PS74 considered structures evolving from spherical collapse dynamics, thus ignoring the role of tides and the complex non-linear dynamics behind structure formation. Despite its drawbacks, PS74 formalism has proven to be a successful approach for small N-Body simulations.

In the PS74 formalism, the number density of structures of mass M, and $M+dM$, is related to the derivative of integral of Eq. (2.2)

$$\frac{dn}{dM}dM = \frac{\bar{\rho}}{M^2}\left|\frac{dF}{dM}\right|dM. \tag{2.5}$$

In terms of mass variance (or peak-height),

$$\begin{aligned}\frac{dn}{dM}dM &= \sqrt{\frac{2}{\pi}}\frac{\bar{\rho}}{M^2}\frac{\delta_c}{\sigma}\left|\frac{d\ln\sigma}{d\ln M}\right| e^{-\delta_c^2/2\sigma^2}dM \\ &= \sqrt{\frac{2}{\pi}}\frac{\bar{\rho}}{M^2}\nu\left|\frac{d\ln\nu}{d\ln M}\right| e^{-\nu^2/2}dM.\end{aligned} \tag{2.6}$$

2.1.2 Correction to Press-Schechter framework: Excursion Set Approach

As highlighted in the previous section, PS74 approach does not account for the fact that at a particular smoothing scale $\delta(x,R)$ may be less than δ_c, yet it may be larger than δ_c at some larger smoothing scale $R' > R$, and can subsequently collapse to form structures at those scales. As a result, under-dense regions are not considered in PS74 formalism, which ultimately give rise to the discrepancy of a factor of 2. To correct for this, Eq. (2.2) can be modified as

$$F(M) = \int_{\delta_c}^{\infty} P_{\delta_l}(\delta_l,R)d\delta_l + \int_{-\infty}^{\delta_c} C(\delta_c,\delta_l)d\delta_l. \tag{2.7}$$

Here, the second term takes into account the trajectories of the points that were under-dense for scale R, but are over-dense for scale $R' > R$.

The *Excursion set approach* was proposed by [44], assuming initial density perturbations to be a continuous hierarchy of filters of radius R_f *i.e.* the density contrast, δ_c vary for a given region as a function of R_f. For a sequence of R_f: $R_1, R_2 ..... R_n$, δ_l executes a random walk $\delta_1, \delta_2 ..... \delta_n$. Analogous to the absorbing barrier problem of random walk [61], for the instant when $\delta_l > \delta_c$ (for $l = 1, 2 .... n$), a bound structure will be formed irrespective of any further down-crossing event. This probability can be related to the HMF.

In this context, Excursion set approach considers the simplest k-space filter, for which the window function for a given smoothing scale R is $W_k(R) = \theta(R^{-1} - k)$, and

$$\langle \delta_l \delta_{l+1} \rangle = \sigma_l^2 = 0. \tag{2.8}$$

In the continuum limit, random walk is the diffusion equation. The probability that the particle is at $(\delta, \delta + d\delta)$ and dispersion σ^2 obeys

$$\frac{\partial P}{\partial \sigma^2} = \frac{1}{2} \frac{\partial^2 P}{\partial \delta^2}.$$

For the barrier at $\delta = \delta_c$, the probability that a random walk crosses the barrier for the first time

$$P(\delta, \sigma^2) = \frac{1}{\sigma\sqrt{2\pi}} \left[\exp\left(-\frac{\delta^2}{2\sigma^2} \right) - \exp\left(-\frac{(\delta - 2\delta_c)^2}{2\sigma^2} \right) \right]. \tag{2.9}$$

The probability of considering the crossing of the barrier only for the first time is used to avoid any double counting. This gives

$$\frac{dn}{dM} dM = \sqrt{\frac{2}{\pi}} \frac{\bar{\rho}}{M^2} \nu \left| \frac{d \ln \nu}{d \ln M} \right| e^{-\nu^2/2} dM. \tag{2.10}$$

Comparing with Eq. (2.6), this is precisely PS74 HMF, with no $ad-hoc$ factor of two

2.1.3 Including ellipsoidal collapse in the Excursion Set Approach

Using Eq. (1.27), the HMF associated with the ellipsoidal collapse can be obtained from the mass distribution of the first crossing of the ellipsoidal collapse barrier, $\delta_{ec}(\sigma, z)$ (Eq. (1.27)). The resulting HMF is given by (Sheth Mo and, Tormen 2001, [251], hereafter referred to as HMF-SMT)

$$F(\nu) = A \left[1 + \frac{1}{\tilde{\nu}^{2q}} \right] F(\nu)_{\text{PS-74}}. \tag{2.11}$$

Here, $A \approx 0.322$ is the normalisation, $\tilde{\nu} = 0.84\nu$, $q = 0.3$, and $F(\nu)_{\text{PS-74}} = \sqrt{\frac{2}{\pi}} \nu \exp\left(-\frac{\nu^2}{2} \right)$ is the PS74 HMF (Eq. (2.6)).

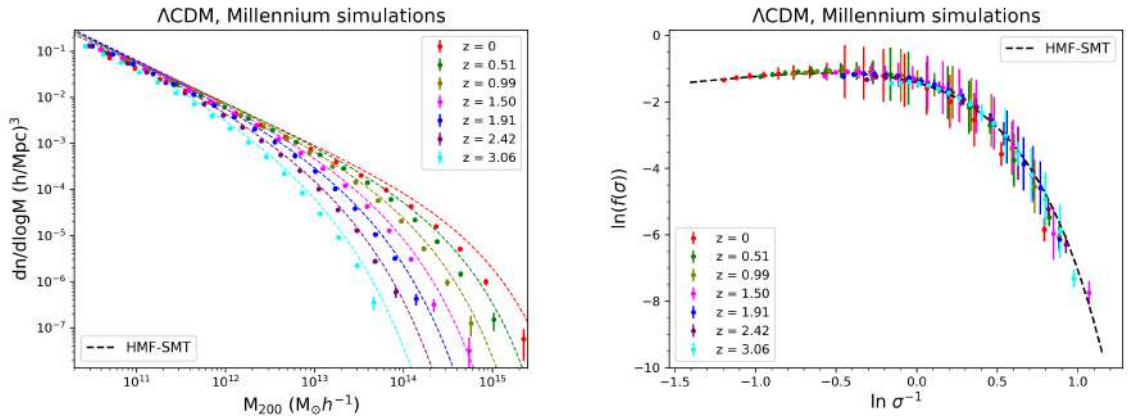

Figure 2.1: *Left plot:* ΛCDM HMF trend obtained as a function of halo mass, M_{200} ($M_\odot h^{-1}$). *Right plot:* HMF, expressed in terms of $F(\sigma)$−ln σ^{-1} relation. Here, the dashed lines correspond to SMT-01 HMF formula (Eq. (2.11)). The error bars illustrate the Poisson errors. These HMF computations were done using the publicly available halo catalogs for the MILLENNIUM2 simulations [51]

2.2 Universality of the scaled Halo Mass Function

The basic halo count $n(M) \equiv \frac{dn}{dM}$ is not directly comparable between redshifts or cosmologies, because halos grow over time and their number depends on cosmological parameters. Instead we convert halo count into something termed as the halo multiplicity function $F(\sigma)$. This term, originally introduced in Eq. (2.1), encapsulates the non-linear dynamics associated with halo collapse.

Variance of the density field $\sigma(M,z)$ (defined in Section 1.3.1) gives a relation between the halo mass and corresponding density fluctuations. This relation encapsulates the dependencies on the linear background density field evolution, cosmology, and redshift (which can also be inferred from Fig. 1.2 and Fig. 1.3). As a result, length scales can be expressed in terms of a redshift-dependent $\sigma(M,z)$, rather than a physical entity, like the halo mass. When $F(\sigma)$ is plotted as a function of ln σ^{-1}, the resulting $F(\sigma)$−ln σ^{-1} relation becomes independent of redshift in ΛCDM [137]. This *universality* of the halo multiplicity function was shown to hold across redshifts, and a range of σ^{-1} [251, 137, 282, 277, 185, 278, 83], and various fitting functions have been proposed which exploits this universal property of $F(\sigma)$. For the times and scales where this universality holds, we can describe the abundance of structures using one uniform functional shape of the $F(\sigma)$. We highlight this property of HMF in Fig. 2.1 using results from MILLENNIUM2 simulations [51], across a range of redshifts. In the left plot, we show the ΛCDM HMF trend obtained as a function of halo mass, M_{200} (expressed in the units of $M_\odot h^{-1}$). We plot the same results in the right plot, but now in terms of $F(\sigma)$−ln σ^{-1} relation. We can clearly see that the explicit redshift dependence of HMF in the left plot is captured in the right plot, and here HMF can be expressed approximately as a single curve across redshifts. The dashed lines in both plots are HMF predictions from Eq. (2.11). This theoretical expression is also built on this property of universality of

HMF across redshifts.

We further investigate how HMF behaves in the MG models that we consider in this work. Given the difference in the perturbation equations, and as a result, structure formation in MG *w.r.t.* the standard GR paradigm, we expect a change in the halo number count, and in-turn HMF in these MG models. In the subsequent section, we probe these differences across length and time scales.

2.3 Summary of the attached article: S. Gupta, W. A. Hellwing, M. Bilicki, and J. E. García-Farieta, Phys. Rev. D 105, 043538 (2022)

In this section, we provide a comprehensive summary of our findings presented in [112]. The article is attached at the end of this chapter.

Moving from ΛCDM to MG, HMF modelling in beyond-GR theories has been addressed in the past using multiple approaches: The authors in [246] used N-body simulations to study the HMF trend in $f(R)$ chameleon cosmologies, whereas [172, 181, 180] adopted the δ_c determined by the mass- and environment-dependent spherical collapse model to compute HMF in $f(R)$ gravity. The authors in [162] used the Excursion set theory approach to compute the first-crossing distribution with the moving barrier defined by the linear chameleon collapse density. As an alternative to the top-hat approximation implemented in the chameleon spherical collapse computations, [152] considered the $f(R)$ evolution of an initial density profile to develop an analytic Halo Mass Function based on excursion set theory with a drifting and diffusing barrier. HMF in Vainshtein nDGP was first reported in [242] using N-body simulations, showing qualitatively and quantitatively different HMF trends between chameleon and Vainshtein screening mechanisms. Meanwhile, [32] showed that the HMF in beyond-GR models like cubic and quartic Galileon can be well modelled using re-calibrated HMF-SMT formula .

In our work, we extended the $F(\sigma)$−ln σ^{-1} relation to our MG models: $f(R)$ and nDGP. The results for this relation are shown in the top panels of Fig. 2.2, where we have plotted the $F(\sigma)$−ln σ^{-1} relation obtained from ELEPHANT simulations. The solid line denotes the MG model, and dashed are ΛCDM results. The latter are plotted for a lucid comparison. Given that these MG models have the same background metric as GR, we see similar trends as ΛCDM. We also note approximate universality in the MG HMF across redshift ranges, as has been discussed in the previous section for ΛCDM. This shows that the self-similar nature of hierarchical structure formation in ΛCDM [231] is, to some extent, preserved even for the case of the MG models. We obtained the similar universality trend in MG models as some of the MG-induced effects will be already encapsulated in the changes of the $\sigma(M)$ relation (illustrated in Fig. 1.3), as shown from both the linear theory and simulation-based power spectrum studies [11, 242, 30, 125, 213, 276, 286, 127].

For the case of ΛCDM scenario, many works have reported a departure from univer-

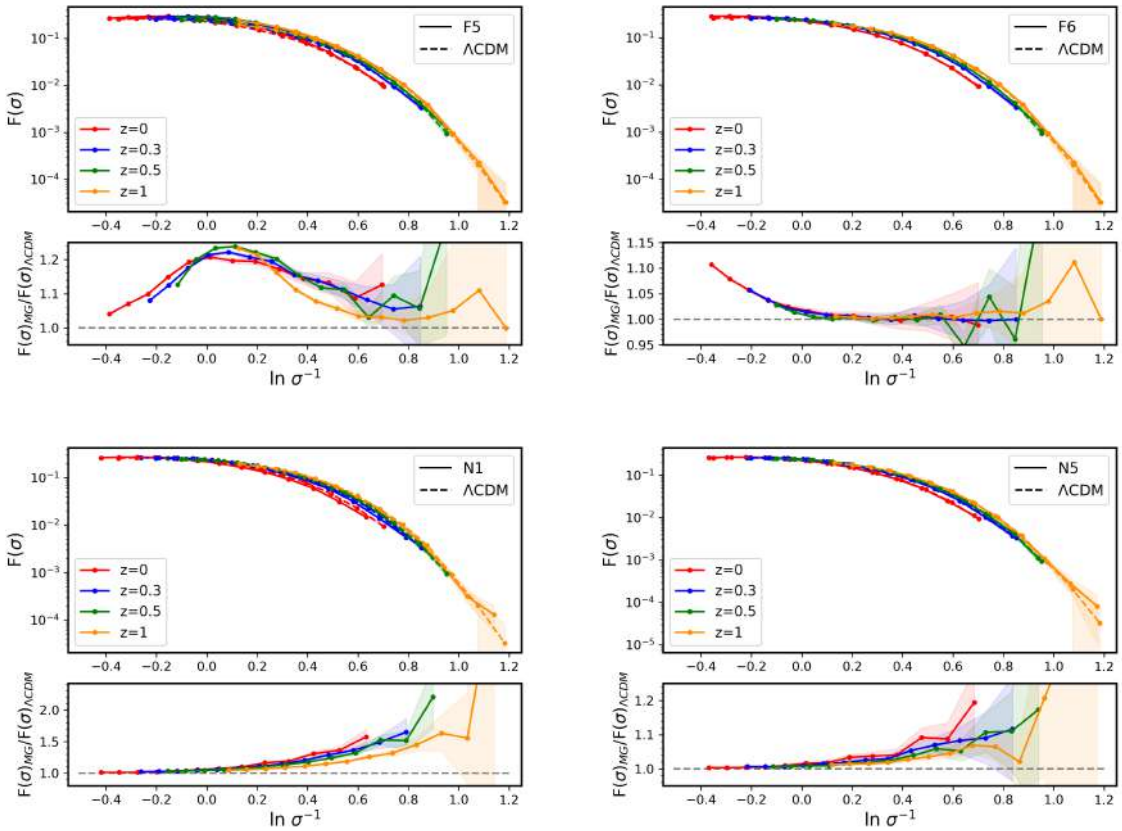

Figure 2.2: *Top panel:* $F(\sigma)$-ln σ^{-1} relation, for MG models (solid lines) and ΛCDM (dashed lines) at $z = 0.0.3, 0.5$ and $z = 1$. *Lower panel:* Comparison of MG $F(\sigma)$ w.r.t. ΛCDM. The top plots corresponds to the variants of $f(R)$ gravity, and the bottom plots corresponds to the nDGP variant results.

sality in HMF. This has been identified as the dependence of HMF on several factors: redshift, cosmology, non-linearities associated with halo collapse, artificially induced factors like the type of mass definition employed to define a halo etc. [281, 282, 267, 278, 84, 75, 205, 83]. It is clear that the simulation results for both ΛCDM and MG case are admitting the universality only approximately. For the case of our MG models, this universal trend in the HMF then becomes even less certain, given the explicit dependence of the fifth-force, and of the associated screening mechanisms on the scales and environment [172, 181, 6, 243, 242].

As a result, in this article, we do not attempt to provide a fitting function for the MG HMF. *N*-body simulations, even for the case of ΛCDM, have not yet explored the extent to which the universality in the HMF relation is applicable (in terms of redshifts, cosmological parameters, resolution of the simulation). Instead, we focus on the relative ratios of the MG to ΛCDM HMF: $F(\sigma)_{\rm MG}/F(\sigma)_{\Lambda CDM}$. We plot this ratio from simulations in the bottom panel of Fig. 2.2. We can clearly see that the F5 variant has a peak in enhancement at some intermediate halo mass scale, and F6 has a monotonically decreasing enhancement with halo masses. Meanwhile in both the nDGP variants, HMF increases monotonically with halo mass.

More interestingly, we see that for the $f(R)$ gravity, this relation exhibits a universal trend, independent of redshift, and the $F(\sigma)$ ratio follows a very similar pattern as a function of ln σ^{-1}. The ratio peaks for F5, and monotonically decreases for F6. This trend in both these variants is an interplay of the MG effects, local density and the associated chameleon screening mechanism.

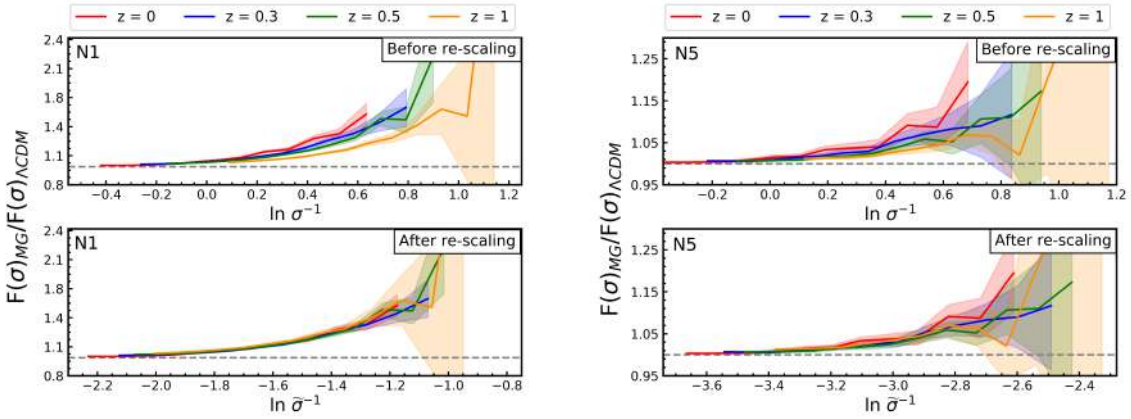

Figure 2.3: *Top panel:* The ratio $F(\sigma)_{\rm nDGP}/F(\sigma)_{\Lambda\rm CDM}$ as a function of ln σ^{-1} for N1 (left) and N5 (right). *Bottom panel:* The same ratio, but as a function of re-scaled matter variance, ln $\widetilde{\sigma}^{-1}$ (Eq. (2.12)).

However, unlike $f(R)$, nDGP shows redshift-dependent trend. This redshift-dependence can be attributed to the fact that the general force enhancement factor and the resulting growth rate of structures in nDGP is only time-dependent, but scale-independent (as also seen in the right plot of Fig. 1.3), which forbids the self-tuning mechanism in nDGP.

To get a redshift independent ratio, we needed to perform an additional rescaling from σ to $\widetilde{\sigma}$ in nDGP, where

$$\widetilde{\sigma} = \sigma/\Xi(z). \tag{2.12}$$

Here, $\Xi(z) \equiv F_5/F_{GR}$ is the gravitational force enhancement in nDGP w.r.t. GR. The details of this substitution can be studied in Section 1.7.2 and in the appendix of [112]. We do this additional time-dependent re-scaling to capture the redshift dependence in the $F(\sigma)$ ratio for nDGP.

In the top panel of Fig. 2.3, we plot the ratio $F(\sigma)_{\rm nDGP}/F(\sigma)_{\Lambda\rm CDM}$ as a function of ln σ^{-1} for N1 (left) and N5 (right). And in the bottom panel, we plot the same ratio, but as a function of the re-scaled matter variance, ln $\widetilde{\sigma}^{-1}$. Here, we can clearly see that the redshift-dependent trend in this ratio from the top panel is eliminated in the bottom panel after this substitution.

Now, using this property of universality in the ratio $F(\sigma)_{\rm MG}/F(\sigma)_{\Lambda\rm CDM}$ (MG = $f(R)$, nDGP) as a function of the matter variance σ (or $\widetilde{\sigma}$), we characterise targeted MG HMF as a functional deviation from ΛCDM, given by

$$F(\sigma)_{\rm MG} = \Delta_{\rm MG} \times F(\sigma)_{\Lambda\rm CDM}. \tag{2.13}$$

Here, $F(\sigma)_{\Lambda\mathrm{CDM}}$ is the input HMF from ΛCDM, and Δ_{MG} is the functional form for the fitting functions that we propose for this universal ratio $F(\sigma)_{\mathrm{MG}}/F(\sigma)_{\Lambda\mathrm{CDM}}$. Δ_{MG} in Eq. (2.13) depends on the MG model.

For instance, in the $f(R)$ gravity variants

$$\Delta_{\mathrm{MG}} \equiv \Delta_{f(R)} = 1 + a \exp\left[-\frac{(X-b)^2}{c^2}\right]. \tag{2.14}$$

Here, $X \equiv \ln(\sigma^{-1})$ and (a,b,c) are the parameters of the fit, which depend on the $f(R)$ variant under consideration. The values of these parameters are given in Table I of the attached article.

Similarly, for the nDGP variants

$$\Delta_{\mathrm{MG}} \equiv \Delta_{n\mathrm{DGP}} = p + q \arctan(sX + r). \tag{2.15}$$

Here, X is the *re-scaled* mass density variance, $X \equiv \ln\left(\widetilde{\sigma}^{-1}\right)$, and we recall that $\widetilde{\sigma} = \sigma/\Xi(z)$. Again, (p,q,r,s) are the parameters of the fit which depend on the nDGP variants. Table 2 of the attached article gives the values for these parameters.

In Fig. 2.4, we plot a comparison of $F(\sigma)_{\mathrm{MG}}$ from Eq. (2.13), with the $F(\sigma)$ from simulations ($F(\sigma)_{\mathrm{MG,\,sim}}$), for both $f(R)$ (left) and nDGP (right) gravity variants. It is evident that our HMF modelling gives results with %-level accuracy with the simulation results across a wide range of halo mass and redshift ranges probed in this work.

As noted, Eq. (2.13) requires only the input of ΛCDM HMF predictions. This is advantageous, primarily due to the availability of advanced and sophisticated ΛCDM simulations, which have benefited from the imposition of stringent constraints on the parameter space.

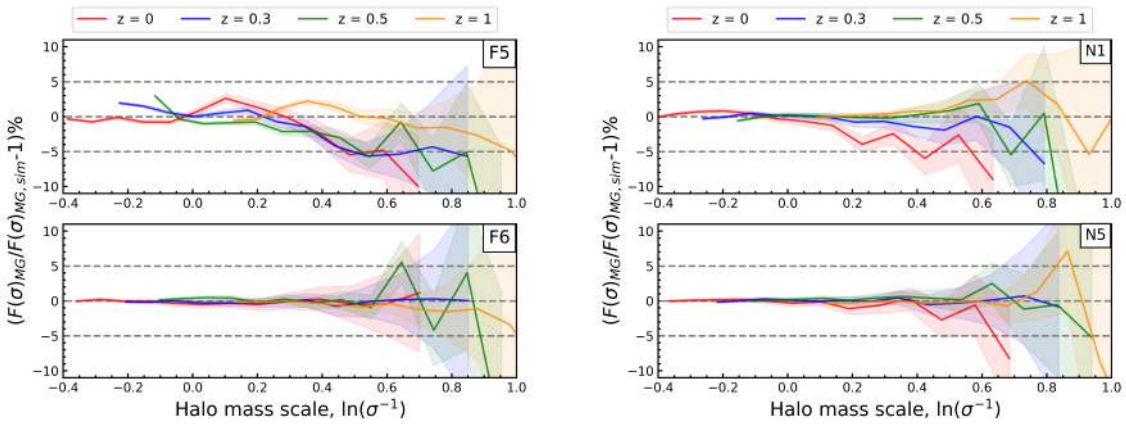

Figure 2.4: Comparison of the $F(\sigma)_{\mathrm{MG}}$ obtained from Eq. (2.13), with the $F(\sigma)$ from simulations, $F(\sigma)_{\mathrm{MG,\,sim}}$. Left plots are the $f(R)$ variants, and the right plots are the nDGP models. This comparison is plotted for $z = 0, 0.3, 0.5$ and 1. The horizontal gray dashed lines correspond to the 5% accuracy regime.

In contrast, the parameter space of MG models remains largely unconstrained in

light of unknown physics, leading to a significantly higher number of degrees of freedom. Furthermore, the additional calculations of the fifth-force, and the the screening mechanisms further increases the complexities in these MG computations. Consequently, MG simulations are characterised by their considerably higher costs and time requirements. All these factors make MG simulations orders of magnitude more expensive and time-consuming than the standard ΛCDM N-body runs. In addition to this, the field of ΛCDM HMF analytical modelling has made significant advancements. Numerous works have been dedicated to exploring HMF for larger mass ranges with increased accuracy and precision [251, 267, 51, 75, 15, 278, 83, 124, 118]. As a result, these advancements in ΛCDM HMF, both from simulations and theory in-still a high level of reliability in our input predictions.

Since we focus on modelling the HMF ratio and not absolute HMF, our analytical expressions can be extended to any background cosmology. We also show this in [112], where we test our HMF modelling on simulations which were not used in the original calibrations, and obtained results within percent level accuracy, even for the halo mass (or σ range) that were not used in this calibration.

This analytical HMF modelling is subsequently used in our theoretical formalism to compute the non-linear matter power spectrum in these MG models. The details are further presented in the subsequent Chapter 3.

Universality of the halo mass function in modified gravity cosmologies

Suhani Gupta,* Wojciech A. Hellwing, Maciej Bilicki, and Jorge Enrique García-Farieta
Center for Theoretical Physics, Polish Academy of Sciences, Al. Lotników 32/46, 02-668 Warsaw, Poland

(Received 7 December 2021; accepted 7 February 2022; published 28 February 2022)

We study the halo mass function (HMF) in modified gravity (MG) models using a set of large N-body simulations—the ELEPHANT suite. We consider two popular beyond-general-relativity scenarios: the Hu-Sawicki chameleon $f(R)$ model and the normal branch of the Dvali-Gabadadze-Porrati (nDGP) braneworld. We show that in MG, analytic formulation based on the Press-Schechter framework offers a grossly inaccurate description of the HMF. We find, however, that once the HMF is expressed in terms of the dimensionless multiplicity function it approximately assumes a redshift-independent universal character for all the models. Exploiting this property, we propose universal fits for the MG HMF in terms of their fractional departures from the ΛCDM case. We find two enclosed formulas, one for $f(R)$ and another for nDGP, that provide a reliable description of the HMF over the mass range covered by the simulations. These are accurate to a few percent with respect to the N-body data. We test the extrapolation potential of our fits against separate simulations with a different cosmological background and mass resolution and find very good accuracy, within ∼10%. A particularly interesting finding from our analysis is a Gaussian-like shape of the HMF deviation that seems to appear universally across the whole $f(R)$ family, peaking at a mass variance scale characteristic for each $f(R)$ variant. We attribute this behavior to the specific physics of the environmentally dependent chameleon screening models.

DOI: 10.1103/PhysRevD.105.043538

I. INTRODUCTION

Our current standard model of cosmology—*Lambda cold dark matter* (ΛCDM)—is a very successful description of the evolution of the Universe from the hot relativistic big bang until the present time, some 13.8 billion years later. This simple six-parameter model can account very well for the primordial nucleosynthesis light elements abundance, the precisely observed properties of the cosmic microwave background, the large-scale clustering of matter, and the late-time accelerated expansion history [1–4].

However, ΛCDM is of inherent phenomenological nature, due to the necessity to include dark matter and dark energy fluids in the cosmic matter-energy budget [2,5], when general relativity (GR) is assumed as the underlying theory of gravity. The phenomenological character of ΛCDM, together with known theoretical issues related to reconciling the absurdly small value of the cosmological constant with quantum vacuum theory predictions [6] and the observed anomalies associated with ΛCDM [7–9], have motivated searches for alternative scenarios or extensions to the concordance model. One particularly vibrant research theme in the last decade focused on attributing the accelerated late-time expansion to some beyond-GR extensions (usually scalar-tensor theories), rather than to the vanishingly small cosmological constant. Such models are commonly dubbed as "modified gravity" and have been put forward and studied in their many rich flavors in numerous works (e.g., Refs. [10–19]).

It is important to note that these so-called modified gravity (MG) theories cannot be so far considered as fully flagged competitors of Einstein's GR since they are not new independent metric theories of gravity. These are rather a collection of useful phenomenological models, exploring the freedom of modifying the Einstein-Hilbert action to produce a physical mechanism effectively mimicking the action of the cosmological constant [10,18,20]. This is usually achieved by introducing some extra degrees of freedom in the spacetime Lagrangian. The MG models provide a very useful framework that allows us to both test GR on cosmological scales and explore the physics of cosmic scalar fields. Most of the popular MG scenarios are constructed in such a way that they have negligible consequences at early times and share the same expansion history as ΛCDM. Owing to this, the extra physics of MG models does not spoil the great observational success of the standard model. Most of the viable beyond-GR theories assume the same cosmological background as ΛCDM, which sets the stage for the formation and evolution of the large-scale structure (LSS).

To satisfy the observational constraints on gravity *e.g.,* [21–26], namely, to recover GR in high-density regimes where it is well tested and to match the ΛCDM expansion

*gupta@cft.edu.pl

history, MG theories need to be supplemented with screening mechanisms. Among these, Chameleon [27] and Vainshtein [28] effects are most frequently studied. The physics of these screening mechanisms is the strongest factor that differentiates various MG models, and their interplay and backreaction with the LSS and cosmological environment can have a pivotal role in administering the MG-induced effects. Thus, a meaningful classification of various MG theories can be made based on the virtues of the screening mechanism they invoke [12,17,29–32].

Because of the shared cosmological background, it is in the properties of LSS where we can expect the predictions of MG models to differ from ΛCDM. The formation and evolution of the LSS is governed by gravitational instability, responsible for the aggregation of dark matter (DM) and gas from primordial fluctuations into bound clumps: DM halos, which are sites of galaxy formation. This mechanism applied on the initial Gaussian adiabatic fluctuations, described by a collisionless cold dark matter power spectrum, yields one of the most important predictions for the structure formation: a hierarchical buildup of collapsed halos. The most fundamental characteristic of this theory is the halo mass function (HMF), which describes the comoving number density of halos of a given mass over cosmic time. Within the ΛCDM paradigm, the HMF assumes a universal power-law shape in the low halo mass regime, $\mathrm{d}n/\mathrm{d}M \sim M^{-\alpha}$, with the slope approximating $\alpha \sim 1$. This is supplemented by an exponential cutoff at the cluster and higher mass scales, and the amplitude, shape, and scale of HMF evolve with redshift [33]. However, when the HMF is expressed in dimensionless units of the cosmic density field variance, it assumes a universal, time-independent character (e.g., Refs. [34–40], but see Refs. [41–45] for differing results).

The HMF forms the backbone of many theoretical predictions related to late-time LSS and galaxy formation models and is widely invoked in numerous cosmological studies (e.g., Refs. [46–50]). Given the central role of this cosmological statistic in the study and analysis of the LSS, it is of paramount importance to revisit its universal properties and characterize its deviations from ΛCDM in viable MG theories in both linear and nonlinear density regimes. This is the main topic of our work here.

Given the rich phenomenology of potentially viable MG theories, it would be unfeasible to explore deeply each model's allowed parameter space, whether analytically or via computer simulations. Thus, we will limit our studies to two popular cases of such MG theories. They can be both regarded as good representatives of a wider class of models exhibiting similar beyond-GR physics. The first one is the $f(R)$ gravity [15], which considers nonlinear functions of the Ricci scalar, R, due to additional scalar fields and their interaction with matter. The second one is the normal branch of the Dvali-Gabadadze-Porrati (nDGP) model [51], which considers the possibility that gravity propagates in extra dimensions, unlike other standard forces. Both of these nontrivial MG theories exhibit the universal feature of a fifth force arising on cosmological scales, a consequence of extra degrees of freedom. Their gradient, expressed usually as fluctuations of a cosmological scalar field, induces extra gravitational forces between matter particles. Modifications to GR on large scales result in a different evolution of perturbations than in ΛCDM in both linear and nonlinear regime. The fifth force is expected to leave an imprint on structure formation scenarios, which would lead to testable differences in the properties of the LSS in such beyond-GR theories as compared to ΛCDM (e.g., Refs. [52–66]).

We will be most interested in the nonlinear and mildly nonlinear regimes of such theories, where new physics can have a potentially significant impact on the formation and evolution of DM halos. To take full advantage of the wealth of data from current and upcoming surveys (DES [67], DESI [68], EUCLID [69], and LSST [70], to name a few), which aim to constrain the cosmological parameters, and the underlying theory of gravity to percent precision, significant efforts are required on the side of theoretical and numerical modeling to reach similar level of precision in constraining possible deviations from the ΛCDM scenario.

As mentioned above, the HMF when expressed in scaled units is expected to exhibit a nearly universal behavior as a function of redshift. This property has been exploited extensively to devise empirical fits for the HMF, which can be then readily used for forecasting various LSS properties [35–37,39,40]. The availability of such HMF models or simulation based fits, precise to a few percent or better, is essential to obtain the accuracy needed for the ongoing and future LSS surveys. However, as we will elaborate below, these kinds of HMF prescriptions developed for ΛCDM capture neither the nonlinear and scale-dependent dynamics nor the screening mechanisms associated with the MG models (e.g., Refs. [62,63,71]).

The inadequacy of the standard approach to HMF in MG scenarios has led to various other methodologies being developed. Among them are those based on the spherical collapse model and excursion set theory, studied in Refs. [64,71–75] to formulate the HMF for $f(R)$ gravity models with chameleon screening. In Ref. [64], this was further extended to formulate the conditional mass function and linear halo bias, while Ref. [75] included also massive neutrinos. In Ref. [76], the spherical collapse theory was used to develop the HMF and halo model in braneworld DGP scenarios. Other approaches, developed more recently, include machine learning based emulation techniques for modeling the nonlinear regime in MG [77–81].

Here, we adopt a different approach to characterize the MG HMF. Instead of fitting for the absolute HMF values across redshifts and masses, we calibrate the deviation with respect to the GR trend, obtained by comparing the MG

HMF with the ΛCDM one. We have found this deviation to be universal across redshifts when expressed as a function of the cosmic density field variance $\ln(\sigma^{-1})$. A related approach was used in Refs. [54,60], where the $f(R)$ HMF was computed by taking a product of the ΛCDM HMF and a prefactor given by the ratio of the HMF of $f(R)$ to ΛCDM. However, these works were confined to using theoretical HMF predictions, whereas in our study, we rely on the results from inherently nonlinear N-body simulations. In this context, in Refs. [58,82], the authors also used simulation results to devise an empirical fit for the $f(R)$ and nDGP deviation with respect to ΛCDM, but all these above-mentioned works do not exploit the universality trend in the deviation of MG, which we address here.

The paper is organized as follows. In Sec. II, we describe the simulations and MG models under consideration. In Sec. III, we elaborate on the HMF both from simulations and analytical fitting functions. In Sec. IV, we explore the mass function universality in both ΛCDM and MG models, while Sec. V is devoted to the method we devised to find MG HMF. In Sec. VI, we extend our work to other simulation runs to check the reliability of our approach. Finally, Sec. VII includes our conclusions, discussion, and future work prospects. In the Appendix, we discuss the additional re-scaling of the scales needed for the case of nDGP gravity models in our analysis.

II. MODIFIED GRAVITY MODELS AND N-BODY SIMULATIONS

Our analysis focuses on dark matter halo catalog data generated using the ELEPHANT (Extended LEnsing PHysics using ANalaytic ray Tracing [65,83]) cosmological simulation suite. This N-body simulation series was designed to provide a good test bed for models implementing two most frequently studied screening mechanisms: Chameleon [27] and Vainshtein [28] effects. These two ways of suppressing the fifth force are both extremely nonlinear and have fundamental physical differences. The Chameleon mechanism makes a prospective cosmological scalar field significantly massive in high-density regions by inducing an effective Yukawa-like screening, and the effectiveness of the Chameleon depends on the local density; thus, it induces environmental effects in the enhanced dynamics. The Vainshtein screening mechanism, on the other hand, makes the scalar field kinetic terms very large in the vicinity of massive bodies, and as a result, the scalar field decouples from matter, and the fifth force is screened. Vainshtein screening depends only on the mass and distance from a body and shows no explicit dependence on the cosmic environment. An elaborate and exhaustive description of these screening mechanisms is discussed in, e.g., Refs. [12,27–31,84–87].

In our work, we consider the following cosmological branch models: ΛCDM, the Hu-Sawicki $f(R)$ model with Chameleon screening [84], and the normal branch of the Dvali-Gabadadze-Porrati (nDGP) model [51] with Vainshtein screening. The parameter space of these MG models is sampled to vary from mild to strong linear-theory level differences from the ΛCDM case. We consider three $f(R)$ variants with its free parameter $|f_{R0}|$ taken to be 10^{-6}, 10^{-5}, and 10^{-4} (increasing order of deviation from ΛCDM) dubbed as $f6$, $f5$, and $f4$, respectively, and two variants of the nDGP model, with the model parameter $r_c H_0 = 5$ and 1 (again in increasing order of departure from ΛCDM), marked consequently as nDGP(5) and nDGP(1), respectively.

The simulations were run from $z_{\rm ini} = 49$ to $z_{\rm fin} = 0$ employing the ECOSMOG code [88–91], each using 1024^3 N-body particles in a 1024 h^{-1} Mpc box. The mass of a single particle and the comoving force resolution were $m_p = 7.798 \times 10^{10}\ M_\odot h^{-1}$ and $\varepsilon = 15\ h^{-1}$ kpc, respectively. Each set of simulations has five independent realizations, except for $f4$.[1] All these simulations were evolved from the same set of initial conditions generated using the Zel'dovich approximation [92]. A high value of the initial redshift ensures long enough time for the evolution of the system to wipe out any transients that would affect the initial particle distribution, which is a consequence of employing the first-order Lagrangian perturbation theory [93]. The cosmological parameters of the fiducial background model were consistent with the WMAP9 cosmology [94], namely, $\Omega_m = 0.281$ (fractional matter density), $\Omega_b = 0.046$ (fractional baryonic density), $\Omega_\Lambda = 0.719$ (fractional cosmological constant density), $\Omega_\nu = 0$ (relativistic species density), $h = 0.697$ (dimensionless Hubble constant), $n_s = 0.971$ (primordial spectral index), and $\sigma_8 = 0.820$ (power spectrum normalization). These parameters apply to background cosmologies in both MG and ΛCDM simulations.

For further processing, we take simulation snapshots saved at $z = 0, 0.3, 0.5$, and 1. For each epoch, we analyzed the N-body particle distribution with the ROCKSTAR halo finder [95] to construct dark matter halo catalogs. Halos are truncated at the R_{200c} boundary, which is a distance at which the enclosed sphere contains an overdensity equal to 200 times the critical density, $\rho_{\rm crit} \equiv 3H_0^2/8\pi G$, and the corresponding enclosed halo mass is M_{200c}. We restrict our analysis to halos with at least 100 particles to avoid any shot noise or resolution effects, which sets the minimum halo mass in our catalog to $M_{\rm min} = 8.20 \times 10^{12}\ M_\odot h^{-1}$. Therefore, the halo mass range we study typically covers galaxy groups and clusters.

For additional tests, we have worked with two extra nDGP(1) runs based on Planck15 cosmology [96]: one realization of nDGP-HR-1280 in a simulation box of size 100 h^{-1} Mpc, with 1280^3 particles of mass

[1]For $f4$, we have two realizations at $z = 0$, two at $z = 0.3$, four at $z = 0.5$, and three at $z = 1$.

$m_p = 4.177 \times 10^7\ M_\odot h^{-1}$, and one realization of nDGP-HR-1400 in a box of size $1000\ h^{-1}$ Mpc, with 1400^3 particles of mass $3.192 \times 10^{10}\ M_\odot h^{-1}$.

III. HALO MASS FUNCTION

The halo mass function (HMF), $n(M)$, quantifies the comoving number density of dark matter halos: their abundance is expressed as a function of halo (virial) mass at a given epoch (redshift) normalized to a unit volume. We can make a further distinction: the differential mass function $\mathrm{d}n(M)/\mathrm{d}M$ and its cumulative variant: $n(<M)$. In this work, we have considered the former for our analyses.

The amplitude of the HMF depends both on the matter power spectrum at a given redshift, $P(k,z)$ and on the background cosmology. The analytical modeling of this statistical quantity has a long history, which dates back to the seminal paper of Press and Schechter [33], in which they formulated a simple theory of a fixed barrier in the Gaussian density fluctuation field. The collapse of structures of different sizes is modeled by applying density smoothing using a spherical function of a given comoving scale R. The collapse of a peak of size R with mass M occurs when the enclosed overdensity surpasses the critical density threshold,[2] $\delta_c \simeq 1.686$. In essence, the Press-Schechter (PS) theory is an application of the spherical collapse [98] to the cosmological Gaussian random density fluctuations.

In this approach, halos are considered as statistical fluctuations in the Gaussian random field. For a spherical halo (peak) of mass M and background matter density $\rho_m(z)$, the linear variance in the density fluctuation field smoothed using a top-hat filter is

$$\sigma^2(R_L,z) = \frac{1}{2\pi^2}\int_0^\infty k^2 W^2(kR_L)P(k,z)dk. \tag{1}$$

Here, $P(k,z)$ is the linear theory matter power spectrum at a given redshift, $W(x) = 3(\sin x - x\cos x)/x^3$ is the Fourier counterpart of the top-hat window function, and R_L is the halo Lagrangian radius, which is the smoothing radius of the filter scale, given by

$$R_L = \left(\frac{3M}{4\pi\rho_m}\right)^{1/3}. \tag{2}$$

Now, the differential HMF can be expressed as [33,35,99]

$$\frac{dn}{dM} = \frac{\rho_m}{M^2}F(\sigma)\left|\frac{d\ln\sigma}{d\ln M}\right|. \tag{3}$$

From the above equations, we can see that the HMF can be related to fluctuations in the matter density field by employing the so-called *halo multiplicity function*, $F(\sigma)$ [35], which describes the mass fraction in the collapsed volume. The original PS model was amended later by the excursion set approach (also termed as the extended Press-Schechter formalism; see, e.g., Ref. [100]), and the following functional form of $F(\sigma)$ was postulated:

$$F_{\rm PS}(\sigma) = \sqrt{\frac{2}{\pi}}\frac{\delta_c}{\sigma}\exp\left(-\frac{\delta_c^2}{2\sigma^2}\right). \tag{4}$$

For such a simple model, the PS HMF showed remarkably good consistency with the simulation results, especially in the intermediate halo mass regime. The onset of precision cosmology, accompanied by the rapid growth of both size and resolution of N-body simulations allowed for a robust numerical estimation of HMF across many orders of magnitude [39,41–43,101–105]. These have indicated that the original $F_{\rm PS}(\sigma)$ grossly overpredicts the abundance of low-mass halos, simultaneously underestimating the number of the very massive ones, in the cluster mass regime. A number of amended models have been put forward, and the literature of this subject is very rich (see, e.g., Refs. [36,37,39–43,99,106]). All of these alternatives have their pros and cons and usually vary with performance across masses, redshifts, and fitted cosmologies [107].

We have tested many different HMF models and found that the majority of them have very similar accuracy. For brevity, we take one particular model as our main choice for the analytical HMF predictions. We use the $F(\sigma)$ formula proposed by Sheth *et al.* [36] (hereafter SMT-01), given as

$$F_{\rm SMT-01}(\sigma) = A\sqrt{\frac{2a}{\pi}}\left[1+\left(\frac{\sigma^2}{\delta_c^2 a}\right)^p\right]\frac{\delta_c}{\sigma}\exp\left(-\frac{a\delta_c^2}{2\sigma^2}\right). \tag{5}$$

Here, the constants $A = 0.3222$, $a = 0.707$, and $p = 0.3$ were found by relaxing the PS assumptions and allowing for an ellipsoidal peak shape along with the possibility of a moving barrier.

An equally important ingredient, along with the form of the halo multiplicity function, to obtain an analytical HMF prediction is the linear theory matter density power spectrum. To calculate this quantity, we use a modified version of the CAMB cosmological code [108], including a module implementing the $f(R)$ and nDGP models [109]. We examined the modified δ_c values adjusted for a specific MG model, as suggested by Ref. [76] for the nDGP model and by Ref. [74] for the $f(R)$. This, however, yielded HMF theoretical predictions that also significantly differ from our simulations results and fail to the same extent as the ΛCDM based δ_c theoretical model we examine (see the text below and Fig. 2). Thus, for the sake of simplicity and clarity, we will use a standard ΛCDM spherical collapse based δ_c values for obtaining all our analytical HMF predictions.

[2]This is the standard spherical collapse threshold value obtained in GR [97].

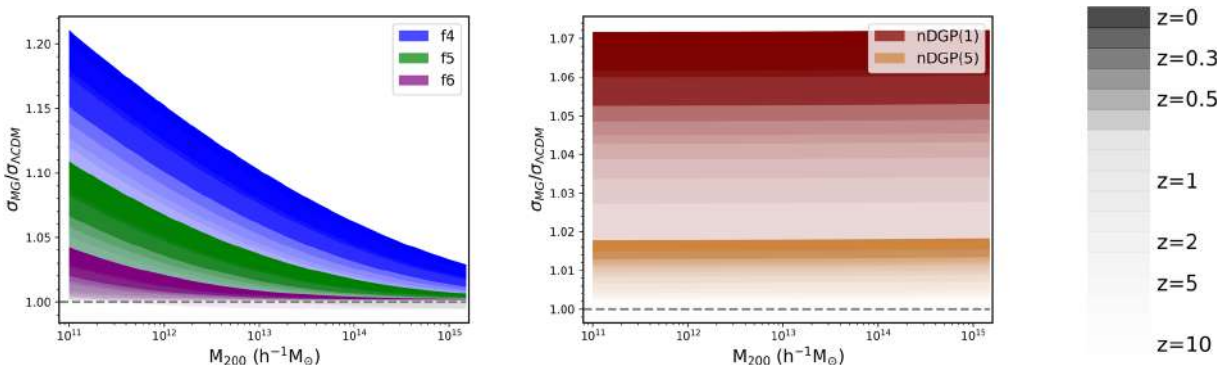

FIG. 1. Ratio of the MG to ΛCDM linear theory density variance $\sigma(M)$, defined in Eq. (1), for three variants of $f(R)$ (left-hand plot), and two variants of the nDGP gravity model (right-hand plot). The color gradient ranges from the darkest at $z = 0$ to the lightest at $z = 10$.

We begin by taking a look at the differences between linear theory matter density variance of our models. In Fig. 1, we show the ratio of $\sigma(M)$ of a given MG model with respect to the fiducial ΛCDM case. The results are expressed as a function of the halo mass scale and are shown for a range of redshifts $0 \leq z \leq 10$. The differences in the density variance are driven by the differences in the shape and amplitude of the linear-theory power spectra of the corresponding models. We show the $f(R)$ and nDGP families in separate panels to emphasize a clearly scale-dependent nature of $f(R)$ linear matter variance deviation from ΛCDM.

In Fig. 2, we compare the analytical SMT-01 prediction for the HMF with the results obtained from N-body simulations. To reduce the potential impact of model inaccuracies and cosmological dependencies, we focus on the ratio of the MG to ΛCDM differential HMFs: $n_{\rm MG}/n_{\Lambda\rm CDM}$. Departures of this ratio from unity mark the deviations from the GR based structure formation scenario induced by the action of the fifth force. We consider two

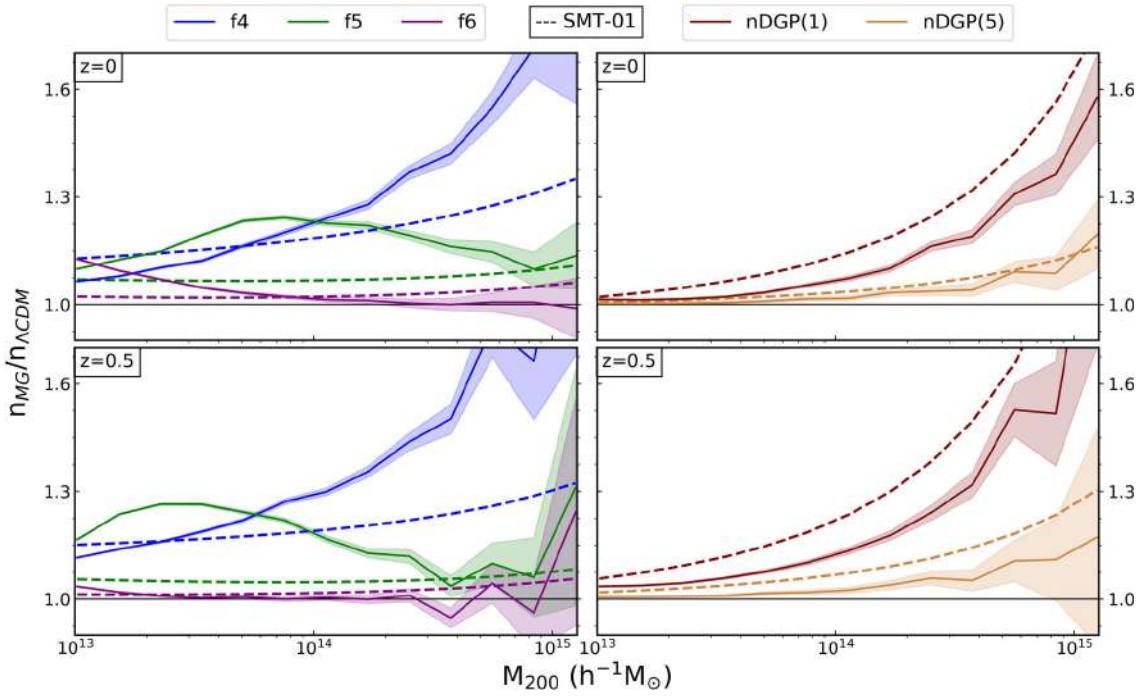

FIG. 2. Ratio of the differential HMF between MG models and ΛCDM, $n_{\rm MG}/n_{\Lambda\rm CDM}$, as a function of halo mass, M_{200}, at two redshifts: $z = 0$ (top panels) and 0.5 (bottom panels). The MG models considered here are three variants of $f(R)$ [$f6$, $f5$ and $f4$ (left-side plots)] and two variants of nDGP [nDGP(5) and nDGP(1) (right-side plots)]. The dashed lines mark the ratio of SMT-01 predictions [36], and the solid lines of the same color are the corresponding simulation results. The shaded regions illustrate the propagated Poisson errors from simulations.

epochs as an example: $z = 0$ (plots in the top row) and $z = 0.5$ (plots in the bottom row). For clarity, we compare the $f(R)$ model family (left-hand plots) and the nDGP branch (right-hand plots) separately. In each case, the dashed lines mark the ratio of the SMT-01 model predictions obtained using the linear theory power spectra of the relevant models. The solid lines in corresponding colors highlight the results obtained from simulations, and the shaded regions illustrate propagated Poisson errors obtained from the halo number count. We see that the theoretical HMF model provides a rather poor match to the MG simulation results. The trend is that the empirical predictions for MG models fostering weaker deviations from GR, i.e., nDGP(5) and $f6$, are closer to the N-body results. For all our stronger models, the SMT-01 predictions catastrophically fail to capture the real nonlinear HMF. However, there are trends present in these mismatches, depending on both the redshift and the model. For the nDGP gravity, the theoretical HMF model overpredicts deviations from ΛCDM for both epochs, while in the case of the $f(R)$ family, the SMT-01 model generally underpredicts the real MG effect. We note that for the mass scales considered the mismatch is larger for $z = 0.5$ than for $z = 0$ for all the gravity variants, except for $f6$.

Figure 2 illustrates a clear failure of the HMF modeling to capture the real MG physical effect seen in the abundance of halos. For this exercise, we have found that all of the popular HMF models that we tested (e.g., Refs. [35,37,39–41,106]) fail here in a similar fashion as the SMT-01 model. This is a clear signal that the HMF models, which are based on the extended Press-Schechter theory, are missing some important parts of the physics of the MG models. One, and probably the most significant, missing piece is the screening mechanism (as was previously discussed in Refs. [62,63]). Both the Vainshtein and Chameleon introduce additional complexities to the structure formation, such as the departure from self-similarity in the halo collapse. In addition, the screening in $f(R)$ gravity is environmentally dependent, which further alters the $n_{\rm MG}/n_{\Lambda\rm CDM}$ ratio. This can be very well appreciated by observing the peaklike feature for the $f5$ model, in which the mass scale of the peak changes with redshift. The combined effects that we have just listed make the construction of accurate analytical HMF models for MG very challenging [64,71–74,91,110,111].

IV. TESTING THE UNIVERSALITY OF THE MULTIPLICITY FUNCTION IN MODIFIED GRAVITY MODELS

The halo mass and the corresponding scale rms density fluctuations are connected via a redshift-dependent relation, $\sigma(M, z)$, obtained by plugging Eq. (2) into Eq. (1). When the multiplicity function, $F(\sigma)$, is expressed as a function of $\ln(\sigma^{-1})$, rather than of the halo mass, the resulting $F(\sigma) - \ln(\sigma^{-1})$ relation becomes independent of redshift in ΛCDM [35]. This *universality* of the halo multiplicity function was shown to hold for various redshifts and a range of σ^{-1} [34–40]. For the times and scales where this universality holds, one can describe the abundance of structures using only one uniform functional shape of the halo multiplicity function. This approximately universal behavior is a result of the scaling term between M and σ, $d\ln\sigma/d\ln M$, in Eq. (3), which encapsulates the dependencies on the linear background density field evolution, cosmology, and redshift. The universality of the HMF can also be understood as a result of the interplay of two effects in hierarchical cosmologies: first, at a fixed mass, enhancement of fluctuations is greater at smaller redshifts, and second, a fixed mass would correspond to a larger amplitude of fluctuation at larger z compared to that at a smaller z.

Some of the MG-induced effects will be already encapsulated in the changes of the $\sigma(M)$ relation (illustrated in Fig. 1), as shown from both the linear theory and simulation based power spectrum studies [62,83,91,112–116]. Thus, one can hope that when we express HMF using the natural units of the density field fluctuation variance, rather than a specific physical mass, the MG features from Fig. 2, which display strong time- and scale-dependent variations, will become more regular. This in turn would admit more accurate and straightforward HMF modeling in MG.

We are now interested in studying the halo multiplicity function, $F(\sigma)$, in our MG models. We want to check its behavior and relation with respect to the standard ΛCDM case across fluctuation scales, $\ln(\sigma^{-1})$, and for different epochs. The combined results for all our models are collected in the six plots of Fig. 3. First, let us take a look at the ΛCDM results, which is shown in the upper-left plot. The colors mark the $F(\sigma)$ computed from snapshots at different redshifts, and the shaded regions illustrate the scatter around the mean for different realizations, estimated as Poisson errors from halo number counts (using the definition given in Ref. [38]). With the dotted line, we show the SMT-01 model prediction to verify the predicted universal shape of the halo multiplicity function. It is clear that the simulation results already for the vanilla ΛCDM case are admitting the universality only approximately. Remembering that here $M \propto \sigma^{-1}$, we can say that in the intermediate-mass regime the agreement between the simulation and the SMT-01 formula is the best. For the negative $\ln(\sigma^{-1})$ regime, the simulations contain a bit fewer halos with respect to the theoretical prediction, and such deficiency is also visible in the high mass (i.e., small σ) regime, although there the discrepancy appears somewhat more significant. The $z = 0$ case merits a separate comment. Here, the disagreement with the SMT-01 formula, and simultaneously also with all the higher redshift simulation data, is very noticeable. The small- and high-mass deficiency of the simulated $F(\sigma)$ is a well-known effect due to the impact of both the discreteness (small

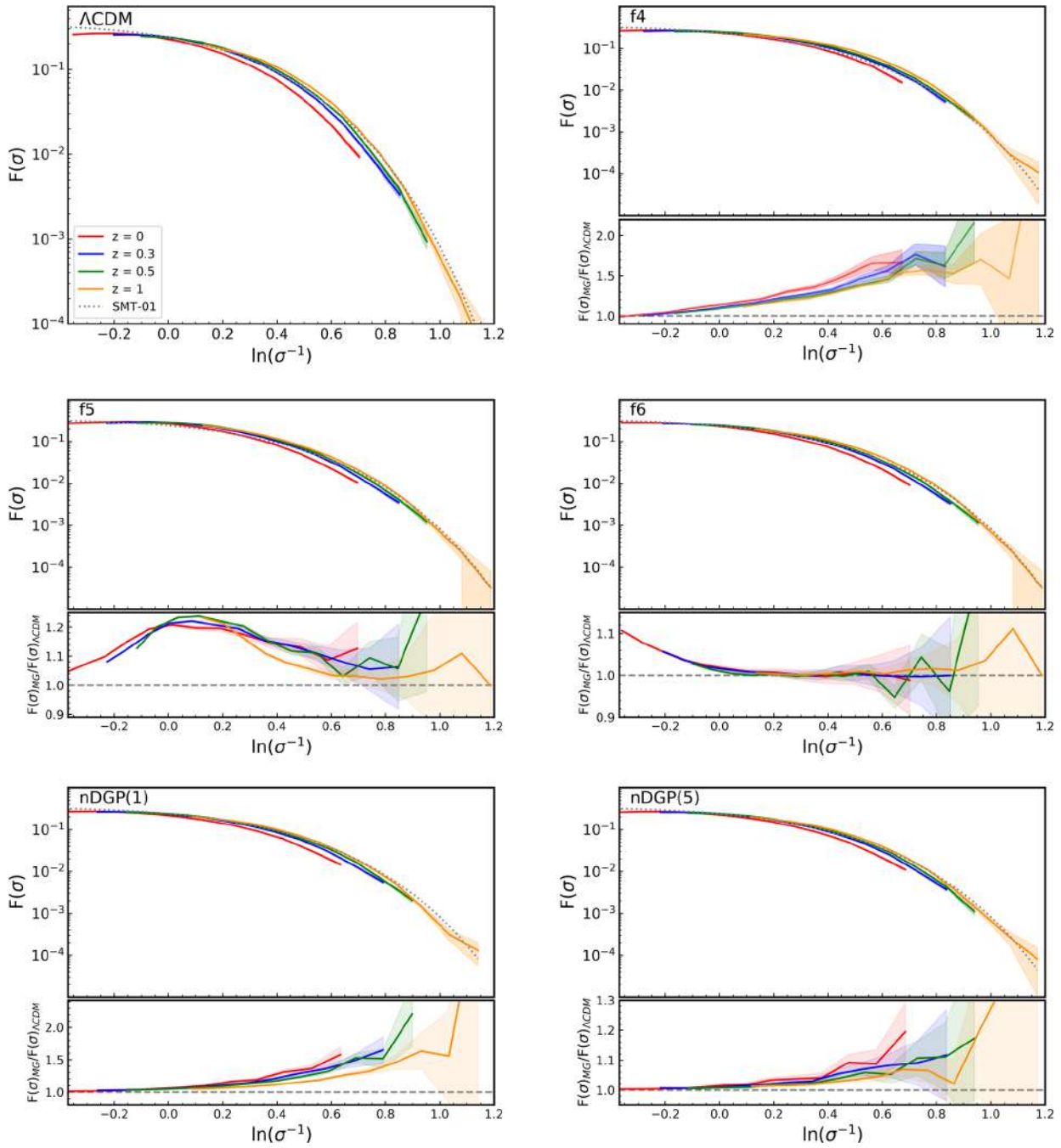

FIG. 3. Top subpanels: Halo multiplicity function, $F(\sigma)$, for the six gravity models (solid lines with shaded uncertainty regions) as a function of $\ln(\sigma^{-1})$. Each color corresponds to a different redshift as indicated in the legend in the top-left panel. Dotted grey lines are the analytical SMT-01 predictions [36]. Bottom subpanels: Ratio of the MG $F(\sigma)$ to that of ΛCDM for each redshift.

masses) and the finite volume (large masses) on the resulting simulated DM density field [37,117–120]. These effects are combined and especially pronounced for the $z = 0$ case, where the density field is most evolved, and thus the most nonlinear. However, given the vast dynamical scale both in $F(\sigma)$ and σ^{-1}, the regular and approximately universal results for the ΛCDM run are very encouraging.

Moving to the MG HMF, we present each variant of the models separately. In the top subpanel of each MG plot, we observe that the $F(\sigma)$ trend is very similar to the one observed in ΛCDM, as discussed above. What seems more interesting, though, are the lower subpanels of these plots, where we show the relative difference taken with respect to the ΛCDM case at each redshift consequently. Each model exhibits a unique and specific combination of both

amplitude and scale of departure from the fiducial GR case. For both $f4$ and nDGP(1), the excess of $F(\sigma)$ can reach up to ∼60% or greater in the rare density fluctuation regime, $\ln(\sigma^{-1}) \geq 0.7$. At the same time, both mild variants, $f6$, and nDGP(5) do not depart from GR by more than $\sim 15\% - 20\%$. The departure of $f5$ from ΛCDM, which is $\sim 20\% - 25\%$ maximum, lies between the results of $f4$ and $f6$, as expected.

The most striking and important observation is the much more enhanced regularity of $F(\sigma)$ departures from the ΛCDM case when compared with the previous plot of the HMF itself (Fig. 2), where the abundance of objects was shown as a function of their mass. Now, when we express $F(\sigma)$ in its natural dimensionless units of the density field variance, $\ln(\sigma^{-1})$, the MG effects are much more regular across the redshifts.

However, we see an exception for the $f4$ gravity case in which there are clear signs of deviation from universality, especially at $z = 0$. We attribute this to the enhanced fifth force in this $f(R)$ variant, which accumulates as time elapses and has a maximum effect at later redshifts. We note, however, that this rather extreme MG model is unlikely to be valid taking into account the current observational constraints [54,84]. Nevertheless, we have considered $f4$ in our analysis for completeness.

In general, the $F(\sigma)$ modification for the $f(R)$ variants follows a very similar pattern as a function of $\ln(\sigma^{-1})$, and the universality of $F(\sigma)$ over the redshifts is largely established. In addition, the shape of the $F(\sigma)$ modification displays a peak for $f5$, monotonically increases for $f4$, and monotonically decreases for $f6$. This is a clear manifestation of a complicated and nonlinear interplay between the local density and the Chameleon screening efficiency. The interpretation could be that the Chameleon mechanism is self-tuned by the environment-dependent nonlinear density evolution. As a result, as clearly shown for the $f(R)$ plots of Fig. 3, the self-similarity of the HMF and density field evolution is restored.

The nDGP case is less clear to interpret. The $\sigma(M)$ rescaling brings the $F(\sigma)$ at all the different redshifts much closer together when we compare with nDGP plots for the HMF in Fig. 2. Some resonant time-dependent evolution can be, however, still noticed; this can be appreciated especially in the case of nDGP(1). This residual redshift dependence reflects the fact that the screening mechanism in this model family is the Vainshtein, which does not depend on the local density field (i.e., the environment). Thus, the general force enhancement factor and the resulting growth rate of structures is only time dependent but scale independent (as also seen in the right plot of Fig. 1), which forbids the self-tuning mechanism in nDGP, unlike the case of $f(R)$. However, the nDGP force enhancement factor, $\Xi(z)$, can be easily calculated for any given redshift [85]. We exploit this to introduce time-dependent physical rescaling for nDGP, $\tilde{\sigma} \equiv \sigma/\Xi(z)$, which has been defined and discussed in the Appendix. This physically tuned rescaled factor removes nearly all the redshift dependence in the nDGP $F(\sigma)$ modification (see also Fig. 8). Thus, this one additional step can restore the expected self-similar and universal behavior of the HMF in the normal branch of the Dvali-Gabadadze-Porrati model.

V. RESCALING THE MULTIPLICITY FUNCTION IN MODIFIED GRAVITY

We will now exploit the universality of the MG halo multiplicity function, which was established in the previous section, to characterize the essential effects induced by beyond-GR dynamics on the abundance of halos. We do this by first finding an enclosed formula that describes well the shape of the MG HMF departure from the fiducial ΛCDM case. Then, we obtain the best fit for a given MG variant for all redshifts. Finally, we test our newly found MG HMF model against datasets that were not used for the fitting. In this section, we will cover the first two steps, leaving the testing for Sec. VI.

As we have already highlighted, $F(\sigma)$ displays some degree of universality for each of the gravity models in a sense that it takes approximately the same form for all the considered redshifts (as shown in Fig. 3). This has already been studied extensively for ΛCDM, and many authors have taken advantage of this property of universality in HMF to propose fitting functions for the ΛCDM HMF (e.g., Refs. [35–37,39,40]). However, some other authors have, in contrast, reported a departure from universality in ΛCDM. This has been identified as the dependence of HMF on several factors: redshift and cosmology [41–43,45,106], nonlinear dynamics associated with structure formation [40,43], some artificially induced factors like the type of mass definition employed to define a halo [34,39–41,121,122], the value of the linking length [43,123], or numerical artifacts in the simulations and computations of the HMF [38,106]. For the case of MG models like $f(R)$ and nDGP, the universal trend in the HMF is even less certain, given the explicit dependence of the fifth force and of the associated screening mechanisms on the scale and environment [32,62,64,71,73,110].

Considering the failure of the empirical relations devised for the ΛCDM HMF to capture MG effects (as discussed in Sec. III), rather than searching for a universal MG $F(\sigma)$ fit, we adopt a different approach. We instead characterize the beyond-GR HMF as a functional deviation from the ΛCDM case. Thus, we express the targeted MG HMF as a function of the ΛCDM case at a fixed σ, i.e., $F_{\rm MG}[F(\sigma)_{\Lambda\rm CDM}]$, and the general form of the relation between ΛCDM and MG multiplicity functions is given by

$$F(\sigma)_{\rm MG} = \Delta_{\rm MG} \times F(\sigma)_{\Lambda\rm CDM}. \tag{6}$$

TABLE I. Parameters for the $f(R)$ gravity model fit, $\Delta_{f(R)}$ [Eq. (7)].

Model	a	b	c
$f4$	0.630	1.062	0.762
$f5$	0.230	0.100	0.360
$f6$	0.152	−0.583	0.375

Here, $F(\sigma)_{\Lambda\mathrm{CDM}}$ is obtained from ΛCDM simulations. As we are using N-body derivations to characterize $F(\sigma)$, the resulting MG HMF model will automatically incorporate nonlinear effects to the limit of our simulations.

The general conclusion from Sec. IV is that the ratio $F(\sigma)_{\mathrm{MG}}/F(\sigma)_{\Lambda\mathrm{CDM}}$ has an approximately universal, redshift-independent shape after rescaling the fluctuation scales in terms of $\ln(\sigma^{-1})$. We calibrate the relation (6) based on the ELEPHANT data and find enclosed formulas to capture Δ_{MG} as probed by the simulations for each of the MG variants we have considered.

A. $f(R)$ gravity

We have found that the following analytical expression can be used to fit Δ_{MG} in $f(R)$ simulations,

$$\Delta_{\mathrm{MG}} \equiv \Delta_{f(R)} = 1 + a \exp\left[-\frac{(X-b)^2}{c^2}\right], \qquad (7)$$

where $X \equiv \ln(\sigma^{-1})$. Here, the parameter a sets the maximum value of $F(\sigma)_{f(R)}/F(\sigma)_{\Lambda\mathrm{CDM}}$, b corresponds to the value of $\ln(\sigma^{-1})$ at the maximum enhancement, and c determines the range of $\ln(\sigma^{-1})$ across which $F(\sigma)_{f(R)}$ is enhanced with respect to $F(\sigma)_{\Lambda\mathrm{CDM}}$. These best-fit parameters were obtained by solving for the minimum reduced χ^2, which were procured by comparing the ratio $F(\sigma)_{f(R)}/F(\sigma)_{\Lambda\mathrm{CDM}}$ from simulations with our analytical expression (7) across all redshifts and for each $\ln(\sigma^{-1})$ bin. For $f(R)$, the best-fit values of the parameters are given in Table I.

In Fig. 4, we illustrate the performance of our analytical formula with the best-fit parameters from Table I by comparing it with the simulation data for each redshift. As we can observe, generally the accuracy of our formula is good at high-σ (or low-mass) regime, where also the lines indicating different redshifts are close to each other, which is not surprising given the good statistics of our simulation in this regime. At the low-σ (high-mass and rare-object) regime, the data are characterized by a much bigger scatter. This drives our best fit sometimes in between the different redshift lines, an effect most visible for the $f5$ case. As the fit was obtained together for all the redshifts, and the assumed universality holds only approximately, we expect that the deviation at some redshifts might be larger compared to others. Nonetheless, given the scatter of both the mean trends and their corresponding errors, our fitting formula does a remarkably good job.

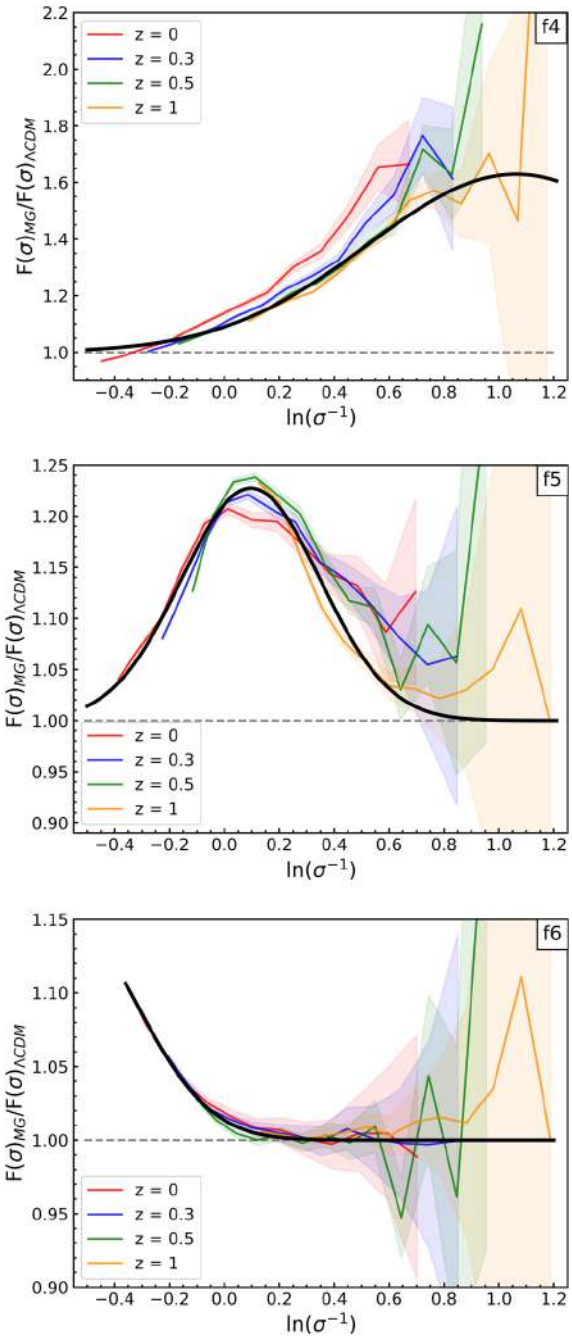

FIG. 4. Ratio of the halo multiplicity functions $\Delta_{f(R)} = F(\sigma)_{f(R)}/F(\sigma)_{\Lambda\mathrm{CDM}}$ for $f4$, $f5$, and $f6$. Colored lines indicate the four different redshifts. The black line in each panel is our universal fit [Eq. (7)] with the best-fit parameters provided for each model in Table I. Poisson errors in both $F(\sigma)_{f(R)}$ and $F(\sigma)_{\Lambda\mathrm{CDM}}$ are propagated to plot the error ranges of the ratio.

The general Gaussian form of Eq. (7) fosters a "peak-like" feature with some specific $\ln(\sigma^{-1}) = b$ value for the peak location. This suggests that the HMF of $f(R)$-gravity

TABLE II. Parameters for the nDGP gravity model fit, $\Delta_{\rm nDGP}$ [Eq. (8)].

Model	p	q	r	s
nDGP(1)	1.35	0.258	5.12	4.05
nDGP(5)	1.06	0.0470	11.8	4.19

models can be characterized by a new universal scale: a scale at which the combined effect of the enhanced structure formation and ineffective screening mechanism maximizes the halo abundance for the case of $f(R)$ gravity.

Given the limitations of the ELEPHANT simulations, we can expect that our best-fit parameters could be probably still tuned even more, if bigger and higher-resolution simulations became available. Nonetheless, considering these limits, we appreciate that the resulting reduced χ^2 values of the best fits, both for individual redshifts as well as for the concatenated redshift data, are very reasonable. These reduced χ^2 values were obtained by comparing the MG HMF obtained using simulations and our Eq. (6), with parameters taken from Table I. We give them in Table III.

B. nDGP gravity

For this class of models, we found a different shape of $\Delta_{\rm MG}$, as the formula that works for $f(R)$ failed to provide a good fit to the data. Instead, we use an arctan parametrization that much better captures the nDGP shape of $\Delta_{\rm MG}$, given by

$$\Delta_{\rm MG} \equiv \Delta_{n\rm DGP} = p + q \arctan(sX + r). \tag{8}$$

Here, X is the *rescaled* mass density variance, $X \equiv \ln(\tilde{\sigma}^{-1})$, and we recall that $\tilde{\sigma} = \sigma/\Xi(z)$. The parameter p shifts the lower asymptote of the curve, q sets the amplitude of $F(\sigma)_{n\rm DGP}/F(\sigma)_{\Lambda\rm CDM}$, r dictates the range of $\ln(\tilde{\sigma}^{-1})$, and s determines the slope of the deviation curve. These best-fit parameters were obtained using the method analogous to the one discussed for $f(R)$ and are given in Table II. Also, we plot in Fig. 5 the resulting best-fit arctan curves alongside the simulation data at various redshifts. A quick look at the reduced-χ^2 values in Table III indicates that our nDGP fits on average characterize the data even better than for the case of $f(R)$ fits.

VI. TESTING THE FITS

We want to test our best fits obtained for various MG models with simulation data that were not used for the original fitting. This test will inform us of the degree of both applicability and accuracy of our HMF modeling.

However, as we did not have access to $f(R)$ simulations other than ELEPHANT, we limit this cross-check to two nDGP(1) runs. These will be our test beds that have better resolution than the data that we used to derive the scaling

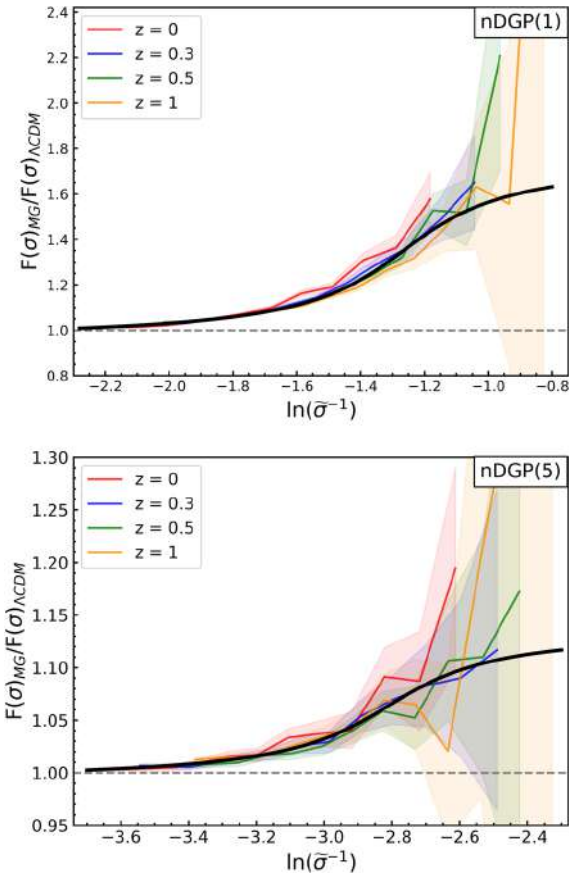

FIG. 5. Ratio of the halo multiplicity functions $\Delta_{\rm nDGP} = F(\sigma)_{\rm nDGP}/F(\sigma)_{\Lambda\rm CDM}$ for nDGP(1) and nDGP(5). Colored lines indicate the four different redshifts. The black line in each panel is our universal fit [Eq. (8)] with the best-fit parameters provided for each model in Table II. Poisson errors in both $F(\sigma)_{\rm nDGP}$ and $F(\sigma)_{\Lambda\rm CDM}$ are propagated to plot the error ranges of the ratio.

relations from the previous section. The description of these two independent runs is given in Sec. II.

We note that the differences between ELEPHANT and the independent simulations that we use here may lead to some complications in the comparisons. We expect that the effects from the different cosmologies will be secondary, as long as we compare the ratios, $\Delta_{\rm MG}$, rather than the absolute HMF values. This is because the expansion history

TABLE III. Reduced χ^2 values obtained by comparing our fit equations [Eqs. (7) and (8)] with the respective simulation results. We show values for individual redshift and for the joint all-z data.

Model	$z = 0$	$z = 0.3$	$z = 0.5$	$z = 1$	All z
$f4$	18.9	6.55	1.46	4.45	7.60
$f5$	4.95	6.96	6.11	4.30	5.58
$f6$	0.300	0.236	1.04	0.290	0.470
nDGP(1)	3.66	0.834	1.23	0.860	1.64
nDGP(5)	0.364	0.203	0.332	0.428	0.385

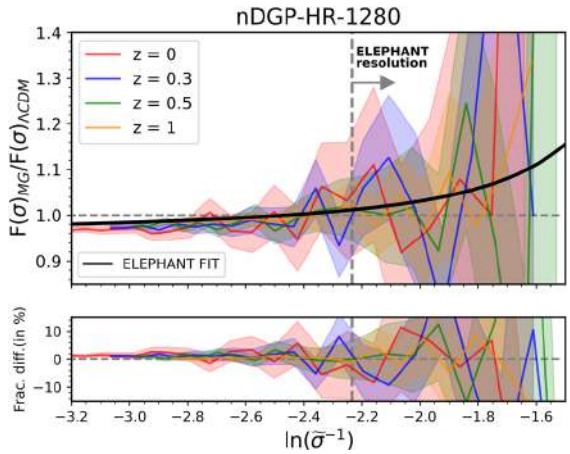

FIG. 6. Top panel: the ratio, $F(\sigma)_{\mathrm{nDGP}(1)}/F(\sigma)_{\Lambda\mathrm{CDM}}$, obtained using nDGP-HR-1280 simulations for $z = 0$, 0.3, 0.5, and 1. The black curve represents the nDGP ELEPHANT fit [Eq. (8)] with the best-fit parameters for nDGP(1) given in Table II. Bottom panel: percentage difference between the $F(\sigma)$ values from the simulation and the corresponding values from the proposed fit. The gray vertical dashed lines in both panels illustrate the minimum $\ln(\sigma^{-1})$ accessible with the ELEPHANT simulations.

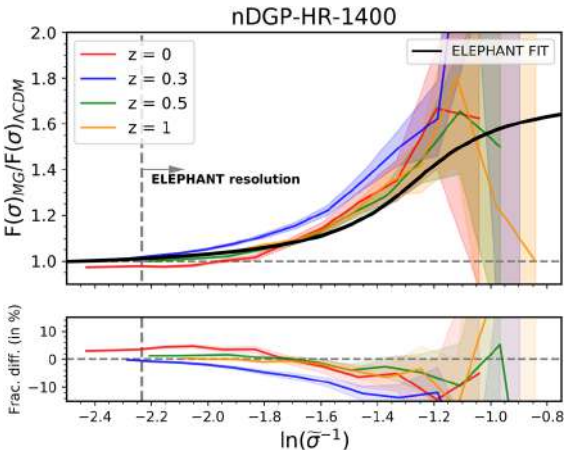

FIG. 7. Analogously to Fig. 6, but for nDGP-HR-1400.

and power-spectrum normalization will be the same for ΛCDM-Planck15 and nDGP(1)-Planck15, so to the first order, the value of Δ_{MG} will be driven mostly by the fifth-force induced effects. Nonetheless, the rescaling from σ to $\tilde{\sigma}$ in nDGP is cosmology dependent and could contribute to possible discrepancies (see Appendix).

The most valuable aspect of this exercise is that we shall test our best-fit Δ_{MG} models on simulation data that cover a different $\sigma(M)$ range than the original ELEPHANT suite. The halo masses at various redshifts in the nDGP-HR-1280 run are contained within $0.50 \lesssim \sigma(M) \lesssim 4.1$, while for nDGP-HR-1400, this range is roughly $0.27 \lesssim \sigma(M) \lesssim 1.9$, whereas for ELEPHANT, the values lie between $0.32 \lesssim \sigma(M) \lesssim 1.5$. Thus, the mass variance of the smaller box reaches to nearly three times higher $\sigma(M)$, while the mass variance of larger box is ∼40% greater than ELEPHANT suite.

We start with nDGP-HR-1280, which goes much deeper into the small-scale nonlinear regime than our original runs. In Fig. 6, we illustrate how our best fit of Eq. (8) performs in capturing the HMF deviations of nDGP(1) in this run. The bottom panel of this figure shows the percentage deviation in Δ_{MG} between the nDGP-HR-1280 simulations and our best fit for this model, treated as a reference. The increased scatter in the nDGP-HR-1280 simulations at the low-$\sigma(M)$ regime is expected, given nearly a 1000 times smaller volume of this run compared to ELEPHANT. What is, however, outstanding is a remarkable agreement of our best-fit in the high-σ range. Here, the differences are kept well below a few percent, even deep in the regime outside the original ELEPHANT. The overall performance of our fit is very good.

An analogous test for nDGP-HR-1400 is shown in Fig. 7. Here, we observe that the agreement between our best-fit model prediction and the independent simulation data is worse than in the previous case. While the mismatch that we can see in the high-σ range is still relatively small, usually staying within 5%, the disagreement in the low-variance regime is noticeably bigger. We note, however, that for this run also the overall degree of Δ_{MG} universality is substantially reduced. Still, the overall performance of our model is satisfactory as it stays within ±10% consistency with the data for the trusted $\ln(\sigma^{-1})$ range, given the variance of nDGP-HR-1400 simulation runs.

The results of the above tests reassure us that the universal nature of the $\Delta_{\mathrm{MG}}(\sigma)$ we have found seems to be a real feature of the nDGP MG-class model. Moreover, it seems that the fitting formula we put forward for this gravity variant in Eq. (8) offers a very good and fully nonlinear model of the MG HMF. However, the accuracy for the $f(R)$ family case [see Eq. (7)] would have to be further ascertained with high-resolution $f(R)$ runs. We leave this exercise for future work.

VII. CONCLUSIONS

In this work, we have studied the dark matter halo mass function in modified gravity scenarios where structure formation differs from that in ΛCDM. For that purpose, we employed the ELEPHANT suite—a set of N-body simulations, which cover GR and selected MG models, namely, Hu-Sawicki $f(R)$ and nDGP. We focused on the intermediate to high-mass end of the halo distribution in the redshift range $0 \leq z \leq 1$. In this regime, all the considered MG models display a redshift-dependent deviation in the HMF with respect to the ΛCDM case, when analyzed as a function of halo mass.

We first verified that the MG HMFs as measured from simulations are not well matched by analytical models originating from the Press-Schechter framework [33], such

as the Sheth *et al.* formula [36], which describe the halo multiplicity function, $F(\sigma)$. We attribute this failure of the analytical models to their ignorance of the complicated and inherently nonlinear screening mechanism, which is a necessary ingredient in the cosmological MG scenarios, needed to satisfy observational constraints on gravity on both local scales and in high-energy conditions.

We note that the theoretical HMF models already show noticeable inaccuracies when contrasted with ΛCDM N-body results. These inaccuracies are expected to be propagated, and most likely increased, when applied to MG models. To eliminate such leading-order discrepancies, instead of comparing the predictions of the absolute HMF amplitudes, we have focused on the relative ratios to the ΛCDM case, i.e., $n_{\rm MG}/n_{\Lambda\rm CDM}$. The predictions for this ratio based on the Sheth *et al.* formula [36] fails to capture the halo-mass-dependent shape of the MG deviations as obtained from simulation results.

For the $f(R)$ case, the SMT model underpredicts the HMF amplitude, while in contrast, for the nDGP family, we observe an overprediction. This is again a clear manifestation of the shortcomings of these analytical models in capturing the extra MG physics, which is essentially related to the presence of intrinsically nonlinear screening mechanisms operating at small scales in both models.

In hierarchical structure formation scenarios, the abundance of collapsed objects is better characterized as a function of the rarity of the density peaks they originated from, rather than of a certain virial halo mass. The former is quantified by the density field variance $\sigma(M)$ at a given halo mass scale and redshift. Following this, we observed that $F(\sigma)$ shows a much more universal character across redshifts for a given gravity model when expressed as a function of $\ln(\sigma^{-1})$. Furthermore, we have found that when we characterized the MG-induced effects as relative ratios of MG $F(\sigma)$ to the ΛCDM case a new shape emerges, which is universal across redshift. While the deviations from ΛCDM $F(\sigma)$ for $f(R)$ models show a universal character already at their face values, the nDGP case required an additional $\sigma(M)$ rescaling. This extra step was needed to include the additional redshift-dependent magnitude of the fifth force in this class of models.

We have demonstrated that, once the MG HMF is expressed conveniently as a deviation from ΛCDM case at a given $\sigma(M)$ scale, it exhibits a shape that is universal across redshifts. This is an important result, indicating that for models that employ such specific nonlinear screening mechanisms their effectiveness at the statistical level is well captured by the filtering and expressing the density field in the natural units of its variance.

To better quantify and test this newly found universality, we invoked redshift-independent analytical fitting functions to describe the $\Delta_{\rm MG} \equiv F(\sigma)_{\rm MG}/F(\sigma)_{\Lambda\rm CDM}$ ratio. These fits were calibrated on the ELEPHANT N-body simulations covering the redshift range from $z = 0$ to $z = 1$. For the $f(R)$ case, we used a Gaussian-like form of the fitting function which captures a peaklike feature in $\Delta_{f(R)}$, the amplitude and position of which depends on the given $f(R)$ model's specifications. In the nDGP case, an arctan form proved to be a reasonably good fit for $\Delta_{\rm nDGP}$, as it captures a monotonic increase at high-σ (low-mass) end and suggests a limit of constant positive deviation at the high-mass range. Our best fits turned out to provide quite good descriptions of the $F(\sigma)$ for all tested MG variants, except for the $f4$ model data at $z = 0$, which was a clear outlier. The fact that a single enclosed formula can provide a good fit for a given MG model at all redshifts reflects well that our N-body data supports the hypothesis of the redshift universality of $\Delta_{\rm MG}$.

Using independent simulation runs with better resolution than the ELEPHANT and a slightly different background cosmology, we were able to subsequently test our analytic approximations in the nDGP case. The level of agreement between our fits and these external data varied depending on the redshift and mass range, but overall, it was satisfactory, with the departure of the fit well within 10% of data points in the trusted regime. This is a strong test indicating that the uncovered universal deviation of the HMF is a result of real physical phenomenology of the MG models in question, rather than a random chance effect unique to the particular ELEPHANT suite. One could worry that a 10% accuracy here is not an impressive precision, given that 1% statistical precision will be demanded by the forthcoming Big-Data cosmological surveys. However, on the simulation side, it has been shown that the agreement between present-day different halo finders is at most 10% in ΛCDM [124,125]. Thus, our accuracy reported here is already approaching the current numerical limit. On the other hand, the magnitude of deviations from GR as fostered by our MG models typically reaches a factor a few × 10% at $\ln(\sigma^{-1})$ values where our accuracy limit is set.

The resolution of the ELEPHANT simulations allowed us to robustly probe only intermediate and large mass halos. In this limited mass σ regime, the abundance of structures in MG increases with respect to ΛCDM, as small mass halos accrete and merge faster to form larger structures. However, owing to the conservation of mass in the Universe, we can expect that there should be a simultaneous decrease in the number of small-mass halos in the MG models when compared to ΛCDM. This was found to be indeed the case for some of MG variants (e.g., Refs. [58,111,126]). A similar effect is also hinted at in our results of the high-resolution nDGP-HR-1280 runs at small $\ln(\sigma^{-1}) < -2.75$. Thus, a natural extension of our study and an important further test of the $\Delta_{\rm MG}$ universality will be to probe a smaller mass (and larger σ) regime. Such a study will require a completely new set of high-resolution N-body simulations, and we plan it as a future project.

The HMF and its time evolution is one of the most important and prominent predictions of the theory of gravitational instability and formation of the large-scale structures [97]. In the ΛCDM framework and within its GR paradigm, there is strong evidence for the universality of the HMF with redshift, when the HMF is expressed in the units of the dimensionless cosmic density field variance. Once we admit a model with an extra fifth force acting at intergalactic scales, such as the MG models studied here, the universality of the HMF could no longer be taken for granted. We have shown that once the density field is rescaled both of our MG models exhibit an approximately universal $F(\sigma)$, similar to the trend seen in the case of ΛCDM. Moreover, its ratio with respect to the ΛCDM case can now be modeled by a single enclosed formula, with a good fit for each of the specific $f(R)$ and nDGP model variants. This opens an avenue for building accurate, yet relatively simple, effective models of the HMF in MG scenarios. Such models can then be implemented in studies on galaxy-halo connection, galaxy bias, and nonlinear clustering (e.g., Refs. [63,64,71,76,127–130]). This will be of paramount importance for robust predictions on cosmological observables and their covariance. Such calculations for many observables of interest have been so far severely limited, mainly because N-body simulations, with a full nonlinear implementation of screening mechanisms, are prohibitively expensive for the case of most nontrivial MG scenarios.

From this standpoint, the results of our analysis are the first step toward building a versatile, accurate, and numerically cheap model of nonlinear matter and galaxy clustering for MG cosmologies.

ACKNOWLEDGMENTS

The authors would like to thank Hans A. Winther for kindly providing us with MGCAMB version with specific forms of $\mu(a,k)$ and $\gamma(a,k)$ functions implementing our $f(R)$ and nDGP models. We also thank the anonymous referee whose comments help improve this manuscript. This work is supported via the research project "VErTIGO" funded by the National Science Center, Poland, under Grant No. 2018/30/E/ST9/00698. We also acknowledge the support from the Polish National Science Center within research Projects No. 2018/31/G/ST9/03388, No. 2020/39/B/ST9/03494 (W. A. H. and M. B.), No. 2020/38/E/ST9/00395 (M. B.), and the Polish Ministry of Science and Higher Education (MNiSW) through Grant No. DIR/WK/2018/12. This project also benefited from numerical computations performed at the Interdisciplinary Centre for Mathematical and Computational Modelling (ICM), University of Warsaw, under Grants No. GA67-17 and No. GB79-7.

APPENDIX: RESCALING THE MATTER VARIANCE IN nDGP GRAVITY

Force enhancement due to the scalar field gradient in the case of nDGP gravity is given by

$$\Xi(z) \equiv \frac{F_{5th}}{F_N} = \left(\frac{\mathrm{d}\phi}{\mathrm{d}r}\right) \Big/ \left(\frac{\mathrm{d}\Psi_N}{\mathrm{d}r}\right), \tag{A1}$$

where ϕ is the scalar degree of freedom associated with the fifth force and Ψ_N is the standard (i.e., Newtonian) gravitational potential. Considering the Vainshtein screening for a spherically symmetric body with a Lagrangian radius, R_L, $\Xi(z)$ is given by [32,76,85]

$$\Xi(z) = \frac{2}{3\beta}\left(\frac{R_L}{r_v(z)}\right)^3 \left(\sqrt{1+\left(\frac{R_L}{r_v(z)}\right)^{-3}} - 1\right), \tag{A2}$$

where the Vainshtein radius $r_v(z)$ is

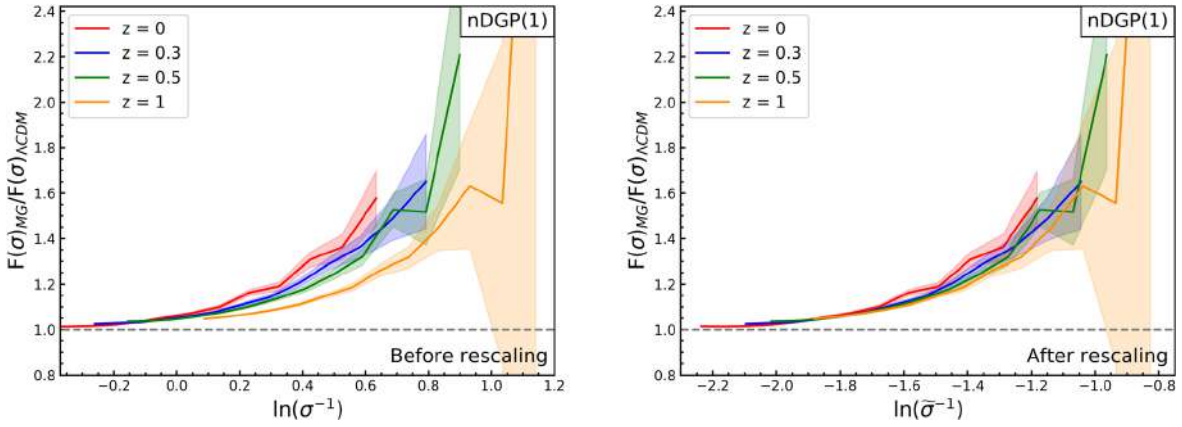

FIG. 8. Left: the ratio $\frac{F(\sigma)_{\mathrm{nDGP}(1)}}{F(\sigma)_{\Lambda\mathrm{CDM}}}$ as a function of $\ln(\sigma^{-1})$. The trend becomes less universal as the scales increase and clearly depends on redshift at larger values of $\ln(\sigma^{-1})$. Right: the same ratio as to the left, but after rescaling the matter variance, by including the force enhancement term, $\Xi(z)$, in $\ln(\tilde{\sigma}^{-1})$, where $\tilde{\sigma}(z) \equiv \sigma/\Xi(z)$. The resultant plot shows a comparatively more universal trend across epochs.

$$r_v(z) = \left(\frac{16 r_c^2 G m(r)}{9\beta(z)^2}\right)^{1/3} \tag{A3}$$

and

$$\beta(z) = 1 + 2H(z) r_c \left(1 + \frac{\dot{H}}{3H(z)^2}\right). \tag{A4}$$

As the crossover scale r_c increases, $r_v(z)$ becomes larger, and $\Xi(z)$ in Eq. (A2) goes to zero, thereby screening the fifth force and recovering GR. Since the Vainshtein radius depends on redshift, this makes the force enhancement factor in nDGP an intrinsically time-dependent function.

We used the formula for $\Xi(z)$ to remove this first-order intrinsic time-dependent enhancement in nDGP with respect to the GR case, by considering rescaled matter variance $\tilde{\sigma}(z) \equiv \sigma(z)/\Xi(z)$.

In the left-hand plot of Fig. 8, we have plotted the quantity $\frac{F(\sigma)_{\rm nDGP(1)}}{F(\sigma)_{\Lambda\rm CDM}}$ without rescaling, and we see explicit dependence of this ratio on redshift. After rescaling of matter variance in the right plot, we can acknowledge the resultant universal ratio of the nDGP(1) HMF with respect to ΛCDM across redshifts. A similar trend is seen in the case of nDGP(5), and we show the resultant rescaled plots in the main text.

[1] R. H. Cyburt, B. D. Fields, K. A. Olive, and T.-H. Yeh, Rev. Mod. Phys. **88**, 015004 (2016).
[2] P. Collaboration, Astron. Astrophys. **641**, A6 (2020).
[3] S. Alam, M. Aubert, S. Avila, C. Balland, J. E. Bautista, M. A. Bershady, D. Bizyaev, M. R. Blanton, A. S. Bolton, J. Bovy *et al.*, Phys. Rev. D **103**, 083533 (2021).
[4] M. Betoule, R. Kessler, J. Guy, J. Mosher, D. Hardin, R. Biswas, P. Astier, P. El-Hage, M. Konig, S. Kuhlmann *et al.*, Astron. Astrophys. **568**, A22 (2014).
[5] T. M. C. Abbott, A. Alarcon, S. Allam, P. Andersen, F. Andrade-Oliveira, J. Annis, J. Asorey, S. Avila, D. Bacon, N. Banik *et al.*, Phys. Rev. Lett. **122**, 171301 (2019).
[6] S. Weinberg, Rev. Mod. Phys. **61**, 1 (1989).
[7] J. S. Bullock and M. Boylan-Kolchin, Annu. Rev. Astron. Astrophys. **55**, 343 (2017).
[8] A. G. Riess, L. M. Macri, S. L. Hoffmann, D. Scolnic, S. Casertano, A. V. Filippenko, B. E. Tucker, M. J. Reid, D. O. Jones, J. M. Silverman *et al.*, Astrophys. J. **826**, 56 (2016).
[9] E. Lusso, E. Piedipalumbo, G. Risaliti, M. Paolillo, S. Bisogni, E. Nardini, and L. Amati, Astron. Astrophys. **628**, L4 (2019).
[10] T. Clifton, P. G. Ferreira, A. Padilla, and C. Skordis, Phys. Rep. **513**, 1 (2012).
[11] T. Baker, D. Psaltis, and C. Skordis, Astrophys. J. **802**, 63 (2015).
[12] K. Koyama, Rep. Prog. Phys. **79**, 046902 (2016).
[13] S. Nojiri, S. D. Odintsov, and V. K. Oikonomou, Phys. Rep. **692**, 1 (2017).
[14] P. G. Ferreira, Annu. Rev. Astron. Astrophys. **57**, 335 (2019).
[15] T. P. Sotiriou and V. Faraoni, Rev. Mod. Phys. **82**, 451 (2010).
[16] T. Baker, A. Barreira, H. Desmond, P. Ferreira, B. Jain *et al.*, Rev. Mod. Phys. **93**, 015003 (2021).
[17] K. Koyama, Int. J. Mod. Phys. D **27**, 1848001 (2018).
[18] A. Joyce, L. Lombriser, and F. Schmidt, Annu. Rev. Nucl. Part. Sci. **66**, 95 (2016).
[19] P. Bull, Y. Akrami, J. Adamek, T. Baker, E. Bellini, J. Beltrán Jiménez, E. Bentivegna, S. Camera, S. Clesse, J. H. Davis *et al.*, Phys. Dark Universe **12**, 56 (2016).
[20] S. Capozziello and M. de Laurentis, Phys. Rep. **509**, 167 (2011).
[21] C. M. Will, Living Rev. Relativity **17**, 4 (2014).
[22] J. H. Taylor and J. M. Weisberg, Astrophys. J. **253**, 908 (1982).
[23] B. P. Abbott, R. Abbott, T. D. Abbott, F. Acernese, K. Ackley, C. Adams, T. Adams, P. Addesso, R. X. Adhikari, V. B. Adya *et al.*, Phys. Rev. Lett. **119**, 161101 (2017).
[24] B. P. Abbott, R. Abbott, T. D. Abbott, F. Acernese, K. Ackley, C. Adams, T. Adams, P. Addesso, R. X. Adhikari, V. B. Adya *et al.*, Phys. Rev. Lett. **116**, 061102 (2016).
[25] R. Abuter, A. Amorim, M. Bauböck, J. P. Berger, H. Bonnet, W. Brandner, V. Cardoso, Y. Clénet, P. T. de Zeeuw *et al.* (Gravity Collaboration), Astron. Astrophys. **636**, L5 (2020).
[26] I. I. Shapiro, Phys. Rev. Lett. **13**, 789 (1964).
[27] J. Khoury and A. Weltman, Phys. Rev. D **69**, 044026 (2004).
[28] A. I. Vainshtein, Phys. Lett. **39B**, 393 (1972).
[29] A. Joyce, B. Jain, J. Khoury, and M. Trodden, Phys. Rep. **568**, 1 (2015).
[30] P. Brax, Classical Quantum Gravity **30**, 214005 (2013).
[31] J. Sakstein, Int. J. Mod. Phys. D **27**, 1848008 (2018).
[32] F. Schmidt, Phys. Rev. D **81**, 103002 (2010).
[33] W. H. Press and P. Schechter, Astrophys. J. **187**, 425 (1974).
[34] M. White, Astrophys. J. Suppl. Ser. **143**, 241 (2002).
[35] A. Jenkins, C. S. Frenk, S. D. M. White, J. M. Colberg, S. Cole, A. E. Evrard, H. M. P. Couchman, and N. Yoshida, Mon. Not. R. Astron. Soc. **321**, 372 (2001).
[36] R. K. Sheth, H. J. Mo, and G. Tormen, Mon. Not. R. Astron. Soc. **323**, 1 (2001).
[37] M. S. Warren, K. Abazajian, D. E. Holz, and L. Teodoro, Astrophys. J. **646**, 881 (2006).
[38] Z. Lukić, K. Heitmann, S. Habib, S. Bashinsky, and P. M. Ricker, Astrophys. J. **671**, 1160 (2007).

[39] W. A. Watson, I. T. Iliev, A. D'Aloisio, A. Knebe, P. R. Shapiro, and G. Yepes, Mon. Not. R. Astron. Soc. **433**, 1230 (2013).
[40] G. Despali, C. Giocoli, R. E. Angulo, G. Tormen, R. K. Sheth, G. Baso, and L. Moscardini, Mon. Not. R. Astron. Soc. **456**, 2486 (2016).
[41] J. Tinker, A. V. Kravtsov, A. Klypin, K. Abazajian, M. Warren, G. Yepes, S. Gottlöber, and D. E. Holz, Astrophys. J. **688**, 709 (2008).
[42] M. Crocce, P. Fosalba, F. J. Castander, and E. Gaztañaga, Mon. Not. R. Astron. Soc. **403**, 1353 (2010).
[43] J. Courtin, Y. Rasera, J. M. Alimi, P. S. Corasaniti, V. Boucher, and A. Füzfa, Mon. Not. R. Astron. Soc. **410**, 1911 (2011).
[44] S. Bhattacharya, K. Heitmann, M. White, Z. Lukić, C. Wagner, and S. Habib, Astrophys. J. **732**, 122 (2011).
[45] L. Ondaro-Mallea, R. E. Angulo, M. Zennaro, S. Contreras, and G. Aricò, Mon. Not. R. Astron. Soc. **509**, 6077 (2021).
[46] G. Kauffmann, S. D. M. White, and B. Guiderdoni, Mon. Not. R. Astron. Soc. **264**, 201 (1993).
[47] C. Lacey and S. Cole, Mon. Not. R. Astron. Soc. **262**, 627 (1993).
[48] R. K. Sheth and G. Tormen, Mon. Not. R. Astron. Soc. **308**, 119 (1999).
[49] A. Cooray and R. Sheth, Phys. Rep. **372**, 1 (2002).
[50] A. V. Kravtsov and S. Borgani, Annu. Rev. Astron. Astrophys. **50**, 353 (2012).
[51] G. Dvali, G. Gabadadze, and M. Porrati, Phys. Lett. B **485**, 208 (2000).
[52] B. Jain, A. Joyce, R. Thompson, A. Upadhye, J. Battat *et al.*, arXiv:1309.5389.
[53] B. Jain and J. Khoury, Ann. Phys. (Amsterdam) **325**, 1479 (2010).
[54] M. Cataneo, D. Rapetti, F. Schmidt, A. B. Mantz, S. W. Allen, D. E. Applegate, P. L. Kelly, A. von der Linden, and R. G. Morris, Phys. Rev. D **92**, 044009 (2015).
[55] M. A. Mitchell, J.-h. He, C. Arnold, and B. Li, Mon. Not. R. Astron. Soc. **477**, 1133 (2018).
[56] M. A. Mitchell, C. Arnold, and B. Li, Mon. Not. R. Astron. Soc. **502**, 6101 (2021).
[57] D. S. Y. Mak, E. Pierpaoli, F. Schmidt, and N. Macellari, Phys. Rev. D **85**, 123513 (2012).
[58] M. A. Mitchell, C. Hernández-Aguayo, C. Arnold, and B. Li, Mon. Not. R. Astron. Soc. **508**, 4140 (2021).
[59] A. Barreira, B. Li, E. Jennings, J. Merten, L. King, C. M. Baugh, and S. Pascoli, Mon. Not. R. Astron. Soc. **454**, 4085 (2015).
[60] S. Peirone, M. Raveri, M. Viel, S. Borgani, and S. Ansoldi, Phys. Rev. D **95**, 023521 (2017).
[61] F. Schmidt, A. Vikhlinin, and W. Hu, Phys. Rev. D **80**, 083505 (2009).
[62] F. Schmidt, Phys. Rev. D **80**, 123003 (2009).
[63] F. Schmidt, M. Lima, H. Oyaizu, and W. Hu, Phys. Rev. D **79**, 083518 (2009).
[64] I. Achitouv, M. Baldi, E. Puchwein, and J. Weller, Phys. Rev. D **93**, 103522 (2016).
[65] M. Cautun, E. Paillas, Y.-C. Cai, S. Bose, J. Armijo, B. Li, and N. Padilla, Mon. Not. R. Astron. Soc. **476**, 3195 (2018).
[66] E. Paillas, M. Cautun, B. Li, Y.-C. Cai, N. Padilla, J. Armijo, and S. Bose, Mon. Not. R. Astron. Soc. **484**, 1149 (2019).
[67] The Dark Energy Survey Collaboration, arXiv:astro-ph/0510346.
[68] M. Levi, C. Bebek, T. Beers, R. Blum, R. Cahn, D. Eisenstein, B. Flaugher, K. Honscheid, R. Kron, O. Lahav *et al.*, arXiv:1308.0847.
[69] R. Laureijs, J. Amiaux, S. Arduini, J. L. Augueres, J. Brinchmann, R. Cole, M. Cropper, C. Dabin, L. Duvet, A. Ealet *et al.*, arXiv:1110.3193.
[70] Ž. Ivezić, S. M. Kahn, J. A. Tyson, B. Abel, E. Acosta, R. Allsman, D. Alonso, Y. AlSayyad, S. F. Anderson, J. Andrew *et al.*, Astrophys. J. **873**, 111 (2019).
[71] L. Lombriser, B. Li, K. Koyama, and G.-B. Zhao, Phys. Rev. D **87**, 123511 (2013).
[72] T. Y. Lam and B. Li, Mon. Not. R. Astron. Soc. **426**, 3260 (2012).
[73] B. Li and G. Efstathiou, Mon. Not. R. Astron. Soc. **421**, 1431 (2012).
[74] M. Kopp, S. A. Appleby, I. Achitouv, and J. Weller, Phys. Rev. D **88**, 084015 (2013).
[75] S. Hagstotz, M. Costanzi, M. Baldi, and J. Weller, Mon. Not. R. Astron. Soc. **486**, 3927 (2019).
[76] F. Schmidt, W. Hu, and M. Lima, Phys. Rev. D **81**, 063005 (2010).
[77] C. Arnold, B. Li, B. Giblin, J. Harnois-Déraps, and Y.-C. Cai, arXiv:2109.04984.
[78] N. Ramachandra, G. Valogiannis, M. Ishak, and K. Heitmann (LSST Dark Energy Science Collaboration), Phys. Rev. D **103**, 123525 (2021).
[79] T. McClintock, E. Rozo, M. R. Becker, J. DeRose, Y.-Y. Mao, S. McLaughlin, J. L. Tinker, R. H. Wechsler, and Z. Zhai, Astrophys. J. **872**, 53 (2019).
[80] S. Bocquet, K. Heitmann, S. Habib, E. Lawrence, T. Uram, N. Frontiere, A. Pope, and H. Finkel, Astrophys. J. **901**, 5 (2020).
[81] H. A. Winther, S. Casas, M. Baldi, K. Koyama, B. Li, L. Lombriser, and G.-B. Zhao, Phys. Rev. D **100**, 123540 (2019).
[82] M. Cataneo, D. Rapetti, L. Lombriser, and B. Li, J. Cosmol. Astropart. Phys. 12 (2016) 024.
[83] S. Alam, C. Arnold, A. Aviles, R. Bean, Y.-C. Cai *et al.*, J. Cosmol. Astropart. Phys. 11 (2021) 050.
[84] W. Hu and I. Sawicki, Phys. Rev. D **76**, 064004 (2007).
[85] K. Koyama and F. P. Silva, Phys. Rev. D **75**, 084040 (2007).
[86] M. Crisostomi and K. Koyama, Phys. Rev. D **97**, 021301 (2018).
[87] J. E. García-Farieta, W. A. Hellwing, S. Gupta, and M. Bilicki, Phys. Rev. D **103**, 103524 (2021).
[88] B. Li, G.-B. Zhao, R. Teyssier, and K. Koyama, J. Cosmol. Astropart. Phys. 01 (2012) 051.
[89] S. Bose, B. Li, A. Barreira, J.-h. He, W. A. Hellwing, K. Koyama, C. Llinares, and G.-B. Zhao, J. Cosmol. Astropart. Phys. 02 (2017) 050.
[90] B. Li, G.-B. Zhao, and K. Koyama, J. Cosmol. Astropart. Phys. 05 (2013) 023.
[91] A. Barreira, S. Bose, and B. Li, J. Cosmol. Astropart. Phys. 12 (2015) 059.

[92] Y. B. Zel'Dovich, Astron. Astrophys. **500**, 13 (1970).
[93] M. Crocce, S. Pueblas, and R. Scoccimarro, Mon. Not. R. Astron. Soc. **373**, 369 (2006).
[94] G. Hinshaw, D. Larson, E. Komatsu, D. N. Spergel, C. L. Bennett, J. Dunkley, M. R. Nolta, M. Halpern, R. S. Hill, N. Odegard *et al.*, Astrophys. J. Suppl. Ser. **208**, 19 (2013).
[95] P. S. Behroozi, R. H. Wechsler, and H.-Y. Wu, Astrophys. J. **762**, 109 (2013).
[96] P. Collaboration, Astron. Astrophys. **594**, A13 (2016).
[97] P. J. E. Peebles, *The Large-Scale Structure of the Universe* (Princeton University Press, Princeton, NJ, 1980).
[98] J. E. Gunn and I. Gott, J. Richard, Astrophys. J. **176**, 1 (1972).
[99] J. A. Peacock and A. F. Heavens, Mon. Not. R. Astron. Soc. **243**, 133 (1990).
[100] J. R. Bond, S. Cole, G. Efstathiou, and N. Kaiser, Astrophys. J. **379**, 440 (1991).
[101] W. A. Hellwing, C. S. Frenk, M. Cautun, S. Bose, J. Helly, A. Jenkins, T. Sawala, and M. Cytowski, Mon. Not. R. Astron. Soc. **457**, 3492 (2016).
[102] K. Heitmann, N. Frontiere, E. Rangel, P. Larsen, A. Pope, I. Sultan, T. Uram, S. Habib, H. Finkel, D. Korytov *et al.*, Astrophys. J. Suppl. Ser. **252**, 19 (2021).
[103] M. Boylan-Kolchin, V. Springel, S. D. M. White, A. Jenkins, and G. Lemson, Mon. Not. R. Astron. Soc. **398**, 1150 (2009).
[104] R. E. Angulo, V. Springel, S. D. M. White, A. Jenkins, C. M. Baugh, and C. S. Frenk, Mon. Not. R. Astron. Soc. **426**, 2046 (2012).
[105] A. Pillepich, D. Nelson, L. Hernquist, V. Springel, R. Pakmor *et al.*, Mon. Not. R. Astron. Soc. **475**, 648 (2018).
[106] D. S. Reed, R. E. Smith, D. Potter, A. Schneider, J. Stadel, and B. Moore, Mon. Not. R. Astron. Soc. **431**, 1866 (2013).
[107] S. G. Murray, C. Power, and A. S. G. Robotham, Astron. Comput. **3**, 23 (2013).
[108] A. Lewis and A. Challinor, CAMB: Code for Anisotropies in the Microwave Background (2011), ascl:1102.026.
[109] A. Hojjati, L. Pogosian, and G.-B. Zhao, J. Cosmol. Astropart. Phys. 08 (2011) 005.
[110] F. von Braun-Bates and J. Devriendt, J. Cosmol. Astropart. Phys. 12 (2018) 028.
[111] D. Shi, B. Li, J. Han, L. Gao, and W. A. Hellwing, Mon. Not. R. Astron. Soc. **452**, 3179 (2015).
[112] W. A. Hellwing, K. Koyama, B. Bose, and G.-B. Zhao, Phys. Rev. D **96**, 023515 (2017).
[113] H. Oyaizu, M. Lima, and W. Hu, Phys. Rev. D **78**, 123524 (2008).
[114] F. von Braun-Bates, H. A. Winther, D. Alonso, and J. Devriendt, J. Cosmol. Astropart. Phys. 03 (2017) 012.
[115] H. A. Winther, F. Schmidt, A. Barreira, C. Arnold, S. Bose, C. Llinares, M. Baldi, B. Falck, W. A. Hellwing, K. Koyama *et al.*, Mon. Not. R. Astron. Soc. **454**, 4208 (2015).
[116] C. Hernández-Aguayo, C. Arnold, B. Li, and C. M. Baugh, Mon. Not. R. Astron. Soc. **503**, 3867 (2021).
[117] R. E. Smith, J. A. Peacock, A. Jenkins, S. D. M. White, C. S. Frenk, F. R. Pearce, P. A. Thomas, G. Efstathiou, and H. M. P. Couchman, Mon. Not. R. Astron. Soc. **341**, 1311 (2003).
[118] D. S. Reed, R. E. Smith, D. Potter, A. Schneider, J. Stadel, and B. Moore, Mon. Not. R. Astron. Soc. **431**, 1866 (2013).
[119] J. Comparat, F. Prada, G. Yepes, and A. Klypin, Mon. Not. R. Astron. Soc. **469**, 4157 (2017).
[120] R. Seppi, J. Comparat, K. Nandra, E. Bulbul, F. Prada, A. Klypin, A. Merloni, P. Predehl, and J. Ider Chitham, Astron. Astrophys. **652**, A155 (2021).
[121] M. White, Astron. Astrophys. **367**, 27 (2001).
[122] B. Diemer, Astrophys. J. **903**, 87 (2020).
[123] S. More, A. V. Kravtsov, N. Dalal, and S. Gottlöber, Astrophys. J. Suppl. Ser. **195**, 4 (2011).
[124] A. Knebe, S. R. Knollmann, S. I. Muldrew, F. R. Pearce, M. A. Aragon-Calvo *et al.*, Mon. Not. R. Astron. Soc. **415**, 2293 (2011).
[125] C. Grove, C.-H. Chuang, N. Chandrachani Devi, L. Garrison *et al.*, arXiv:2112.09138.
[126] W. A. Hellwing and R. Juszkiewicz, Phys. Rev. D **80**, 083522 (2009).
[127] A. Barreira, B. Li, W. A. Hellwing, L. Lombriser, C. M. Baugh, and S. Pascoli, J. Cosmol. Astropart. Phys. 04 (2014) 029.
[128] A. Barreira, B. Li, W. A. Hellwing, C. M. Baugh, and S. Pascoli, J. Cosmol. Astropart. Phys. 09 (2014) 031.
[129] C.-Z. Ruan, T.-J. Zhang, and B. Hu, Mon. Not. R. Astron. Soc. **492**, 4235 (2020).
[130] L. Lombriser, K. Koyama, and B. Li, J. Cosmol. Astropart. Phys. 03 (2014) 021.

Chapter 3: Analytical modelling of the Power Spectrum in Modified Gravity cosmologies

You look at science (or at least talk of it) as some sort of demoralizing invention of man, something apart from real life, and which must be cautiously guarded and kept separate from everyday existence. But science and everyday life cannot and should not be separated.

-Rosalind Franklin

Chapter 3

Analytical modelling of the Power Spectrum in Modified Gravity cosmologies

The matter power spectrum, PS of the cosmic density distribution is an important quantity in the studies of large-scale structure formation theories. PS quantifies the variance of density fluctuations for a given wavenumber, k. On large scales, PS agrees with the linear theory predictions, and is a direct measurement of primordial density fluctuations. On small scales, PS carries information of the non-linear evolution of cosmic density fields. The accurate measurement of the PS allows us to test some of the most fundamental questions in cosmology today, such as the shape of the primordial PS [67, 68] and further its relation to fundamental theories of structure formation, the mass of the neutrino [8, 284, 178] and the nature of DM and DE [207, 247, 128, 148, 23, 274, 115, 193]. Hence, determination of the PS of mass fluctuations, and its evolution across redshifts is one of the main goals of the modern observational cosmology.

In Fig. 3.1, we show the ΛCDM PS from both linear theory predictions (obtained using CAMB [171], dashed lines) and simulations (solid lines) across redshifts indicated in the legend. We can clearly see that the linear and simulation predictions match well on large scales (for $k < 0.2\ h/\mathrm{Mpc}$). As we move to the smaller scales, there is an enhancement in mode coupling, which increases the non-linear contribution. Also, we can clearly see that the amplitude of PS enhances with redshift. This signifies that the amplitude of PS is sensitive to the underlying dynamics associated with structure formation in the universe.

In addition, we plot the PS for different MG models at $z = 0$ in Fig. 3.2. In the top panel, we show how the simulation PS behaves across different scales, and in the bottom panel, how the PS varies in MG models *w.r.t.* ΛCDM predictions. Here, we can clearly see that all models have departures from ΛCDM, with distinct trends especially at the small non-linear scales. PS in stronger variants (F5 and N1) can depart from ΛCDM by 20% on small scales. These differences result from the interplay between

the effects of the fifth-force and the screening mechanisms. This makes PS and the associated measures and observables sensitive to the modifications to the underlying theory of gravity.

From Fig. 3.1 and Fig. 3.2, we can deduce that the PS is sensitive to the underlying gravitational physics across length and redshift scales. These plots show that it becomes imperative to study MG PS in order to constrain cosmology, as well as understand the MG signatures that are expected in the observational studies that consider PS as an input, for instance in galaxy clustering, cluster abundances, weak lensing, peculiar galaxy measures etc. [92, 148, 129, 182, 10, 269, 270].

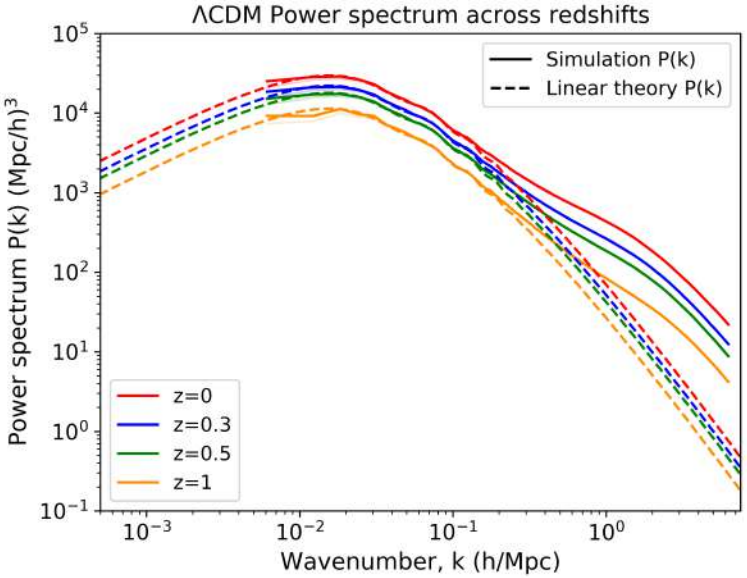

Figure 3.1: ΛCDM PS from linear theory (dashed line) and simulations (solid) for $z = 0, 0.3, 0.5$ and 1. The shaded region corresponds to the uncertainty in the ELEPHANT results, which is the inverse of the square root of the number of statistically independent modes contributing to each k-bin.

3.1 Need for analytical modelling

Apart from relying on data from future experiments, progress in the theoretical understanding of the PS for MG theories will be crucial in improving the sensitivity of observables associated with various structure formation scenarios. Modelling the PS is useful for many cosmological studies, for instance, in weak lensing, where the lensing signal is sourced by the distribution of all matter in the Universe. Cosmological N-body simulations give the most reliable estimates for the PS across length and time scales. These are essential for modelling the structure growth at quasi-linear and non-linear scales where linear perturbation theory breaks down, and higher-order perturbation theory is difficult to perform. At large scales, results from simulations match the linear theory predictions. However, when we move to smaller scales, non-linear effects become

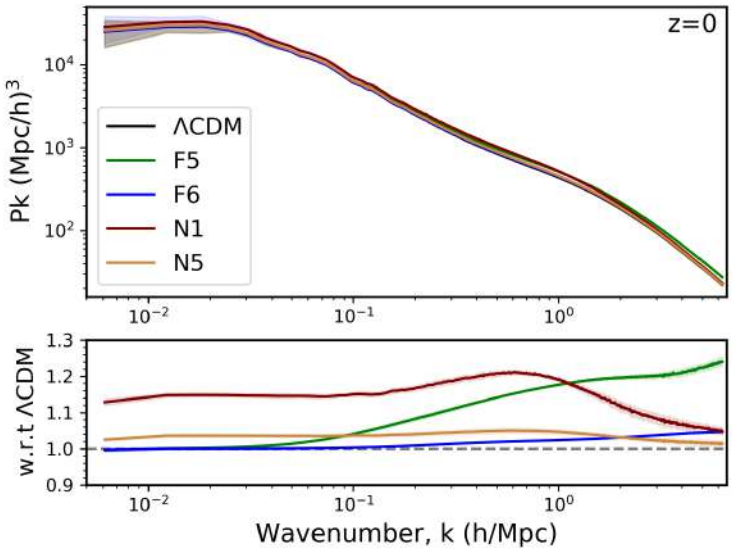

Figure 3.2: *Top panel:* Simulation PS from all gravity models, at $z = 0$. *Lower panel:* Comparison of MG to ΛCDM PS.

more significant. The linear theory fails to capture the intrinsic non-linearities associated with the evolution of density perturbations. This is the regime where we expect the constraining power of the present and future surveys. We need to rely on N-body simulations to probe the PS for smaller non-linear scales.

However, as we already highlighted in Chapters 1 and 2, full N-body simulations are computationally expensive and time-consuming. This limits our abilities to use them as cheap and quick tools to study the density perturbations in the non-linear regime, and to compute the PS.

Given the considerable computational expenses of MG simulations, it is worthwhile to develop alternative approaches to simulations, which capture the main MG effects, and simultaneously help enable reliable and quick forecasts of cosmological parameters. A promising solution to address this problem is through the use of emulation techniques (e.g., [16, 164, 209]). The process involves running a grid of cosmological simulations spanning a specific cosmological parameter space, followed by the utilisation of an emulator to swiftly and accurately interpolate the results for any chosen cosmological parameters within the boundaries of the initial suite. These emulators, once constructed, can be executed in mere fractions of a seconds, making them highly applicable in cosmological likelihood analyses. For MG models, emulators have been proposed in e.g. [21, 287, 237, 195, 98, 106]. This approach is sophisticated and promising, however, it is still developing, and carries its own limitations. For instance, there is a trade-off between the accuracy of the emulator prediction, the range of parameter values included, and the number of simulations that can feasibly be run from the base grid. In addition, adding new extensions of MG e.g. fifth-force computations, and additional non-linear screening physics, or probing a larger or a different cosmological

parameter space often requires one to considerably adapt the base grid of simulations used to build the emulator, which again can be computationally expensive.

Other than emulators, there has been development on the theoretical side to analytically compute PS in MG models (for *e.g.* [134, 156, 55, 198]). However, the level of prediction in these approaches is significantly limited by a number of approximations.

To be able to derive constraints, or to provide forecasts for how well the future experiments will constrain deviations from GR, we need to have an accurate model for the non-linear matter PS. This generally has to be derived on a model-by-model basis. Taking this as the motivation, we opt for a more general and flexible *Halo-model approach* (HM). The HM formalism has been used to model non-linear MG PS in [6, 180, 236, 32, 33, 55, 244]. However, in these works, HM is mainly based on the theoretical spherical collapse model, and is explicitly solved for each MG variant. In our approach, however, we rely on the calibration of the phenomenological components of HM to N-body simulations.

The main advantage of using the semi-analytic approach, like HM, over simulations is that it is computationally inexpensive. It can flexibly be applied to a different set of background cosmological parameters usually without re-calibrating whereas, in simulations, we need to perform a new run for each new set of parameters. The development of these semi-analytical models enables a clearer way of pinpointing the physical effects for both standard and non-standard cosmologies.

In the next section, we describe the HM framework, and further extend it to our MG models. Later, we test the HM performance with the simulation results.

3.2 Halo Model framework

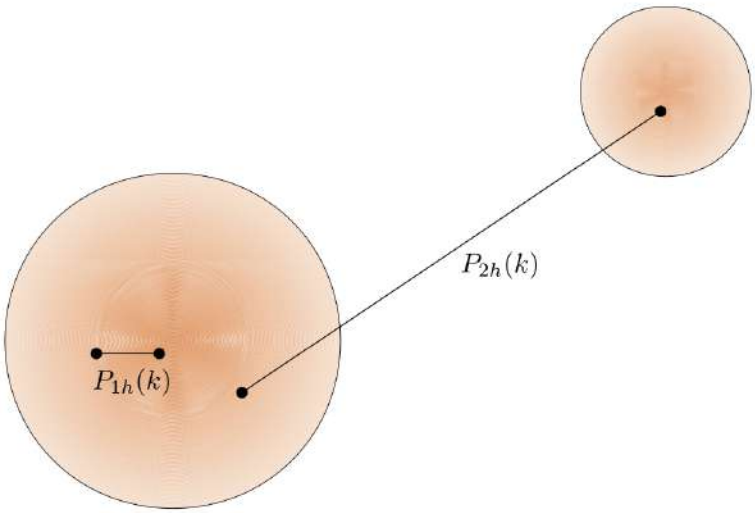

Figure 3.3: Pictorial representation of the 1-halo ($P(k)_{1h}$) and 2-halo ($P(k)_{2h}$) components of the Halo model (Eq. (3.8)). $P(k)_{1h}$ dominates the power spectrum within a halo, and the large scales are dominated by $P(k)_{2h}$. Image credits: [86]

As highlighted in the previous section, we build our theoretical template for computing the non-linear matter PS using the Halo model approach (HM) [248]. This formalism is reviewed in detail in [73, 22]. HM describes the statistics of the density field well into the regimes where the perturbation theory fails. HM approach is phenomenological *i.e.* it is not based on any first principles, and describes the Universe as we see in simulations. In our work, we exploit the flexibility of this framework, and its ability to model the non-linear scales. This makes the HM approach very attractive for analysing data from a multitude of probes of large-scale cosmological structure, and to extract information from smaller scales where linear or quasi-linear perturbation theory no longer applies.

The basic assumption in the HM build-up is that each DM particle belongs to one and only one halo. Using this assumption, the HM approach combines the linear theory predictions, with the empirical properties of halos to compute the total matter PS.

In the HM framework, the total matter density field consists of superposition of halos, i at locations x_i with masses M_i, and can be written as

$$\rho_m^{HM}(x) = \sum_i \rho_h(|x-x_i|, M_i), \tag{3.1}$$

where $\rho_h(x,M)$ is the halo density profile which is assumed to be spherically symmetric for simplicity, and depends only on the mass M.

This sum over all halos can be written as an integral over number density of halos (HMF) *i.e.* $n_h(x) = \int d\ln M dn(x)/d\ln M$, and this equation becomes

$$\rho_m^{HM}(x) = \int d^3x' \int d\ln M \frac{dn(x')}{d\ln M} \rho_h(|x-x'|, M), \tag{3.2}$$

where x' is the center-of-mass of the halo. We define normalised profile $y(x,M) \equiv \rho_h(x,M)/M$, which obeys

$$\int d^3y \;\; y(x,M) = 1. \tag{3.3}$$

This yields

$$\rho_m^{HM}(x) = \int d^3x' \int d\ln M \frac{dn(x')}{d\ln M} M y(|x-x'|, M). \tag{3.4}$$

Since all matter particles are contained in halos, the integral over the Halo Mass Function, weighted by mass, should return the mean matter density *i.e.*

$$\int d\ln M \;\; M \frac{dn}{d\ln M} = \rho_m. \tag{3.5}$$

Also, as the matter is not biased *w.r.t.* itself,

$$\int d\ln M M^2 b(M) \frac{dn}{d\ln M} = \rho_m. \tag{3.6}$$

Using Eqs. (3.4) and (3.5),and $\delta_m = \rho/\rho_m - 1$, we obtain

$$\delta_m^{HM}(x) = \int d\ln M \frac{M}{\rho_m} \frac{dn}{d\ln M} \int d^3x' \delta_h(x', M) y(|x - x'|, M). \tag{3.7}$$

This equation shows that we can compute the matter PS in the HM using HMF ($\frac{dn}{d\ln M}$), the halo profile $y(x, M)$, and the clustering of halos (via the δ_h term).

In the Fourier space, the PS in HM naturally breaks into two components:

$$P(k)_{HM} = P(k)_{1h} + P(k)_{2h}. \tag{3.8}$$

We represent this equation pictorially in Fig. 3.3. Here $\mathrm{P}(k)_{1h}$ is the power from within a halo (called *one-halo* term) and dominates the small scales. $\mathrm{P}(k)_{2h}$ (the *two-halo* term) is the power contribution among halos, and dominates on large-scales (*i.e.* $k \leq 0.5h/\,\mathrm{Mpc}$). We can expand these two contributions, which are given by

$$P(k)_{1h} = \int_0^\infty dM |\tilde{u}(k|M)|^2 \left(\frac{M}{\bar{\rho}}\right)^2 n(M), \tag{3.9}$$

and

$$P(k)_{2h} = I_m^2(k) P(k)_{\mathrm{lin}}, \tag{3.10}$$

where,

$$I_m(k) = \frac{1}{\bar{\rho}} \int_0^\infty dM |\tilde{u}(k|M)| M n(M) b(M). \tag{3.11}$$

$I_m \to 1$ for $k \to 0$ in order to match the linear theory predictions at large scales. The integrals in Eq. (3.9) and Eq. (3.11) should in principle cover all possible halo mass ranges, but in practice, some limits on the minimum mass ($\mathrm{M_{min}}$), and maximum mass ($\mathrm{M_{max}}$) are introduced.

Here, $P(k)_{\mathrm{lin}}$ is the linear theory matter PS. $n(M)$ is the HMF, $b(M)$ is the *linear halo bias* that quantifies the relation between halos and the underlying density fields on the large-scales. The term $|\tilde{u}(k|M)|$ is the normalized Fourier transform of the internal density profile of a halo of mass M, such that $\tilde{u}(k \to 0, M) \to 1$. To compute $|\tilde{u}(k|M)|$, we use the NFW concentration-mass relation, $c(M)$ which is a halo density fitting parameter [208]. Both $b(M)$ and $c(M)$ are further elaborated in Chapter 4. These fundamental components of HM enable the PS predictions from HM at any given redshift where these halo properties are well-defined.

In Fig. 3.4, we plot the total matter PS for ΛCDM, obtained from Eq. (3.8). Here, we can see that the small scales (or large k values) are dominated by the one-halo term, $P(k)_{1h}$ (blue line). Two-halo term, $P(k)_{2h}$ (shown in orange line) dominates the large-scales. This latter contributor matches well with the linear theory predictions (green line) for $k \leq 1h/\,\mathrm{Mpc}$. The total power contribution, $P(k)_{TOT}$ is given as a sum of both $P(k)_{1h}$ and $P(k)_{2h}$ terms, denoted here by the red line.

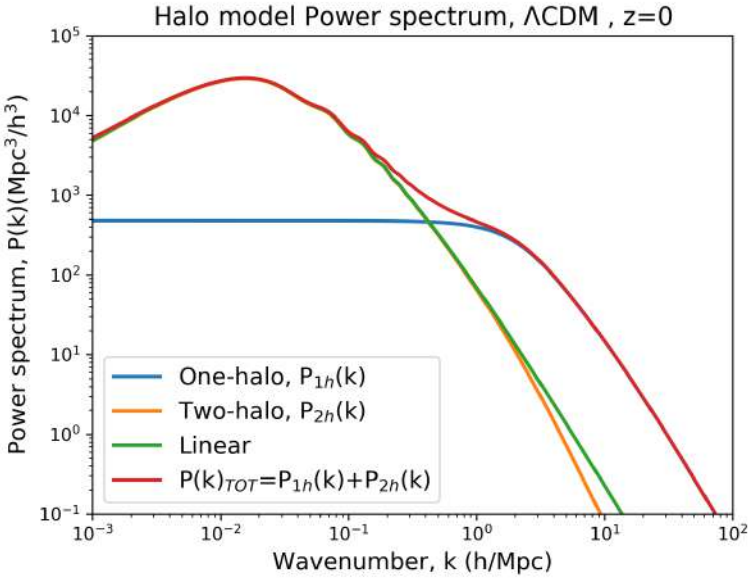

Figure 3.4: Non-linear matter PS computed using the Halo Model approach. The blue line is the one-halo term ($P(k)_{1h}$, Eq. (3.9)), the orange line is to the two-halo term ($P(k)_{2h}$, Eq. (3.10)), and the red line corresponds to the total Halo Model PS ($P(k)_{TOT}$, Eq. (3.8)).

As we see here, the HM provides a framework for modelling the matter variance, and its tracers in a way that is not limited to a specific cosmological model, and can be used to make predictions for non-linear cosmological observables in a variety of non-standard scenarios. Originally, HM has been proposed for standard ΛCDM cosmology. However, this HM framework can be applied to a variety of alternative cosmologies, as long as we have estimates for the HM ingredients.

As we show in Eq. (3.9) and Eq. (3.11), we need to integrate over wide halo mass ranges. For our work, we consider integration from $M_{min} = 1\ M_\odot/h$, to $M_{max} = 10^{16}\ M_\odot/h$. However, our simulations probe only the large mass ranges encompassing galaxy groups or clusters ($> 7.80 \times 10^{12} M_\odot/h$). As a result, we resort to analytical approaches to compute the halo properties for the HM build-up, which can, in principle, be extended to wide ranges of halo masses. Namely, we used the following analytical expressions for these HM inputs:

1. For the **Halo Mass Function**, we use the fitting function that we proposed in [112] (mentioned here inEqs. (2.14) and (2.15)) to compute the response functions for these MG models, Δ_{MG} ($=F(\sigma)_{MG}/F(\sigma)_{\Lambda CDM}$). To obtain the MG HMF (Eq. (2.13)) we further multiply Δ_{MG} with the ΛCDM HMF predictions. For the latter, we tested various theoretical HMF functions in the literature (for e.g. [251, 277, 234, 267, 77, 75, 278, 83]). HMF expression from Watson et al. (W13, [278]) gives the most optimum results for our HM fitting, which is given by

$$F(\sigma)_{\Lambda CDM} = A\left[\left(\frac{\beta}{\sigma}\right)^{\alpha} + 1\right] e^{-\gamma/\sigma^2}. \tag{3.12}$$

Here, σ is the variance of density fluctuations (Eq. (1.23)), A $= 0.282$, $\alpha = 2.163$, $\beta = 1.406$ and $\gamma = 1.210$.

2. For the **linear halo bias** computations, we again test various bias functions in the literature [251, 249, 268]. In this work, we stick to the bias predictions from Sheth, Mo and Tormen (2001) ([251], hereafter BIAS-SMT), given by

$$b(M) = \frac{1}{\sqrt{a}\delta_c(z)}\left(\sqrt{a}(a\nu^2) + \sqrt{a}b(a\nu^2)^{1-c} - \frac{(a\nu^2)^c}{(a\nu^2)^c + b(1-c)(1-c/2)}\right). \quad (3.13)$$

Here, $a = 0.707, b = 0.5$ and $c = 0.6$.

This relation has been proposed for ΛCDM. However, we extrapolate this expression even for the case of our MG models by substituting the peak-height, $\nu(M) = \delta_c/\sigma(M)$, specific to each MG variant. We find that the SMT-BIAS for the MG scenarios gives similar performance as for the case of ΛCDM (also shown in the top panels of Fig. 4.1). Additionally, it also captures the MG to ΛCDM bias ratio as is obtained from the simulation predictions. In the appendix of [110], we provide a much more comprehensive justification for the validity of this substitution.

3. For computing the **concentration-mass, $c(M)$ relations**, we use the analytical response functions proposed in [202] for $f(R)$ ($c(M)_{f(R)}/c(M)_{\Lambda CDM}$), and [203] for nDGP ($c(M)_{\rm nDGP}/c(M)_{\Lambda CDM}$). These expressions have been obtained by direct NFW fitting to the density profiles of halos. The response functions from these works are multiplied the ΛCDM $c(M)$ (which we use from Ludlow et al. (2016) [L16], [183]) to obtain $c(M)_{\rm MG=f(R),nDGP}$. Considering this ratio instead of absolute $c(M)_{\rm MG}$ eliminates the leading-order systematics due to different background cosmologies.

From L16,

$$c(\nu)_{\Lambda\rm CDM} = c_0\left(\frac{\nu}{\nu_0}\right)^{-\gamma_1}\left[1+\left(\frac{\nu}{\nu_0}\right)^{1/\beta}\right]^{-\beta(\gamma_2-\gamma_1)}. \quad (3.14)$$

ν is the peak-height ($= \delta_c/\sigma(M)$), $c_0 = 3.395\times(1+z)^{-0.215}$, $\beta = 0.307\times(1+z)^{0.540}$, $\gamma_1 = 0.628\times(1+z)^{-0.047}$, $\gamma_2 = 0.317\times(1+z)^{-0.893}$, and $\nu_0 = (4.135 - 0.564a^{-1} - 0.210a^{-2} + 0.0557a^{-3} - 0.00348a^{-4})\times D(z)^{-1}$.

For the $f(R)$ gravity model,

$$y(x) = \frac{1}{2}\left(\frac{\lambda}{\omega_s}\phi(x')\left[1+erf\left(\frac{\alpha x'}{\sqrt{2}}\right)\right]+\gamma\right)(1-\tan h(\omega_t[x+\xi_t])), \quad (3.15)$$

where $y = log_{10}(c(M)_{f(R)}/c(M)_{\Lambda CDM} - 1)$, $x' = (x-\xi_s)/\omega_s$, $x = \log_{10}(M_{500}/10^{p_2})$, $p_2 = 1.5\log_{10}\left[\frac{f_R(z)}{1+z}\right] + 21.64$, $\lambda = 0.55\pm0.18$, $\xi_s = -0.27\pm0.09$, $\omega_s = 1.7\pm0.4$, $\alpha = -6.5\pm2.4$, $\gamma = -0.07\pm0.04$, $\omega_t = 1.3\pm1.0$ and $\xi_t = 0.1\pm0.3$.

For the nDGP gravity model,

$$c(M)_{\rm nDGP}/c(M)_{\Lambda CDM} = [A - B\log_{10}(M_{200}M_{\odot}h^{-1})](H_0 r_c)^{-0.71\pm0.05} + 1. \quad (3.16)$$

Here, $A = (0.35 \pm 0.01)(H_0 r_c)^{-0.71\pm0.05}$, and $B = (0.0302 \pm 0.0008)(H_0 r_c)^{-0.71\pm0.05}$.

Using the analytical expressions from Eq. (3.8) to Eq. (3.11), we extend the standard HM to both $f(R)$ and nDGP cosmologies. We further compare the resultant PS from HM, $P(k)_{\rm HM}$ with the simulation results, $P(k)_{\rm sim}$. This is shown in Fig. 3.5, where we compare all the gravity models and redshifts considered in our study.

Here, we can clearly see that HM performs qualitatively similarly in MG, as it does for the case of standard ΛCDM: namely, the HM predictions match within per-cent level accuracy with simulations upto $k \leq 0.2 - 0.3\ h/\text{Mpc}$. HM further under-predicts power at $k \approx 0.5h/\text{Mpc}$, corresponding to the scale at which the dominant PS contributor transitions between the $P(k)_{1h}$ and $P(k)_{2h}$ terms. This particular discrepancy has been documented as a well-established caveat within the HM framework for the standard ΛCDM [196]. We observe that this underestimation persists and extends even in our MG models. The main conclusion from this plot is that, in order to obtain per-cent level (or better) predictions for cosmological parameters from present and future cosmological surveys, we cannot use HM predictions in their naive form. As mentioned, HM performs at best well within a per-cent level up to $k \leq 0.2 - 0.3\ h/\text{Mpc}$, which are quasi-linear scales. However, it is in the non-linear small scales where much of the constraining power from cosmological surveys is expected [163, 182, 115, 274].

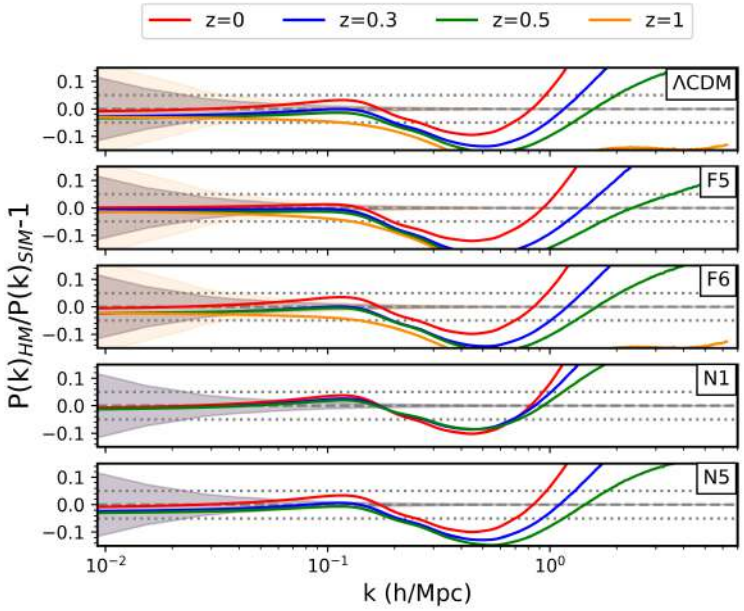

Figure 3.5: Comparison of the PS from halo-model, $\text{P(k)}_{\rm HM}$ for ΛCDM and the variants of MG models, with ELEPHANT simulations, P(k)_{sim}. This comparison is done for $z = 0, 0.3, 0.5$ and 1 (here we have simulation PS results only at $z = 0, 0.3$ and 0.5 for N1 and N5). The shaded regions are the errors from the simulations, and the horizontal gray dotted lines correspond to the 5% accuracy regime.

3.3 Modelling the standard ΛCDM non-linear Matter Power Spectrum

As we mentioned, in order to match the accuracy of current and future large-scale surveys, the accuracy of HM isn't good enough. Nevertheless, notable progress has been made by extending the HM framework to yield fitting functions, which are close to or at par with the accuracy required by the current and upcoming surveys. However, such advancements have primarily focused on the extensively studied and well-constrained ΛCDM cosmological scenario. Here, we mention two main approaches:

1. HALOFIT: This approach has been proposed originally in [256], and further improved in [263]. HALOFIT is an HM inspired fitting function, which breaks the total PS as a sum on *quasi-linear* and *halo* terms, that are analogous to the two-halo and one-halo terms from HM. In the left plot of Fig. 3.6, we compare HALOFIT PS predictions, $P(k)_{\rm HALOFIT}$ with $P(k)_{\rm sim}$. Here we can clearly see that HALOFIT performs much better than HM, reaching a percent level accuracy for non-linear scales beyond $k > 1{\rm h}/\,{\rm Mpc}$.

2. HMCODE: This approach has been originally proposed in [197], with later modifications in [200]. HMCODE builds its framework on the standard Halo Model, with additional corrections in regard to physical constraints. In the right plot of Fig. 3.6, we show the performance of HMCODE PS, $P(k)_{\rm HMCODE}$ with $P(k)_{\rm sim}$ predictions. Again, we see that this approach also gives a a percent level accuracy with simulation predictions, that, similar to HALOFIT, extends to the non-linear scales of $k > 1{\rm h}/\,{\rm Mpc}$.

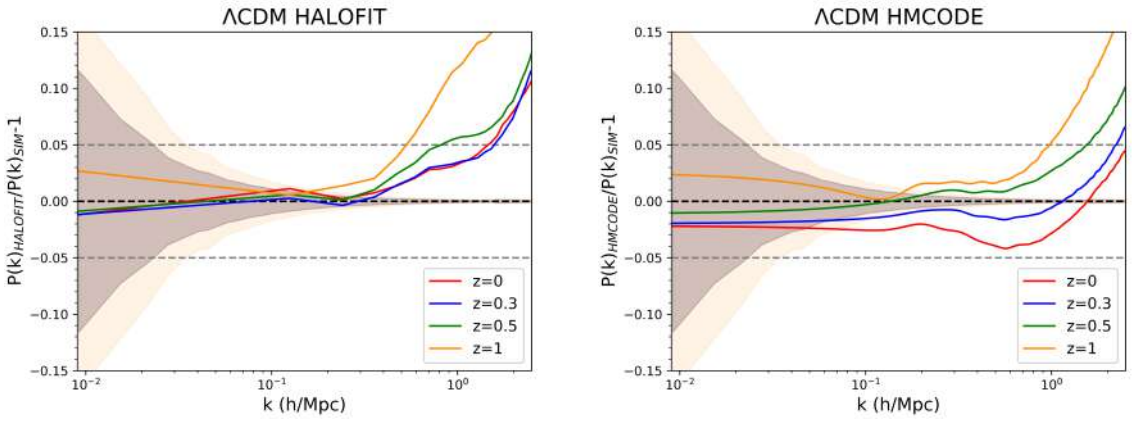

Figure 3.6: Comparison of the PS from HALOFIT (left) and HMCODE (right) for ΛCDM with ELEPHANT simulations, $\mathrm{P(k)}_{sim}$. This comparison is plotted for $z = 0, 0.3, 0.5$ and 1. The shaded regions are the errors from the simulations, and the horizontal gray dashed lines correspond to the 5% accuracy regime.

3.4 Summary of the attached article: S. Gupta, W. A. Hellwing, and M. Bilicki, Phys. Rev. D 107, 083525 (2023)

In the previous section, we mentioned the widely used tools to compute the ΛCDM PS, particularly at small non-linear scales. Nevertheless, it is important to note that MG models face a deficiency in terms of such flexible methodologies. In the following attached article [110], our objective is to rectify this gap, and we propose a framework to compute the non-linear matter PS in MG models.

First, we study the HM framework in the context of these MG models. This is analogous to Section 3.2, where we define the HMF, $b(M)$ and $c(M)$ relations for these models across different redshifts. The performance of the PS from HM, for both MG and ΛCDM, is not at par with the %-level (and better) parameter estimation accuracy we expect from our current and future surveys.

To get a better PS modelling for our MG models, we further investigate the ratio $\Upsilon(k) = \frac{P(k)_{\rm MG}}{P(k)_{\Lambda\rm CDM}}$ from linear theory ($\Upsilon(k)_{\rm lin}$), Halo Model ($\Upsilon(k)_{\rm HM}$), and simulations ($\Upsilon(k)_{\rm sim}$) in Fig. 2 on the attached article. We observe that all ratios converge to the linear theory predictions on the large scales. However, trends peculiar to each MG model emerge in simulations as we move to the smaller non-linear scales. Namely, $f(R)$ variants have a monotonic enhancement with k, whereas nDGP has a constant, and then a peak-like enhancement at an intermediate k-scale. The main point to note from this plot is that HM predictions qualitatively agree with this ratio from simulations *i.e.* $\Upsilon(k)_{\rm HM}$ captures the scales and shapes of $\Upsilon(k)_{\rm sim}$ for both the $f(R)$ and nDGP models.

Using these results, we propose to use the $\Upsilon(k)_{\rm HM}$ ratio to compute the non-linear predictions for the P(k)$_{\rm MG}$. Our approach takes two main inputs:

1. Response function from HM, $\Upsilon_{\rm HM}(k) = \frac{P(k)_{\rm HM,\ MG}}{P(k)_{\rm HM,\Lambda CDM}}$ (MG = $f(R)$, nDGP).
2. Non-linear prediction for the ΛCDM PS, $P(k)_{\Lambda\rm CDM}$. In this article, we use both HALOFIT and HMCODE for this purpose.

Here, both $P(k)_{\rm HM,\ MG}$ and $P(k)_{\rm HM,\Lambda CDM}$ are the HM PS predictions for MG (=$f(R)$, nDGP) and ΛCDM models respectively computed using Eq. (3.8)-Eq. (3.11). The respective inputs for HMF, $b(M)$ and $c(M)$ relations are explicitly mentioned in Section 3.2.

From these inputs, the non-linear PS in these MG models, $P(k)_{\rm MG}$ can be obtained by multiplying $\Upsilon(k)_{\rm HM}$ with any non-linear prescription for $P(k)_{\Lambda\rm CDM}$, *i.e.*

$$P(k)_{\rm MG} = \Upsilon(k)_{\rm HM} \times P(k)_{\Lambda\rm CDM}. \tag{3.17}$$

The results obtained from the above equation are plotted in Fig. 3.7. In this figure, we show the performance of Eq. (3.17) obtained using the ΛCDM PS inputs from both HALOFIT (left) and HMCODE (right). We can clearly see that on comparing these results with the standard HM plot (Fig. 3.5), we have an improvement in the performance of

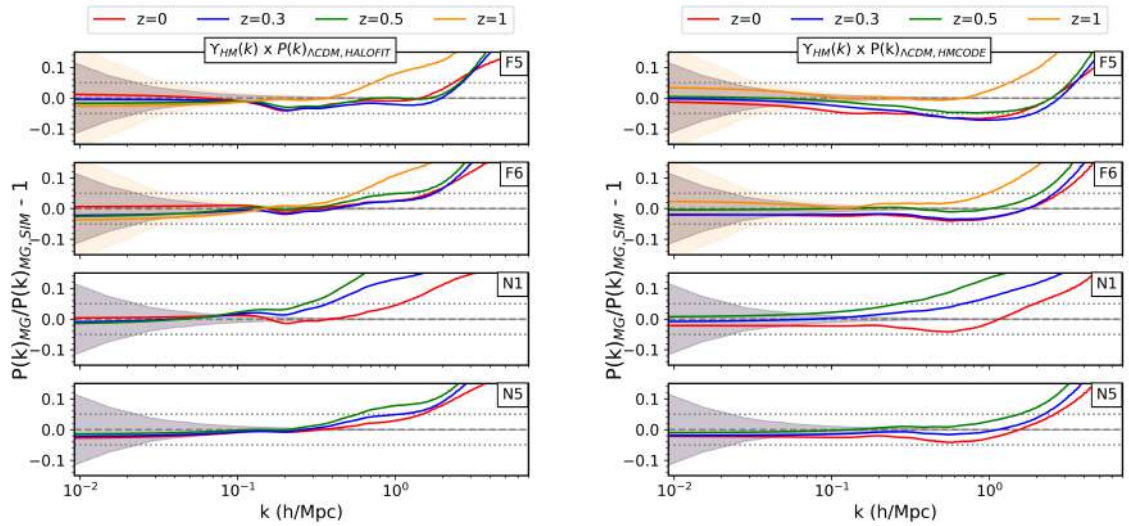

Figure 3.7: Comparison of the $P(k)_{\rm MG}$ (from Eq. (3.17)) with the ELEPHANT simulations $\mathrm{P(k)_{sim}}$. Left plot is the input of $P(k)_{\Lambda\rm CDM}$ predictions from HALOFIT, and right is the $P(k)_{\Lambda\rm CDM}$ input from HMCODE. This comparison is plotted for $z = 0, 0.3, 0.5$ and 1 (here we have simulation PS results only at $z = 0, 0.3$ and 0.5 for N1 and N5). The shaded regions are the errors from the simulations, and the horizontal gray dotted lines correspond to the 5% accuracy regime.

the analytical modelling. More quantitatively, HM reaches a 5% accuracy only upto quasi-linear scales of $0.2-0.3\ h/\mathrm{Mpc}$. Now, by using HM only to compute $\Upsilon_{\rm HM}(k)$, and combining with both HALOFIT and HMCODE ΛCDM predictions, we improve the accuracy of 5% accuracy, which is now up-to $k \leq 0.5-3h/\mathrm{Mpc}$, depending on the model and redshift. We can see here that the performance of Eq. (3.17) generally worsens with increase in redshift, but still remains significantly improved when compared to the naive predictions of HM. This level of accuracy is enough for forecasting constraints on modern-era cosmological observables.

More generally, the accuracy of Eq. (3.17) depends on the user-inputs for both the baseline $\mathrm{P(k)_{\Lambda CDM}}$, and the predictions for the halo properties used in the HM-buildup. In Fig. 3.7, we can clearly see that both HALOFIT and HMCODE perform similarly, but with exceptions at smalls scales and higher redshifts. One can employ any other best-fit $P(k)_{\Lambda\rm CDM}$ to further improve the final accuracy of $P(k)_{\rm MG}$. Also, higher-resolved MG simulations can give better calibration for the input halo properties to formulate $\Upsilon_{\rm HM}(k)$, which can further improve the predictions of our analytical framework.

Furthermore, our framework possesses an additional advantage in terms of its versatility. In this attached article, we build the $\Upsilon_{\rm HM}(k)$ only for $f(R)$ and nDGP. However, it can be readily extended, not only to a wider range of model parameter space but also, in principle, to encompass other models of large-scale cosmological structure formation that involve modifications to gravity. Such flexibility opens up exciting possibilities for exploring and analysing diverse modified cosmological scenarios. Also, here we focus only on PS modelling for DM. Baryonic suppression does not significantly influence the PS at the scales we probe in this work [63, 7]. However, [199, 200, 7] have shown that

the flexibility of the HM framework allows to add additional parameters to incorporate baryonic effects from hydrodynamical simulations. Accounting for such effects in the $P(k)_{\rm MG}$ modelling is indeed a significant endeavour, and is well-beyond the scope of this thesis.

We also test our approach on a different suite of MG simulations for $f(R)$ and nDGP, that were not used in the original calibration of the halo properties (simulations described in [206]). Fig. 4 of the article shows a comparison from the predictions of our analytical framework with the simulation results. This plot shows that our theoretical modelling performs similarly even in these simulations suite, and gives percent accuracy in MG PS computations, way up-to the non-linear scales ($k \leq 0.5 - 2.5$ $h/\,$Mpc). This test assure the validity of our approach, and it can be further extended to both simulations and cosmologies which were not used in the original calibration of the halo properties.

PS serves not only as a valuable end-goal prediction from cosmological analysis, but also forms the basis which is used to model and forecast a number of other LSS observables. Consequently, our reliable and quick analytical modelling of the PS marks as a pivotal initial step towards accurately modelling other LSS properties that rely on the PS as a fundamental input parameter.

Improved analytical modeling of the nonlinear power spectrum in modified gravity cosmologies

Suhani Gupta,[*] Wojciech A. Hellwing,[†] and Maciej Bilicki[‡]
Center for Theoretical Physics, Polish Academy of Sciences, Aleja Lotników 32/46, 02-668 Warsaw, Poland

(Received 27 January 2023; accepted 31 March 2023; published 21 April 2023)

Reliable analytical modeling of the nonlinear power spectrum (PS) of matter perturbations is among the chief prerequisites for cosmological analyses from the largest sky surveys. This is especially true for the models that extend the standard general-relativity paradigm by adding the fifth force, where numerical simulations can be prohibitively expensive. Here we present a method for building accurate PS models for two modified gravity (MG) variants: namely the Hu-Sawicki $f(R)$, and the normal branch of the Dvali-Gabadadze-Porrati (nDGP) braneworld. We start by modifying the standard Halo Model (HM) with respect to the baseline lambda-cold-dark-matter (ΛCDM) scenario, by using the HM components with specific MG extensions. We find that our $P(k)_{\rm HM}$ retains 5% accuracy only up to mildly nonlinear scales ($k \lesssim 0.3\ h/{\rm Mpc}$) when compared to PS from numerical simulations. At the same time, our HM prescription much more accurately captures the ratio $\Upsilon(k) = P(k)_{\rm MG}/P(k)_{\Lambda{\rm CDM}}$ up to nonlinear scales. We show that using HM-derived $\Upsilon(k)$ together with a viable nonlinear ΛCDM $P(k)$ prescription (such as HALOFIT), we render a much better and more accurate PS predictions in MG. The new approach yields considerably improved performance, with modeled $P(k)_{\rm MG}$ being now accurate to within 5% all the way to nonlinear scales of $k \lesssim 2.5$–$3\ h/{\rm Mpc}$. The magnitude of deviations from GR as fostered by these MG models is typically $\mathcal{O}(10\%)$ in these regimes. Therefore reaching 5% PS modeling is enough for forecasting constraints on modern-era cosmological observables.

DOI: 10.1103/PhysRevD.107.083525

I. INTRODUCTION

The standard model of cosmology, the lambda-cold-dark-matter (ΛCDM), has been remarkably well tested observationally in the last two decades. Presently, it is our best approximation of the real Universe [1–5]. The precise observations of the cosmic microwave background (CMB) radiation [2,6], large-scale galaxy clustering [4,7–9], and the abundance of massive galaxy clusters [10] among others, form a long list where the standard cosmological model predictions are successful.

So far, the bulk of these ΛCDM observational tests concerns the linear regime, the large scales, and/or early times. But it is the mildly nonlinear and fully nonlinear density fluctuation regimes where the vast majority of the modifications to ΛCDM are expected to deviate significantly from the standard model predictions [11–16]. It is also in this regime, stretching usually from hundreds down to a few Megaparsecs, where the present and upcoming cosmological surveys like DESI [17], LSST [18], and Euclid [19] aim to measure various statistics concerning the large-scale structure to a percent level accuracy. As a result, with the influx of data from these surveys, the level of the statistical errors can get so small that the measurements start to be more sensitive to systematic effects. If both the new level of accuracy of base-level predictions as well as the control of the known systematics will be successfully implemented, these new large-scale surveys will yield new unprecedentedly accurate estimates and constraints on cosmological parameters: like the DE equation of state, the growth rate of structure, or parameters quantifying possible departures from the standard general relativity (GR)-based structure formation scenario.

In this context, one of the most useful and widely used theoretical quantities is the power spectrum (PS) of density fluctuations, $P(k)$. This statistic generally characterizes the properties of large-scale structures across vast cosmological epochs and scales. Not only it can be used as an end-goal model prediction on its own, but it is also a basic quantity that is used to model and forecast a number of other useful LSS observables, including galaxy clustering measures, cluster abundance, weak-lensing shear and convergence, the amplitude of the bulk peculiar galaxy motions, and many others [1,4,18,20–23].

Since the PS forms a basis for the predictions of many cosmological LSS observational statistics, the accuracy,

[*]gupta@cft.edu.pl
[†]hellwing@cft.edu.pl
[‡]bilicki@cft.edu.pl

and scales to which we know the input PS limits our abilities to forecast the derived observables. Thus, obtaining robust estimates of the PS beyond the linear theory regime (i.e., scales of $k > 0.1\ h/\mathrm{Mpc}$) became of paramount importance to modern cosmology, and has been a subject of extensive effort in recent years [24–27]. A classical approach is to either directly use the results of a number of N-body simulations of LSS evolution to predict PS, or use the simulation results for calibration of more or less approximate models [24–26,28,29]. Recently, machine-learning-based-emulators are also employed for computing nonlinear PS [e.g., [27,30]]. This approach especially depends on the growing computational power.

In recent years, the progress in modeling the PS has been truly significant. The resulting current state-of-the-art PS models for ΛCDM are already, or close to, attaining subpercent accuracy in the nonlinear regime, as required for the success of the cosmological tests offered by the incoming big survey data. However, this amazing progress has been mostly limited to the ΛCDM alone. When it comes to many interesting extensions and modifications of the standard model, such as the whole family of beyond-GR modified gravity (MG) scenarios, the current accuracy, and versatility of PS modeling is still very much lacking. The reasons for this are both higher theoretical complications of such models, and their increased levels of nonlinearity [16,31–35]. For MG models, N-body simulations play an even more important role in fully assessing the effect of the fifth force, and are crucial for disentangling pure MG effects from the standard GR-based scenarios [36–38]. This is connected with the richer phenomenology of such models [39–48]. Given the fact that the MG simulations are usually many times more expensive than the standard ΛCDM case [14,15], it becomes computationally prohibitive to obtain simulation libraries of the same volume and precision for MG, as is possible for ΛCDM. However, such libraries are necessary to be applied to the proven state-of-the-art emulating or fitting methods to achieve the same precision, and success in modeling MG effects, as we have for the case of ΛCDM.

In this work, we attempt to remedy the deficit of accurate MG PS modeling. To circumnavigate the problem of prohibitively expensive MG simulations, we explore a different approach. Instead of trying to model the absolute MG PS predictions, we take ΛCDM to always be our baseline, and build a semianalytical model for the relative MG effects on the ΛCDM PS. We build our model on the basis of a more general Halo Model (HM) approach ([49], reviewed by [e.g., [24,50]]). Next, we demonstrate how various degrees of modeling freedom can be calibrated and constrained already by a relatively small library of N-body simulations, to achieve an unprecedented level of PS modeling in the MG scenarios studied here.

There are many models that can be considered beyond-GR structure formation scenarios. Most of the viable, and at the same time cosmologically interesting ones usually involve some extra couplings to the metric in the Einstein-Hilbert action that manifests themselves as additional degrees of freedom (*d.o.f.*). The propagation (gradient) of this *d.o.f.* induces an additional gravitational force component, called as the *fifth force*, which acts on top of the Newtonian gravitational force on the cosmological scales. However, propagation of a significant fifth force both on small galaxy scales, and in the strong field regime is tightly constrained observationally [51–56]. Thus, only MG models that exhibit some kind of a fifth force screening mechanism, which, as the name suggests, would *screen* the fifth force in these observationally tested regimes are viable MG candidates [41,46,57–59].

The clockwork of MG models and their involved screening mechanisms can differ in many ways. From our point of view, however, we can significantly simplify the subject by focusing just on phenomenological effective modifications to the density fluctuations PS. As our test-case models, we choose variants of two popular MG set-ups: namely $f(R)$ [44] and nDGP gravity [60], which will serve as a good representative for their whole respective families. Further in the text, we offer a more detailed description and definitions of these models.

Most of the works that have considered computing the nonlinear PS in MG models either rely on simulations [31,32], post-Friedmann (PPF) formalism [33], or perturbation theory focusing on quasilinear scales [16,34]. In Ref. [61], the nonlinear PS is computed using the HMcode [26] for a variety of extensions to the standard cosmological model, including $f(R)$ and nDGP. The level of this prediction is however significantly limited by a number of approximations. For example, a simplified spherical collapse theoretical formalism is used there to estimate DM halo properties. From another perspective, MG-HALOFIT was proposed in [62] as an extension of standard HALOFIT for $f(R)$ gravity models, but [63] showed that the former has limited applicability and accuracy.

The HM formalism has been used to model nonlinear MG PS in [34,35,64–68], which is mainly based on the theoretical spherical collapse model, and is explicitly solved for each MG variant. In our approach, however, we rely on the calibration of phenomenological components of HM to N-body simulations. An additional strength of our approach is that it is general enough to be quite straightforwardly extended, not only to a wider part of the model parameters space but also, in principle, to other modified structure formation models.

This paper is organized as follows: In Sec. II, we describe the MG models, numerical datasets, and simulations. In Sec. III, we elaborate on the HM formalism and describe the empirical halo properties: halo mass function (Sec. III A), halo bias (Sec. III B) and halo density profile (Sec. III C). In Sec. IV, we discuss the results obtained from extending the standard HM predictions to the MG models

considered in this work (Sec. IV A), and from our new approach (Sec. IV B). In (Sec. IV C), we test our approach on another suite of MG simulations, and the final Sec. V includes our conclusions, discussion, and future work prospects. Details of the Appendices are mentioned in the respective subsections.

II. MODIFIED GRAVITY MODELS, NUMERICAL DATA SETS AND TOOLS

As our main data for calibration of the nonlinear PS amplitude, we take the Elephant (Extended LEnsing PHysics using ANalytic ray Tracing) suite of N-body simulations [32]. These simulations provide a good test bed to model the impact of $f(R)$ and nDGP physics on formation of the large-scale structure.

In $f(R)$, the fifth force is manifested as a result of additional degrees of freedom from the interaction between an auxiliary scalar field (or *scalaron*) and matter. This additional force appears as a nonlinear function of the Ricci scalar, R in the Einstein-Hilbert action, hence the term $f(R)$. We work with the Hu-Sawicki form of $f(R)$ gravity, where *Chameleon screening* screens the fifth force [69]. In this screening, the scalaron becomes very massive in the high curvature (and high matter density) regimes, and the fifth force exponentially decays above the length scale determined by the inverse of the mass of the scalaron. This length scale is termed the Compton wavelength. As a result of this decay, the scalar interaction diminishes above the Compton wavelength, and GR is recovered [70].

In the nDGP model, gravity, unlike other standard forces, mediates from 4D brane to 5D Minkowski spacetime [60,71]. In this model, the scalar is identified as the brane-bending mode which describes the deformation of the 4D brane in the 5D bulk spacetime. The brane bending mode has a second-order term in the equation of motion. On small scales, this term dominates over the linear term. As a result, the coupling between the scalar field and matter is suppressed, and the solutions for metric perturbations approach GR. This is referred to as the *Vainshtein screening* [72].

In Elephant, along with ΛCDM, two $f(R)$ variants have been employed, with their free parameter $|f_{R0}|$ (the strength of the scalar field today), taken to be 10^{-6} and 10^{-5} (increasing order of deviation from ΛCDM) dubbed as F6 and F5, respectively. For nDGP gravity, we have two variants with the model parameter $r_c H_0 = 5$ and 1 (which is the dimensionless crossing-over scale characterizing transition from 4D to 5D gravity), marked consequently as N5 and N1, respectively.

The simulations were run from $z_{\rm ini} = 49$ to $z_{\rm fin} = 0$ employing the ECOSMOG code [14,73,74], each using 1024^3 N-body particles in a cubic box of a size 1024 Mpc/h. The mass of a single particle is $m_p = 7.798 \times 10^{10} M_\odot/h$, and the comoving force resolution is $\varepsilon = 15$ kpc/h. Each set of simulations has five independent realizations, evolved from the same set of initial conditions. The cosmological parameters of the fiducial background model are given as $\Omega_m = 0.281$ (fractional matter density), $\Omega_b = 0.046$ (fractional baryonic density), $\Omega_\Lambda = 0.719$ (fractional cosmological constant density), $\Omega_\nu = 0$ (relativistic species density), $h = 0.697$ (dimensionless Hubble constant), $n_s = 0.971$ (primordial spectral index), and $\sigma_8 = 0.842$ (power spectrum normalization). These parameters apply to background cosmologies in the simulations of all the gravity models. For further processing, we take simulation snapshots saved at $z = 0$, 0.3, 0.5, and 1.

As indicated above, the Elephant-suite will be our main calibration dataset. To test the accuracy of our PS modeling and the general quality of extrapolation, we also use different N-body data. For these additional tests, we take the MG simulations for F5 and N1, described in [75]. These simulations have background cosmological parameters different from our parent Elephant simulations, with $\Omega_m = 0.3111$, $\Omega_b = 0.049$, $\Omega_\Lambda = 0.6889$, $\Omega_\nu = 0$, $h = 0.6766$, $n_s = 0.9665$, and $\sigma_8 = 0.8245$. This simulation set is run using MG-COLA [13] in a 500 Mpc/h box. For each model, we build an ensemble based on five independent realizations.

Linear matter power spectra, $P(k)_{\rm lin}$, used in this work were calculated using a modified version of the CAMB cosmological code [76], which includes a module implementing both the $f(R)$ and nDGP models. The simulation power spectra, $P(k)_{\rm sim}$, were computed using POWMES [77]. In what follows, by $P(k)$ we will be denoting the fully nonlinear matter power spectrum, unless indicated otherwise.

III. Halo Model FORMALISM

As a baseline prediction and our starting point, we take the Halo Model (HM) approach. It has been proposed as an attempt to analytically model the variance of density fluctuations into the nonlinear regime using the properties and clustering of halos as main input parameters. HM describes the statistics of the density field up to the mildly nonlinear regimes (i.e., $k \lesssim 0.5\ h$/Mpc). Despite its inferior accuracy compared to heavy N-body simulations, the HM has been successfully used for modeling observables and constraining cosmological parameters [24,49,78].

In HM, the main presumption is that all contributions to the cosmic density field variance come from the matter collapsed into halos. This allows for moderately accurate modeling of the nonlinear two-point clustering statistics, although HM can be used to compute the density field at even higher levels of the n-point hierarchy [79].

Following HM, the total matter power spectrum $P(k)_{\rm HM}$ can be described as a sum of two contributions:

$$P(k)_{\rm HM} = P(k)_{1h} + P(k)_{2h}, \tag{1}$$

where $P(k)_{1h}$ models the contribution from the matter clustered inside halos (called the *one-halo term*) and $P(k)_{2h}$ is the contribution from clustering of separate halos (the *two-halo term*). In practice, the one-halo term dominates at small scales (i.e., $k \gtrsim 1\ h/\mathrm{Mpc}$) and saturates to a constant value at larger scales, where the two-halo term becomes the dominant component of the power spectrum.

These contributions are further defined as:

$$P(k)_{1h} = \int_0^\infty dM |\tilde{u}(k|M)|^2 \left(\frac{M}{\bar{\rho}}\right)^2 n(M) \tag{2}$$

and

$$P(k)_{2h} = I_m^2(k) P(k)_{\mathrm{lin}}, \tag{3}$$

where,

$$I_m(k) = \frac{1}{\bar{\rho}} \int_0^\infty dM |\tilde{u}(k|M)| M n(M) b(M) \tag{4}$$

and $I_m \to 1$ for $k \to 0$ in order to match the linear theory predictions at large scales. The integrals in Eqs. (2) and (4) should in principle cover all possible halo mass ranges, but in practice, some $\mathrm{M_{min}}$ and $\mathrm{M_{max}}$ are introduced (these mass limits are discussed in more details in the next subsections).

Here, $\bar{\rho}$ corresponds to the mean density of the universe, $P(k)_{\mathrm{lin}}$ is the linear theory matter power spectrum, $n(M)$ is the *halo mass function*, and $b(M)$ is the *linear halo bias*. The term $|\tilde{u}(k|M)|$ is the normalized Fourier transform of the internal density profile of a halo of mass M, such that $\tilde{u}(k \to 0, M) \to 1$. The above HM building blocks are intrinsically redshift-dependent functions, which, in principle, allows one to obtain HM prediction at any redshift for which the integrands are well defined.

All the components of the HM can be varied independently from each other, and each specific choice of fitting functions, formulas, or tabulated data creates a unique realization. Thus, HM is a general framework under which one can create many different families of PS models. Motivated by literature and our own studies for each of our cosmological models (i.e., ΛCDM, and all MG variants), we find an optimal combination of analytic formulas and fitting functions to describe the input properties of halo mass function, halo bias, and halo concentrations. Below we provide a more detailed description of the particular choices we make. For a quick summary and look-up, we refer the reader to Table I which contains a concise list and references of all the fitting functions for the halo properties used in this work, and for each model.

A. Halo mass function

The halo mass function (HMF), $n(M)$, quantifies the number of halos per unit mass per unit comoving volume. The most commonly adopted theoretical formulation of the HMF is via the extended Press–Schechter (EPS) formalism [88,89], in which HMF is given by:

$$n(M) \equiv \frac{dn}{dM} = \frac{\rho}{M^2} F(\sigma) \left| \frac{d \ln \sigma}{d \ln M} \right|. \tag{5}$$

The *halo multiplicity function*, $F(\sigma) = \nu F(\nu)$ denotes the fraction of matter collapsed into halos, in a logarithmic bin around the peak height, $\nu = \delta_c(z)/\sigma(M, z)$. Here, $\delta_c(z)$ is the spherical collapse density threshold, and $\sigma(M, z)$ is the linear variance in the density fluctuation field smoothed using a top-hat filter. This scaling relation has been modeled extensively in the literature and it has been shown to be approximately universal across redshifts for ΛCDM [80,83,90–92]. In our earlier work [81], we have shown that after simple rescaling, the $F(\sigma)$ in both $f(R)$ and nDGP also exhibits a similar degree of universality as in the ΛCDM-case.

Following our previous study, we will model MG HMF as a fractional deviation, Δ_{MG} from the ΛCDM fiducial baseline, $n(\sigma_M)_{\Lambda\mathrm{CDM}}$. We have shown that such an approach allows for achieving quite a good accuracy (5–10%), which also holds for different background cosmologies. However, to obtain such precision, a careful choice of the baseline ΛCDM HMF model is paramount.

Thus, for our baseline ΛCDM, we tested various HMF models in the literature (e.g., [80,83,90–94]), as these functions can in principle be extrapolated to desired halo mass ranges. We found that the fitting function proposed in Watson *et al.* 2013 [[80], hereafter W13] proved to be optimal for HM power-spectrum forecasting. Therefore, we used W13 for our ΛCDM HMF computations.

For completeness, we now recall the essential steps of Ref. [81]. Here the target MG HMF is modeled as:

$$n(\sigma_M)_{\mathrm{MG}} = \Delta_{\mathrm{MG}}(\sigma_M) \cdot n(\sigma_M)_{\Lambda\mathrm{CDM}}, \tag{6}$$

where $\sigma_M \equiv \sigma(M)$ is simply the linear mass variance at the Lagrangian top-hat halo mass scale, M.

For $f(R)$ gravity models, the fractional deviation fit is expressed as:

$$\Delta_{\mathrm{MG}} \equiv \Delta_{f(R)} = 1 + a \exp\left[-\frac{(X-b)^2}{c^2}\right], \tag{7}$$

$X \equiv \ln(\sigma^{-1})$. Here, (a, b, c) are parameters of the fit that were calibrated using simulations. They depend on the variant of $f(R)$ gravity model under consideration. See Table I for the specific values that we use in this work.

For nDGP gravity models:

$$\Delta_{\mathrm{MG}} \equiv \Delta_{\mathrm{nDGP}} = p + q \arctan(s\,X + r). \tag{8}$$

Here, X is the *rescaled* mass density variance, $X \equiv \ln(\tilde{\sigma}^{-1})$, $\tilde{\sigma} = \sigma/\Xi(z)$. Again, (p, q, r, s) are the

TABLE I. Compilation of the fitting functions used in this work for the halo properties in HM build-up, for both ΛCDM and MG models.

Halo properties	Fitting functions	Notes
Halo mass function, HMF ΛCDM: Watson *et al.* [80]	$f(\sigma)_{\Lambda\mathrm{CDM}} = A[(\frac{\beta}{\sigma})^{\alpha}+1]e^{-\gamma/\sigma^2}$ $A=0.282$, $\alpha=2.163$, $\beta=1.406$ and $\gamma=1.210$.	For MG$(=f(R),\mathrm{nDGP})$, $f(\sigma)_{\mathrm{MG}} = \Delta_{\mathrm{MG}} \times f(\sigma)_{\Lambda\mathrm{CDM}}$
$f(R)$: Gupta *et al.* [81]	$\Delta_{f(R)} = 1 + a\exp[-\frac{(X-b)^2}{c^2}]$ For F5: a $=0.230$, b $=0.100$ and c $=0.360$ For F6: a $=0.152$, b $=-0.583$ and c $=0.375$ $X \equiv \ln(\sigma^{-1})$	Additional cutoff expression at low-mass scales for $f(R)$ [Eq. (9)]
nDGP: Gupta *et al.* [81]	$\Delta_{\mathrm{nDGP}} = p + q\arctan(sX+r)$ For N1: p $=1.35$, q $=0.258$, r $=5.12$, s $=4.05$ For F6: p $=1.06$, q $=0.0470$, r $=11.8$, s $=4.19$ $X \equiv \ln(\tilde{\sigma}^{-1})$, $\tilde{\sigma} = \sigma/\Xi(z)$	$\Xi(z)$: nDGP force enhancement with respect to GR [82].
Linear halo bias, $b(M)$ All models: Sheth *et al.* [83]	$b(M) = \frac{1}{\sqrt{a}\delta_c(z)}(\sqrt{a}(a\nu^2)+\sqrt{a}b(a\nu^2)^{1-c} - \frac{(a\nu^2)^c}{(a\nu^2)^c+b(1-c)(1-c/2)})$ $a=0.707$, $b=0.5$ and $c=0.6$.	This expression has been proposed for ΛCDM. We extrapolated the relation for MG.
Concentration-mass relation, $c(M)$ ΛCDM: Ludlow *et al.* [84]	$c(\nu)_{\Lambda\mathrm{CDM}} = c_0(\frac{\nu}{\nu_0})^{-\gamma_1}[1+(\frac{\nu}{\nu_0})^{1/\beta}]^{-\beta(\gamma_2-\gamma_1)}$ $c_0 = 3.395\times(1+z)^{-0.215}$ $\beta = 0.307\times(1+z)^{0.540}$ $\gamma_1 = 0.628\times(1+z)^{-0.047}$ $\gamma_2 = 0.317\times(1+z)^{-0.893}$ $\nu_0 = (4.135 - 0.564a^{-1} - 0.210a^{-2} + 0.0557a^{-3} - 0.00348a^{-4})\times D(z)^{-1}$	For MG$(=f(R),\mathrm{nDGP})$, $c(M)_{\mathrm{MG}} = \Delta_{c(M),\mathrm{MG}} \times c(M)_{\Lambda\mathrm{CDM}}$
$f(R)$: Mitchell *et al.* [85]	$y(x) = \frac{1}{2}(\frac{\lambda}{\omega_s}\phi(x')[1+erf(\frac{\alpha x'}{\sqrt{2}})]+\gamma)(1-\tan h(\omega_t[x+\xi_t]))$ $y = \log_{10}(\Delta_{c(M),f(R)})$ $x' = (x-\xi_s)/\omega_s$ $x = \log_{10}(M_{500}/10^{p_2})$ $p_2 = 1.5\log_{10}[\frac{f_R(z)}{1+z}] + 21.64$ [86] $\lambda = 0.55\pm0.18$ $\xi_s = -0.27\pm0.09$ $\omega_s = 1.7\pm0.4$ $\alpha = -6.5\pm2.4$ $\gamma = -0.07\pm0.04$ $\omega_t = 1.3\pm1.0$ $\xi_t = 0.1\pm0.3$	For M $\leq 10^{12}M_{\odot}/h$, $c(M)_{f(R),\mathrm{nDGP}} = c(M)_{\Lambda\mathrm{CDM}}$
nDGP: Mitchell *et al.* [87]	$\Delta_{c(M),\mathrm{nDGP}} = [A - B\log_{10}(M_{200}M_{\odot}h^{-1})](H_0r_c)^{-0.71\pm0.05}+1$ $A = (0.35\pm0.01)(H_0r_c)^{-0.71\pm0.05}$ $B = (0.0302\pm0.0008)(H_0r_c)^{-0.71\pm0.05}$	

parameters of the fit, whose values are determined by the variant of the nDGP gravity model.

The resolution of our simulations allowed us to probe only intermediate- and large-mass halos to compute the HMF. In this mass regime, HMF in MG increases with respect to ΛCDM, as small-mass halos accrete matter and merge faster to form larger structures. However, this enhanced structure formation at large halo mass-end is happening at the expense of the abundance of smaller halos used up in this process [see, e.g., [81,95–97]]. Thus, we can expect that there should be a simultaneous decrease in the number of small-mass halos in the MG models when compared to ΛCDM.

Equation (8) for nDGP allows the possibility of $\Delta_{\mathrm{nDGP}} < 1$ for small mass halos. However, our fit for $\Delta_{f(R)}$ is never below 1. To admit for low-mass halo

deficiency also in the $f(R)$, we impose an artificial decrease in $f(R)$ HMF for $M < 10^{11} M_\odot/h$, when compared to ΛCDM results. For low halo masses, we assume that $\Delta_{f(R)}$ is a linear function of $\ln(\sigma^{-1})$, and is given by:

$$\Delta_{f(R)} \to (m \ln(\sigma^{-1}) + n) \times \Delta_{f(R)}. \tag{9}$$

We tested for different combinations of the (m, n) parameters values. The combination $(m, n) = (0.06, 0.99)$ turned-out to be optimal for our both $f(R)$ variants. Thus we use these values in this work. A note of caution is in place here. There is no clear physical justification for our particular choice of both m and n, other than that they are providing optimal HM power spectrum predictions. An interested reader can play around and search for a different choice of (m, n). However, the overall impact of the particular (m, n) choice on the resulting HM remains small.

B. Halo bias

The relation between the clustering amplitude of the underlying DM density field and halos is quantified in terms of the linear halo bias relation, $\delta_h(M) = b(M)\delta$. In the context of power spectra, it is convenient to consider the following Fourier-space estimator of the halo bias:

$$\hat{b}(k, M) = \frac{P_{hm}(k, M)}{P(k)}. \tag{10}$$

Here, $P_{hm}(k, M)$ is the halo-matter cross power spectrum, and $P(k)$ is the matter power spectrum. One can find an optimal value of the linear bias by taking a limit, or an average of this estimator at the smallest possible k's. We consider such a power-spectrum-based bias estimator to use results from Elephant suite for testing and finding optimal analytic bias formula for HM.

For this purpose, we tested various $b(M)$ fitting functions for ΛCDM [98–100]. Sheth *et al.* 2001 $b(M)$ [[83], hereafter S01] gave the best match to the simulations. Thus, this will be our choice for the $b(M)$ computations in this work.

In the Appendix A, we show the performance of S01, both in capturing the ratio of MG $b(M)$ versus ΛCDM (Fig. 5), and the absolute $b(M)$ relation (Fig. 6). We find that S01 gives reasonable predictions in both cases. Given that $b(M)$ impacts only the two-halo term, which by construction matches the $P(k)_{\rm lin}$ on large scales, the choice of $b(M)$ does not impact the HM results to a great extent.

C. Halo density profile: Concentration-mass relation

The scale-free nature of structure formation in CDM scenarios results in self-similar density profiles for individual DM halos, which was first pointed out by Navarro, Frenk, and White in [[101], hereafter NFW]. As a result, DM density profiles are rescaled by a characteristic central density, ρ_s, and radial scale, r_s, (or mass M and concentration $c(M)$, respectively). The $c(M)$ relation is defined as the ratio of the virial radius, R_v of the halo to r_s, and determines the density profile of NFW halos.

To obtain relatively unbiased and good-quality NFW fits, the simulated halos need to be well resolved. The convergence of the halo density profile depends on the simulation's force and mass resolution. Thus $c(M)$ can be reliably estimated only for a limited halo mass range, usually for halo with masses corresponding to at least a few $\times 10^3$ particles [see, e.g., [102]]. The resolution of the Elephant suite allow only for probing the $c(M \geq 10^{13} M_\odot/h)$. Because of this, we need to resort to the fitting functions for $c(M)$ here.

We use relations proposed in [85,87] to compute the $c(M)$ relation in $f(R)$ and nDGP gravity models, respectively. In these works, direct NFW fitting was used to compute the halo density profiles, and functional forms were derived for the ratio $c(M)_{\rm MG(=f(R),nDGP)}/c(M)_{\Lambda\rm CDM}$ (refer to Table I for explicit expressions). The MG $c(M)$ can be therefore obtained as a product of this ratio times the concentration-mass relation for ΛCDM, for which we use the form proposed in [84]. Considering the ratio instead of absolute MG $c(M)$ would eliminate the leading-order systematic uncertainties coming from the background cosmology.

The authors in [85] proposed functional form for $\log(c(M)_{f(R)}/c(M)_{\Lambda\rm CDM})$. When expressed as a function of $M_{500}/10^{p_2}$, this ratio is independent of the background scalar field and z. The parameter p_2 defined in [86], encapsulates these dependencies, and in turn allows different variants of $f(R)$ gravity model to be studied in a unified way.

For the case of the nDGP gravity model, in Ref. [87], the ratio $c(M)_{\rm nDGP}/c(M)_{\Lambda\rm CDM}$ is fitted as a decreasing function of M_{200}. This fitting also captures the z dependence, hence making the ratio only dependent on the nDGP parameter, $\mathrm{r_c H_0}$.

The halo mass range probed in both Mitchell *et al.* [85,87] is confined to $\geq 10^{12} M_\odot/h$. Therefore, we restrict the use of their fitting functions to the calibrated mass range, and artificially impose $c(M)_{f(R)}$, nDGP $= c(M)_{\Lambda\rm CDM}$ for $M < 10^{12} M_\odot/h$.

IV. RESULTS

In this section, we combine all the HM components to give an analytical prediction for matter overdensity PS. As a reference case to gauge our results against, we always take the PS from Elephant simulations. At large scales, the linear perturbation theory gives accurate and reliable predictions both for ΛCDM and MG PS. Hence, we focus here only on the scales corresponding to mildly and fully nonlinear regimes. In practice, we will be interested in the performance of our models for $k \geq 0.1h/\rm Mpc$.

A. Halo Model predictions for modified gravity

We start by testing the standard set-up for HM, which aims to yield a theoretical prediction for the PS amplitude in a given cosmology. For ΛCDM alone, this approach has at best limited accuracy, since the classical HM fails to accurately capture PS already in the mildly nonlinear regime, i.e., $k \gtrsim 0.2$–$0.3\ h/\mathrm{Mpc}$ [25,26,103,104]. Thus, we do not expect that it will perform better in MG cosmologies, which have even richer phenomenology. However, it is still an illustrative exercise, since we will be using this basic HM setup to obtain much more accurate PS predictions for MG.

Using the inputs of the HMF, $b(M)$, and $c(M)$ relation in their MG versions discussed in the previous section, we compute the resultant power spectra for a number of redshifts. For this, we employ Eqs. (2)–(4), integrating from $\mathrm{M_{min}} = 1M_\odot/h$ to $\mathrm{M_{max}} = 10^{16}M_\odot/h$. We choose a sufficiently broad halo mass range so as to account for the maximum possible halo masses that still have an impact on the resulting PS.

For the integral in Eq. (4) to approach unity at large scales, the bias needs to attain unity when integrated over all the halo masses, i.e.,

$$\frac{1}{\bar{\rho}}\int_0^\infty b(M)n(M)dM = 1. \tag{11}$$

In practice, this integral yields a value below unity, even when the integration is taken over the maximum possible halo mass range. Changing the high mass limit for the integration does not impact the results to a great extent, because on these scales, halos become exponentially rare which makes their contribution to the total power negligible. On the other hand, we expect a significant contribution from the low-mass regime. However, owing to resolution limits, the properties of low mass halos cannot be properly calibrated using simulations.

Therefore, to add the contribution of the low-mass halos to HM computations, we use the correction proposed in [105,106]. This correction adds the contribution of the missing halos to the two-halo term, in order to recover $P(k)_{\mathrm{lin}}$ at large scales. The correction term is simply yielded by:

$$A = 1 - \frac{1}{\bar{\rho}}\int_{M_{\mathrm{min}}}^{M_{\mathrm{max}}} b(M)n(M)dM, \tag{12}$$

and it is used as an additive component in the two-halo term:

$$C = \frac{A\tilde{u}(k|\mathrm{M_{min}})}{\mathrm{M_{min}}}. \tag{13}$$

Here, $\tilde{u}(k|\mathrm{M_{min}})$ is the normalized Fourier transform of the density profile for the lowest resolved mass $\mathrm{M_{min}}$. Equation (3) is then modified and the resultant two-halo term is given by:

$$P(k)_{2h} = P(k)_{\mathrm{lin}}(I_m + C)^2. \tag{14}$$

One could instead replace the $P(k)_{2h}$ term with $P(k)_{\mathrm{lin}}$, as the former differs from the latter only for $k \geq 1\ h/\mathrm{Mpc}$, where already $P(k)_{1h}$ takes over as the dominant contributor. However, for completeness, we use the full above expression for the two-halo term.

The results of such direct HM computations for our MG models are illustrated in Fig. 1, where we compare $P(k)_{\mathrm{HM}}$ (solid lines), as well as linear theory $P(k)_{\mathrm{lin}}$ (dotted lines), with the Elephant simulations for all our models at $z = 0$. The shaded region corresponds to the uncertainty in the Elephant results, which is the inverse of the square root of the number of statistically independent modes contributing to each k-bin, and the horizontal dashed lines correspond to the 5% accuracy regime. The performance of HM in these MG models is similar to the ΛCDM results and is not much better than the actual linear theory. With respect to the simulation prediction, $P(k)_{\mathrm{HM}}$ gives better than 5% accuracy for $k \leq 0.2$–$0.3\ h/\mathrm{Mpc}$, and stays within 10% for $k \leq 0.4$–$0.5\ h/\mathrm{Mpc}$. An interesting exception is the F5 $f(R)$ variant, where better than 2% accuracy is kept all the way to $k \sim 0.2\ h/\mathrm{Mpc}$.

In all the models, we also encounter an underprediction with respect to the simulation results for $k \approx 0.5\ h/\mathrm{Mpc}$. This is a well-known problem of the HM formalism in ΛCDM [26,104], and further propagates to the MG scenarios (also seen for Galileon models in [66]). Similar behavior is observed also for other redshifts that

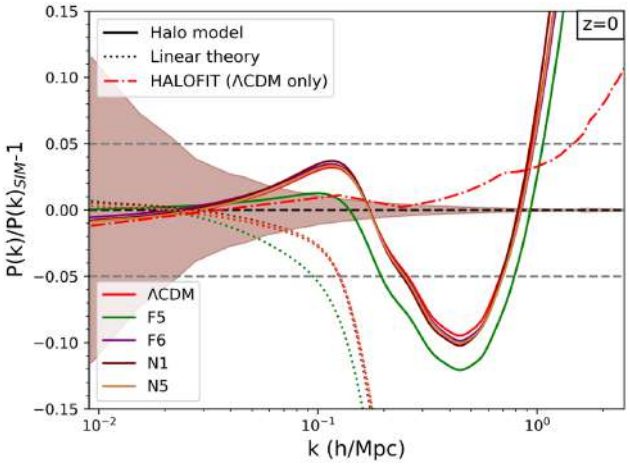

FIG. 1. Comparison of the power spectrum from halo-model, $P(k)_{\mathrm{HM}}$ (solid lines), linear theory, $P(k)_{\mathrm{lin}}$ (dotted lines) for ΛCDM and the variants of MG models, and ΛCDM HALOFIT (red dot-dashed line) with Elephant simulations $P(k)_{\mathrm{sim}}$, for $z = 0$. The horizontal gray dashed lines correspond to the 5% accuracy regime.

our simulations probe, but we do not show them here for brevity.

Our results clearly indicate that HM alone cannot provide modeling accuracy that will be sufficient for the percent level accuracy of future LSS surveys. On the other hand, HALOFIT, which is widely used for ΛCDM PS modeling can perform substantially better. We illustrate this in addition to HM performance in the Fig. 1. Considering the 5%-level accuracy for the comparison, ΛCDM HM can only be used up to $k \leq 0.3\ h/\mathrm{Mpc}$, while with the HALOFIT one can do much better reaching up to 5% for $k \leq 1.5\ h/\mathrm{Mpc}$. Thus, we can exploit this much better HALOFIT performance, by using it as a fiducial ΛCDM baseline, and model only MG-induce deviation form the base-line by the means of HM.

However, noticing the above, the positive result here is that HM can be actually employed to yield predictions for MG power spectra with the same-level accuracy as for ΛCDM. This is a somewhat surprising result because the standard HM does not include any room for extra MG physics (like the fifth-force and screening). Yet it seems that self-consistent modifications of HMF, $b(M)$, and $c(M)$ are enough to obtain the usual ΛCDM HM-level predictions also for different MG cosmologies. This is very encouraging, and as we show below this can be used as a strong advantage to build an even better and more accurate PS model for MG.

B. An improved model for MG power spectrum

In the previous section, we have shown that when HM is applied to model the PS amplitude, it offers limited accuracy, and is comparable to what can be achieved for the standard ΛCDM. In this section, we will demonstrate that we can build a much more accurate PS model for MG. This can be realized when we apply HM to estimate the fractional departure from the ΛCDM baseline, rather than trying to predict the absolute amplitude of PS alone.

Our starting point will be the generic ratio of the MG to ΛCDM power spectra:

$$\Upsilon(k) \equiv P(k)_{\mathrm{MG}}/P(k)_{\Lambda\mathrm{CDM}}. \tag{15}$$

Here, both numerator and denominator are general terms for MG and ΛCDM PS respectively. By modeling this ratio, rather than the MG PS itself, we can benefit from a number of properties, namely: (i) the dependence on the background cosmological parameters (such as Ω_m, H_0, or σ_8) should cancel out from the ratio to the leading order; and (ii) the scale of significant departure from ΛCDM (i.e., from $\Upsilon = 1$) is naturally determined in terms of the ΛCDM baseline, rather than some arbitrary nonlinear amplitude or scale.

In Fig. 2, we compare the ratios $\Upsilon(k)$ estimated from Elephant simulations (solid line), linear theory (dotted line), and HM (dashed line), for both $f(R)$ (left panels), and

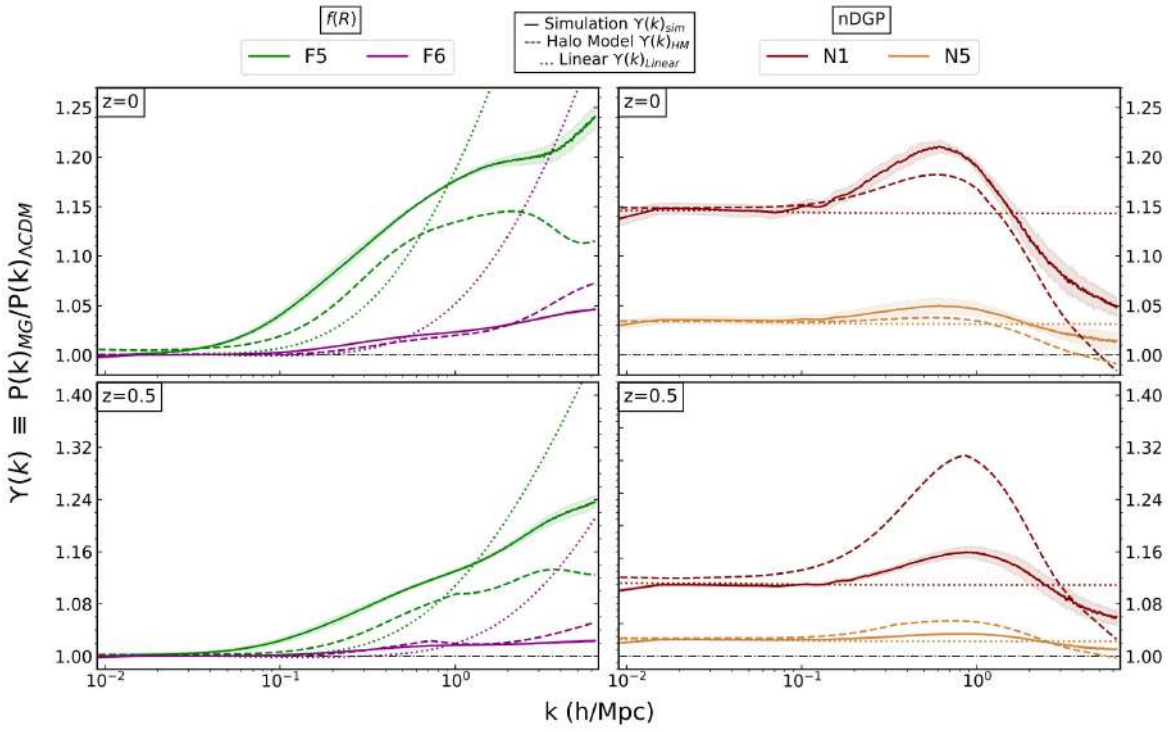

FIG. 2. The ratio $\Upsilon(k) \equiv P(k)_{\mathrm{MG}}/P(k)_{\Lambda\mathrm{CDM}}$ obtained from linear theory (dotted lines), Elephant simulation (solid lines) and the Halo Model (dashed lines), at $z = 0$ (top panels) and $z = 0.5$ (bottom panels). The left panels correspond to $f(R)$ gravity variants: F5 and F6, and the right panels correspond to nDGP gravity variants: N1 and N5. Shaded regions are the standard deviations obtained for this ratio across five realizations of the simulation box.

nDGP (right panels), at $z = 0$ (top panel) and $z = 0.5$ (bottom panel). Naturally, both the simulation and HM results for $\Upsilon(k)$ are expected to match the linear theory prediction at large scales for both models. As we approach smaller scales, the departure from linear predictions increases (namely, linear theory runs away for $f(R)$ and stays constant for nDGP), and trends peculiar to each model emerge. This is a well-known result, which highlights the fact that these family of MG models usually exhibits an increased degree of nonlinearity of the density field, owing to both the fifth force and their respective screening mechanisms [16,31,38,44,57,107,108]. For $f(R)$ gravity models, PS approaches ΛCDM on the large-scales, and we see a monotonic increase in the ratio with k (although slower than what the linear theory would predict). Whereas, for nDGP, $\Upsilon(k)$ enhancement is maximum at the intermediate scales, and this enhancement decreases for large k.

A crucial observation from our study is that HM prediction agrees qualitatively with the simulations. We note that the agreement is far from perfect, especially around the peaklike features, but the HM captures the essential shape and scales of the PS ratios.

As mentioned in the previous section, one perennial problem with the HM has been the *transition* region, where both two- and one-halo terms have a similar magnitude, and both contribute equivalently to the predicted signal. In general, the HM underpredicts the strength of clustering in this region, with the exact amount depending on redshift and cosmology [26]. We also highlight a similar problem with the HM-based MG predictions in Fig. 1 at $k \approx 0.5\ h/\mathrm{Mpc}$. These scales are also called the *quasilinear* regime because the evolution of perturbations at these scales is not exactly governed by linear perturbation theory.

For standard ΛCDM, the inaccuracies of the HM in this transition regime are addressed by devising empirical fitting functions. One of the earliest, yet successful examples was HALOFIT [25], which is motivated by the principles of HM, and calibrated using N-body simulations. It was later improved, in particular by [28] who updated its fitting functions from higher resolution simulations and ameliorated the modeling for dark energy cosmologies. Methods and prescriptions to predict the nonlinear PS in ΛCDM are numerous, but in this work we will use HALOFIT as it is sufficiently accurate for our purposes.

Having seen that the ratio $\Upsilon(k)$ between HM-derived PS for MG and ΛCDM, $\Upsilon(k)_{\rm HM}$ correctly captures the simulation trends, we propose to use it to obtain the fully nonlinear PS in MG. This is done by multiplying $\Upsilon_{\rm HM}$ with an accurate model for the ΛCDM baseline $P(k)$. Therefore, we characterize the beyond-ΛCDM PS ($P(k)_{\rm MG}$) as:

$$P(k)_{\rm MG} = \Upsilon(k)_{\rm HM} \times P(k)_{\Lambda\rm CDM}. \tag{16}$$

Here, $\Upsilon(k)_{\rm HM} = P(k)_{\rm MG,HM}/P(k)_{\Lambda\rm CDM,HM}$. Both the numerator and the denominator terms are obtained using inputs from Table I.

In this prescription, $P(k)_{\rm MG}$ and $P(k)_{\Lambda\rm CDM}$ are different from Eq. (15). Here, $P(k)_{\rm MG}$ is the main quantity of focus that we compute in this work, and $P(k)_{\Lambda\rm CDM}$ is the nonlinear ΛCDM power spectrum, for which we take the HALOFIT predictions using the parameters of a given background cosmology.

The results of applying our proposed methodology are illustrated in Fig. 3, where we plot $P(k)_{\rm MG}$ obtained using $\Upsilon(k)_{\rm HM}$ multiplied by the HALOFIT ΛCDM-baseline. The top panels present the power spectra directly: $P(k)_{\rm sim}$ from Elephant (dots), and $P(k)_{\rm MG}$ derived with Eq. (16) (solid lines). In the bottom panels, we show departures of thus-obtained $P(k)_{\rm MG}$ from $P(k)_{\rm sim}$ treated as reference. These new results, when compared with the standard HM predictions from Fig. 1, clearly perform much better. The standard HM reaches 5% accuracy only up to $k \leq 0.2$–$0.3\ h/\mathrm{Mpc}$. Now, by using HM only for predicting $\Upsilon(k)_{\rm HM}$, and combining it with HALOFIT ΛCDM-baseline, we improve the scale at which modeling is accurate within 5% by an order of magnitude, reaching up to $k \leq 0.5$–$2.5\ h/\mathrm{Mpc}$ (depending on the model and redshift). We note that the performance of $P(k)_{\rm MG}$ generally worsens for higher redshifts, but still remains significantly improved when compared to the standard HM.

More generally, the accuracy of $P(k)_{\rm MG}$ will depend on the user input of baseline $P(k)_{\Lambda\rm CDM}$. As already mentioned, other approaches are being developed to further improve the limited accuracy of HALOFIT, especially for models departing from the flat Planck-based ΛCDM. We tested one such alternative way of deriving the nonlinear ΛCDM PS, that goes into our $P(k)_{\rm MG}$ prediction (16): the so-called HMcode [26,109]. The results, detailed in Appendix B, indicate that both HALOFIT and HMcode give similar accuracy, however with different trends at different scales and redshifts.

Given the fact that we have calibrated our MG HM with a limited-resolution Elephant simulation suite, it is encouraging that this allowed for already an order-of-magnitude improvement of the scale at which we can obtain accurate PS predictions. Obtaining accurate MG PS into the fully nonlinear regime at $k \geq 1\ h/\mathrm{Mpc}$ with so straightforward modifications to HM opens up an avenue for even better PS predictions for the MG phenomenology. This could be achieved by incorporating possible improvements to HM that are better informed about the clustering and properties of small halo mass regime in MG.

C. Testing nonlinear $P(k)_{\rm MG}$ beyond Elephant

In this subsection, we extend our work beyond the Elephant simulations to test the performance of our new

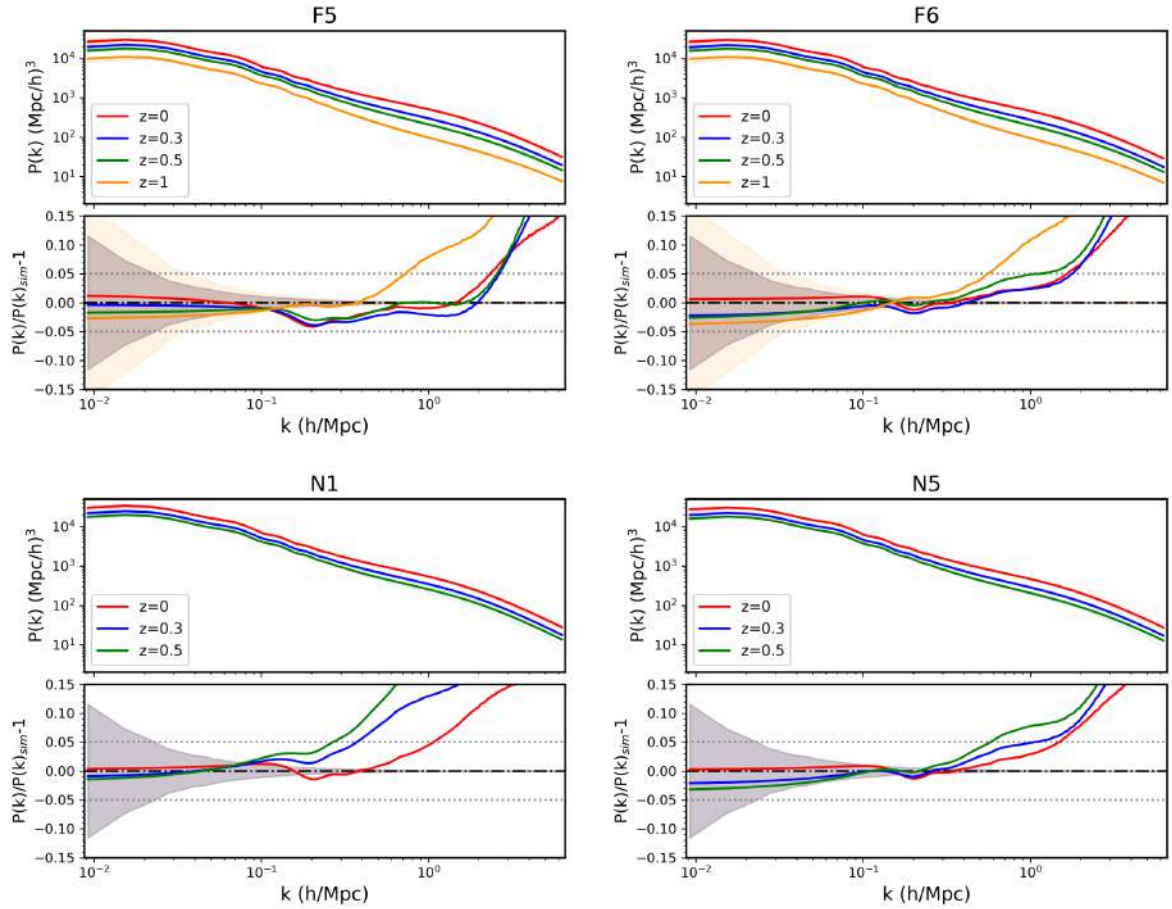

FIG. 3. Top panel: matter power spectra obtained from our new approach [$P(k)_{\rm MG}$ from Eq. (16)] for all the MG variants considered in this work, at redshifts as indicated in the legends. Bottom panel: comparison of $P(k)_{\rm MG}$, derived with our new method, with $P(k)_{\rm sim}$. The shaded region in all the plots corresponds to the uncertainty in the $P(k)_{\rm sim}$, and the horizontal dotted lines shows a 5% accuracy regime.

approach. For this purpose, we consider different N-body simulation runs for the F5 and N1 models, performed using MG-COLA [13], and described in [75]. The most important factors for us are that these runs have a different background cosmology than Elephant (see Sec. II), and were run using different codes. Unlike standard N-body approach, these simulations employ the COLA method [110], that can straightforwardly trade accuracy at small-scales in order to gain computational speed without sacrificing accuracy at large scales. On one hand, this approach is much faster than the standard N-body, but the price to pay is the approximations made, which do not allow us to use this suite of simulations as the calibration data. Hence, we use these simulations but only as a test bed.

Here, the HM ingredients were calculated using the same methodology and setup as above, described in Sec. III and summarized in Table I. The main difference with respect to Sec. IV B was that different background cosmological parameters were used in the linear power spectra that go into the particular ingredients of the HM build-up, namely HMF, $b(M)$ and $c(M)$. Everything else, including the halo mass integration ranges for the HM components, were the same as before.

Using the HM outputs and ΛCDM HALOFIT predictions for the background cosmology of this alternative simulation suite, we computed $P(k)_{\rm MG}$ [using Eq. (16)]. A comparison of our results with the simulation predictions is in Fig. 4, for both N1 (left plot) and F5 (right plot). Given the small box size of these simulations ($L = 500$ Mpc$/h$), we obtain a discrepancy $> 5\%$ with the simulation predictions on large scales, for $k < 0.1$–0.2 h/Mpc. Now, contrary to the Elephant results for N1, our new PS model performs better than before. However, for F5, the performance of our approach decreases with increasing redshift. Overall, we see a similar performance of the new $P(k)_{\rm MG}$ in both the simulations that we tested, with 5% accuracy from mildly nonlinear to nonlinear scales ($k \leq 0.5$–2.5 h/Mpc).

This test with a different simulation and cosmology reassures us that our new approach is a valid technique to compute the nonlinear PS in these MG scenarios, and can be successfully extended to simulations and cosmologies beyond our original data that was used for calibration and fitting.

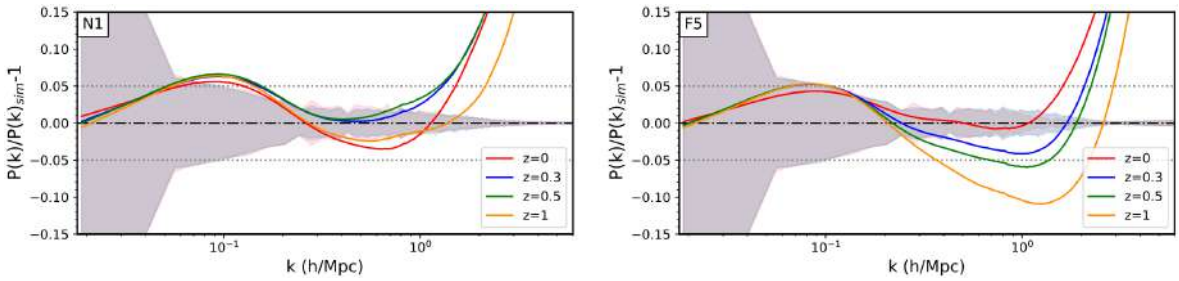

FIG. 4. Comparison of our $P(k)_{\rm MG}$ modeling, with simulation results from MG-COLA [13,75], for two MG variants: N1 (left) and F5 (right). The redshifts are as indicated in the legends. Dotted gray lines are the 5% accuracy regime. The shaded region is the simulation error, which is the standard deviation obtained from five realizations at each redshift.

V. DISCUSSION AND CONCLUSION

In this work, we combined Halo Model (HM) predictions with an accurate ΛCDM baseline for building an analytical framework to compute the nonlinear power spectrum (PS) in modified gravity (MG) scenarios, where structure formation differs from that in ΛCDM. For calibration and testing, we used the Elephant suite—a set of N-body simulations, which incorporates standard ΛCDM and two MG models: Hu-Sawicki $f(R)$ and the normal branch of the Dvali-Gabadadze-Porrati braneworld (nDGP). HM has been extensively studied for ΛCDM [49,78], and we further extended it to these MG cosmologies. This formalism is advantageous as it is a quick and reliable tool to obtain predictions for statistics of density fields well into the regimes, where linear and perturbation theory fails to reproduce simulation results.

The HM framework requires the input of three main halo properties: halo mass function (HMF), which quantifies the number density of halos; linear halo bias $b(M)$, describing the relation between halos and the underlying DM density field; and the concentration-mass relation $c(M)$, which describes the internal distribution of mass in halos. For the HM framework, we needed to compute these quantities over large range of halo masses, that go much beyond the range of our simulations. As a result, we relied on fitting functions for the halo properties in these MG scenarios (Table I).

Using these three inputs, we obtained the HM-based predictions, $P(k)_{\rm HM}$ for these two MG models. We showed that $P(k)_{\rm HM}$ is within 5–15% of the simulation results across the k-ranges, from $k = 0.01$ to $k = 1\ h/\mathrm{Mpc}$. However, MG signatures from these models that quantify deviations from GR are typically in itself a factor of a few dozen per cent. Hence, we cannot use HM predictions in its standard form to complement the expected accuracy from future LSS surveys in order to detect these MG signals. Additionally, similar to the case of ΛCDM, HM also faces the consistent problem of underprediction of power in the transition regime for both $f(R)$ and nDGP. These scales correspond to $k \approx 0.5\ h/\mathrm{Mpc}$.

To get a better PS model, we further investigated, using HM, the relative ratio $\Upsilon(k)_{\rm HM} = P(k)_{\rm MG,HM}/P(k)_{\Lambda\rm CDM,HM}$, instead of employing the absolute PS amplitudes alone. From this, we obtained new analytical PS by taking a product of $\Upsilon(k)_{\rm HM}$, with the nonlinear prediction for ΛCDM, $P(k)_{\Lambda\rm CDM}$ [Eq. (16)]. For the latter, we used HALOFIT [25,28], as it has been a successful approach for ΛCDM to circumvent the HM underprediction of PS in the intermediate scales, and is widely used to analytically compute nonlinear ΛCDM PS. One could use other approaches for the input nonlinear $P(k)_{\Lambda\rm CDM}$ to multiply our ratio $\Upsilon_{\rm HM}(k)$ with, and we tested one of them: HMcode [26,109]. The test with HMcode is shown in Appendix B, and we report that it gives comparable accuracy as HALOFIT for our cosmology.

Using this approach, we significantly improved the accuracy of PS modeling compared to standard HM prediction. For HM, we obtained results within 5% accuracy with the simulation predictions for $k \leq 0.2$–$0.3\ h/\mathrm{Mpc}$. With our new approach, we now matched simulations within this accuracy for k between 0.5–2.5 h/Mpc, with the performance of the method depending on the MG model and redshift. The k-range probed in this work corresponds to the mildly nonlinear and the fully nonlinear regime: a range of scales crucial to constrain modern era cosmological observables. The sensitivity of these observables to changes in the matter PS will be very important for making powerful observational cosmological tests of the theory of gravity, or dark energy.

The main advantage of our approach over using simulations is that it is computationally inexpensive. The two main inputs: HM and HALOFIT (or, e.g., HMcode) can be flexibly applied to different background cosmologies, whereas, in simulations, we need to perform a new run for each new set of parameters. HM also gives the flexibility of employing different combinations of HMF, $b(M)$ and $c(M)$ that is best suited to probe a particular cosmology, scale, halo mass range, or redshift.

To test the limits and accuracy of our approach, we applied Eq. (16) to another suite of MG N-body simulations, run with MG-COLA [13,75]. Using the same fitting

functions as described for the Elephant simulations, we computed halo properties for the MG-COLA cosmology, and in turn $P(k)_{\rm HM}$, $\Upsilon(k)_{\rm HM}$, and $P(k)_{\rm MG}$. We compared $P(k)_{\rm MG}$ with the $P(k)_{\rm sim}$ results, and obtained similar accuracy as with the original data of Elephant. For both MG models, $P(k)_{\rm MG}$ gives consistency with simulation results within 5% for k between 0.5–2.5 h/Mpc. However, for the case of F5, overall performance of our approach decreases with z.

We need to appreciate that another promising solution for analytical modeling of the MG PS is via the fast and reliable emulation techniques [e.g [30,111,112]]. For MG models, emulators have been proposed in, e.g., [113–117]. This approach is sophisticated and promising, however, is still in its infancy, and has limitations. For instance, predictions from emulators are confined to the parameter space defined in the starting base grid of the calibrating simulations. In addition, new extensions in emulators (e.g., new degrees of freedom, or additional screening mechanisms in MG models) often requires one to substantially adapt the base grid of simulations used to build the emulator, which can in itself be computationally expensive.

On the other hand, HM potentially provides a simple, physically-motivated semianalytical picture of the clustering of matter. We showed that HM, in its standard form, can be qualitatively used to predict estimates for MG signatures in cosmological observables which relate to matter perturbations. Furthermore, using HM for modeling the PS ratio $\Upsilon(k)$, and combining it with a high-quality baseline ΛCDM predictions yields significantly better results. This method is advantageous as contrary to MG scenarios, we have much tighter constraints on ΛCDM physics, and the field of modeling ΛCDM PS is much more sophisticated and advanced [25–28]. As a result, more precise ΛCDM results will provide MG PS with similarly improved performance. Here we present our results by incorporating the HALOFIT and HMcode predictions for ΛCDM. These results in themselves give a percent level of accuracy in both quasi-linear and nonlinear regimes.

In order to further improve HM modeling in the MG variants studied here, we need to probe deeper into the nonlinear scales. For this, the behavior of halo density profiles and HMF in both $f(R)$ and nDGP at low halo masses requires deeper investigation, as the full effect of the respective screening mechanisms comes to play in the nonlinear regime of gravitational collapse. As mentioned above, the accuracy of $c(M)$ fitting functions for both $f(R)$ and nDGP has not been tested for $\mathrm{M_{halo}} < 10^{12} M_\odot/h$ [85,87]. Additionally, we also extrapolated our earlier HMF fits for these MG models [81] to small halo mass scales, which are not resolved by our 7N-body simulations (the limit being $\mathrm{M_{halo}} \lesssim 8 \times 10^{12} M_\odot/h$). Both $c(M)$ and HMF are important ingredients in modeling the one-halo term, which is the dominant nonlinear contributor in the HM approach. Such a study will require a completely new set of high-resolution MG N-body simulations, and we plan it as a future project.

We also note that in this work, we focus on modeling only the dark matter PS. At our scales of interest (k between 0.1–2.5 h/Mpc), PS is not significantly influenced by baryons, as baryonic suppression in PS is of the order of a few percent for $k < 1$–5 h/Mpc [118–120]. However, [106,109,118] have shown that HM provides the flexibility, which allows it to add additional parameters that can incorporate baryonic effects from hydrodynamical simulation. Accounting for such effects in our MG PS modeling is a significant endeavor, and is well beyond the scope of this work.

The data used here is publicly available on our website.[1] We provide $\Upsilon(k)_{\rm HM}$ for a wide range of z, from $z = 0$ to $z = 2$ for each MG model considered in this work. A description of the dataset is also enclosed in the directory. Also, the data used to make the figures in this article is available on request to the authors.

ACKNOWLEDGMENTS

We would like to thank Hans A. Winther for kindly providing us with MGCAMB version for specific forms of $\mu(a, k)$ and $\gamma(a, k)$ functions implementing our $f(R)$ and nDGP models. The authors also thank Krishna Naidoo for giving his suite of MG-COLA simulations that we used as a testbed in our work. We also acknowledge constructive discussions with Marika Asgari, Alberto Acuto, and Bartolomeo Fiorini. We also thank the anonymous referee whose comments help improve this manuscript. Matter power spectrum calculations to compute linear halo bias have been done using Pylians [121]. This work is supported via the research project "VErTIGO" funded by the National Science Center, Poland, under Agreement No. 2018/30/E/ST9/00698. We also acknowledge the support from the Polish National Science Center within Research Projects No. 2018/31/G/ST9/03388, No. 2020/39/B/ST9/03494 (W. A. H. and M. B.), No. 2020/38/E/ST9/00395 (M. B.), and the Polish Ministry of Science and Higher Education (MNiSW) through Grant No. DIR/WK/2018/12. This project also benefited from numerical computations performed at the Interdisciplinary Centre for Mathematical and Computational Modeling (ICM), the University of Warsaw under Grants No. GA67-17 and No. GB79-7.

APPENDIX A: COMPARISON OF THEORETICAL AND SIMULATION HALO BIAS

Here we compare the simulation results for the linear halo bias, $b(M)$, with the theoretical predictions from Sheth *et al.* 2001 [[83], hereafter S01]. The formula proposed by S01 is given by:

[1] https://data.cft.edu.pl/UPSILON_PK/UpsilonPk.tar.gz.

$$b(M) = \frac{1}{\sqrt{a}\delta_c(z)}(\sqrt{a}(a\nu^2) + \sqrt{a}b(a\nu^2)^{1-c} - \frac{(a\nu^2)^c}{(a\nu^2)^c + b(1-c)(1-c/2)}, \quad \text{(A1)}$$

with the parameters $a = 0.707$, $b = 0.5$ and $c = 0.6$.

To apply the S01 expression to our MG variants, we used $P(k)_{\rm lin}$ to compute $\sigma(M, z)$, and then $\nu = \delta_c(z)/\sigma(M, z)$, specific to each MG model. For that, we used standard ΛCDM spherical collapse based δ_c values. We stay with the ΛCDM δ_c baseline since we have found that using slightly different values suggested for either $f(R)$ [122], or for the nDGP model [68] impacts the final HM results by less than a subpercent.

The results of our substitution are shown in Fig. 5, where we plot the bias ratios between MG and ΛCDM, as a function of halo mass, M_{200}. Here, we include the two models most departing from ΛCDM: N1 (left column) and F5 (right column). These variants illustrate the most extreme behavior in $b(M)$ for the two MG models we work with. Points illustrate simulation results, with error bars corresponding to the standard deviation from simulations. For comparison, ratios of S01 predictions for MG and ΛCDM are also shown, but they are extended outside of the M_{200} ranges probed by our simulations, to show the asymptotic behavior at small and large halo masses. Depending on the redshift and the model, departures in MG $b(M)$ from ΛCDM can reach up to ∼10%. Contrary to the HMF, MG-induced increase in the strength of gravity lowers the bias, as a result of enhanced DM clustering. Similar trends have also been reported in [68,119,123]. The ratios predicted analytically from the S01 framework do not match the simulation amplitudes exactly, but they still qualitatively capture the trends.

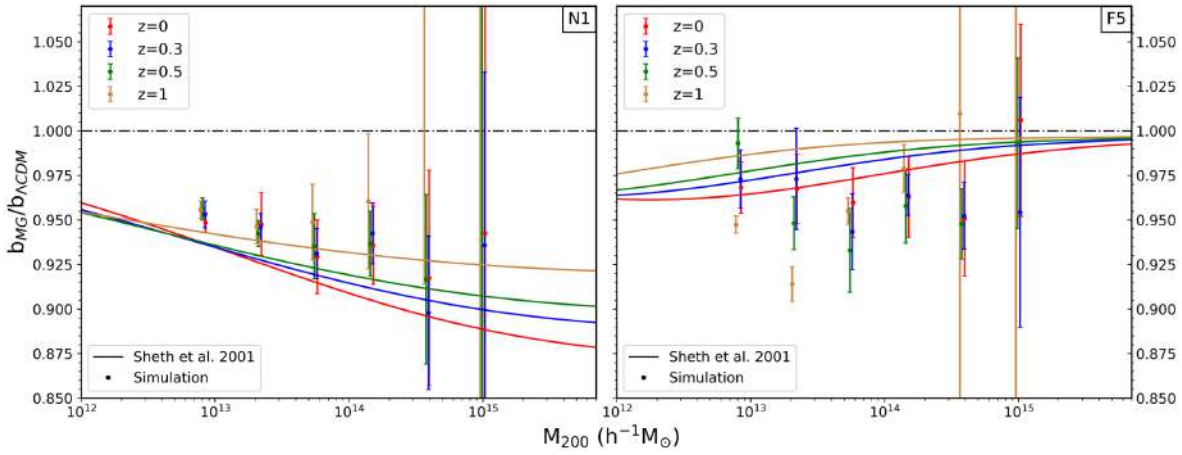

FIG. 5. Ratios of halo bias, $b(M)$, between MG and ΛCDM for N1 (left plot), and F5 (right plot), across range of redshifts as indicated in the legends. Solid lines are the analytical results from Sheth *et al.* [83], and the respective dots of the same color are from simulations. Error bars illustrate the standard deviation across five realizations of the simulation boxes.

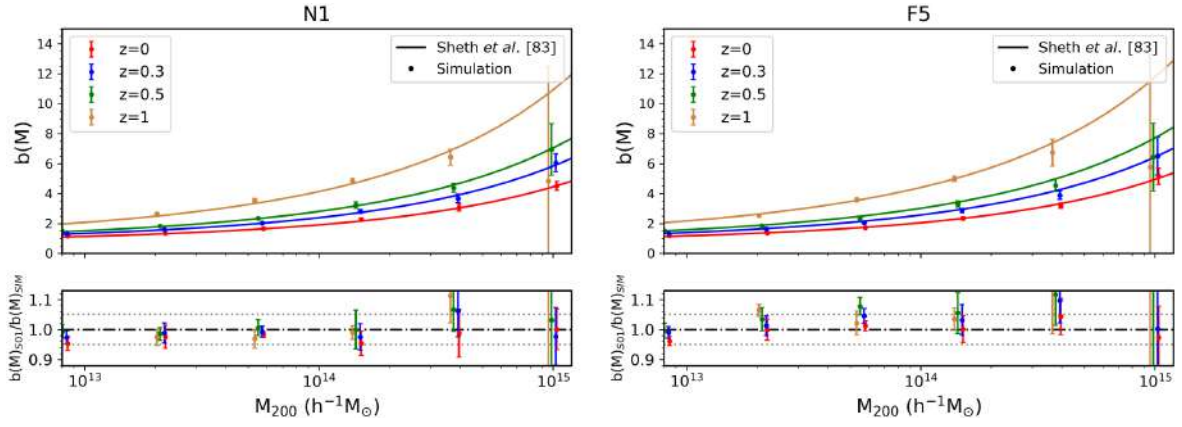

FIG. 6. Top panels: Linear halo bias, $b(M)$, as a function of halo mass, M_{200} for N1 (left column) and F5 (right column). The solid lines correspond to theoretical Sheth *et al.* 2001 [[83], S01] predictions, and the respective dots of the same color are the simulation results obtained using Eq. (10). Error bars correspond to the standard deviation across five realizations of the simulation box. Bottom panels: Ratio between S01 and simulation linear halo bias predictions. Gray dotted lines are 5% accuracy regimes.

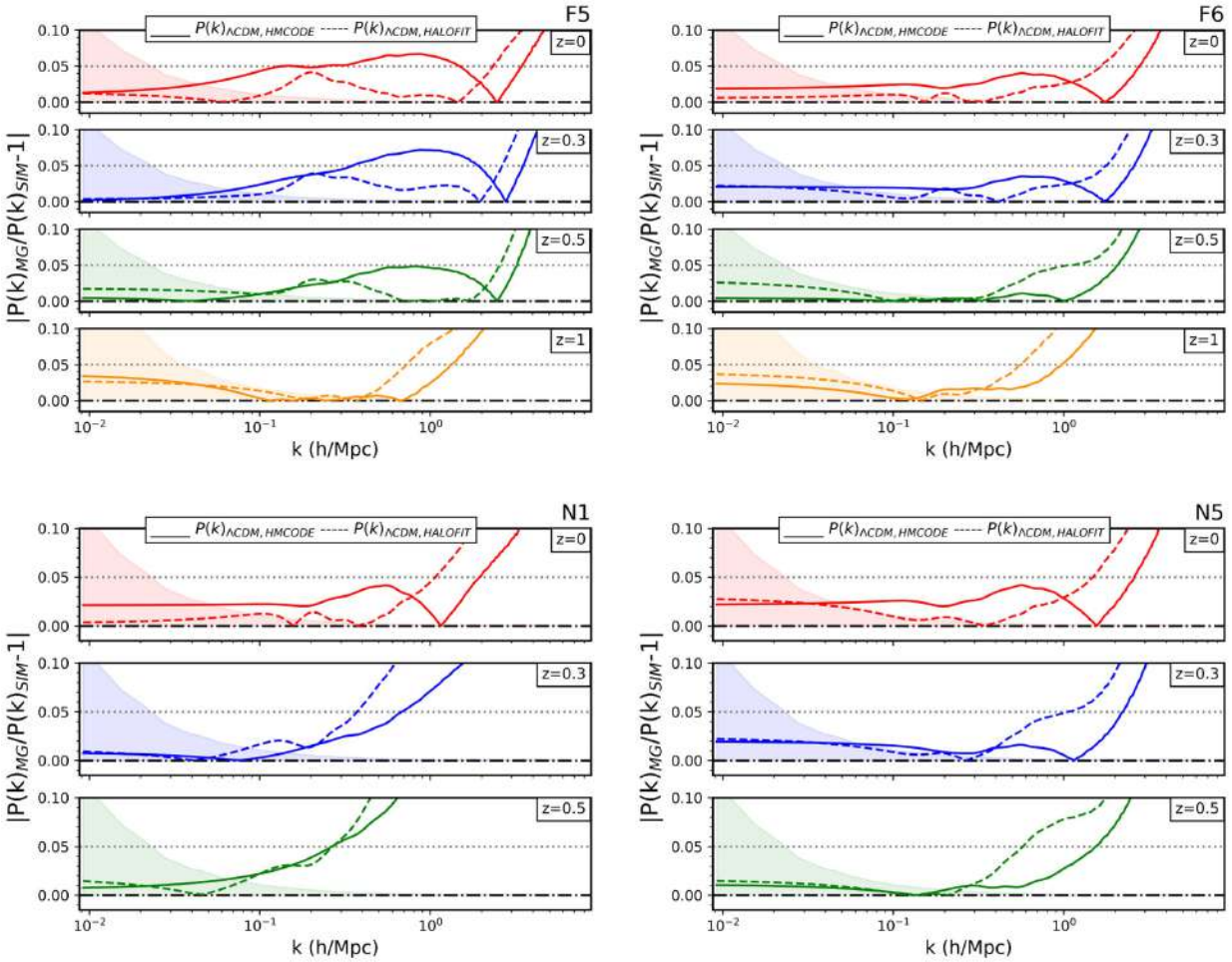

FIG. 7. Comparison of $P(k)_{\rm MG}$ obtained from the input of $P(k)_{\Lambda{\rm CDM,HMcode}}$ (solid lines) and $P(k)_{\Lambda{\rm CDM,HALOFIT}}$ (dashed lines), with the Elephant simulation results, for a range of redshifts as indicated in the legends. The error contours correspond to the uncertainty in the simulation PS results, and the vertical gray dotted line is the 5% accuracy regime.

Further, in Fig. 6, we plot the $b(M)$ in these MG models as a function of M_{200}. The top panels present absolute $b(M)$ values, while the bottom ones include the ratio between S01 predictions and the simulation-based bias. Here, we can clearly see that the analytical model matches the simulation results within 5%–10%. This affirms our approach in extending S01 to beyond ΛCDM, for the $f(R)$ and nDGP models we study.

As for the HM build-up, we need a bias prescription for a much wider halo mass range than what our simulations cover. This overall consistency between the analytical and simulation results is sufficient for us, and thus we can use the S01 modeling for $b(M)$ also in our MG variants.

APPENDIX B: COMPARISON OF HALOFIT AND HMcode RESULTS

As discussed in Sec. IV B, for our baseline PS modeling in MG we multiply the HM-based ratio $\Upsilon(k)$ with HALOFIT PS derived for ΛCDM. Here we test our approach for the case where the ΛCDM PS is obtained from the HMcode [26] instead. Similarly to HALOFIT, HMcode is also built on the principles of HM, incorporating however additional corrections in the standard HM build-up, owing to physical constraints. The parameters of the corrections are based on high-resolution simulated ΛCDM power spectra from the emulator introduced in Ref. [124]. Here we use the latest HMcode-2020 version[2] [109].

We compute $P(k)_{\rm MG}$ by multiplying $\Upsilon(k)_{\rm HM}$ with both HALOFIT and HMcode inputs for $P(k)_{\Lambda{\rm CDM}}$. Then, in Fig. 7, we compare both predictions with the Elephant simulation results. Here we see a similar performance of both the methods, with some exceptions at small scales and high-z, where HMcode occasionally performs better. Interestingly, at $z = 0$, the HALOFIT framework seems to lead to better results for a range of k-scales. We emphasize

[2]https://github.com/alexander-mead/HMcode.

however that as our simulations were done for one particular set of cosmological parameters, these trends between HALOFIT and HMcode-based predictions could change for other background cosmologies. In any case, as what we provide is the ratio $\Upsilon(k)_{\rm HM}$ to be multiplied by the ΛCDM PS prediction, one can employ any best-fit $P(k)_{\Lambda\rm CDM}$ for the latter to possibly improve the final accuracy of $P(k)_{\rm MG}$.

[1] D. J. Eisenstein, I. Zehavi, D. W. Hogg, R. Scoccimarro, M. R. Blanton *et al.*, Astrophys. J. **633**, 560 (2005).
[2] Planck Collaboration, Astron. Astrophys. **641**, A6 (2020).
[3] R. H. Cyburt, B. D. Fields, K. A. Olive, and T.-H. Yeh, Rev. Mod. Phys. **88**, 015004 (2016).
[4] S. Alam, M. Aubert, S. Avila, C. Balland, J. E. Bautista *et al.*, Phys. Rev. D **103**, 083533 (2021).
[5] M. Betoule, R. Kessler, J. Guy, J. Mosher, D. Hardin *et al.*, Astron. Astrophys. **568**, A22 (2014).
[6] G. Hinshaw, D. Larson, E. Komatsu, D. N. Spergel, C. L. Bennett *et al.*, Astrophys. J. Suppl. Ser. **208**, 19 (2013).
[7] S. Cole, W. J. Percival, J. A. Peacock, P. Norberg, C. M. Baugh *et al.*, Mon. Not. R. Astron. Soc. **362**, 505 (2005).
[8] C. Blake, E. A. Kazin, F. Beutler, T. M. Davis, D. Parkinson, S. Brough, M. Colless, C. Contreras, W. Couch, S. Croom *et al.*, Mon. Not. R. Astron. Soc. **418**, 1707 (2011).
[9] A. Pezzotta, S. de la Torre, J. Bel, B. R. Granett, L. Guzzo *et al.*, Astron. Astrophys. **604**, A33 (2017).
[10] Planck Collaboration, Astron. Astrophys. **571**, A20 (2014).
[11] R. Bean and M. Tangmatitham, Phys. Rev. D **81**, 083534 (2010).
[12] W. A. Hellwing, K. Koyama, B. Bose, and G.-B. Zhao, Phys. Rev. D **96**, 023515 (2017).
[13] H. A. Winther, K. Koyama, M. Manera, B. S. Wright, and G.-B. Zhao, J. Cosmol. Astropart. Phys. 08 (2017) 006.
[14] S. Bose, B. Li, A. Barreira, J.-h. He, W. A. Hellwing, K. Koyama, C. Llinares, and G.-B. Zhao, J. Cosmol. Astropart. Phys. 02 (2017) 050.
[15] A. Barreira, S. Bose, and B. Li, J. Cosmol. Astropart. Phys. 12 (2015) 059.
[16] K. Koyama, A. Taruya, and T. Hiramatsu, Phys. Rev. D **79**, 123512 (2009).
[17] DESI Collaboration, arXiv:1611.00036.
[18] LSST Science Collaboration, arXiv:0912.0201.
[19] R. Laureijs, J. Amiaux, S. Arduini, J. L. Augueres, J. Brinchmann *et al.*, arXiv:1110.3193.
[20] M. Kilbinger, L. Fu, C. Heymans, F. Simpson, J. Benjamin *et al.*, Mon. Not. R. Astron. Soc. **430**, 2200 (2013).
[21] C. Hikage, M. Oguri, T. Hamana, S. More, R. Mandelbaum *et al.*, Publ. Astron. Soc. Jpn. **71**, 43 (2019).
[22] C. To, E. Krause, E. Rozo, H. Wu, D. Gruen *et al.*, Phys. Rev. Lett. **126**, 141301 (2021).
[23] R. J. Turner, C. Blake, and R. Ruggeri, Mon. Not. R. Astron. Soc. **518**, 2436 (2023).
[24] A. Cooray and R. Sheth, Phys. Rep. **372**, 1 (2002).
[25] R. E. Smith, J. A. Peacock, A. Jenkins, S. D. M. White, C. S. Frenk, F. R. Pearce, P. A. Thomas, G. Efstathiou, and H. M. P. Couchman, Mon. Not. R. Astron. Soc. **341**, 1311 (2003).
[26] A. J. Mead, J. A. Peacock, C. Heymans, S. Joudaki, and A. F. Heavens, Mon. Not. R. Astron. Soc. **454**, 1958 (2015).
[27] E. Lawrence, K. Heitmann, M. White, D. Higdon, C. Wagner, S. Habib, and B. Williams, Astrophys. J. **713**, 1322 (2010).
[28] R. Takahashi, M. Sato, T. Nishimichi, A. Taruya, and M. Oguri, Astrophys. J. **761**, 152 (2012).
[29] R. E. Smith and R. E. Angulo, Mon. Not. R. Astron. Soc. **486**, 1448 (2019).
[30] R. E. Angulo, M. Zennaro, S. Contreras, G. Aricò, M. Pellejero-Ibañez, and J. Stücker, Mon. Not. R. Astron. Soc. **507**, 5869 (2021).
[31] H. Oyaizu, M. Lima, and W. Hu, Phys. Rev. D **78**, 123524 (2008).
[32] S. Alam, A. Aviles, R. Bean, Y.-C. Cai, M. Cautun *et al.*, J. Cosmol. Astropart. Phys. 11 (2021) 050.
[33] W. Hu and I. Sawicki, Phys. Rev. D **76**, 104043 (2007).
[34] M. Cataneo, L. Lombriser, C. Heymans, A. J. Mead, A. Barreira, S. Bose, and B. Li, Mon. Not. R. Astron. Soc. **488**, 2121 (2019).
[35] C.-Z. Ruan, T.-J. Zhang, and B. Hu, Mon. Not. R. Astron. Soc. **492**, 4235 (2020).
[36] M. Baldi, F. Villaescusa-Navarro, M. Viel, E. Puchwein, V. Springel, and L. Moscardini, Mon. Not. R. Astron. Soc. **440**, 75 (2014).
[37] H. A. Winther, F. Schmidt, A. Barreira, C. Arnold, S. Bose *et al.*, Mon. Not. R. Astron. Soc. **454**, 4208 (2015).
[38] E. Puchwein, M. Baldi, and V. Springel, Mon. Not. R. Astron. Soc. **436**, 348 (2013).
[39] T. Clifton, P. G. Ferreira, A. Padilla, and C. Skordis, Phys. Rep. **513**, 1 (2012).
[40] T. Baker, D. Psaltis, and C. Skordis, Astrophys. J. **802**, 63 (2015).
[41] K. Koyama, Rep. Prog. Phys. **79**, 046902 (2016).
[42] S. Nojiri, S. D. Odintsov, and V. K. Oikonomou, Phys. Rep. **692**, 1 (2017).
[43] P. G. Ferreira, Annu. Rev. Astron. Astrophys. **57**, 335 (2019).
[44] T. P. Sotiriou and V. Faraoni, Rev. Mod. Phys. **82**, 451 (2010).
[45] T. Baker, A. Barreira, H. Desmond, P. Ferreira, B. Jain *et al.*, Rev. Mod. Phys. **93**, 015003 (2021).
[46] K. Koyama, Int. J. Mod. Phys. D **27**, 1848001 (2018).
[47] A. Joyce, L. Lombriser, and F. Schmidt, Annu. Rev. Nucl. Part. Sci. **66**, 95 (2016).

[48] P. Bull, Y. Akrami, J. Adamek, T. Baker, E. Bellini *et al.*, Phys. Dark Universe **12**, 56 (2016).
[49] U. Seljak, Mon. Not. R. Astron. Soc. **318**, 203 (2000).
[50] M. Asgari, A. J. Mead, and C. Heymans, arXiv:2303.08752.
[51] C. M. Will, Living Rev. Relativity **17**, 4 (2014).
[52] J. H. Taylor and J. M. Weisberg, Astrophys. J. **253**, 908 (1982).
[53] B. P. Abbott, R. Abbott, T. D. Abbott, F. Acernese, K. Ackley *et al.*, Phys. Rev. Lett. **119**, 161101 (2017).
[54] B. P. Abbott, R. Abbott, T. D. Abbott, F. Acernese, K. Ackley, C. Adams, T. Adams, P. Addesso, R. X. Adhikari, V. B. Adya *et al.*, Phys. Rev. Lett. **116**, 061102 (2016).
[55] R. Abuter, A. Amorim, M. Bauböck, J. P. Berger, H. Bonnet *et al.* (Gravity Collaboration), Astron. Astrophys. **636**, L5 (2020).
[56] I. I. Shapiro, Phys. Rev. Lett. **13**, 789 (1964).
[57] A. Joyce, B. Jain, J. Khoury, and M. Trodden, Phys. Rep. **568**, 1 (2015).
[58] P. Brax, Classical Quantum Gravity **30**, 214005 (2013).
[59] J. Sakstein, Int. J. Mod. Phys. D **27**, 1848008 (2018).
[60] G. Dvali, G. Gabadadze, and M. Porrati, Phys. Lett. B **485**, 208 (2000).
[61] A. J. Mead, C. Heymans, L. Lombriser, J. A. Peacock, O. I. Steele, and H. A. Winther, Mon. Not. R. Astron. Soc. **459**, 1468 (2016).
[62] G.-B. Zhao, Astrophys. J. Suppl. Ser. **211**, 23 (2014).
[63] N. Tessore, H. A. Winther, R. B. Metcalf, P. G. Ferreira, and C. Giocoli, J. Cosmol. Astropart. Phys. 10 (2015) 036.
[64] I. Achitouv, M. Baldi, E. Puchwein, and J. Weller, Phys. Rev. D **93**, 103522 (2016).
[65] L. Lombriser, K. Koyama, and B. Li, J. Cosmol. Astropart. Phys. 03 (2014) 021.
[66] A. Barreira, B. Li, W. A. Hellwing, L. Lombriser, C. M. Baugh, and S. Pascoli, J. Cosmol. Astropart. Phys. 04 (2014) 029.
[67] A. Barreira, B. Li, W. A. Hellwing, C. M. Baugh, and S. Pascoli, J. Cosmol. Astropart. Phys. 09 (2014) 031.
[68] F. Schmidt, W. Hu, and M. Lima, Phys. Rev. D **81**, 063005 (2010).
[69] W. Hu and I. Sawicki, Phys. Rev. D **76**, 064004 (2007).
[70] J. Khoury and A. Weltman, Phys. Rev. D **69**, 044026 (2004).
[71] C. Deffayet, G. Dvali, G. Gabadadze, and A. Vainshtein, Phys. Rev. D **65**, 044026 (2002).
[72] A. I. Vainshtein, Phys. Lett. **39B**, 393 (1972).
[73] B. Li, G.-B. Zhao, R. Teyssier, and K. Koyama, J. Cosmol. Astropart. Phys. 01 (2012) 051.
[74] B. Li, G.-B. Zhao, and K. Koyama, J. Cosmol. Astropart. Phys. 05 (2013) 023.
[75] K. Naidoo, W. A. Hellwing, M. Bilicki, N. Libeskind, S. Pfeifer, and Y. Hoffman, Phys. Rev. D **107**, 043533 (2023).
[76] A. Lewis, A. Challinor, and A. Lasenby, Astrophys. J. **538**, 473 (2011).
[77] S. Colombi, A. Jaffe, D. Novikov, and C. Pichon, Mon. Not. R. Astron. Soc. **393**, 511 (2009).
[78] J. A. Peacock and R. E. Smith, Mon. Not. R. Astron. Soc. **318**, 1144 (2000).
[79] A. Cooray and W. Hu, Astrophys. J. **554**, 56 (2001).
[80] W. A. Watson, I. T. Iliev, A. D'Aloisio, A. Knebe, P. R. Shapiro, and G. Yepes, Mon. Not. R. Astron. Soc. **433**, 1230 (2013).
[81] S. Gupta, W. A. Hellwing, M. Bilicki, and J. E. García-Farieta, Phys. Rev. D **105**, 043538 (2022).
[82] K. Koyama and F. P. Silva, Phys. Rev. D **75**, 084040 (2007).
[83] R. K. Sheth, H. J. Mo, and G. Tormen, Mon. Not. R. Astron. Soc. **323**, 1 (2001).
[84] A. D. Ludlow, S. Bose, R. E. Angulo, L. Wang, W. A. Hellwing, J. F. Navarro, S. Cole, and C. S. Frenk, Mon. Not. R. Astron. Soc. **460**, 1214 (2016).
[85] M. A. Mitchell, C. Arnold, J.-h. He, and B. Li, Mon. Not. R. Astron. Soc. **487**, 1410 (2019).
[86] M. A. Mitchell, J.-h. He, C. Arnold, and B. Li, Mon. Not. R. Astron. Soc. **477**, 1133 (2018).
[87] M. A. Mitchell, C. Hernández-Aguayo, C. Arnold, and B. Li, Mon. Not. R. Astron. Soc. **508**, 4140 (2021).
[88] W. H. Press and P. Schechter, Astrophys. J. **187**, 425 (1974).
[89] J. R. Bond, S. Cole, G. Efstathiou, and N. Kaiser, Astrophys. J. **379**, 440 (1991).
[90] A. Jenkins, C. S. Frenk, S. D. M. White, J. M. Colberg, S. Cole, A. E. Evrard, H. M. P. Couchman, and N. Yoshida, Mon. Not. R. Astron. Soc. **321**, 372 (2001).
[91] M. S. Warren, K. Abazajian, D. E. Holz, and L. Teodoro, Astrophys. J. **646**, 881 (2006).
[92] G. Despali, C. Giocoli, R. E. Angulo, G. Tormen, R. K. Sheth, G. Baso, and L. Moscardini, Mon. Not. R. Astron. Soc. **456**, 2486 (2016).
[93] J. Tinker, A. V. Kravtsov, A. Klypin, K. Abazajian, M. Warren, G. Yepes, S. Gottlöber, and D. E. Holz, Astrophys. J. **688**, 709 (2008).
[94] R. E. Angulo, V. Springel, S. D. M. White, A. Jenkins, C. M. Baugh, and C. S. Frenk, Mon. Not. R. Astron. Soc. **426**, 2046 (2012).
[95] W. A. Hellwing and R. Juszkiewicz, Phys. Rev. D **80**, 083522 (2009).
[96] T. Y. Lam and B. Li, Mon. Not. R. Astron. Soc. **426**, 3260 (2012).
[97] B. Falck, K. Koyama, and G.-B. Zhao, J. Cosmol. Astropart. Phys. 07 (2015) 049.
[98] U. Seljak and M. S. Warren, Mon. Not. R. Astron. Soc. **355**, 129 (2004).
[99] J. L. Tinker, B. E. Robertson, A. V. Kravtsov, A. Klypin, M. S. Warren, G. Yepes, and S. Gottlöber, Astrophys. J. **724**, 878 (2010).
[100] J. Comparat, F. Prada, G. Yepes, and A. Klypin, Mon. Not. R. Astron. Soc. **469**, 4157 (2017).
[101] J. F. Navarro, C. S. Frenk, and S. D. M. White, Astrophys. J. **462**, 563 (1996).
[102] C. Power, J. F. Navarro, A. Jenkins, C. S. Frenk, S. D. M. White, V. Springel, J. Stadel, and T. Quinn, Mon. Not. R. Astron. Soc. **338**, 14 (2003).
[103] J. L. Tinker, D. H. Weinberg, Z. Zheng, and I. Zehavi, Astrophys. J. **631**, 41 (2005).
[104] A. J. Mead and L. Verde, Mon. Not. R. Astron. Soc. **503**, 3095 (2021).
[105] F. Schmidt, Phys. Rev. D **93**, 063512 (2016).

[106] A. J. Mead, T. Tröster, C. Heymans, L. Van Waerbeke, and I. G. McCarthy, Astron. Astrophys. **641**, A130 (2020).
[107] F. Schmidt, Phys. Rev. D **80**, 123003 (2009).
[108] B. Li, W. A. Hellwing, K. Koyama, G.-B. Zhao, E. Jennings, and C. M. Baugh, Mon. Not. R. Astron. Soc. **428**, 743 (2013).
[109] A. J. Mead, S. Brieden, T. Tröster, and C. Heymans, Mon. Not. R. Astron. Soc. **502**, 1401 (2021).
[110] S. Tassev, M. Zaldarriaga, and D. J. Eisenstein, J. Cosmol. Astropart. Phys. 06 (2013) 036.
[111] K. Heitmann, D. Higdon, C. Nakhleh, and S. Habib, Astrophys. J. Lett. **646**, L1 (2006).
[112] S. Habib, K. Heitmann, D. Higdon, C. Nakhleh, and B. Williams, Phys. Rev. D **76**, 083503 (2007).
[113] N. Ramachandra, G. Valogiannis, M. Ishak, and K. Heitmann (LSST Dark Energy Science Collaboration), Phys. Rev. D **103**, 123525 (2021).
[114] H. A. Winther, S. Casas, M. Baldi, K. Koyama, B. Li, L. Lombriser, and G.-B. Zhao, Phys. Rev. D **100**, 123540 (2019).
[115] C. Arnold, B. Li, B. Giblin, J. Harnois-Déraps, and Y.-C. Cai, Mon. Not. R. Astron. Soc. **515**, 4161 (2022).
[116] J. Harnois-Déraps, C. Hernandez-Aguayo, C. Cuesta-Lazaro, C. Arnold, B. Li *et al.*, arXiv:2211.05779.
[117] C.-Z. Ruan, C. Cuesta-Lazaro, A. Eggemeier, B. Li, C. M. Baugh *et al.*, arXiv:2301.02970.
[118] A. Acuto, I. G. McCarthy, J. Kwan, J. Salcido, S. G. Stafford, and A. S. Font, Mon. Not. R. Astron. Soc. **508**, 3519 (2021).
[119] C. Arnold, P. Fosalba, V. Springel, E. Puchwein, and L. Blot, Mon. Not. R. Astron. Soc. **483**, 790 (2019).
[120] N. E. Chisari, A. J. Mead, S. Joudaki, P. G. Ferreira, A. Schneider *et al.*, Open J. Astrophys. **2**, 4 (2019).
[121] https://pylians3.readthedocs.io/en/master/.
[122] M. Kopp, S. A. Appleby, I. Achitouv, and J. Weller, Phys. Rev. D **88**, 084015 (2013).
[123] F. Schmidt, M. Lima, H. Oyaizu, and W. Hu, Phys. Rev. D **79**, 083518 (2009).
[124] K. Heitmann, E. Lawrence, J. Kwan, S. Habib, and D. Higdon, Astrophys. J. **780**, 111 (2014).

Chapter 4: Large-scale clustering and Halo Assembly Bias in Modified Gravity Cosmologies

My methods are really methods of working and thinking; that is why they have crept in everywhere anonymously.

-Emmy Noether

Chapter 4

Large-scale clustering and Halo Assembly Bias in Modified Gravity cosmologies

---

According to the standard structure formation paradigm, halos are formed from the collapse of peaks in the initial density field [231, 27, 44]. Within this paradigm, high density peaks of the density field cluster more strongly than the corresponding background matter density field. This induces the *halo bias*, which describes the relation between clustering of halos and the underlying DM density field.

Early numerical works of [145, 170] showed that this halo bias relation is a function of only halo mass, and there is no significant dependence of this quantity on other halo properties. Subsequent developments in cosmological simulations showed that low-mass halos in the high redshift tail of formation time distribution are much strongly clustered than halos of similar mass in the low-redshift tail [104]. This dependence of halo clustering on the assembly history of halos at a fixed mass is known as the *Halo assembly bias* (HAB). The later numerical works confirmed this detection, and showed that halo clustering at a fixed mass depends not only on the formation time, but also on other halo properties: like concentration, spin, shape, environment, tidal anisotropy etc. [279, 105, 81, 114, 95, 233, 290, 165, 219, 192, 71, 204, 160]. The dependence of the bias relation on halo mass turns out to be different when different properties are used to split the halo population. Thus, this shows that the clustering of simulated halos not only depends on the halo mass, but also, in a complex way, on how halos assemble, and on the large-scale environment that hosts the halo. Also, it is likely that the HAB effect is further imprinted in the galaxies that form in the halos (called as Galaxy Assembly bias (GAB)). Hence, it becomes important to model both HAB and GAB in cosmological analyses which uses galaxy clustering, in order to reduce significant systematics from the studies of galaxy evolution and clustering [292]. However, in this work, we only focus on HAB.

To relate halos to galaxies, many semi-analytical models are formulated, which are

originally built by considering only the property of halo mass [220, 73, 289, 272]. Detailed HAB studies challenge this rationale, and accurate calibration of HAB could further be useful in building better methodologies, or improving the existing ones that can help us understand the galaxy-halo relation with better accuracy, and reduced systematics [117, 62, 169, 70, 69, 72, 221].

Various studies have shown how HAB depends on different properties within the standard ΛCDM paradigm. Given the advancements in ΛCDM simulations, the nature of HAB and its dependence on a number of internal halo properties, and the environment is well-understood (references same as the first paragraph). However, our understanding of the HAB in cosmological models different from ΛCDM is far from being established. This venture is essential as MG physics could influence the HAB in a way that can lead to unknown systematics. In [166, 258], the authors explore the impact of massive neutrinos on HAB and observed no notable signatures. Further studies in [71] also showed no significant impact of changing the parameters of the background cosmology (whilst staying within the ΛCDM paradigm) on the HAB effect.

We further work in this domain of extending HAB studies to our beyond-GR models. In this chapter, we first discuss the standard halo bias relation in Section 4.1. We quantify this relation in both GR and MG scenarios, and studied the differences in the latter *w.r.t.* the former. In the next section (4.2), we discuss the halo properties that we use to investigate to explore the HAB effect: halo density concentration (Section 4.2.1), and halo spin (Section 4.2.2). The impact on HAB in these MG models is discussed in the subsequent Section 4.3: In Section 4.3.1, we discuss the HAB from halo concentration, and further compare both ΛCDM and MG results. In Section 4.3.2, we performed the same exercise, but this time using halo spin as the secondary property for the HAB analysis. In Section 4.4, we summarise, and discuss further implications of our results.

4.1 Large-scale clustering: Halo bias relation

As highlighted, halos are *biased* tracers of the underlying DM density distribution. Massive halos are formed from high-σ fluctuations in the primordial density field, inducing a positive correlation between high mass halos and the clustering amplitude, which is steepest for cluster-sized objects. On the other hand, low-mass halos are preferentially found in regions of the Universe with low densities, thus making these objects anti-biased with respect to the underlying density field.

Observations of large-scale structures involve a process of relating the galaxies and clusters, to halos that host them, as well as to the underlying DM distribution. This relation is obtained first using the halo bias formalism; and the final link to galaxies is through galaxy bias, which describes the galaxy-halo connection. In this work, we only focus on halo bias, and this relation is further used to define the large-scale clustering of halos.

As mentioned in the previous chapters, halos evolved from fluctuations in the density field. These halo perturbations δ_h, on large linear scales, are proportional to the matter density perturbation, δ_m, with a proportionality constant b. This linear halo bias relation, $b(M,z)$ has shown to be dependent only on halo mass and redshift, and is independent of the scales [143, 65, 251, 249]. More massive halos tend to be more biased than the less massive ones. Similarly, halos of the same mass were more strongly biased at higher redshifts than they are today.

Mathematically, in terms of the variance of density field, the halo bias relation is given by

$$b(k,M) = \frac{\langle \delta_h(k,M)\delta_h^*(k,M)\rangle}{\langle \delta_m(k)\delta_m^*(k)\rangle}. \tag{4.1}$$

Here, $\delta(k)$ is the overdensity. This equation is only valid when $|\delta| \ll 1$, *i.e.*, on large cosmological scales. On smaller scales, where the matter overdensity is larger, higher order terms are needed [82]. Our estimate for the linear halo bias is given by the asymptotic value of $b(k,M)$ on large scales (or small k), where this estimator approaches a scale-independent linear value.

More conveniently, we can compute halo bias in Fourier space as the ratio of halo-halo power spectrum to the DM power spectrum, *i.e.*

$$b(k,M) = \sqrt{\frac{P_{hh}(k,M)}{P_{mm}(k)}}. \tag{4.2}$$

Using the DM density fields, and halo catalogues generated from our simulations, we compute the matter-matter power spectrum, $P_{mm}(k)(=\langle \delta_m(k)\delta_m^*(k)\rangle)$, halo-halo power spectrum, $P_{hh}(k)(=\langle \delta_h(k,M)\delta_h^*(k,M)\rangle)$, and halo-matter cross power spectrum, $P_{hm}(k)(=\langle \delta_h(k,M)\delta_M^*(k)\rangle\langle \delta_h^*(k,M)\delta_M(k)\rangle/2)$ using pylians python package [1]. We computed the power spectra by Fourier transforming the density field over 32^3 grid, using Triangular-Shaped-Cloud (TSC) technique. We have used a coarser grid size to reduce the impact of shot-noise from sparse halo number count.

The measurement of halo power spectrum, $P_{hh}(k,M)$ is affected, to some level, by shot noise due to the discrete nature of halos. Halos are extended objects and cannot be modelled as the Poisson sampling of a continuous distribution. On the other hand, discreteness effects are expected to be much smaller for the matter power spectrum, $P_{mm}(k)$, or the halo-matter cross power spectrum $P_{hm}(k)$ due to the large number density of DM particles in the simulations. As a result, more reliable estimator for halo bias is given by the following equation

$$b(k,M) = \frac{P_{hm}(k,M)}{P_{mm}(k)}. \tag{4.3}$$

The cross-power spectrum, denoted as $P_{hm}(k,M)$, represents the cross-correlation

[1] https://pylians3.readthedocs.io/en/master/

between halos and the DM density field. Notably, Eq. (4.2) and Eq. (4.3) yield similar predictions for regions of high density and increased number of halos. However, when it comes to rare mass halos, Eq. (4.2) provides an enhanced bias estimate due to the influence of shot noise effects [226]. In this work, we use $b(k,M)$ defined in Eq. (4.3).

4.1.1 Halo bias in Modified Gravity scenarios

Similar to the HMF trends (Section 2.2), when we express bias using the natural units of the density field fluctuation variance ($\sigma(M)$, or peak-height $\nu = \delta_c/\sigma(M)$), rather than a specific physical halo mass, the bias trend across redshifts becomes more universal and regular. It is an already established result for ΛCDM [251, 268, 226]. For our purpose, we extend the study of this $b(\nu)$-log ν relation to include our MG models. This analysis is presented in the top panels of Fig. 4.1, where the solid lines depict the bias relation in MG models, with the specific MG variant indicated in the legends. Notably, we observe a universal trend in this relation for our MG models across all the examined redshifts, similar to what is observed in the ΛCDM model. Here, the dashed dotted lines are the theoretical bias predictions from [251] (referred to as the BIAS-SMT, Eq. (3.13)). This relation has been proposed by exploiting the universality in the $b(\nu)$-log ν relation for ΛCDM. Remarkably, this SMT-BIAS relation also gives reliable bias results even for our MG models (for more details on this substitution, we refer the readers to the appendix of [110]).

In the bottom panels on the plots of this figure, we show a comparison of the linear bias from MG with the results from ΛCDM. Here, we note that for both the MG models, the overall $b(\nu)$ value decreases when compared to ΛCDM, and the stronger MG variants (F5 and N1) show a greater decrease compared to the weaker counterparts (F6 and N5). The stronger gravity models can depart from ΛCDM to even upto 10%, whereas the weaker variants remain within 5% from ΛCDM results. This is attributed to stronger DM clustering, which goes in the denominator of $b(\nu)$ computations (Eq. (4.3)). Similar trends in MG bias have also been reported in [246, 244, 20].

These results show that linear halo bias, though weakly, is affected by the modifications to the underlying gravity theory. As a result, if we understand how the distribution of tracers (in our case, halos) is related to the underlying distribution of DM, we can access a wealth of information on the underlying nature of gravity, that forms the basis of large-scale matter clustering. Also, we showed in Chapter 3 that the halo bias relation could be further used in analytical modelling of the non-linear matter power spectrum in these MG scenarios (Section 3.2).

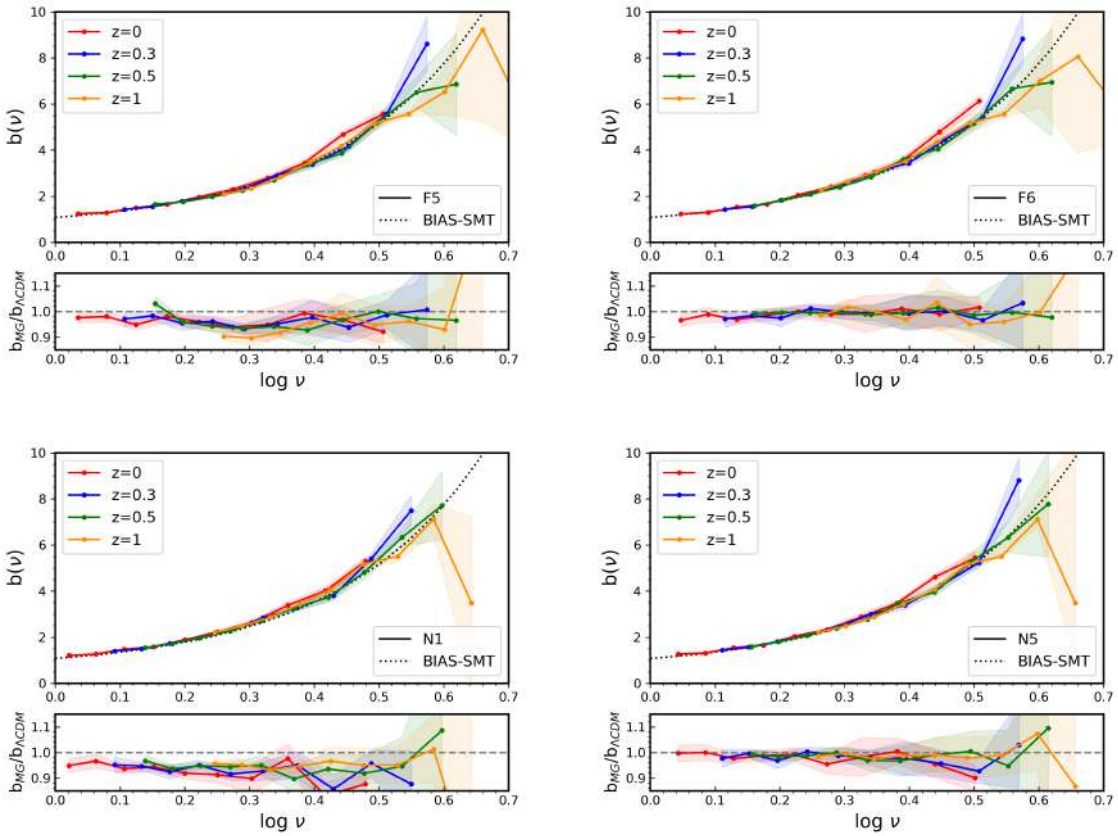

Figure 4.1: *Top panels:* Linear halo bias $b(\nu)$-log ν relation, for MG models (solid lines), at $z = 0, 0.3, 0.5$ and 1. The dotted black lines are the theoretical predictions of the BIAS-SMT relation from [251] (Here, Eq. (3.13)). *Lower panels:* Comparison of MG $b(\nu)$ with ΛCDM. The top plots corresponds to the variants of $f(R)$ gravity, and the bottom panels are the results of nDGP gravity variants. The shaded regions correspond to errors across five realizations.

4.2 Internal halo properties

4.2.1 Halo concentration

The scale-free nature of structure formation in CDM scenarios results in self-similar density profiles for individual DM halos, which was first pointed in the seminal work of Navarro, Frenk and White (1996) [208] (hereafter, NFW). The concentration parameter, defined as the ratio of the virial radius of the halo to its scale radius ($\equiv r_v/r_s$), determines the density profile of NFW halos. Here, r_s is the radius where the logarithmic slope of the density profile is -2. Under the assumption of self-similarity, DM density profiles can be re-scaled by a suitable central density, ρ_s and r_s (or mass and concentration respectively). Here, ρ_s controls the amplitude of the profile.

To define the halo density profile for a given halo of mass M

$$\rho(r|M) = \frac{\rho_s}{(r/r_s)^{\alpha}(1+r/r_s)^{\beta}}. \tag{4.4}$$

For NFW profile: $(\alpha, \beta) = (1, 2)$.

Since the genesis of the NFW profile, a large number of relations between the concentration and mass of halos have been developed [89, 149, 230, 85, 183].

Halos in simulations are identified in the DM particle distribution via a user-set overdensity threshold. Once the overdensity threshold has been set and the halo mass measured, the virial radius is no longer an independent parameter, and is given as

$$r_v = \left(\frac{3M}{4\pi\Delta_v\bar{\rho}}\right)^{1/3}. \tag{4.5}$$

Typically, a value of $\Delta_v = 200$ is taken (Section 1.9), which is loosely based on predictions from the spherical collapse model ($\Delta_v = 180$, as described in Section 1.3.2).

As a result, the only free parameter in the NFW fit to simulations is then r_s, or equivalently the halo concentration. Concentration is an explicit function of halo mass, cosmology and redshift. Halos of higher mass are less concentrated than those of lower mass, as larger halos formed in a more recent past. As Universe expands and becomes less dense at later times, newly formed halos have lower inner densities compared to the older counterparts, as the central density of a halo retains a memory of the cosmological density at its formation time [183].

In order to accurately measure the concentration, it is important that the halo consists of enough particles ($\geq 10^3$ particles) so that it is well-resolved at both the inner and the outer regions [229]. In our simulations, this would correspond to halos with mass $\geq 7.8 \times 10^{13}$ $M_\odot/h$, which is already in the cluster mass regime. Therefore, instead of directly fitting NFW profile to our simulated halos, we compute concentration using an alternate non-parametric "velocity-ratio" concentration, which is given by

$$c = \frac{V_{max}}{V_{200}}. \tag{4.6}$$

Here, V_{max} is the maximum circular velocity of a halo, and V_{200} is the circular velocity at the virial radius

$$V_{200} = \left(\frac{GM_{200}}{R_{200}}\right)^{1/2}. \tag{4.7}$$

By definition, all halos of same M_{200} would have the same V_{200}. However, they would have different values of V_{max}, depending on the degree to which their masses are concentrated towards the halo centre. Hence, using only the measurements of V_{max} and R_{200} from halo catalogs, Eq. (4.6) can be solved to estimate the concentration. This relation also has been used in the past studies of halo concentration [230, 105], and is shown to encode similar information as obtained from direct NFW fitting [275].

Halo concentration in MG models

Internal structures of halos provide information of their formation history, which depends on the underlying gravity theory. In this section, we probe the concentration differences in different MG models *w.r.t.* ΛCDM. We compute concentration from ELEPHANT data using Eq. (4.6) for ΛCDM and each MG variant. The results are shown in Fig. 4.2. Here, on the top panel, we plot the median concentration across log ν scales for $z = 0, 0.3, 0.5$ and 1 for each MG model. To elucidate a direct comparison, we also show the ΛCDM results on each plot in dashed lines. Here, we again use the peak-height, $\nu(M,z)$ relation to encapsulate the redshift dependencies across halo mass scales. The bottom panel of each plot corresponds to the ratio of the median concentration from MG models with ΛCDM across z.

We see that all models, except F5 at $z = 0$, roughly follow the ΛCDM trend. We can clearly see a deviation in this trend for lower values of log ν in F5. Also, we obtain a peak at log ν between $0.04 - 0.2$ in the lower panel of the F5 gravity model. Here, for unscreened halos, the in-falling particles experience a greater bonding potential due to the stronger gravitational force, and this can alter the profile such that the density is raised at the inner regions. Due to this, the halos are formed earlier in F5. As concentration roughly reflects the background density of the universe at the time of when the bulk of the halo mass was assembled, halos in F5 are more concentrated than ΛCDM. On the other hand, F6 shows a decrease in the concentration for this mass range. Here, weaker fifth-force and stronger screening leads to an overall decrease in the concentration when compared to ΛCDM. The concentration from these $f(R)$ variants converges to ΛCDM results on large scales, which can be attributed to the self-screening of halos in these mass ranges.

Among these $f(R)$ gravity models examined, it becomes evident that the interplay between the scale-dependent enhancement in $f(R)$ gravity *w.r.t.* GR, and the density-dependent chameleon screening mechanism gives rise to a complex non-linear relation, resulting in a non-monotonic change in the MG concentration with the levels of modification to the gravity's strength.

Contrary to $f(R)$, for the case of nDGP, the concentration relation behaves monotonically with the strength of the nDGP variant and halo mass. In this gravity model, the concentration relation is lower than ΛCDM, and this decrease increases as the strength of nDGP variant increases: concentration in N1 exhibits a greater reduction when compared with N5, and this decline escalates with increasing halo mass. The velocity of particles are boosted near the halo centres, since particles experience the fifth-force and hence have enhanced velocities before they fall into the halos. As a result, after entering the halos, their higher kinetic energy makes it harder for them to settle towards the central regions, making them less concentrated *w.r.t.* ΛCDM. Greater fifth-force (N1) leads to a greater kinetic energy, and hence lower densities near the halo centres. The largest halos, which are bigger that the Vainshtein radius, are the least screened.

They experience the maximum fifth-force, and hence have the maximum decrease in the concentration.

From our results of this section, we conclude that the halo concentration encodes important non-trivial information about the modifications to the underlying gravity theory. To more accurately probe the impact of MG on this quantity, we need to resort to simulations with better resolutions in order to understand the internal profiles of halos in these MG models. This is our planned future work. The concentration relations for these MG models have also been used to model the properties of clusters [202, 203]. Also, similar to our $b(M)$ analysis, the concentration relation in MG also finds a significant application in the analytical modelling of the power spectrum, as we elaborated in Section 3.2.

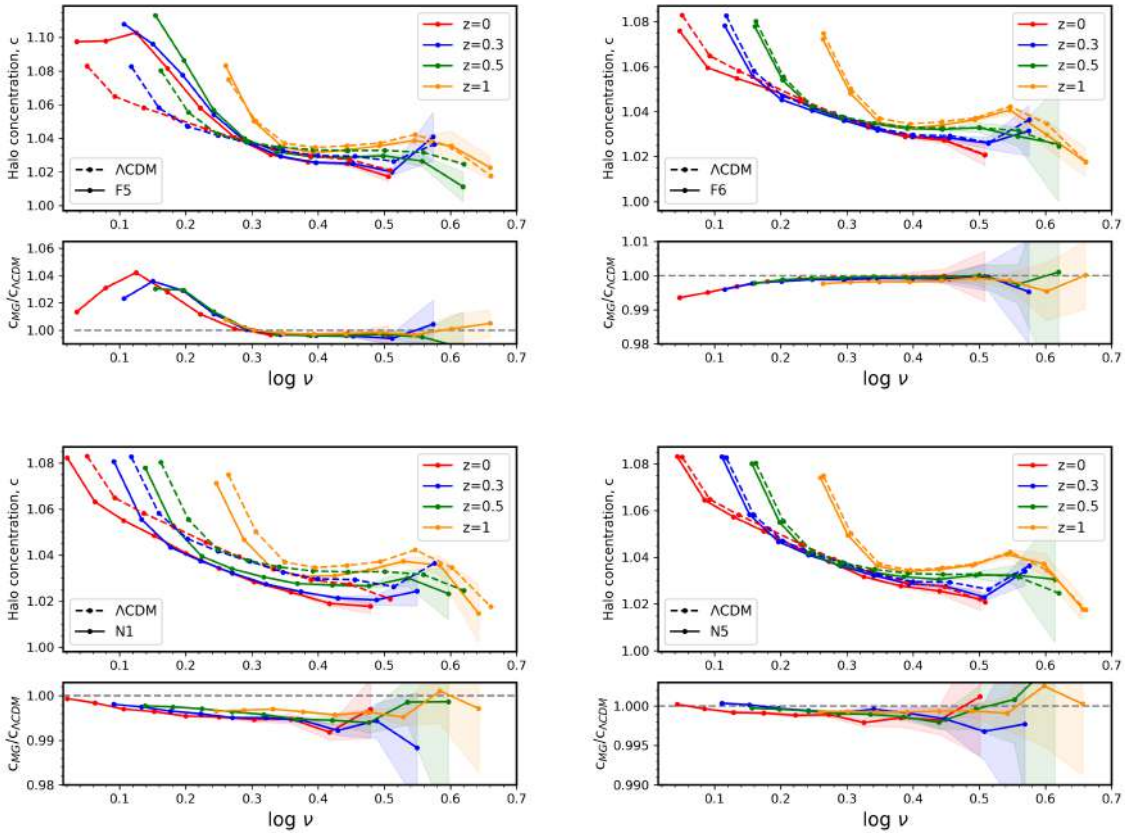

Figure 4.2: *Top panels:* Halo concentration as a function of $\log \boldsymbol{\nu}$ for MG models (solid lines) and ΛCDM (dashed lines), at $z = 0, 0.3, 0.5$ and 1. *Lower panels:* Comparison of MG concentration with ΛCDM. The top plots corresponds to the variants of $f(R)$ gravity, and the bottom panels are the results of nDGP gravity variants. Here, we obtain the concentrations from Eq. (4.6). The shaded regions correspond to errors across five realizations.

4.2.2 Halo spin

The LSS in the Universe are shaped by the large-scale tidal field, which itself is generated by the inhomogeneous distribution of matter. This gives rise to non-zero net rotation

in halos, or the *spin*. There are different ways that have been proposed in which halos acquire a non-vanishing total angular momentum. In this work, we highlight one of them, which is the Tidal Torque Theory (TTT) [132, 283]. TTT explains the origin and growth of angular momentum of haloes and galaxies in an expanding Universe. Within TTT, in the linear and weakly non-linear regimes, the spin is generated by torque induced by tidal fields associated with the surrounding LSS of the intial stages of halo formation.

The halo spin parameter is a dimensionless quantity which was introduced in [222] to quantify the difference between the amount of ordered rotation in a halo *w.r.t.* the internal random motions in a halo. In this scenario, the amplitude of a halo's angular momentum, $J = |\mathbf{J}|$ is usually expressed in terms of a dimensionless spin parameter, λ_p,

$$\lambda_p = \frac{J|E|^{1/2}}{GM_{200}^{5/2}}. \tag{4.8}$$

Here, J, E and M_{200} are total angular momentum, energy and mass of halo respectively. The λ_p parameter characterises the overall importance of angular momentum relative to random motions. Halos with low values of λ_p are dominated by velocity dispersion due to random motions, and have an overall small rotation. On the other hand, halos with higher λ_p rotate faster and show coherent orbital rotations.

In this work, we use the definition of halo spin given by Bullock et al. (2001) [53]. This expression demonstrates greater practicality as it obviates the necessity for explicit computation of energy of halo in Eq. (4.8). In this case, for a region of mass M_{200} enclosed within a region R_{200}, the spin, λ is given by

$$\lambda = \frac{J}{\sqrt{2}M_{200}V_{200}R_{200}}. \tag{4.9}$$

Here, J is the angular momentum within R_{200}. λ reduces to λ_p at the virial radius of truncated isothermal halo.

From the spherical collapse formalism (Section 1.3.2), after the initial overdensity reaches a maximum (or turn-around) radius, the overdensity decouples from the Hubble flow, collapses and virialises. Until turn-around, the angular momentum grows linearly with time as a result of torques exerted by the tidal gravitational fields from local mass distribution. After turn-around, the separation of the overdensity from the neighbouring matter increases. As a result, little or no angular momentum is expected to be tidally exchanged between the collapsed halo, and the background matter density after the turn-around [228]. This preserves the overall angular momentum from before the halo collapse. Under TTT, the total angular momentum acquired by a halo of a given mass at the turn-around is expected to scale as $L \propto M^{5/3}$ [222]. Before turn-around, more massive halos acquire more angular momentum because it takes a long time for more massive halos to reach turn-around and decouple from the Hubble expansion. On the

other hand, as long as the redshift in question is after turn-around, the spin can be expressed independent of halo mass (using virial scaling relation $V \propto (M/R)^{1/2}$) and redshift (Eq. (4.8)).

As a result, angular momentum (or spin) of a halo preserves the information about the initial large-scale matter distribution that sources the gravitational field. This is a good approximation in the linear and quasi-linear regimes. However, it is to expect that further non-linear effects of halo formation, like accretion or merger will produce deviations from the angular momentum predicted by the TTT approximation. For this purpose, spin evolution has been studied in detail using simulations, and these studies reveal that the spin parameter in halos does not show substantial trends with halo mass even in the non-linear regimes [94, 53, 41, 150].

Spin in MG models

As mentioned, halo spin is a result of non-vanishing torque generated by the gravitational field of the surrounding matter distribution in the earlier phases of halo formation. This highlights the dependence of spin on the underlying gravitational theory, and can be an independent discriminator of testing for MG signatures. Previous studies [179, 276, 168, 159, 121] have shown that this in indeed true, and spin is sensitive to modifications to the standard gravity theory, and enhances with enhancement in gravity. This is expected as a greater gravitational force would result in a greater torque, and hence in an enhanced overall spin of the halo.

In Fig. 4.3, we present the spin results for both ΛCDM and our MG models. Here, we obtained the halo spin, λ using Eq. (4.9). In the top panels, we express the λ as a function of halo mass. Solid lines are the MG results (model is highlighted in the legend), and dashed lines are the corresponding standard ΛCDM outputs. Here, we can clearly see that for the dashed ΛCDM results, λ is nearly a constant line for all redshifts, thus supporting the previous claims of weak sensitivity of halo spin to mass. Furthermore, we see that the fifth-force in both $f(R)$ and nDGP tends to speed up halos, consequently increasing the overall spin of halos.

For the case of nDGP gravity models, we observe that the mass independent trend in λ persists, with a small and a constant enhancement of λ for all redshifts, as highlighted in the bottom panels. N1 shows a 4% enhancement in λ, whereas N5 exhibits $\approx 1\%$ enhancement.

Contrary to nDGP results, $f(R)$ variants show more interesting trends. In both F5 and F6, we notice a slight dependence of λ on the halo mass, and the dependence decreases with increase in halo mass and redshift. This is a result of scale-dependent force enhancement in $f(R)$ *w.r.t.* ΛCDM, which is expected to break the TTT approximation *i.e.* we would expect tidal tensor would have different orientation at different scales, and at different stages of collapse and turn-around in $f(R)$. In the lower panels, when we compare $f(R)$ and ΛCDM results, we can clearly see a mass as well a redshift dependent

trend. The enhancement in λ is greater for smaller redshifts. In F5, this enhancement goes upto $\approx 15\%$ for $M_{200} \approx 10^{13}$ $M_\odot/h$. For F6 the maximum enhancement is $\approx 5\%$, which, again, is at the same halo mass range.

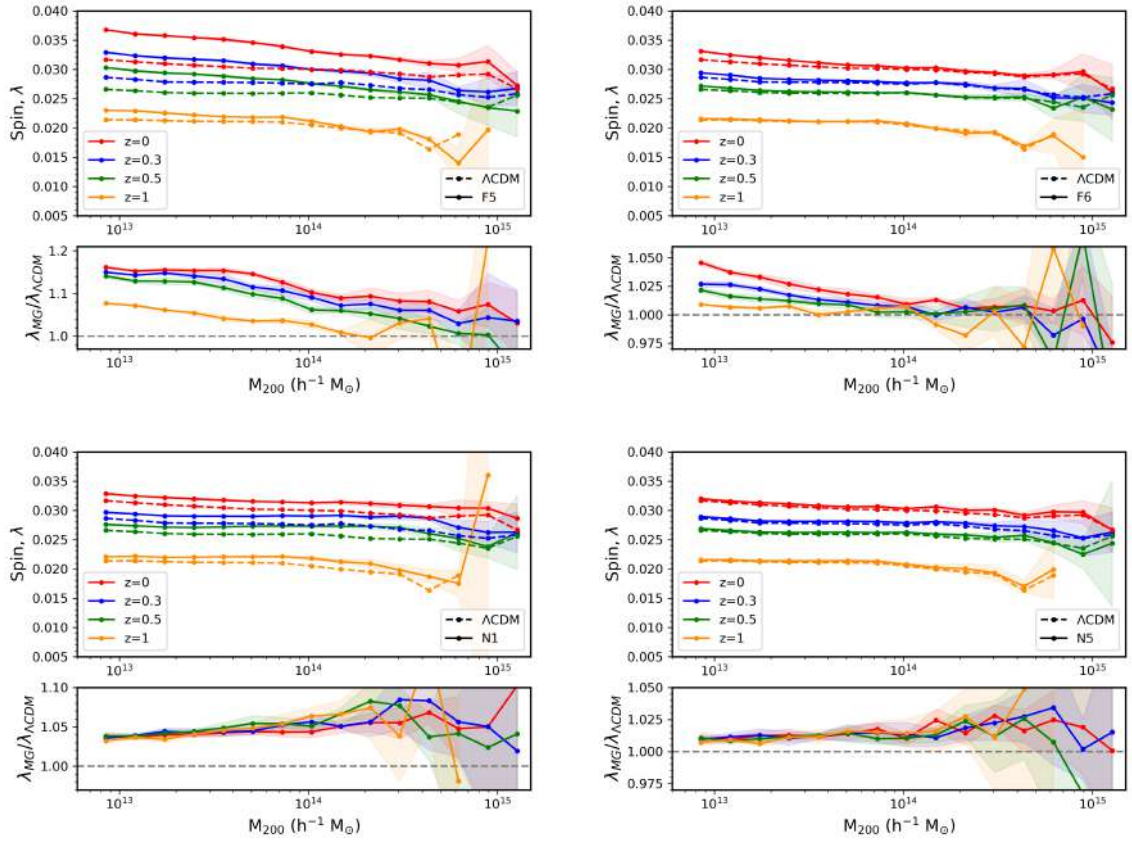

Figure 4.3: *Top panels:* Spin as a function of halo mass for MG models (solid lines) and ΛCDM (dashed lines), at $z = 0, 0.3, 0.5$ and 1. *Lower panels:* Comparison of MG spin with ΛCDM. The top plots corresponds to the variants of $f(R)$ gravity, and the bottom panels are the results of nDGP gravity variants. Here, we obtain the halo spin relation from Eq. (4.9). The shaded regions correspond to errors across five realizations.

4.3 Halo Assembly Bias:

As highlighted in the introduction of this chapter, Halo Assembly bias (or HAB) refers to the difference in the clustering of halos with same mass, but other properties. In this work, we further test whether the HAB in MG models is different *w.r.t.* ΛCDM. In Section 4.1, we looked at the general trends and properties of the $b(\nu)$ relation in MG models to signal-out and quantify any deviations from the ΛCDM case. It is important to understand all possible differences between these models already at the level of the standard $b(\nu)$-log ν relation, since these differences can easily propagate, and manifest later in the HAB analysis.

For the purpose of this work, we study HAB by considering the above described secondary halo properties: *halo concentration*, and *halo spin*. Both these halo attributes

are well-known to have a considerable, and distinct trend in the HAB [105, 279, 71, 160, 293]. Using these, we divide our halo population and study clustering differently in each of the halo sub-samples. For each ν-bin, we choose 20% of halos with the highest value of concentration (TOP20C), and halo spin (TOP20S). Similarly, we select 20% of halos with the lowest value of concentration (BOTTOM20C) and halo spin (BOTTOM20S). In the next sub-sections, we discuss the impact on the $b(\nu)$-log ν relation by categorising the halo populations into these distinct subgroups.

4.3.1 Halo Assembly bias from halo concentration

As previously mentioned, for each halo mass bin and redshift, we distinctly analyse two subsets obtained from halo concentration: TOP20C and BOTTOM20C. We compute the bias for each halo sub-sample across the redshift range from $z = 0$ to $z = 1$. These bias values are, in turn, binned to a specific log ν interval. The resulting binned bias data points are plotted in Fig. 4.4. Here, the errors are computed by propagating the errors independently from each redshift. We do this analysis for all the MG variants (points with error bars), and the ΛCDM (dashed lines with shaded regions). The magenta corresponds to the TOP20C, and the green to the BOTTOM20C.

The results of our exercise clearly illustrate that the $b(\nu)$-log ν relation depends on a secondary halo property of the halo concentration. For the ΛCDM scenario, we obtain trends that are in a qualitative agreement with the well established results in the literature (for *e.g.* [104, 279, 71]). We show that this pattern holds true for our MG models as well. Namely, TOP20C have the largest bias at low mass ends, and BOTTOM20C have the largest bias at high mass ends, with a crossing of the trend at a given scale, which we refer to here as log $\nu_{\rm cross}$. Low concentrated halos are more significant in the lower ranges of $\nu(M,z)$. This results in the rareness, and hence in enhanced bias of these halo samples at the high-ν ends. On the contrary, the high concentrated halos have a greater contribution to the higher $\nu(M,z)$ values, thereby making them less biased at the high-ν ends, and consequently more biased at the lower values of ν.

However, a notable distinction emerges for the case of strong variant of $f(R)$: F5. The scale-dependent enhancement in $f(R)$ leads to a non-linear impact on the concentration parameter in small and intermediate halo mass ranges [254, 202, 20]. Also, the self-screening in $f(R)$ conceals the impact of the fifth-force in large-mass halos. And since the MG effect is cumulative over time, the lower-ν scales experience the maximum impact of $f(R)$. Therefore, we see a difference in both the F5 and ΛCDM halo sub-samples at the lower values of ν. Meanwhile, for the case of weaker F6 model and both the nDGP variants, this distinction with ΛCDM values is not evident.

Now, we want to more directly quantify and compare the bias difference between TOP20C and BOTTOM20C samples. To facilitate this, we plot, for all models, the ratios of bias from these sub-samples *w.r.t.* their respective full halo sample bias in

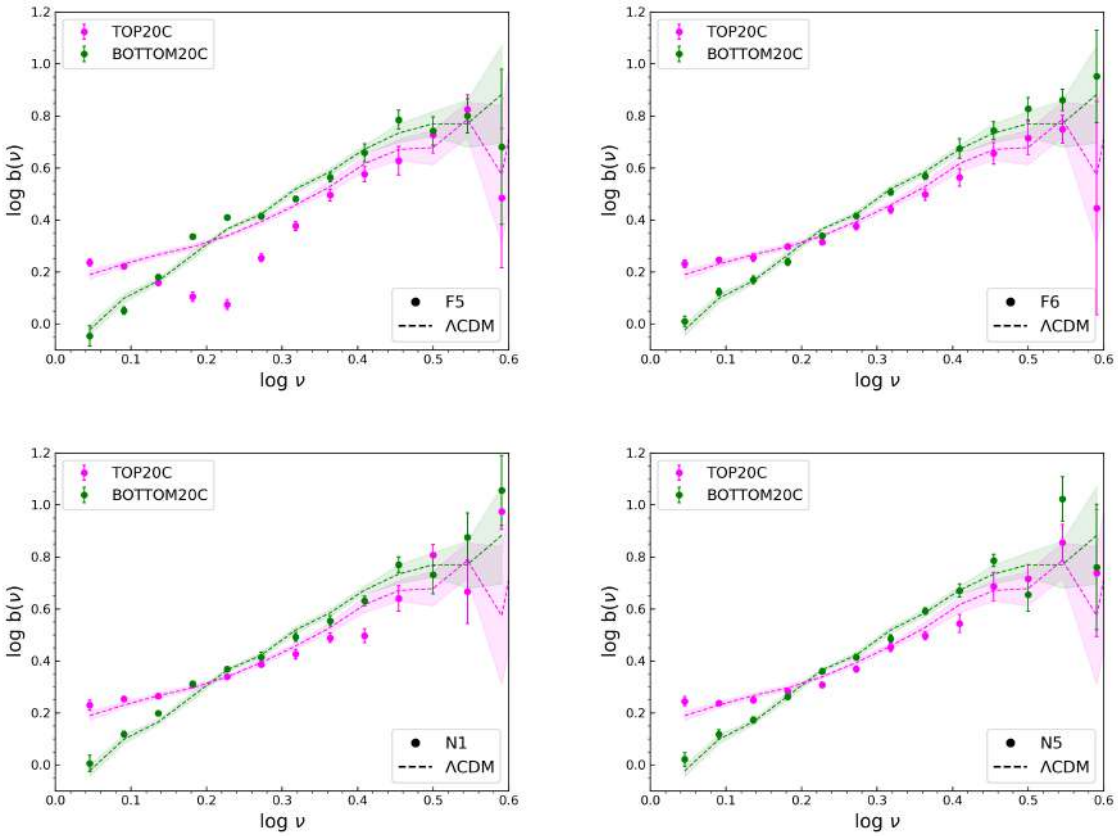

Figure 4.4: Linear halo bias relation, $b(\nu)$-log ν, for all the MG gravity models (points with error bars), and ΛCDM (dashed lines with shaded regions). These bias values are binned across a common log ν interval, from $z = 0$ to $z = 1$. Magenta lines represent TOP20C (20% halos with the highest halo concentration in each ν-bin), and green lines correspond to the BOTTOM20C (20% halos with the lowest halo concentration in each ν-bin). The errors in these plots are computed by propagating the errors obtained on individual bias values at each redshift.

Fig. 4.5. In this figure, magenta lines correspond to the ratio for TOP20C, and green to the ratio from BOTTOM20C. Here, every block corresponds to a specific gravity model, as indicated in the legends.

The HAB reaches a maximum of 25% on the small ν scales. Furthermore, $b(\nu)$ in both the TOP20C and BOTTOM20C samples deviates from the overall bias amplitude similarly across all the gravity models. At low fluctuation mass scales, TOP20C halos are more biased. Above the mass scale given by log $\nu_{\rm cross}$, the BOTTOM20C samples exhibit greater bias values. As highlighted previously, the only distinct signature from ΛCDM in seen in the stronger scale-dependent $f(R)$ variant, F5.

Also, we notice that the value of log $\nu_{\rm cross}$ in each MG model is different. Different gravity models would correspond to a different $\nu(M,z)$ relation (Fig. 1.3). As we can see in Fig. 4.5, F5 experiences the inversion of clustering at the lowest value of log $\nu_{\rm cross}$. In contrast, rest of the models exhibit minor deviations of log $\nu_{\rm cross}$, when compared to the ΛCDM reference.

From Fig. 4.4 and Fig. 4.5, we find that the HAB in all our models, except F5,

appears to follow the scales and amplitudes common to the ΛCDM case. Thus, the effect of change in bias across halo sub-samples seems to be unaffected by the extra physics of MG. The F5 here is only notable exception. For this model, the HAB phenomenon appears to be actually slightly enhanced, when compared to the vanilla ΛCDM case. This disparity in the HAB amplitude for the F5 model *w.r.t.* ΛCDM needs further exploration, particularly with high-resolution MG simulations, since this discrepancy is prominent at the lower values of ν. Investigation of this result with higher resolved simulations will help us to conclusively determine whether this difference is of a physical nature, or simply a numerical artefact.

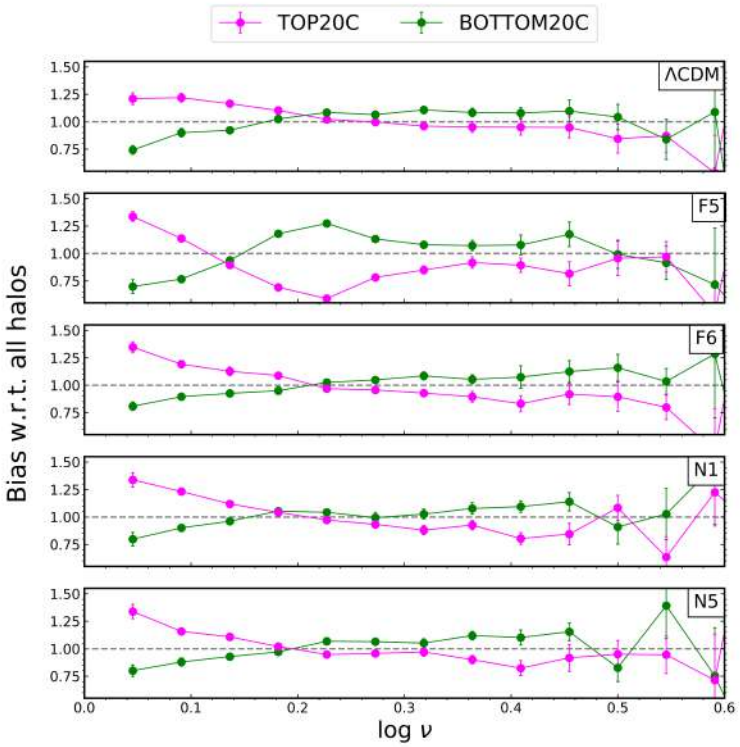

Figure 4.5: Comparison of halo bias from TOP20C (magenta) and BOTTOM20C (green) sub-samples *w.r.t.* the bias obtained from the entire halo sample. Each block represents a specific gravity model, as indicated in the legend. The errors in these plots are computed by propagating the errors obtained on individual bias values at each redshift.

4.3.2 Halo Assembly Bias from halo spin

In this section, we explore the impact of halo spin on the HAB effect. This halo property also serves as an additional tool, particularly to analyse the F5 discrepancy *w.r.t.* ΛCDM. The spin, based on the total halo angular momentum is an integral halo property, in contrast to the halo concentration, which is by definition based on a differential over halo radius. We use the Bullock spin relation, that we described in Eq. (4.9).

Here, we performed analysis similar to the previous section *i.e.* we binned the bias values obtained from $z = 0$ to $z = 1$ in a given log ν interval for the TOP20S and BOTTOM20S. The results of this computation for all the models are shown in Fig. 4.6. Within this figure, the points with error bars represent the bias measured from the MG cases. To foster direct comparison, the ΛCDM fiducial case are plotted as dashed lines with shaded regions. The bias for TOP20S are plotted in magenta, whereas the green markers represent BOTTOM20S.

Trends obtained in these plots, like the results from the previous section, clearly illustrate that the $b(\nu)$-log ν relation depends on the auxiliary property of halo spin. Similar trends have also been reported in [160, 42, 239, 71]. Both the TOP20S and BOTTOM20S samples show distinct bias trends. We note that TOP20S are more strongly clustered than BOTTOM20S across the entire ν range. Halos evolving in denser and more clustered environments are more likely to experience stronger tidal forces. This would result in that population of halos having a greater spin compared to the halos evolving in less dense and less clustered environments. Similar results have also been reported in [160, 42, 239, 71]. In contrast to the concentration plots (Figs. 4.4 and 4.5), which clearly have a crossover in bias between TOP20C and BOTTOM20C, we now notice a nearly consistent bias offset between the TOP20S and BOTTOM20S samples.

The main point to note in all the plots of Fig. 4.6 is that the amplitude of difference in the bias trend across these halo sub-samples again does not seem to be dependent on the gravity model under consideration, and the HAB effect remains predominantly consistent between MG and ΛCDM. Unlike the previous anomaly in F5, our inference for this case holds in both the scale-dependent (*i.e.* $f(R)$), as well as the scale-independent (*i.e.* nDGP) MG variants.

Similar to Fig. 4.5, we plot the ratio of b(ν) for TOP20S (magenta) and BOTTOM20S (green) samples to the b(ν) obtained from the overall halo sample in Fig. 4.7. Here, every block corresponds to the gravity model indicated in the legend. This plot clearly shows that the amplitude of $b(\nu)$ in both the sub-samples deviates from the overall bias amplitude by a similar amount across all the considered gravity models. For the case of concentration, it was evident that the impact of HAB is noticeable only within a limited range of ν values, and with a varying amplitude. In contrast, when we use the spin as a secondary property, a significant HAB effect becomes apparent and remains consistent across the entire range of ν.

Our findings with using halo spin provide additional support to our claims from the previous section, reinforcing the idea that the HAB amplitude remains largely unaffected in these alternative MG scenarios, when compared to the standard ΛCDM results.

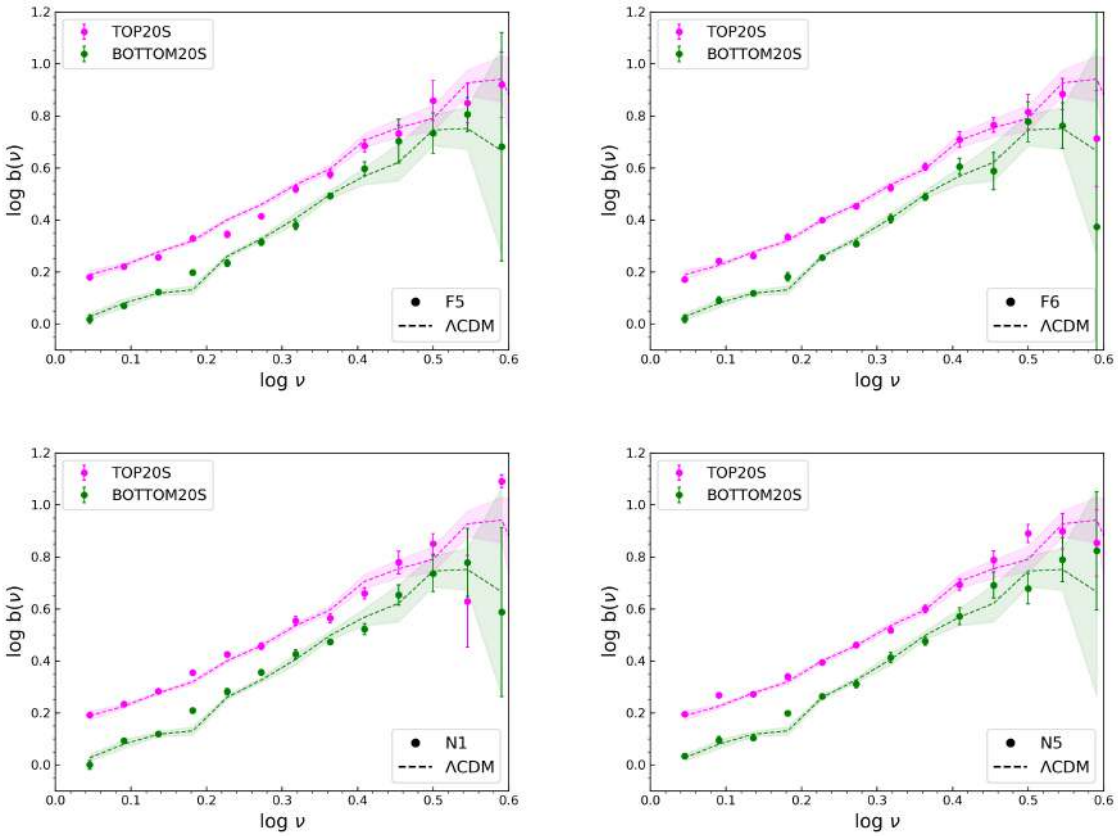

Figure 4.6: Linear halo bias relation, $b(\nu)$-log ν, for all the MG gravity models (points with error bars), and ΛCDM (dashed lines with shaded regions). These bias values are binned across a common log ν interval, from $z = 0$ to $z = 1$. Magenta lines represent TOP20S (20% halos with the highest halo spin in each ν-bin), and green lines correspond to the BOTTOM20S (20% halos with the lowest halo spin in each ν-bin). The errors in these plots are computed by propagating the errors obtained on individual bias values at each redshift.

4.4 Summary and Discussion

In this work, we test whether the Halo Assembly Bias (HAB) differs in the MG scenarios, compared to what is measured for the case of standard ΛCDM.

In Section 4.1, we individually study the halo bias in MG models, and how the signal differs with ΛCDM. We observe that the universality of the halo bias relation, which has been shown for ΛCDM in [251, 268, 226], is preserved also in our MG variants. Furthermore, these MG models foster enhanced late-time large-scale clustering, consequently reducing the halo bias when compared to the ΛCDM case. For the case of stronger MG variants (like F5 and N1), the bias can deviate from the predictions of the standard ΛCDM model by as much as 10%. Conversely, for the milder MG variants, the observed distinctions remain confined within 5% margin across the various length and time scales examined in this work.

We then study the intrinsic halo properties that we use to quantify the HAB effect. For this, we choose *halo concentration* and *halo spin*. We first study the impact of MG

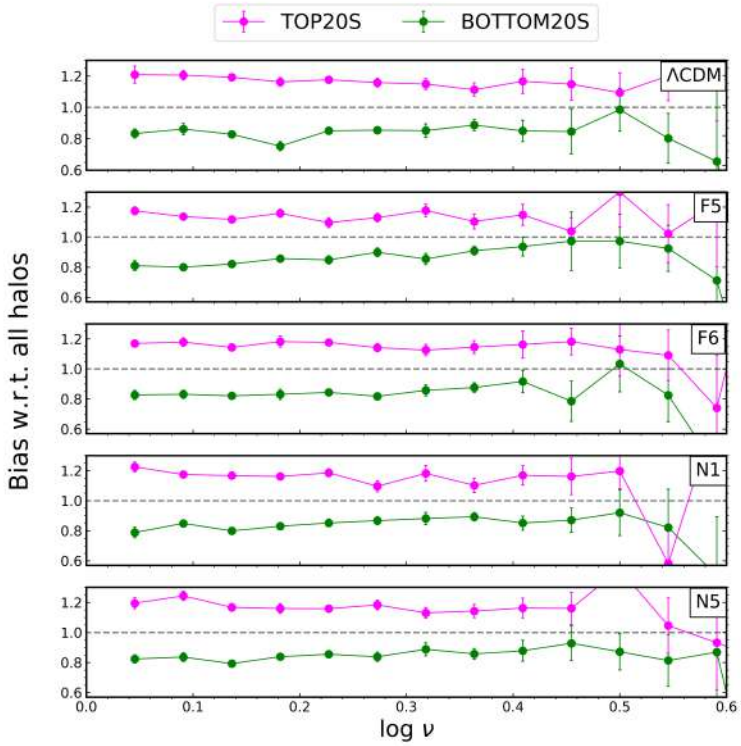

Figure 4.7: Comparison of halo bias from TOP20S (magenta) and BOTTOM20S (green) sub-samples *w.r.t.* the bias obtained from the entire halo sample. Each block represents a specific gravity model, as indicated in the legend. The errors in these plots are computed by propagating the errors obtained on individual bias values at each redshift.

on these properties, and how they differ from ΛCDM across halo mass ranges.

Here, we define the halo concentration using the velocity-ratio parameter (Eq. (4.6)). Using this estimator, we plot the concentration trend in the MG models across redshifts in Fig. 4.2. All models, except F5, follow the trend similar to ΛCDM, with a difference in the amplitude. F5 has a peak-like enhancement *w.r.t.* ΛCDM at log ν between $0.04 - 0.2$. On the contrary, the concentration in F6 decreases for these mass scales. For both the $f(R)$ variants, the concentration converges to the ΛCDM results at large mass scales. This can be attributed to the self-screening of halos at these large masses. On the contrary, both these models have different MG signatures at small mass scales, which can be attributed to the non-linear interplay between the scale-dependent fifth-force and the density-dependent chameleon screening mechanism. For the case of the nDGP variants, we see a monotonic decrease of the halo concentration with both the halo mass and the fifth-force. Stronger N1 variant has a larger decrease compared to the weaker N5 model.

Moving to the halo spin, we observed that for ΛCDM, the spin is nearly mass-independent, as has been reported in previous works [94, 53, 41, 150]. The analysis of the MG models with the halo spin reveals that the fifth-force speeds up the halos, and result in greater spin in these MG scenarios compared to ΛCDM. The enhancement in

both models though is phenomenologically different. $f(R)$ variants show the both mass and time-dependent enhancement in the spin, whereas nDGP variants show redshift independent, though a weakly mass-dependent spin enhancement. Moreover, the spin enhancement in the stronger F5 model reaches upto $\approx 15\%$ for $M \approx 10^{13}$ $M_{\odot}/h$, whereas enhancement in N1 lies between $5-10\%$ across the entire halo mass range studied here. nDGP models also follow the mass-independent trend of spin, whereas $f(R)$ induces mass-dependence.

We then focus on HAB by selecting haloes according to the above described halo properties of *concentration* and *spin*. This choice is driven by the distinct HAB effect that results from choosing halos according to these two properties [105, 279, 71, 160, 293].

In Figs. 4.4 and 4.6, we again plot the halo bias relation, but of the concentration and spin selected halo sub-samples: TOP20C/S and BOTTOM20C/S. In these plots, we can clearly distinguish the bias signal for the different halo populations. Previous works have reported these trend already for ΛCDM [279, 105, 160, 42]. Our analyses with MG models yield analogous trends to ΛCDM, except for F5 in Fig. 4.4, which shows a greater departure from ΛCDM at small log ν scales between 0.05 and 0.35.

To analyse these results quantitatively, we plot Figs. 4.5 and 4.7 to foster a direct comparison between the bias from these halo sub-samples, with the bias obtained for the entire halo sample. For the case of TOP20C and BOTTOM20C (Fig. 4.5), the HAB for all models goes maximum of $\approx 25\%$ at only the lower values of log ν, and encounters an inversion of the trend at a particular fluctuation scale, given here by log $\nu_{\rm cross}$. This crossover scale shows a mild dependence on the gravity model under consideration. Also, similar to Fig. 4.4, only F5 exhibits the most distinct trend, whereas the ratio in other gravity models is similar to ΛCDM. Contrary to these results, we see a constant enhancement/decrement in the bias of TOP20S/BOTTOM20S bias *w.r.t.* the entire halo sample (Fig. 4.7). We also note that for this case, all gravity models show the HAB amplitude of $\approx 20\%$ across the entire ν range, which is more significant than the previous scenario. Also, all panels here (including F5) show the similar impact of HAB, regardless of the underlying gravity variant. From these plots, we infer that the HAB in these MG models is also not impacted by the additional fifth-force interactions, and produces the similar amplitude as for the case of ΛCDM.

Accurate modelling of the clustering properties of LSS have the potential to test the theories of gravity and galaxy formation. Many halo-scaling relations have been constructed for this purpose, which connect clustering of halos to galaxies, and are primary inputs for galaxy clustering models. Some examples include halo occupation distribution (HOD) [220, 73], conditional luminosity function (CLF) [289], subhalo abundance matching (SHAM) [272] etc. Despite different functionalities, most of these approaches rely on the basic parameterization which is based solely on halo mass. However, HAB studies have shown that other halo properties (like we demonstrated for concentration

and spin) are also correlated with clustering. Within a specific mass range, certain types of galaxies may preferentially inhabit different types of halos. Large-scale galaxy clustering depends strongly on halo clustering, background cosmology and underlying gravitational physics. Thus, HAB is an extra systematical effect related to modelling the LSS clustering, and hence has important implications for using galaxy clustering as a probe of cosmology, and for interpreting observations from large-scale cosmological surveys [163, 182, 80, 3]. As a result, HAB studies have attained significant attention over the past couple of years for developing better formalisms to study galaxy-halo connections, and for building more realistic mock catalogs [117, 62, 169, 70, 69, 72, 221]. In this work, we investigate whether exploring the additional degrees of freedom in beyond-GR scenarios could lead to differences in the HAB amplitude, when compared with the results from the standard ΛCDM scenarios. This is an essential study as MG effects on HAB could source potential systematics in the studies of large-scale galaxy clustering, and further bias our inferences.

Our analysis showed that the HAB trend in MG models is comparable to the case of ΛCDM scenario. Furthermore, we observed that the amplitude of HAB is not impacted by the gravity model, as our MG results do not show departure from the ΛCDM HAB amplitude. The only gravity model that induces a slight difference with ΛCDM is the strong variant of $f(R)$ gravity model (F5) when we use the halo concentration as the selection criteria. On the contrary, our analysis of using halo spin does not show HAB differences in any MG variant with ΛCDM. From our results, we can infer that since HAB is insensitive to MG physics, it is reasonable to rely on the already existing ΛCDM based halo-scaling relations to be further extrapolated to these MG scenarios. This is advantageous as it is easier to run the standard formalisms on the existing MG simulations, than constructing separate MG galaxy-halo scaling relations as they would need to incorporate wide range of phenomenological MG parameters. In MG HOD, modeling secondary halo properties and the environmental effects lead to further complications [119, 254, 276], and would require extensive calibrations using MG simulations.

We would like to caution the readers that our results do not imply that having an incorrect theory of LSS formation scenarios when constraining HAB will not affect the analysis, because the overall halo clustering depends on the underlying gravity theory. We emphasised on this point in Section 4.1. Also, when propagated in the context of galaxies, galaxy assembly bias depends both on HAB, and on the galaxy formation model, where latter is strongly impacted by the underlying gravity theory [19, 216, 203]. As a result, even in the case when the HAB effect is identical, discrepancies between ΛCDM and MG in the context of galaxy assembly bias could arise. This would in-turn affect the results from the studies of large-scale clustering in galaxies, and lead to incorrect cosmological parameter estimations. Thus, stringent tests of the theory of gravity on the cosmological scales are necessary in order to coherently understand the

underlying physics that determines the evolution and clustering of the LSS across scales and epochs.

Chapter 5: Modified Gravity in the Cosmic Web

We especially need imagination in science. It is not all mathematics, nor all logic, but it is somewhat beauty and poetry.

-Maria Mitchell

Chapter 5

Modified Gravity in the Cosmic Web

5.1 Motivation

Beyond the linear growth of density perturbations, complex patterns and structures emerge in the DM density fields at large scales. We can clearly see this intricate pattern in the density plots from our ELEPHANT simulations in fig. 1.4, as well as in Fig. 5.1 generated from MILLENNIUM SIMULATIONS [261]. In the density plots from both these simulations, we have the illustrations of large-scale density field at tens of Mpc. The LSS on these scales is manifested in the form of web-like structures, called the *Cosmic Web* (CW) [45]. This web-like geometry consists of dense nodes connecting highly filamentary structures and flattened sheets, which surrounds large under-densities/voids.

It has been shown, both analytically and via cosmological simulations, that the existence of the CW is a consequence of the anisotropic collapse of the overdensity, which is due to gravitational instability [291, 223, 46, 43, 273, 261, 218]. Under the effect of gravity, these structures evolve and cluster from tiny density and velocity perturbations in the early Universe, resulting in the formation of elongated, or flattened structures. Hence, it is expected that any modifications to the gravity theory and, consequently, to the underlying cosmological model would significantly influence the evolution of the CW environment, and the associated statistical properties [35, 9, 158].

The CW structure serves as a natural environment for the DM halos, and in-turn galaxies, to form and evolve. The dependence of DM halo properties on CW environment has been widely studied in the literature. Many works have shown systematic dependencies of the large-scale properties on the environment that hosts them [113, 59, 13, 167, 201, 12, 101, 102, 103, 101, 102, 103, 194, 288, 47, 48, 126, 188]. While substantial efforts are being made to link the properties of the CW elements to the LSS they host, there is currently a limited understanding about the information these environments carry about the underlying cosmological model. Moreover, there have been limited studies that consider the role of MG in the context of CW environments. The influence of $f(R)$ gravity on halo characteristics in various CW environments has

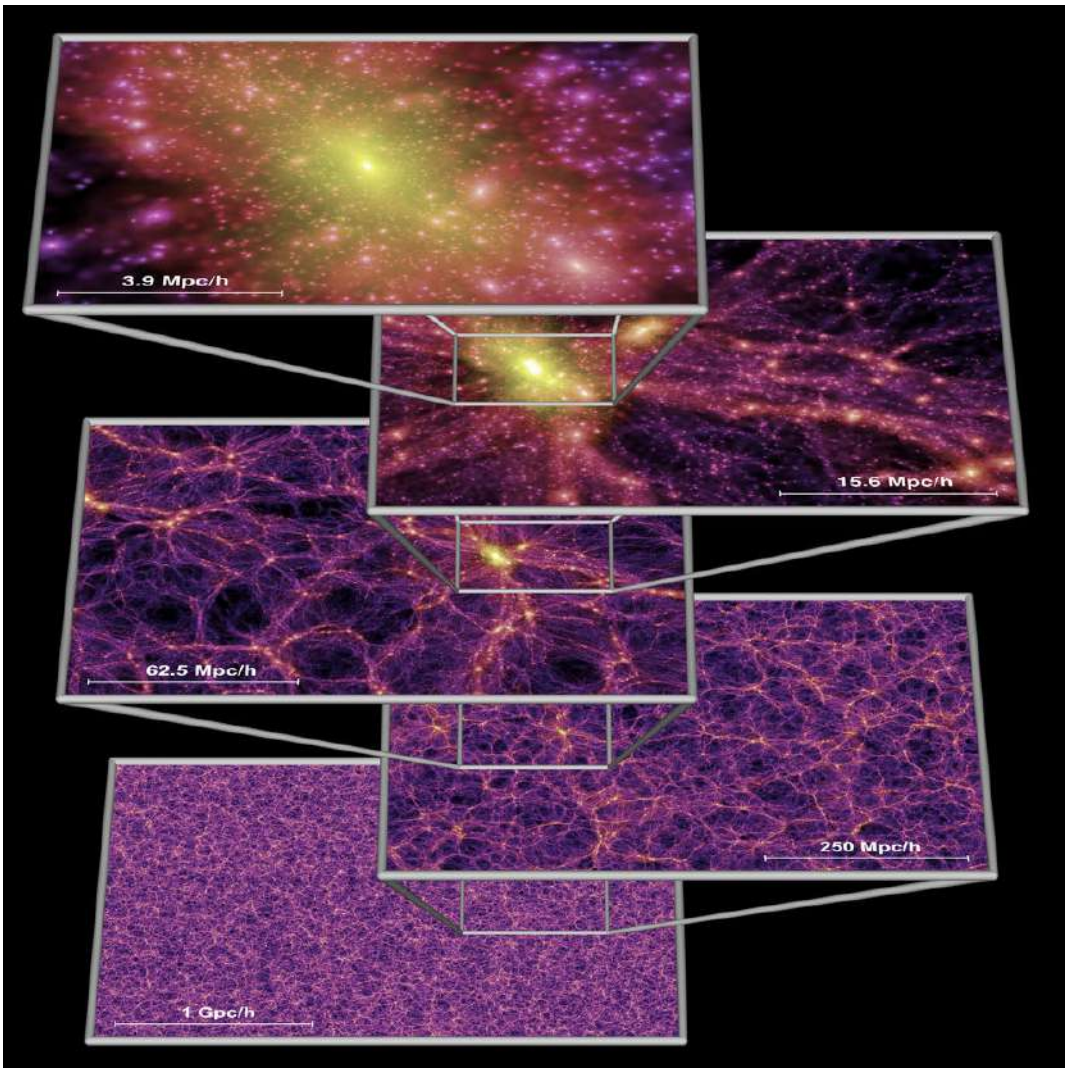

Figure 5.1: Projection of Dark matter density field from Millennium simulations [261]. Beyond tens of Mpc, we can see the density field manifests in the form of web-like structures, called the Cosmic Web. Here, each slice is with a thickness of 15 Mpc/h, representing different cosmic length scales.

been examined in a study by [276], while the effect of $f(R)$ gravity on filamentary structures within the CW is explored in [255]. Moreover, in [87], the authors explore how distinct DM models impact both DM density and halo attributes across diverse CW environments.

Examining the influence of MG on the large-scale properties within varied CW environments is significant for several reasons: *Firstly,* CW is broadly classified on the basis of the density and velocity fields [100, 131, 58], and they are sensitive to modifications to the underlying gravitational forces ([110, 123] and the references within). Consequently, we can expect that the statistics pertaining the LSS would delve more information when studied separately for each CW environment. These studies could break degeneracies, and improve the constraints on the cosmological parameters through the analysis of the cosmological information regarding the matter distribution in different cosmological environments [47, 48, 215]. *Secondly,* CW marks a transition of the density field from a primordial Gaussian random field, to highly non-linear density field that collapses to form cosmic structures, like halos. This shows the significant influence of these intermediate scales where we do not have enough constraints on the theory of gravity. And, it is on these intermediate scales where CW largely manifests. As a result, CW studies in MG theories further provide a potential tool to test alternate structure formation scenarios to GR, and in-turn to constrain gravity. And, *thirdly*, screening is more effective in low-densities, making voids as perfect test-beds to test for MG signatures [60, 214, 264]. And *lastly*, studying the DM and halo properties in different CW environments can help draw a boundary between the halo properties that are both affected, and not affected by screening. Also, considering each environment separately could help us to individually examine the LSS results in both the screened and unscreened regions, rather than averaging the effects over all the environments. This will further help us elucidate the screening physics from the impact of the fifth-force.

Motivated by the factors mentioned above, this chapter delves into the impact of modifications to the underlying gravity model on various LSS properties in different CW environments. The differences in densities, tidal forces, and anisotropies inherent to each CW environment, coupled with the influence of the fifth-force and the screening mechanisms, predominantly contribute to these distinctions. We first describe our CW classification in Section 5.2, then we quantify the MG impact on DM density fields and the associated statistics across CW environments (Section 5.3), and then we study how differently halo properties in each CW environment are impacted by the MG dynamics (Section 5.4).

5.2 T-WEB classification of the Cosmic Web

A variety of different methods have been devised to classify the CW (e.g. [100, 18, 131, 58]). These classifications are based on the morphological or the local geometric

information of the density, tidal or velocity shear fields. The basis of quantifying the LSS using fields can be traced to the seminal work of Zel'dovich (Zel'dovich Approximation (ZA), defined in Section 1.3.2). ZA played a key role in developing a view of the structure formation in which, after the collapse along one axis the density forms *pancakes (or walls/sheets)*, second axis collapse leads to the formation of *filaments*, and third axis collapse forms the *nodes (or knots)*. In the pioneering work of [45], the authors further showed that the formation and the dynamical evolution of the CW is indeed a result of the tidal force fields. Building on these works, the authors in [113] developed an elaborate classification scheme, which is based on the signature of the tidal tensor, hence called as the T-WEB CW classification.

T-WEB works on density field grids and uses the Hessian of the Gravitational potential to determine the CW environment. The Hessian is given as

$$T_{\alpha\beta}(\vec{x},t) = \frac{\partial^2 \phi(\vec{x},t)}{\partial x_\alpha \partial x_\beta}. \tag{5.1}$$

Here, the physical gravitational potential has been normalised by $4\pi G\bar{\rho}$ so that $\phi(\vec{x},t)$ satisfies the Poisson equation $\nabla^2\phi(\vec{x},t) = \delta(\vec{x},t)$, where $\delta(\vec{x},t)$ is the dimensionless matter overdensity, G is the gravitational constant, and $\bar{\rho}$ is the average density of the Universe.

This tidal tensor can be represented by a real symmetric 3×3 matrix with eigenvalues $\lambda_1 > \lambda_2 > \lambda_3$. T-WEB method introduces a threshold λ_{th} to gauge the strength of the eigenvalues of the tidal shear tensor. The number of eigenvalues larger than the threshold is used to classify the CW into four kinds of environments: **Knots** (3 eigenvalues larger than λ_{th}), **Filaments** (2), **Sheets** (1) and **Voids** (0).

Our simulation input is the DM density fields interpolated over the particle data for 256^3 voxels. We use T-WEB to distinguish the DM density field into the four CW environments. Each voxel has a size of 4 Mpc/h. The Poisson equation is solved in Fourier space to obtain the potential over each grid cell, and the shear tensor is computed to obtain and store the corresponding eigenvalues. In the T-WEB approach, λ_{th} is an arbitrary quantity, which is usually considered of order unity. In our work, we set $\lambda_{th} = 0.2$ as suggested by previous studies that aim to capture the visual impression of the CW [100, 176]. Here, we resort to the same threshold even to define the CW elements in our MG models in order to maintain consistency for comparative analysis with the standard ΛCDM baseline.

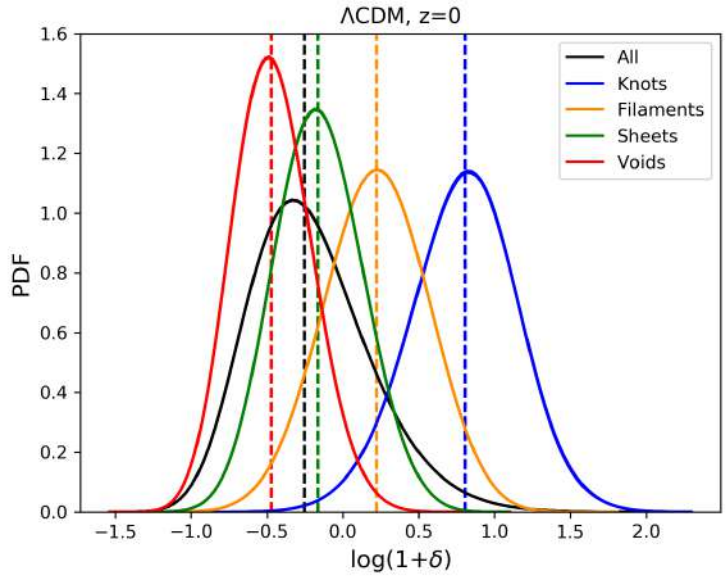

Figure 5.2: Normalised overdensity distribution for ΛCDM at $z = 0$, across CW elements. The solid black line represents the distribution for the overall density, and other colours correspond to different CW environments, as indicated in the legends. The vertical dashed lines of the same colours are the median of the overdensities in each environment.

5.3 Impact of Modified Gravity on Dark matter density fields in different Cosmic Web environments

5.3.1 PDF of density fields

The relationship between the CW and the density field can be quantified by studying the probability distribution function (PDF) of the density field ($\log(1+\delta)$) for each grid cell as a function of the CW environment. We plot this distribution in Fig. 5.2. In this figure, we have the normalised overdensity distribution for ΛCDM, at $z = 0$. The shape of this density distribution looks indistinguishable in all other gravity models. We can clearly see that the PDF systematically shifts towards lower densities as we go from knots to filaments, than to sheets, and to voids. The black line, which represents the overall density, peaks between voids and sheets.

In Fig. 5.3, we individually plot the PDF of each CW element across all the gravity models. Similar to the previous plot, the dashed vertical lines represent the median of the distribution in each gravity model, with the inset axes in each plot to clearly see the difference in the median values across the gravity models. To further study the quantitative differences in these distribution, we compute the moments of distribution in the density fields, which are described in the next sub-sections.

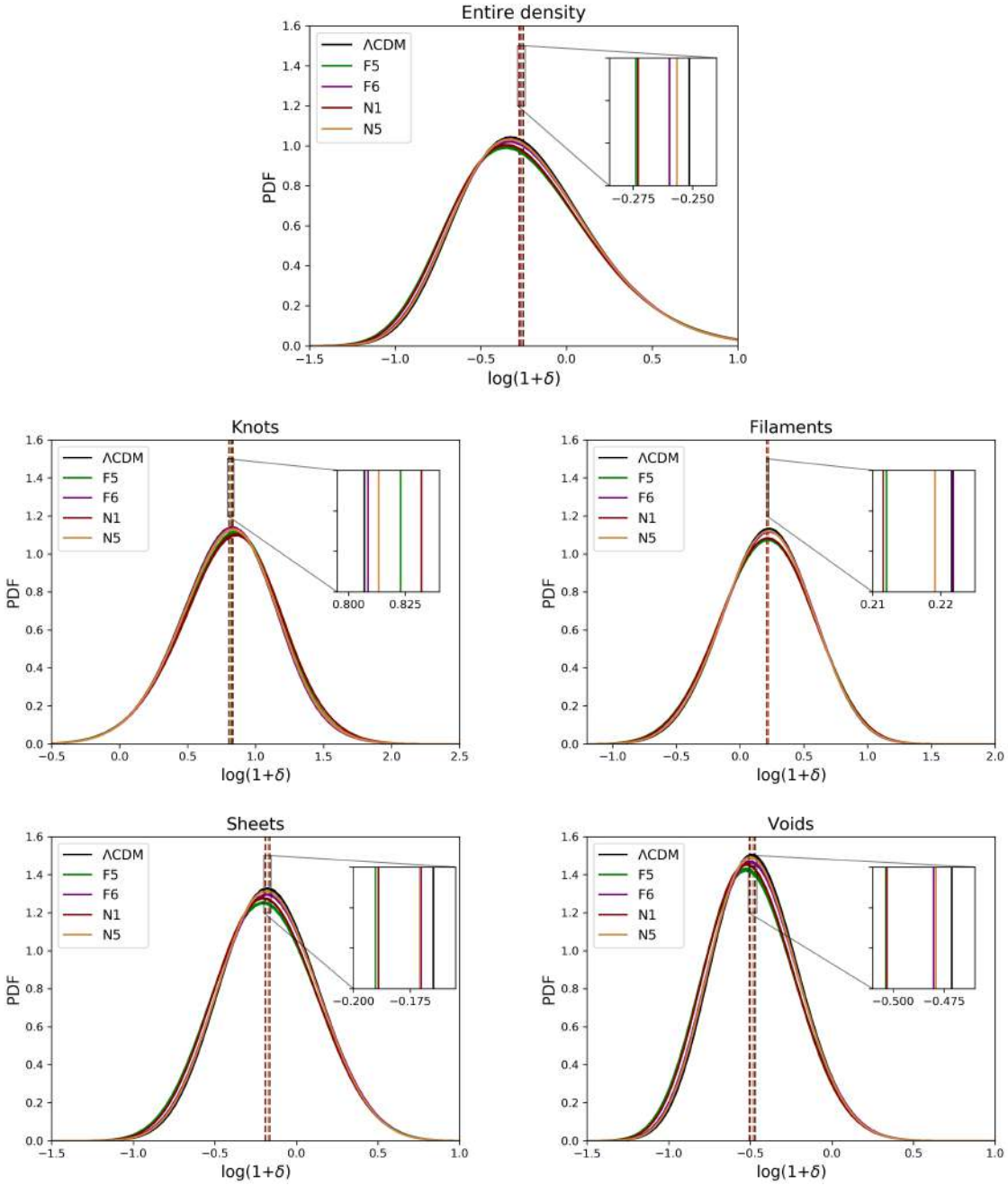

Figure 5.3: Normalised overdensity distribution for each CW environment in different gravity models at $z = 0$. The vertical dashed lines of the same colours are the median of the overdensities for each model. The inset axes in each plot shows differences in the median values for the density distribution in each environment and the gravity model.

5.3.2 Hierarchical clustering in Modified Gravity models

Gaussian random field is symmetrical around the mean density, and positive and negative deviations from the mean density are equally probable. On the other hand, as the density field evolves, it becomes non-linear and highly asymmetric: positive density departures from the mean density can be very strong, while the negative deviations are restricted by the condition that the density cannot be negative, and hence the density contrast, $\delta \geq -1$. This non-linear gravitational evolution yields a non-Gaussian distribution of the density at later times. Therefore, studies of the two-point statistics ($\xi(r)$ or $P(k)$) are no longer enough to fully characterise the density PDF, and higher order moments become non-zero and significant [39, 91].

The central moments, $\langle \delta^i \rangle_R$ of density distribution are given as

$$\langle \delta^i \rangle_R = \frac{1}{N} \sum_{n=1}^{N} (\delta - \langle \delta \rangle)^i_R. \tag{5.2}$$

Here, δ corresponds to the density contrast, and R is the smoothing scale.

In the context of large-scale studies, we operate with the connected moments of the density distribution *i.e.* we subtract the Gaussian expectations from the central moments. For the first four moments [38]

$$\begin{aligned} \langle \delta \rangle_c &= 0 (\text{mean}), \\ \langle \delta^2 \rangle_c &= \langle \delta^2 \rangle \equiv \sigma^2 (\text{variance}), \\ \langle \delta^3 \rangle_c &= \langle \delta^3 \rangle \equiv \mu_3 (\text{skewness}), \\ \langle \delta^4 \rangle_c &= \langle \delta^4 \rangle - 3 \langle \delta^2 \rangle_c^2 \equiv \mu_4 (\text{kurtosis}). \end{aligned} \tag{5.3}$$

In a Gaussian random field, all the connected moments are zero, except the variance. The first two non-vanishing cumulants after variance measure particular shape departures from a Gaussian distribution. Namely, skewness quantifies the asymmetry of the distribution, and the kurtosis characterizes the flattening of the tails of the distribution *w.r.t.* a Gaussian. Higher-order moments measure more complicated shape deviations.

The gravitational evolution of the initial Gaussian density field preserves the quasi-Gaussian clustering hierarchy of cumulants, which is characterized by the hierarchical scaling relation

$$\langle \delta^n \rangle_c = S_n \langle \delta^2 \rangle_c^{n-1} = S_n \sigma^{2n-2}. \tag{5.4}$$

Here, S_n are the hierarchical amplitudes, or the reduced cumulants. For $n = 2, S_2 = 1$. Therefore, the first non-trivial reduced cumulant is of the third order (*i.e.* reduced skewness, S_3).

The *fifth-force* dynamics is expected to cause departures from the standard well-established and tested hierarchical clustering paradigm of ΛCDM. These changes,

should, in turn be imprinted in hierarchical clustering statistics of both matter and DM halos. For the case of our MG models that incorporate different screening mechanisms, it has been shown that their modified dynamics in most cases leave strong imprints on the matter clustering hierarchy, especially in the higher order moments [120, 122, 125, 88].

Since the hierarchical clustering as a main prediction of the gravitational instability scenario was so thoroughly tested in the case of both GR and MG models, we further extend this study for MG models by encoding the impact of different CW environments.

In this thesis, we focus only on the variance, skewness and kurtosis of the density field, as they are most studied for the standard gravity paradigm. Measuring the higher-orders becomes increasingly challenging as these are associated with propagation of errors from the lower statistics, and in-turn leads to greater levels of uncertainty.

Here, we first smoothed the density fields across different smoothing radii, and then compute the clustering statistics for each CW element.

1. Variance

In both $f(R)$ and nDGP gravity theories, the average density remains the same as in the ΛCDM case. Hence, the first affected clustering characteristic is of the second-order, which is the *variance*, $\sigma^2(R)$, of the density field.

The results for our variance computations are shown in Fig. 5.4. The top plot in this figure illustrates the behaviour of ΛCDM variance in different CW environments, at $z = 0$. Here, we can clearly see the environmental dependence. On smaller non-linear scales, we observe that knots exhibit the highest variance, followed by filaments (which closely aligns with the overall density distribution in black), and then sheets and voids. The variance in all these elements eventually converge towards the overall trend at larger smoothing scales. Similar trends are observed in our MG models, and at various redshifts.

In the bottom figures, we delve into the impact of MG on variance in different CW environments. Notably, both $f(R)$ and nDGP show quantitatively different trends. For the $f(R)$ model, we observe a scale-dependent trend in the ratio of MG to ΛCDM variance. As R increases, this ratio decreases, and converges to 1 on larger scales. In contrast, the overall density in nDGP model shows a consistent, scale-independent ratio, which is approximately 19% for N1 and 4% for N5. On comparing with the linear variance plot (Fig. 1.3), we see that the enhancement of variance remains consistent in both the linear and non-linear predictions for all the gravity models. However, compared to the linear theory results, the non-linear effects enhance the variance which is directly computed from simulations.

Within both the $f(R)$ variants, each specific CW environment reveals a unique trend in the ratio. This suggests a complex, and a non-linear interplay between the scale-dependent fifth-force and the environment-dependent chameleon screening mechanism.

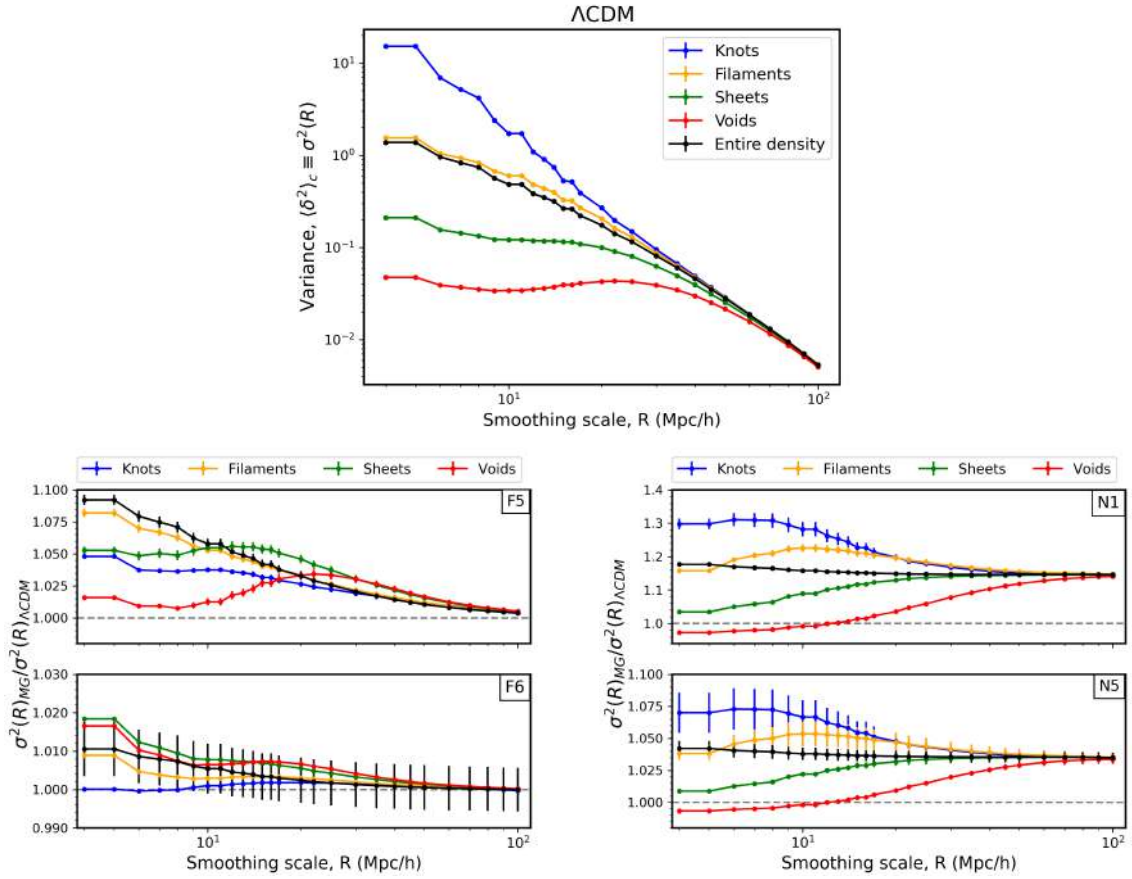

Figure 5.4: *Top plot:* Variance, $\boldsymbol{\sigma^2(R)}$ for $\boldsymbol{\Lambda}$CDM across smoothing radii, $\boldsymbol{R}$, for $z = 0$. Solid black line corresponds to the entire density field, and other colours are different CW environments, as indicated in the legends. *Bottom plots:* Comparison between MG and $\boldsymbol{\Lambda}$CDM variance in different CW environments. Here, the error bars are the standard deviation across 5 realizations.

On the other hand, N1 and N5 ratio exhibit similar trends, albeit with different amplitudes. In these nDGP variants, knots show the maximum enhancement, followed by filaments, sheets and voids. Here, contrary to other environments, voids exhibit a decrease in the ratio of variance at small length scales.

2. Skewness

Skewness quantifies asymmetry of the distribution. In the standard cosmological paradigm, $\delta \geq -1$. However, in principle, there is no upper limit on the value of δ, and δ in the centres of massive cluster-sized DM halos can reach to $\mathscr{O}(10^6)$. As clustering proceeds, there is an enhancement of the high-density tail of the density PDF, which in-turn increases the overall skewness [66]. In this sub-section, we further probe this quantity in the context of our MG models, and study the deviation from ΛCDM across each CW environment. Here, we study the skewness, μ_3 from Eq. (5.2), and reduced skewness, S_3 from Eq. (5.4).

In the top panel of Fig. 5.5, we present the ΛCDM skewness results at $z = 0$. Again, a distinct pattern of environmental dependency is clearly evident. Other models and redshifts show similar trends. Here, similar to variance, knots show the highest skewness, while voids exhibit the lowest skewness values. For the reduced cumulants, the overall density has the highest skewness on small scales. Both the skewness and the reduced skewness of all the CW environments converge to the the overall density field on large scales.

In the middle row plots of Fig. 5.5, again we show a comparison of MG skewness results with ΛCDM. For $f(R)$, we see that there is an overall increase in the ratio of MG skewness with ΛCDM. As we move to higher smoothing radii, the overall ratio trend approaches unity for both the $f(R)$ variants. In contrast, small scales show explicit environmental dependence, with knots having the least enhancement in both the $f(R)$ variants. For the case of nDGP, we notice a mildly scale-dependent overall enhancement of the ratio of the MG skewness with ΛCDM, which is $\approx 40\%$ in N1, and 10% in N5. In this MG model, the MG to ΛCDM ratio depends on the CW environment on small scales, with the results converging to a constant as we move to the larger scales.

In the bottom row plots of this figure, we show the plots of comparison of the reduced skewness in MG with ΛCDM. These plots are clearly distinct and have lower amplitudes than from the middle row plots. Here, for both the $f(R)$ models, we see a decrease in the S_3 for the overall density, knots and filaments. For the nDGP models, we see that the impact of environment is different in both the middle and lower plots.

3. Kurtosis

The *kurtosis* parameter quantifies flattening of distribution tails *w.r.t.* a Gaussian. The top plots in Fig. 5.6 are the ΛCDM kurtosis trend at $z = 0$, individually for each of the CW environment. Here, for the left plot, again knots have the maximum kurtosis

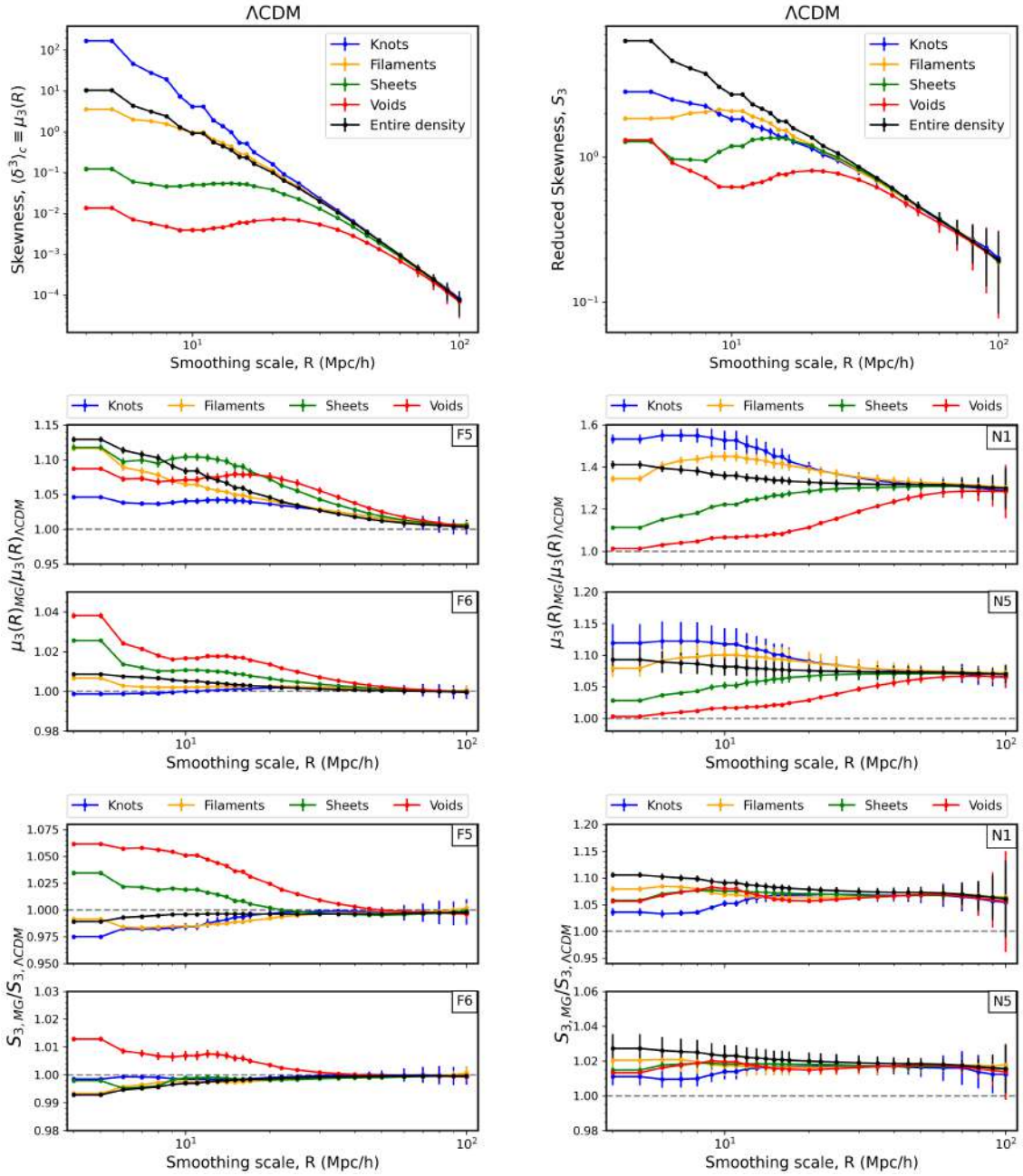

Figure 5.5: *Top row plots:* Skewness, $\mu_3(R)$ (left), and Reduced skewness, S_3 (right) for ΛCDM across smoothing radii, R, for $z = 0$. Solid black line corresponds to the entire density field, and other colours are different CW environments, as indicated in the legends. *Middle row plots:* Comparison between MG and ΛCDM skewness in different CW environments. *Bottom row plots:* Comparison between MG and ΛCDM reduced skewness in different CW environments. In all these plots, the error bars are the standard deviation across 5 realizations.

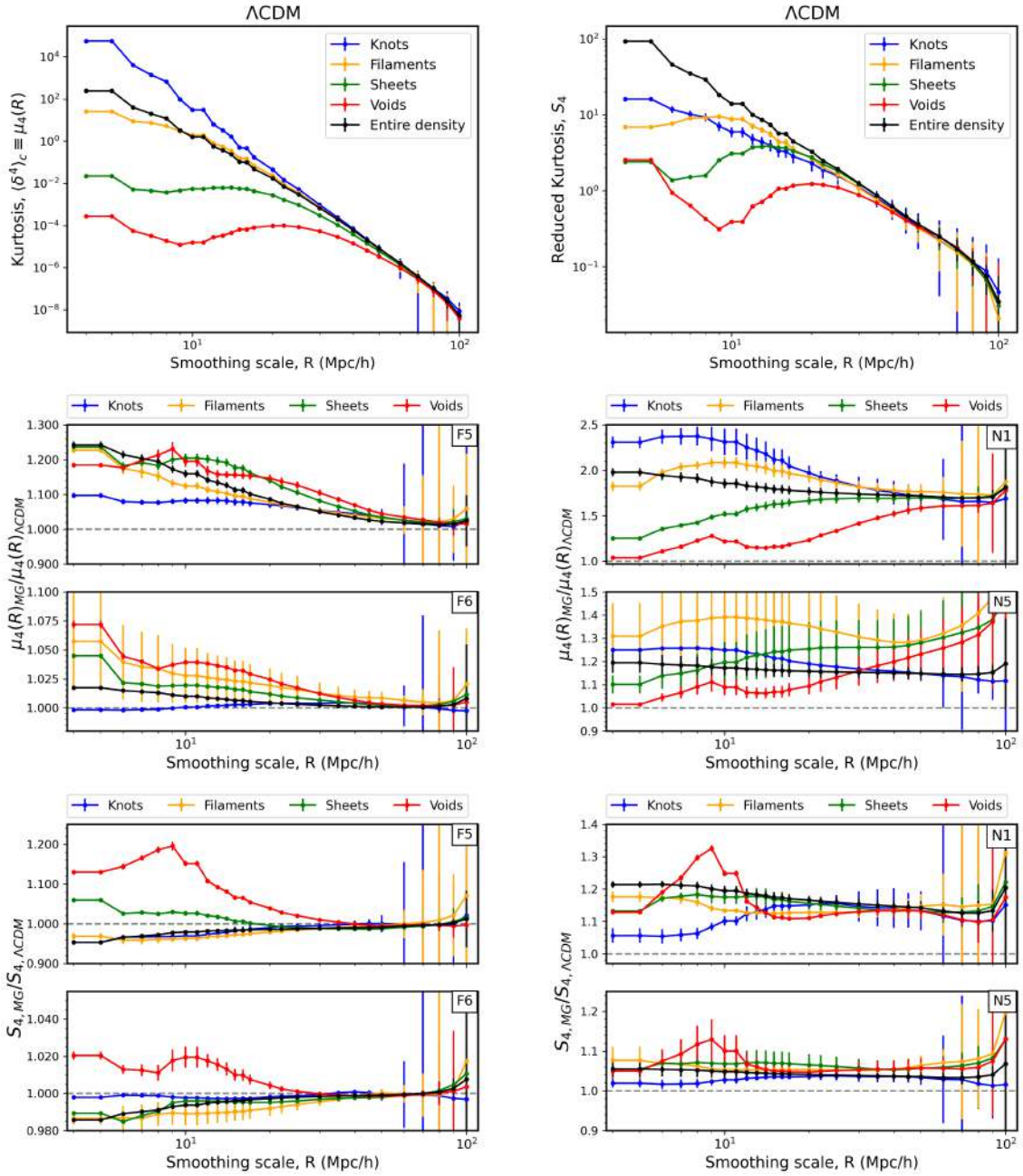

Figure 5.6: *Top row plots:* Kurtosis, $\mu_4(R)$ (left), and Reduced kurtosis, S_4 (right) for ΛCDM across smoothing radii, R, for $z = 0$. Solid black line corresponds to the entire density field, and other colours are different CW environments, as indicated in the legends. *Middle row plots:* Comparison between MG and ΛCDM kurtosis in different CW environments. *Bottom row plots:* Comparison between MG and ΛCDM reduced kurtosis in different CW environments. In all these plots, the error bars are the standard deviation across 5 realizations

on small scales, with all CW environments converging to the overall density on the larger scales. On the contrary, the overall environment in the reduced kurtosis has the maximum enhancement on the small-scales.

In the middle row plots, we show a comparison of the MG kurtosis *w.r.t.* ΛCDM. Again, the kurtosis ratio in $f(R)$ has a scale-dependent enhancement *w.r.t* ΛCDM. Similar to the previous moments, the CW impact on the kurtosis enhancement in $f(R)$ is more significant on smaller scales, with the ratio converging to unity on large scales. For the case of nDGP, kurtosis enhancement of the overall density field is the largest at the smallest scales. The overall density in N5 shows a constant enhancement in kurtosis, whereas we see a mild scale-dependent ratio in the overall trend for N1. For N1, the results of all elements converge at large scales. We do not make any conclusions for N5, given large error bars.

Now we analyse the reduced kurtosis plots in the bottom row plots of this figure. Reduced kurtosis in $f(R)$ for the overall density again shows a decrease on comparing with ΛCDM. Here, again, reduced kurtosis in voids is enhanced, and decreases for knots and filaments. For the case of nDGP models, we see that the reduced kurtosis is most enhanced for the overall density in both variants. For both models, the results of all elements converge at large scales. In both $f(R)$ and nDGP, we observe a peak in the enhancement of the kurtosis in voids at ≈ 10 Mpc/h. It remains uncertain whether this observed trend is an artefact of numerical simulations or a physically meaningful signal.

These two subsections of analysing the skewness and kurtosis highlight that the 2-point variance statistics is not capable of completely describing the non-linearities associated with the density fields, and in fully capturing the otherwise complicated departures of both the $f(R)$ and nDGP cosmic density fields from the fiducial GR case. Additionally, we observe that both the MG models have different impact on these statistics across different CW environment. Also, as the clustering order increases, the impact of MG also becomes more significant on the statistic.

Perturbation theory for GR shows that the reduced cumulants are a decreasing function of the smoothing scale R. We find these results for both GR and beyond-GR models, and for all the CW environments. The dependence of the reduced cumulants on the scales results from the combinations of the growing orders of the matter variance obtained at a given smoothing scale (Eq. (5.4)). Also, the reduced skewness and reduced kurtosis have shown to be sensitive to the spectral index of the initial power spectrum [38]. This makes the studies of higher-order clustering a probe to constrain the initial density distribution [140]. Furthermore, our results from analysing the higher-order statistics show that at the relevant scales for galaxy and halo formation, both the $f(R)$ and nDGP density fields are characterised by change in the clustering across the correlation orders that we studied, and this change depends explicitly on the CW environment. Thus, the CW environment offers a significant systematics in the study

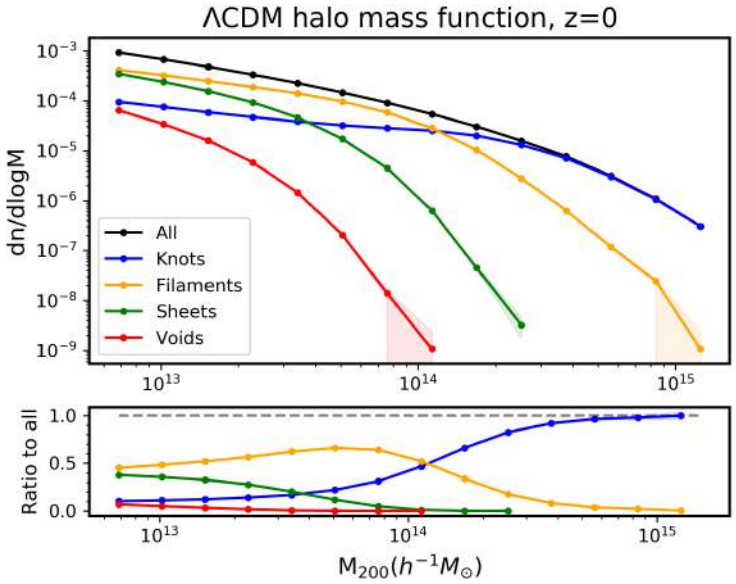

Figure 5.7: *Top plot:* ΛCDM Halo Mass Function, HMF at $z = 0$. Here, HMF is computed by normalising over the whole volume of the simulation box. Solid black line corresponds to the HMF for the entire halo population. Other colours are the HMF results for different CW environments, as indicated in the legends. *Bottom plots:* Comparison of the HMF in each CW environment with the overall HMF. Here, the error bars are the Poisson errors from simulations.

of LSS clustering, and hence should be accurately catered to in order to make unbiased estimates for measures that are associated with the higher-order clustering statistics. This is particularly relevant in the studies involving growth rate of structure formation, primordial non-Gaussianity, galaxy formation models, and large-scale clustering [39, 141, 241, 191, 139, 47, 48].

5.4 Impact of Modified Gravity on halo properties in different Cosmic Web environments

5.4.1 Halo Mass Function

In this sub-section, we study the Halo Mass Function (HMF) in the context of the CW. In Fig. 5.7, we plot the ΛCDM HMF separately for each CW environment, at $z = 0$. Here, HMF is computed by normalising over the whole volume of the simulation box. The black line corresponds to the HMF obtained for the entire halo population, and different colours are the HMF for each CW element. Here, we can clearly see that the HMF trend in all the environments is significantly different. Similar results have also been reported in [12, 126, 103]. Other gravity models and redshifts follow similar trends. Notably, as we expect, voids have the lowest amplitude of HMF at all mass scales. Filaments host most of the halos between $7.8 \times 10^{12} - 10^{14} \mathrm{M}_{\odot}/h$, whereas, for $M > 10^{14}$ $\mathrm{M}_{\odot}/h$, knots are the dominant halo hosting environment. In the lower panel,

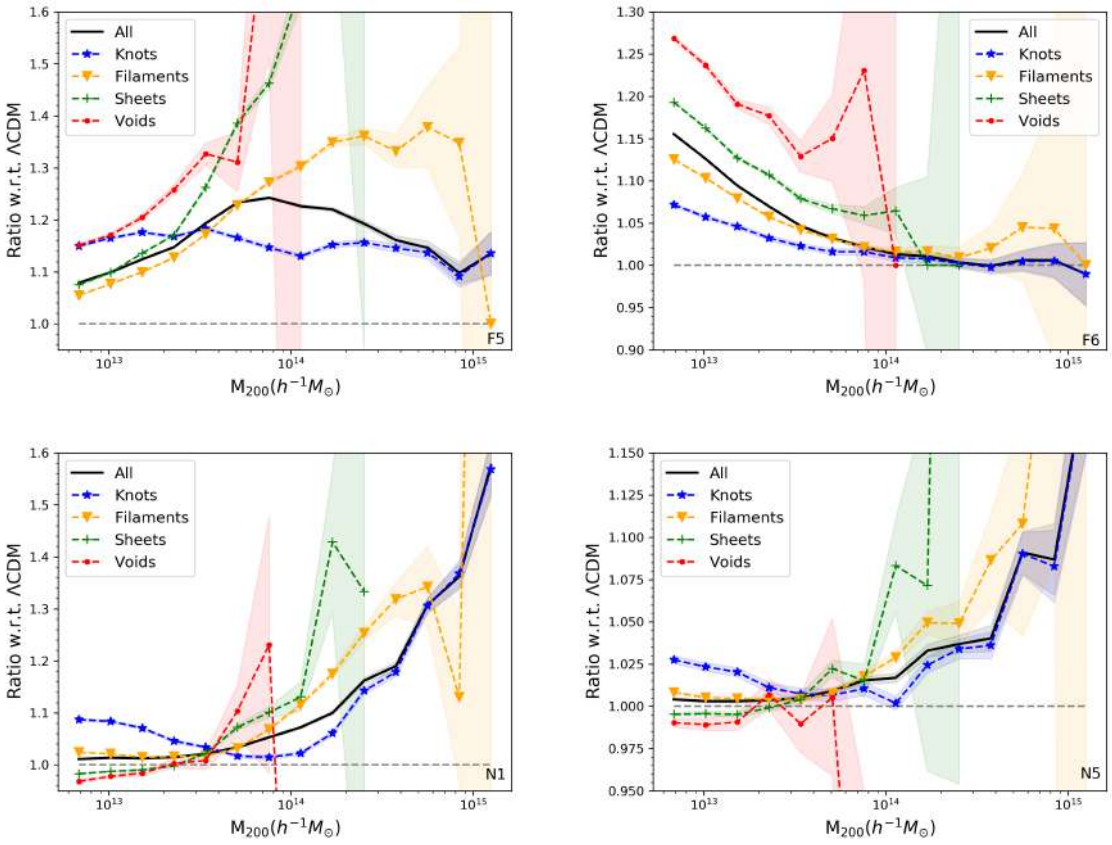

Figure 5.8: Comparison of $f(R)$ (top plots) and nDGP (bottom plots) HMF with ΛCDM, for each CW element at $z = 0$. The shaded regions correspond to the propagated errors from each realization of the simulation box.

we plot the ratio of HMF in each CW environment to the entire halo population. We can clearly see that filaments host maximum halos with mass $\leq 10^{14}$ $M_\odot/h$ ($\approx 50\%$). The percentage of halos residing in knots increases with increase in the halo mass.

We show in Chapter 2 that in both $f(R)$ and nDGP, there is a boost in structure formation. As a result, we have an increase in the MG HMF *w.r.t.* standard ΛCDM for the halo mass range examined in this work. In Fig. 5.8, we present the same comparison with ΛCDM, but now separately for the CW environments. The top plots are the $f(R)$ gravity results, and the bottom plots are the results for the nDGP gravity variants. Both these MG models illustrate different trends in the HMF ratio *w.r.t* ΛCDM.

In all these plots, black solid lines correspond to the ratio of HMF from the entire halo population, and has already been discussed in Chapter 2. Here, we focus only on the HMF trends in CW elements. In both the $f(R)$ models, voids, being the least dense regions, are least screened, and hence have the maximum HMF enhancement on small halo mass scales. In F5, we see that this enhancement in voids is followed by knots, then sheets and then filaments. Whereas, in F6, we see that the void enhancement is followed by sheets, then filaments, and then knots. For both these $f(R)$ variants, the results from the overall HMF trend lies between filaments and sheets, and follows knots' results at the large halo mass ends. Also, it is evident here that for large halo masses, HMF decreases as a result of self-screening. This decrease is more significant in F6 than F5, as the screening is more dominant over the effect of the fifth-force in the weaker F6 variant.

In nDGP, the HMF enhancement increases with halo mass. Contrary to $f(R)$, voids and sheets in nDGP have a decrease in the HMF *w.r.t.* ΛCDM for $M_{200} \leq 3 \times 10^{13}$ $M_\odot/h$. With increase in the halo mass, the size of the halos would increase. As a result, larger mass halos would be beyond the Vainshtein radius, and would have a reduced impact of the Vainshtein screening, and in-turn increase in the resultant fifth-force. Hence, HMF for voids and sheets in nDGP (which mostly host the low-mass halos) is least enhanced. Here, similar to $f(R)$, the overall HMF trend lies between filaments and sheets, and follows the knots' trend as the halo mass increases.

F(σ)-ln σ^{-1} relation in the context of Cosmic Web

We elaborated in Section 2.2 that when plotted as a function of ln σ^{-1}, the halo multiplicity function, F(σ) can be expressed as a universal function independent of redshift. This universal relation has been used to propose analytical expressions in order to compute the ΛCDM HMF [251, 278, 83]. Here, we investigate this relation further by taking into account the CW effect. In Fig. 5.9, we show this relation for various redshifts, only for ΛCDM. Both $f(R)$ and nDGP variants exhibit similar trends. In these plots, solid lines represent the F(σ)-ln σ^{-1} relation for all halos (which have already been discussed in Section 2.2), and the dashed lines are this relation in the respective CW elements, as highlighted in the legends. We see that the universality in

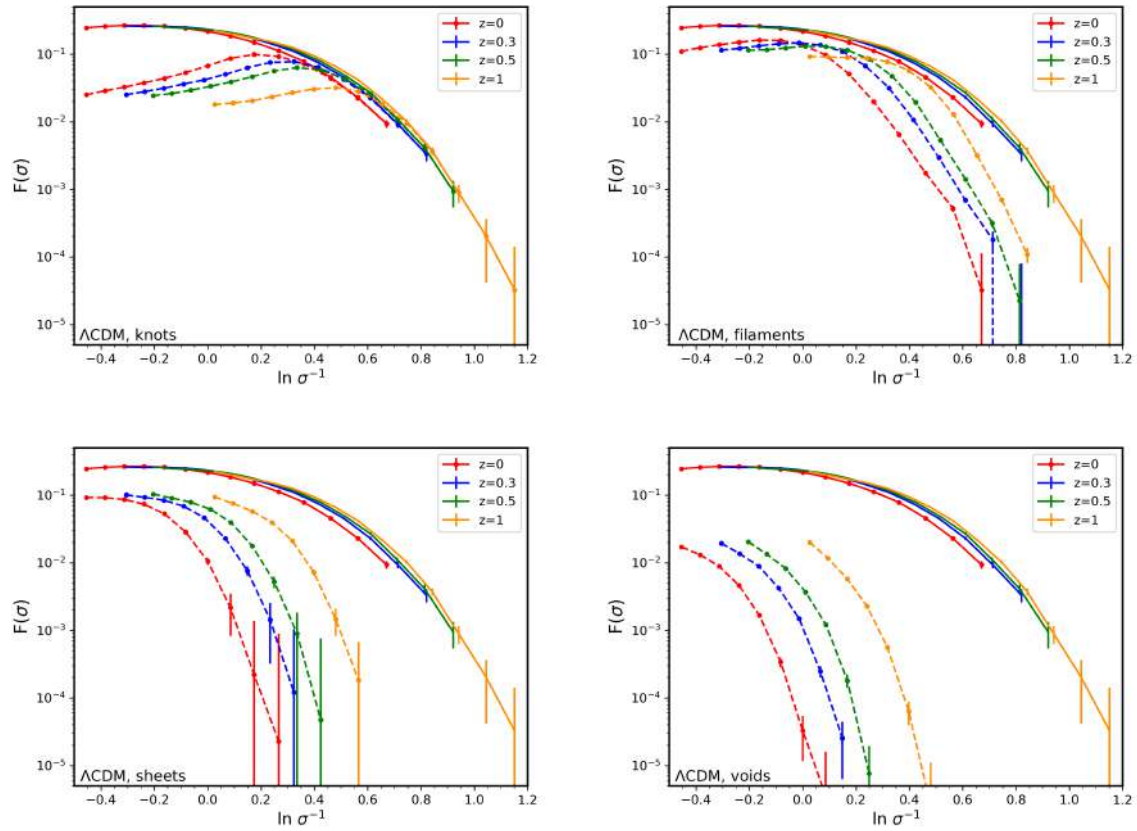

Figure 5.9: ΛCDM F(σ)-ln σ^{-1} relation for knots, filaments, sheets and voids (in dashed lines), across $z = 0, 0.3, 0.5$ and $z = 1$. The solid lines in all plots are the F(σ)-ln σ^{-1} results for the entire halo populations. The error bars illustrate the Poisson errors from the simulations.

this relation tends to break for voids and sheets, whereas filaments obey this universal relation on small scales, and knots approach the universality at large ln σ^{-1} scales. This explicit dependence of the HMF on the CW breaks the assumption of a universal behaviour for this relation. As a result, we need to consider the corrections due to the CW environmental effects to have a more coherent and a reliable HMF modelling.

Moving to the MG framework, in Section 2.3 and in [111, 112], we show that the ratio $\Delta_{\rm MG} \equiv F(\sigma)_{\rm MG}/F(\sigma)_{\Lambda\rm CDM}$ (MG = $f(R)$, nDGP) is independent of redshift, when expressed as a function of ln σ^{-1}. This property helped us come up with fitting functions for this ratio to analytically compute the HMF in these MG models. These explicit

Table 5.1: Parameters for the $\Delta_{F6} = F(\sigma)_{F6}/F(\sigma)_{\Lambda CDM}$ (Eq. (2.14)) in different CW environments.

F6	a	b	c
Knots	0.081	-0.738	0.394
Filaments	0.121	-0.618	0.354
Sheets	0.203	-0.635	0.400
Voids	0.265	-0.586	0.412

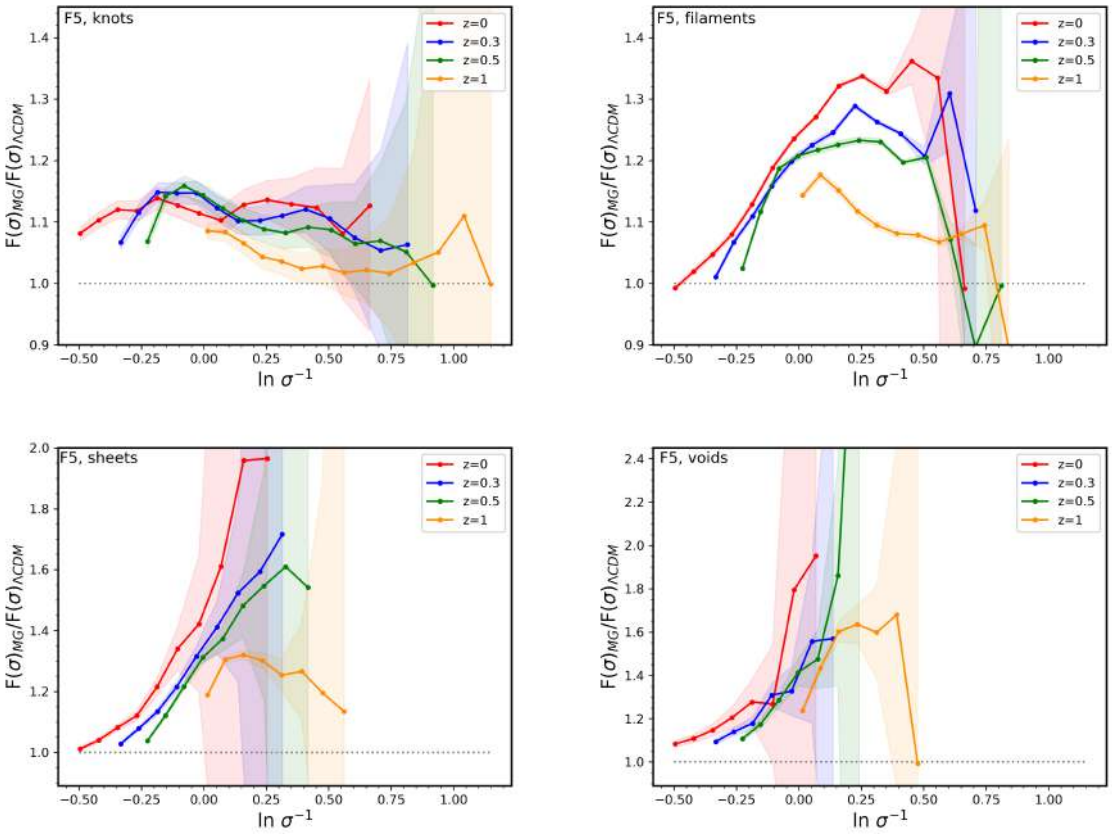

Figure 5.10: Ratio of F5 $F(\sigma)$ with ΛCDM for knots, filaments, sheets and voids, as a function of $\ln \sigma^{-1}$. The shaded regions correspond to the propagated errors from each realization of the simulation box.

expressions are given in Eqs. (2.14) and (2.15), for $f(R)$ and nDGP respectively. Also, the values of the parameters used in these expressions are defined in Table 1 and Table 2 of [112].

In this section, we further probe this ratio to check if the universality in $\Delta_{\rm MG}$ holds even when we separately study it for each CW element. For this, we plot this ratio separately for each model and z from Fig. 5.10 - Fig. 5.13. For the F5 variant (Fig. 5.10), we can clearly see that this universality breaks for each CW element, and, as a result, our fitting functions cannot be used to probe the F5 HMF in the context of different CW environments. For the case of F6, we find that even though the universality in this ratio holds, we cannot use the original fitting parameters ((a,b,c) from Table 1 in [112]) to capture this ratio in each CW environment. In Table 5.1, we provide new values for these parameters, which are individually calibrated for each CW environment. These fits for each environment are plotted as a solid black line in Fig. 5.11. This highlights that our original HMF fitting for both these $f(R)$ variants needs to re-calibrated to take into account the environmental dependence in the HMF of $f(R)$ gravity. We obtained new fits for F6 using the original expression, but with different parameters. However, for the case of F5, this calibration is not so trivial and the correction to the HMF requires greater investigation. We plan this as our future endeavour with better-resolved $f(R)$

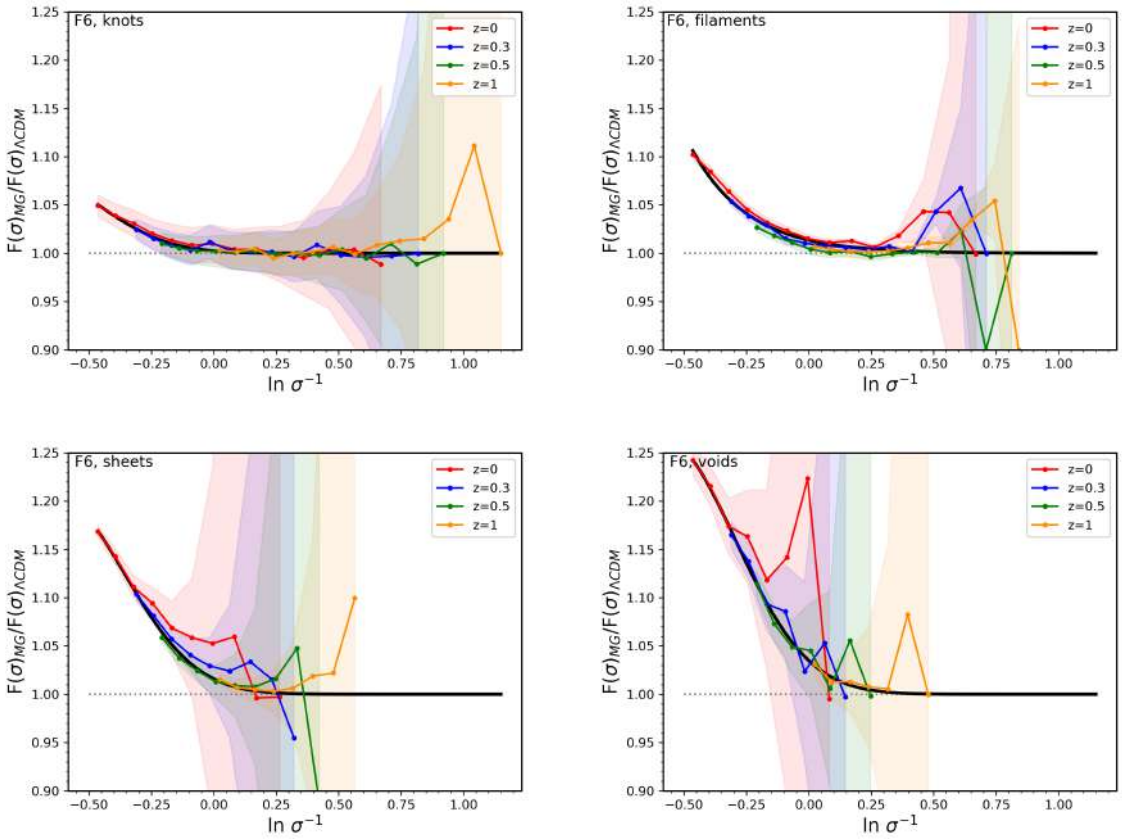

Figure 5.11: Ratio of F6 $F(\sigma)$ with ΛCDM for knots, filaments, sheets and voids, as a function of $\ln \sigma^{-1}$. The black line in each plot is the Δ_{MG} fit for F6 (Eq. (2.14)), with the best-fit parameters provided for each CW environment in Table 5.1. The shaded regions correspond to the propagated errors from each realization of the simulation box.

simulations.

For the nDGP gravity models (Figs. 5.12 and 5.13), the universality in this HMF ratio seems to hold in both the variants and all the CW environments. Furthermore, the original fitting function proposed for this ratio in Eq. (2.15) holds also in different CW environments. The solid black lines in both these figs. are this expression, with the original fitting parameters (p,q,r,s) mentioned in the Table 2 of [112]. This shows that the CW environment does not impact the universality of this ratio in nDGP, and our fitting functions with the same parameters can also be used for studying nDGP HMF in CW. However, we notice minor deviations in filaments for both these models.

In this section, we use the linear value for the $\ln \sigma^{-1}$ relation (Eq. (1.23)). However, in Fig. 5.4, we showcase how the non-linear variance is impacted by MG in different CW environments. As a result, the next step to test the universality of the Δ_{MG} relation would be to separately consider the impact of the non-linear variance from each environment on the universality of this relation. This research is currently in progress.

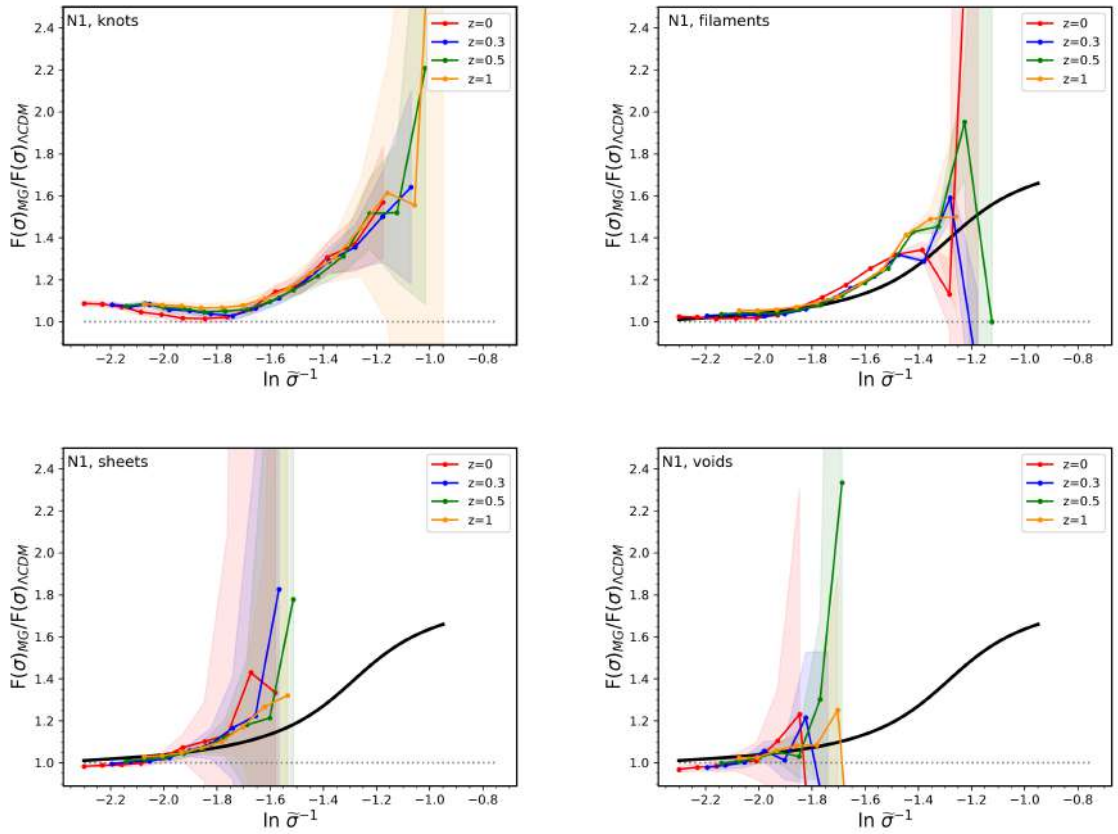

Figure 5.12: Ratio of N1 $F(\sigma)$ with ΛCDM for knots, filaments, sheets and voids, as a function of $\ln \widetilde{\sigma}^{-1}$. The black line in each plot is the $\Delta_{\rm MG}$ fit for N1 (Eq. (2.15)), with the best-fit parameters from Table 2 of [112]. The shaded regions correspond to the propagated errors from each realization of the simulation box.

5.4.2 Halo spin

CW is a quasi-linear manifestation of the same tidal fields that torque up the halo during its initial stages of formation, and are responsible for inducing angular momentum, or spin in halos (Tidal Torque Theory (TTT), more details in Section 4.2.2). As a result, we expect that the spin of halos would correlate with the hosting CW environment. This has already been established in the previous works [113, 188, 126, 103] where the authors have shown significant influence of the environment on the halo spin. In Section 4.2.2, we present the impact of our MG models on halo spin across different halo masses and redshifts. Our analysis show that both the MG phenomenologies enhance the halo spin in a quantitatively different way. The halo spin enhancement in $f(R)$ variants have a much more profound dependence on the halo mass and redshift than the nDGP models. In this section, we delve deeper into this subject of halo spin, and further explore how differently MG models impact the halo spin in different CW environments.

In Fig. 5.14, we first present the ΛCDM spin across different CW environments, at $z = 0$. The solid black line corresponds to the entire halo population, and different colours are the halo spin in different CW environments. Here, we can see a clear, though small, environmental dependence. Knots host the highest spinning halos for $M_{200} \leq 10^{14}$

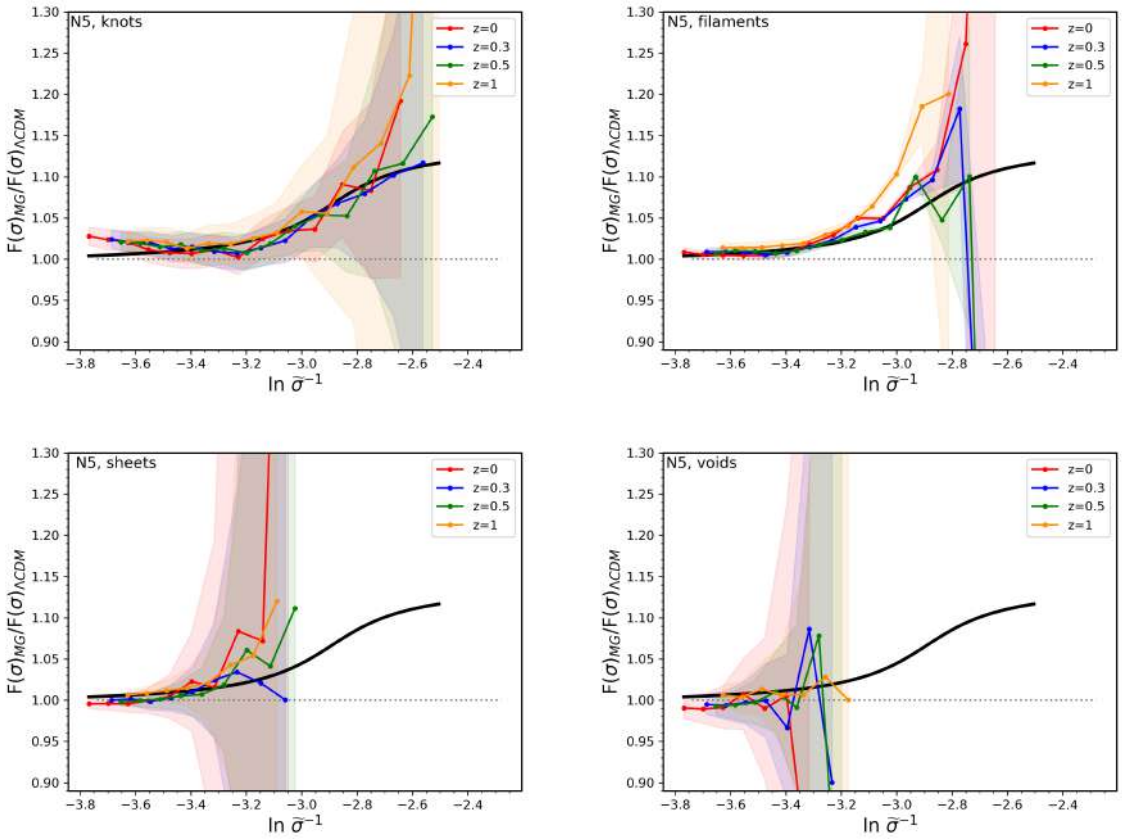

Figure 5.13: Ratio of N5 F(σ) with ΛCDM for knots, filaments, sheets and voids, as a function of $\ln\widetilde{\sigma}^{-1}$. The black line in each plot is the $\Delta_{\rm MG}$ fit for N5 (Eq. (2.15)), with the best-fit parameters from Table 2 of [112]. The shaded regions correspond to the propagated errors from each realization of the simulation box.

$M_\odot/h$, and at larger halo masses, the highest spinning halos reside in filaments. At these large halo mass scales, knots trace the spin of the overall halo population. Sheets and voids host the lowest spinning halos at the intermediate halo mass scales (between $7.8\times10^{12}-10^{14}$ $M_\odot/h$).

In Fig. 5.15, we quantify the impact of MG on halo spin in different CW environments, at $z=0$. Here, top panels correspond to $f(R)$ results, while the bottom plots are for the nDGP variants. The solid black line in these plots is the ratio trend for the MG to ΛCDM spin for the entire halo population (already discussed in Fig. 4.3). For the $f(R)$ gravity, we can see a clear mass and environmental dependent trend in the ratio of $f(R)$ to ΛCDM spin. The spin enhancement in F5 is $\approx 16\%$ on low mass halos, which decreases as we move to larger scales. At the small halo masses, filament halos have the maximum enhancement, and knots have the least enhancement. This can be attributed to more anisotropy in filaments than knots. For F6, voids have the maximum enhancement at small halo masses ($\approx 7\%$), and knots have the least enhancement but follow the trend of all halos at larger masses. This trend in the weaker F6 variant can be attributed to the dominance of chameleon screening in the high-density regions. Here, halos in filaments follow the trend of overall halo samples across the

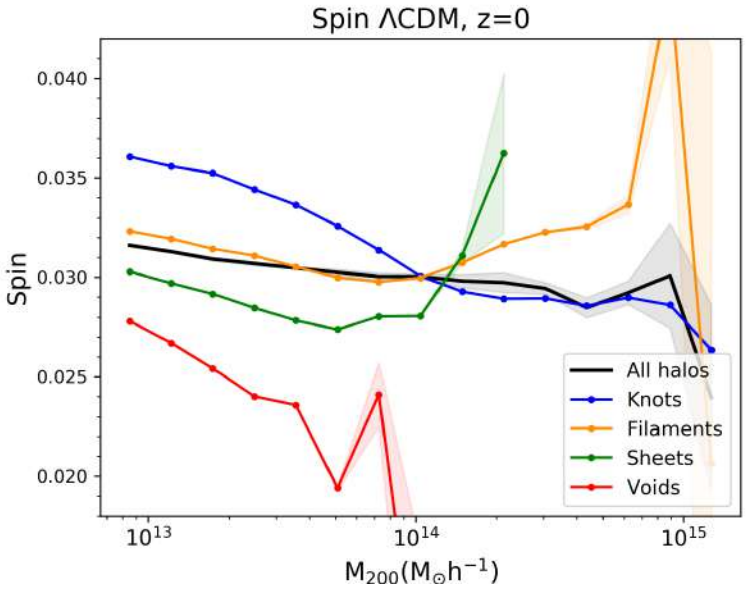

Figure 5.14: ΛCDM spin as a function of halo mass, at $z = 0$. Solid black line corresponds to the spin from all halos, and other colours are the spin results for different CW environments, as indicated in the legends. The shaded regions correspond to the errors across 5 realizations.

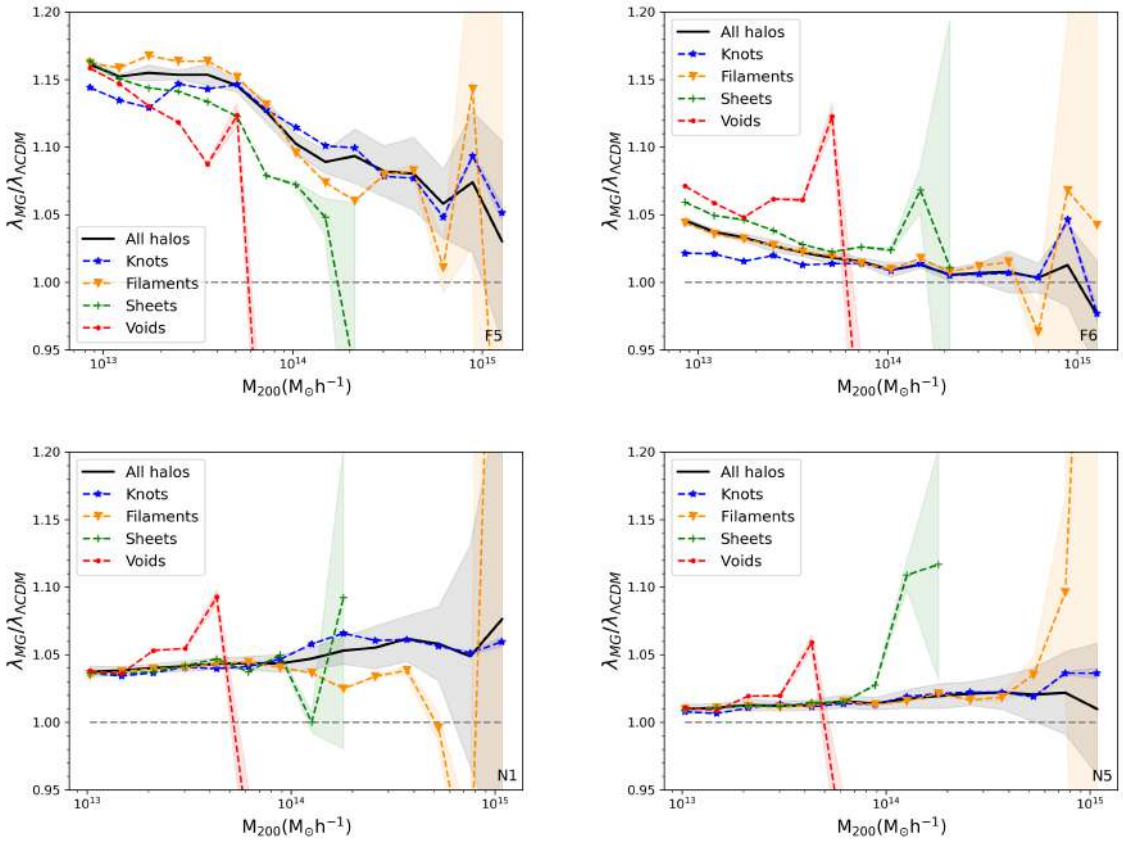

Figure 5.15: Comparison of MG to ΛCDM halo spin for $f(R)$ (top plots) and nDGP (bottom plots) gravity variants, across different CW environments, at $z = 0$. The shaded regions correspond to the propagated errors from each realization of the simulation box.

entire halo mass range. For both the $f(R)$ variants, we can clearly see that at large halo masses, the self-screening is more significant which decreases the enhancement in $f(R)$ spin *w.r.t.* ΛCDM. This result is analogous to the trends in the HMF plots (Fig. 5.8). Clearly, for the $f(R)$ model, we see an interesting interplay between the effect of the environment, halo mass and the strength of the fifth-force on the halo spin. The environment-dependent chameleon screening impacts the torquing of halos in each environment differently, giving rise to distinct MG signature on spin in each environment. This analysis offers additional information to the studies of spin, that what we previously conducted for entire halo populations in Section 4.2.2.

Contrary to $f(R)$ results, we see neither scale nor environmental dependent enhancement trend in nDGP to ΛCDM spin ratio. Halos in all CW environment have similar enhancement as is shown by the overall halo sample,and which we have already discussed in Section 4.2.2. nDGP gravity has both scale and environment-independent effect on the spin. This shows that the studies of halo spin in nDGP models for different CW environment do not reveal additional information than the previous studies pertaining to all halo populations.

The analysis of halo spin in both Section 4.2.2 and this section highlights that investigating this intrinsic halo property serves as a complimentary test-bed to search for MG signatures. Both $f(R)$ and nDGP exhibit distinct effects on halo spin, with $f(R)$ displaying a notably greater sensitivity to redshift, halo mass, and the CW environmental factors in this analysis compared to nDGP. Therefore, the studies related to this property have potential to constrain the MG. Furthermore, the impact of these modifications to gravity on halo spin are expected to extend to the galaxies hosted within these halos. Previous studies have demonstrated the influence of the CW environment on galactic spins [102, 135, 17, 168]. Thus, these analysis offer a potential to search for the fifth-force in the observational domains. However, this is a much more advanced endeavour, and is beyond the scope of this thesis.

5.5 Summary and Discussion

In this chapter, we examine the impact of MG phenomenologies on DM density fields and halo properties across various CW environments. For this purpose, we employ the T-WEB approach to the density fields from the ELEPHANT simulation catalogues. Here, we use the Hessian of the gravitational potential to divide the density field into four different CW environments: namely, knots, filaments, sheets, and voids.

We first analyse the 1-point statistics of the cosmic density fields, which is the 1D probability distribution function (PDF). We show this for the ΛCDM at $z = 0$. All gravity models follow a similar log-normal distribution [66], with knots predominantly at the high density tail, followed by filaments, then sheets, and then voids at the lower end of the density distribution. The overall density peaks between filaments and sheets.

We further study the distribution separately in each CW environment, and for all gravity models, where we find differences in the median of the density distribution. We further resort to the studies of moments of density distribution, and to quantitatively probe as to how differently these statistics are impacted by MG in different CW environments.

For our purpose, we focus on the 2-point and higher-order statistics of skewness and kurtosis in Section 5.3.2. As higher-order moments are induced by gravitational dynamics, these statistics depend on the growth rate, and in turn on the cosmological parameters [39]. Hence, it is important to have robust measurement of these statistics and their uncertainties, in order to obtain accurate cosmological parameter estimations and constrains on our gravity theories. We summarise the findings of this section in the following points.

- We study the ΛCDM variance, skewness, and kurtosis respectively across smoothing radii, R. In all these statistics, we can see a clear environmental dependence, which is the most pronounced at small scales, and all results converge on the larger scales. For the case of variance and the connected moments of skewness and kurtosis, we see that knots have the highest value of variance. On the contrary, for the reduced skewness and reduced kurtosis, value for the overall density is dominant on most of the length scales considered.

- We also compare the MG to ΛCDM variance. Both $f(R)$ and nDGP have significantly different impact on the variance. $f(R)$ variants show a scale-dependent trend in the ratio on smaller scales, with the results of all the environments approaching unity on the larger scales. While, for nDGP, we notice a similar scale and environmental dependent trend on small scales (except for the overall density), with all results converging to a constant value on the large scales.

- We further compare the MG and ΛCDM skewness. The results between $f(R)$ and nDGP are again quantitatively different. All environments on the small-scales exhibit different trends, which converge to unity as we approach larger scales. For the nDGP variants, we obtain a slight scale and environmental-dependent ratio on small scales for the CW environments, with the results converging to a constant enhancement of large scales. Contrary to variance, the reduced skewness in the overall density for $f(R)$ variants decreases when compared to ΛCDM.

- The kurtosis findings exhibit similarities to skewness. However, in the context of kurtosis, MG models demonstrate a more pronounced departure from ΛCDM compared to the skewness results.

- On comparing the connected moments and the reduced cumulants, we see that the impact of MG is more the former compared to the latter. Connected moments are enhanced in MG compared to ΛCDM, and the value of the reduced cumu-

lants decreases in MG *w.r.t.* ΛCDM. Overall, both these statistics show profound influence of the environment.

From these results, we can confirm the potential of studying the hierarchical amplitudes as potential probes to quantify the modified gravitational dynamics, a finding already emphasised in clustering studies for a wider class of MG theories [120, 122, 125, 88]. Furthermore, we showcase the importance of probing these statistics individually in each CW environment. The additional information encoded in the environmental dependence of these higher-order statistics can further be used to break degeneracies present in the measurements of the clustering statistics when averaged across all environments. This, would in turn help forecast better constraints on the cosmological quantities that we obtain from studies of higher-order clustering [191, 139, 47, 48, 141], and aim for better constraints on the theory of gravity.

Moving to the halo properties, we emphasise on the Halo Mass Function (HMF) and the halo spin within our MG models, across CW environments. Notably, both of these properties demonstrated sensitivity to the specific environment hosting the halo. Additionally, upon a comparative analysis of the MG impact on these halo properties, we consistently observed the influencing role of the CW in shaping the effects of MG on these distinct halo characteristics. Here, we first summarise our findings for the HMF section:

- The HMF trend shows an explicit dependence on the CW environment, with the fractions of halos residing in different CW environments varying as a function of their mass. For the mass range probe in this work, we see that the filaments host the maximum halos for $M < 10^{14}$ $M_{\odot}/h$, and the higher mass halos mostly reside in knots. This trend is similar for both ΛCDM and MG models.

- We further study the impact of MG on HMF in different CW environments. Both $f(R)$ and nDGP show quantitatively different trends. In this figure, we see a clear deviation from the overall HMF ratio trend (discussed in Chapter 2) across each environment. This trend is an interplay between the influence of the fifth-force, and the physics of the screening mechanism manifesting across various halo mass ranges. Here, the impact of the CW environment is more significant for $M \leq 10^{14}$ $M_{\odot}/h$.

- We further explore the universality of the $F(\sigma) - \ln(\sigma^{-1})$ relation across different CW environment. We can clearly see that the universality of this relation breaks in all CW environments, with a slight universal character at the large fluctuation scales for knots, and small fluctuation scales for filaments. This shows that the HMF relations proposed by exploiting the universal relation cannot be extended when we want to study HMF across separate CW environments.

- We also study the universality of the $F(\sigma)_{\rm MG}/F(\sigma)_{\Lambda\rm CDM}$ (MG = $f(R)$, nDGP)

relation (already discussed in Chapter 2) in the context of different CW environments. From these HMF results, we conclude the following points for each MG model:

- The time evolution of the density fields is not enough to capture the HMF trends in $f(R)$ variants, as the fifth-force in this gravity model behaves differently in these $f(R)$ variants, depending on the hosting environment. This shows that our HMF modelling should include corrections associated with the mass distribution in each CW environment. For the case of F6, we used the same expression (Eq. (2.14)) but with different parameters (Table 5.1), which are calibrated for each CW environment. However, the stronger F5 variant needs more calibration and will be addressed with better $f(R)$ simulations.
- nDGP ratio plots confirm that the ratio $\Delta_{\rm MG\,=\,N1,\,N5}$ remains universal in all the CW environments. For these models, we can use the fitting functions already proposed in Eq. (2.15), with our original parameters for this equation.

For our studies pertaining to halo spin, we summarise our findings in the following points:

- Halo spin shows an explicit dependence on the environment hosting the halo. We present the results for ΛCDM spin at $z = 0$, with the highest spinning halos mostly residing in the dense environments of filaments and knots. We can see a clear dependence on the environment for halo masses $\leq 10^{14}$ $\mathrm{M}_{\odot}/h$. Other models show similar results.

- We further study the impact of MG on halo spin in different CW environments. Both $f(R)$ and nDGP have a different impact on the spin. $f(R)$ shows much more enhanced spin, with a more pronounced mass and environmental dependence. On the other hand, nDGP does not have significant impact on the spin, and this difference from ΛCDM is also independent of the CW environment.

The results obtain from this chapter highlight that incorporating the morphological classification of the CW into the existing analysis of DM density and halo properties increases their utility as a probe of MG. Every property investigated in this study demonstrates a nuanced dependence on its hosting environment. Additionally, our study also reveals distinct MG effects across various environments. This highlights the importance of CW studies in MG, providing valuable insights into comprehending the dynamics of the fifth-force and screening mechanisms. Our environment-dependent investigation yields richer information compared to the overall analysis averaged across all environments. Consequently, constraints derived from combining LSS properties from each specific environment will be more robust than those obtained from an analysis of the entire density field.

Summary and Future Prospects

When you look at the stars and the galaxy, you feel that you are not just from any particular piece of land, but from the Solar System.

-Kalpana Chawla

Chapter 6

Summary and future prospects

The standard model of the Universe: Lambda Cold Dark Matter (or ΛCDM) has stood the test of time, and forms the foundation of our understanding of the Universe. It is indeed remarkable that such a simple phenomenological model successfully fits the observations, and its predictions can been confirmed by observations: like temperature fluctuations in the cosmic microwave background (CMB) [257, 130, 68], large-scale distribution of matter [10, 225], abundance of light elements from primordial nucleosynthesis [78] etc. Furthermore, continued developments in both observational, theoretical and numerical domains have facilitated the development of both analytical and semi-analytical approaches to test ΛCDM on non-linear scales. This has helped us constrain this model to a really good precision, with much better constraints expected from our current and future surveys [163, 182].

However, at its core, ΛCDM model is still phenomenological, and needs an input of Dark Matter and Dark Energy in the cosmic matter-energy budget [68, 4]. The phenomenological nature of the ΛCDM model, alongr with the theoretical issue of the Λ (known as the cosmological constant problem, [280]), and the observed anomalies associated with ΛCDM [54, 235, 186], have motivated searches for extensions or modifications of the concordance model. One particular extension focused on attributing the accelerated late-time expansion to beyond-GR physics, rather than to Λ. Such models are commonly referred to as the *Modified Gravity* (MG) phenomenologies, and investing these models is now a well-established field of research [64, 25, 153, 211, 97, 259, 26, 154, 138, 52].

While a commonly accepted MG model remains elusive, research in this domain has unveiled numerous intriguing possibilities of deviations from GR. These departures offer useful test-beds to evaluate the applicability of GR in cosmology. In our study, we investigate two such potential deviations that result in distinct phenomenologies, namely $f(R)$ and nDGP theories. Both of these nontrivial MG models exhibit the universal feature of a fifth-force, which acts on top of the standard gravity on cosmological scales. As a result, the extra physics of these MG models modifies the evolution of perturbations in both the linear and non-linear regimes, and hence have a different structure

formation than the standard ΛCDM scenario. This fifth-force is, in-turn, expected to leave an imprint on structure formation scenarios, which would lead to testable differences in the properties of the LSS in such beyond-GR theories as compared to ΛCDM [212, 213, 245, 240, 80, 32, 33, 6, 125, 60, 214, 202, 107, 203, 112, 88, 110]. This forms the core research topic of this study: *To investigate the differences in the underlying properties of large-scale structures (LSS) between MG models and ΛCDM.*

In the following sections, we discuss the topics that we have addressed in this thesis:

6.1 Quantifying and analytically modelling the Modified Gravity Halo Mass Function

As we highlighted, the structure formation differs in these MG frameworks from ΛCDM. We first investigate the Halo Mass Function (HMF), which finds significance in many observational aspects and semi-analytical modelling studies [73, 108, 217]. We obtained that for the halo mass range probed in this work ($\geq 7.8 \times 10^{12}$ $M_\odot/h$), HMF in these MG models is enhanced *w.r.t.* ΛCDM. As a result of enhancement in the underlying gravitational forces, more small mass halos are expected to merge and form larger halos. The more significant result was the trend that we obtained in the enhancement of MG HMF across length and time scales. We discussed these trends in Fig. 2.2. This systematic departure between MG and ΛCDM HMF helped us to come up with different fitting functions for this ratio, that facilitates computing MG HMF without running MG simulations. These results have been discussed in details in Chapter 2 and in [111, 112].

Our HMF fits perform within %-level accuracy for both the original simulations used in the original calibration, as well as with different sets of simulations that probe different halo mass regimes.

6.2 Improved analytical modelling of non-linear matter power spectrum in Modified Gravity models

We use the halo properties of HMF, halo bias, and halo concentration to study the Halo Model (HM) framework. HM was proposed in [73, 220] to study the statistics of the density fields in the non-linear regime, where the perturbation theory fails. The HM was proposed for ΛCDM, and we further extend this formalism to compute the power spectrum in MG scenarios. HM, for both ΛCDM and MG, performs well within % level accuracy up-to quasi-linear scales ($k \leq 0.5$ h/Mpc). However, it is the non-linear scales ($k \geq 1$ h/Mpc) where we expect most of the constraining power of the present and future surveys. Different analytical approaches to compute non-linear ΛCDM power spectrum are already at par with the precision we expect from forthcoming surveys

[256, 263, 200, 197]. However, such convenient modelling is lacking for the wider class of MG models.

In this work, we further aim to rectify this discrepancy, and built our framework to analytically compute the matter power spectrum for these MG models. Our framework uses the response function from HM (*i.e.* $\Upsilon_{\rm HM}(k) = P(k)_{\rm HM,\ MG}/P(k)_{\rm HM,\Lambda CDM}$) to construct our formalism. The details of this study are in Chapter 3 and [110].

Our approach gives %-level accuracy for non-linear scales ($k \geq 1h/\,$Mpc), and is general enough to be further extended to other MG scenarios. We also tested this approach on simulations that weren't used in the original calibration of the halo properties (simulation courtesy from [206]), and obtained similar accuracy like the original simulations.

6.3 Large-scale clustering and Halo Assembly bias effect in Modified Gravity models

Halos form on the peaks of the underlying Dark Matter density field, thereby inducing a bias relation. Dark Matter clustering can be studied in terms of this halo bias relation, which on large scales, can be approximated to first order as a linear function of halo mass and redshift. We further investigate this relation in MG models. Contrary to HMF, bias in MG models decreases *w.r.t.* ΛCDM, which is a consequence of enhanced Dark Matter clustering in MG scenarios. This is discussed in detail in Section 4.1.

We further investigated this halo bias relation as a function of internal halo properties, namely *halo concentration* and *halo spin*. Both these halo properties showcase interesting trends in different MG models across ranges of halo mass and z. These halo properties for our MG variants are discussed in details in Section 4.2.1 and Section 4.2.2.

Halos of a given mass, but different halo properties, can have different clustering. This phenomenon is referred to as the Halo Assembly Bias (or HAB), and is a potential source for systematics in large-scale clustering surveys. HAB has been thoroughly investigated for different attributes in ΛCDM, but such investigations lack for beyond-GR scenarios. We aim to rectify this gap and in Chapter 4, we investigate HAB for our MG scenarios. HAB is as significant in MG as is for the case of ΛCDM and showcases similar dependencies on other halo attributes as is obtained for ΛCDM. Furthermore, we observed that the HAB is not impacted by the MG physics, as our MG results do not show departure from the ΛCDM the HAB amplitude. This is an important investigation as we aim to build unbiased analytical methods to study LSS clustering from ongoing and future surveys.

6.4 Impact of Modified Gravity models in different Cosmic Web environments

Large-scale cosmic density field manifests in the form of web-like structures, which is referred to as the Cosmic Web (CW). CW forms the environment for halos (and in-turn galaxies) to form and evolve, and we expect that the properties of these LSS are influenced by the environment that hosts them. This has been substantiated both in simulations and observations.

Since the existence of the CW is a consequence of the intrinsic anisotropic nature of gravitational collapse of the density field, we expect that any modifications to the underlying gravity theory will impact the influence of CW on LSS properties. Taking this as the motivation, we build this chapter to investigate the impact of both $f(R)$ and nDGP gravity on the Dark Matter density and halo properties in different CW environments.

We begin by studying the density distribution in each CW environment, and for each gravity model. Density in each environment shows similar distribution, so which we further probe the higher order clustering moments to quantitatively differentiate this density distribution. We investigate the variance, skewness and kurtosis for both ΛCDM and MG models. Both the absolute values of these clustering statistics, as well as their ratio with ΛCDM showcased an intricate trend with the CW environment, and the length scales. These results clearly show that the studies with CW encode more significant information than averaging over all the environment. This is an important approach in order to disentangle the effects of MG and CW. We have discussed these results in details in Section 5.3.2. The overall density trend for all the clustering statistics, and in all the gravity models is clearly distinct from the trend seen in different CW environments.

We further quantify the previously investigated halo properties, but this time in different CW environments, and how MG impacts these properties within each distinct environment. In particular, Halo Mass Function and the universality of this relation, which was studied for all halos in Chapter 2, is not dissected in different CW environments in Section 5.4.1. Furthermore, the halo spin, previously examined for all halos in Section 4.2.2, is specifically analysed in individual CW environments in Section 5.4.2.

All these results show that there is much more information that we can extract when we study all these DM density and halo properties in different CW environments, thereby offering the potential to refine the precision of cosmological parameter constraints derived from these LSS properties. Furthermore, this study provides a promising avenue for disentangling the effects of MG, screening mechanisms, and the CW environment.

6.5 Future prospects

6.5.1 Significance in observations

Although gravity has been well-tested on small-scales (like our solar system), strong field regimes (like black holes, or neutron stars) or very early Universe (CMB), there are still regimes where we do not have strong constraints on the theory, like intergalactic or cosmological scales. Present and future cosmological surveys aim to remedy this deficit by observing the large-scale matter distribution in the Universe. As a result, in order to fully explore their capacities, it becomes crucial to understand how possible deviations from GR could alter cosmic structure formation, and the associated measures and observables. In this context, we identify a few key areas where the research presented in this thesis offers potential for extension in the observational domains.

1. Weak lensing

Weak gravitational lensing (WL) [147, 34] is one of the key cosmological probe that offers the possibility to push GR to domains where it is not yet well-tested. WL describes the gravitational effect of the large-scale matter distribution on the image of distinct sources.

At cosmological scales, a deviation from standard GR can leave detectable imprints on the lensing observations. If these deviations are incorporated, it is expected that the clustering of matter on cosmological scales would be different, leading to enhanced or reduced WL signal.

The k- range probed in this work corresponds to the mildly non-linear to non-linear regimes, where most of the contributions from cosmological observables of lensing are expected. On these scales, lensing is significant, and the main contribution comes from Dark Matter clustering. Also the power spectrum at these scales is not influenced by baryonic suppression [20, 63]. Since the sensitivity of lensing to the changes in the matter power spectrum will be very important in determining the correct theory of gravity, the first natural application of our power spectrum modelling is to predict observables measured in WL surveys.

Of particular interest to us is the WL Convergence power spectrum, $C_{\kappa\kappa}(l)$. This measure quantifies the statistical distribution of large-scale matter, and is an integral of the weighted three-dimensional density fluctuations along the line-of-sight. This quantity, for a survey-specific redshift distribution, can be directly computed from the power spectrum, by using Limber approximation [177], instead of full ray-tracing [136, 20]. Our power spectrum modelling offers an input to theoretically compute $C_{\kappa\kappa}(l)$. These theoretical predictions can be used as an input for MCMC analysis to forecast constraints on MG parameters ([14], more details of MG parameters in Section 1.8). The current constraints on these parameters lack the statistical significance necessary

to conclusively establish whether or not there is a departure from GR [5]. Surveys like EUCLID and LSST will be able to forecast much tighter constraints on these parameters.

Our research in this area is presently ongoing and continuously evolving.

2. Cluster count

The abundance of massive clusters across epochs is a sensitive measure of the modifications to the underlying gravity theory. Some previous works (e.g. [245, 96, 57]) have used theoretical predictions of Halo Mass Function, combined with observational data (for e.g. X-ray, and SZ) to forecast constraints on the deviations from the standard GR. Given percent-level accuracy of our Halo Mass Function modelling, which is calibrated against full MG N-body simulations, we expect much better constraints on the amplitude of the fifth-force using our modelling. This represents a promising aspect of our Halo Mass Function results in the observational domains, and we plan to investigate this in our future work.

3. Mock galaxy catalogues for MG

The conversion of Dark Matter halo catalogues into corresponding galaxy populations in the case of MG simulations has been limited [11, 99]. This conversion is essential to make a reliable comparison between the forecasts of these models, and the observational data. Using these catalogues, we can subsequently employ the same analysis on both the simulated and the real survey data to detect any indications of MG influencing the distribution of galaxies.

HAB effect is one of the major systematic in the large-scale clustering studies. Studies that link halos to galaxies have made efforts to incorporate HAB in their semi-analytical models [117, 62, 169, 70, 69, 72, 221]. Our results from the Chapter 4 show that MG does not impact the amplitude of HAB. Hence, we can infer that since HAB is insensitive to MG physics, it is reasonable to rely on the already existing ΛCDM-based galaxy-halo scaling relations to be further extrapolated to these MG models. This is advantageous as it is easier to run the standard scaling relations on the existing MG simulations, than constructing separate galaxy-halo scaling relations for MG as they would need to incorporate wide range of phenomenological MG parameters.

6.5.2 Modelling pairwise velocities for Modified Gravity models in the non-linear regime of structure formation

Pairwise velocities, $v_{12}(x,a)$ refers to the relative velocity between particles or tracers (halos or galaxies) for a given separation, and has shown to be a powerful test of gravity on cosmological scales. This results from the fact that $v_{12}(x,a)$ measure encodes information about the peculiar motions of LSS, which are a result of the underlying gravitational forces [223, 123, 187]. Leveraging the theoretical framework for modelling

$v_{12}(x,a)$ [116, 210, 142], we utilize our power spectrum formalism to generate predictions for modelling $v_{12}(x,a)$ for DM particles in our MG models, extending into the non-linear stages of structure formation. This modelling will be further extended to studies pertaining to halos and galaxies by incorporating the halo and galaxy bias formalisms [253]. This is an ongoing project in our research group.

6.5.3 Investigating higher resolution Modified Gravity *N*-body simulations

The analytical frameworks that have been studied in this work can be used as fast substitutes to full MG simulations, and are powerful tools for quickly exploring a large parameter space of these MG frameworks. However, MG simulations are nevertheless necessary to calibrate these methods or when better accuracy is needed, as well as to study the impact of different theories of gravity on galaxy formation. Also the ELEPHANT simulations, that form the main basis of this thesis, probe the intermediate to high halo mass regimes ($\geq 7.8 \times 10^{12}$ $M_\odot/h$). A more detailed study of MG properties is required even in the context of low mass halos, where both environmental and secondary halo properties show significant influence. Also, the scale-dependent $f(R)$ gravity and the chameleon screening mechanisms have interesting implications on small halo scales. The HMF trends (Chapter 2), HM framework (Chapter 3), direct concentration relation fitting (Section 4.2.1), Halo spin for lower mass halos (Section 4.2.2), HAB analysis (Chapter 4), and CW impact on MG physics (Chapter 5) would all benefit from greater well-resolved simulations for better calibration and scrutiny of LSS properties.

These endeavours will require a completely new set of high-resolution MG *N*-body simulations on which our research group is presently working on. It is our aim to rigorously examine the robustness of our existing models and analysis, and to refine and enhance these results as necessary.

6.6 Caveats: exclusion of baryonic effects

In this thesis, we only focus on the results generated using gravity-only simulations, *i.e.* the non-gravitational forces of baryons of LSS properties is not accounted. It is important to note that disregarding the non-gravitational effects of baryons on galaxy and cluster scales have important implications in the observational domains, and can significantly impact our cosmological inferences. In this context, [20] show the degenerate impact of baryonic feedback and MG in the matter power spectrum on small scales, [19] show that $f(R)$ physics significantly influences galaxy formation, and [203] quantify the impact of MG on cluster observables.

The work presented in this thesis is a first step towards analysing and modelling the impact of MG on the measures impacted by gravitational forces. The focus of

our investigation encompasses the properties of the large-scale structure, where the dominant factors are primarily driven by Dark Matter clustering, and the effects of baryons on these scales can be considered as sub-dominant. This is a crucial step as it helps us to examine the primary impact of MG phenomenologies, and discern any potential effects on the gravitational forces, and the underlying measures. This is much more computationally efficient than directly running the sophistical MG hydrodynamical simulations without quantifying the first-order effects of gravity on Dark Matter and baryons. Our investigation also enables a more targeted exploration of the impacts of MG on the large-scale structure properties. Also, in Chapters 2 and 3 we provide analytical modelling of the response functions instead of absolute values. Baryonic effects, could, in principle be included in our analytical expressions through a baseline ΛCDM Halo Mass Function, and Power Spectrum which would be calibrated against hydrodynamical simulations.

6.7 Concluding remarks

Cosmology has evolved from being a phenomenological science, to a quantitative science which can be tested and validated. This is attributed to high-quality data that we are generating for the past decades, thanks to the advancements in cosmological simulations, and large-scale observations. To fully comprehend the insights that these huge data-sets will unveil about our Universe, including the nature of Dark Matter and Dark Energy, the structure of the Cosmic Web, the underlying gravitational physics governing LSS formation and evolution, and the large-scale distribution of matter, it is imperative to generate accurate and comprehensive theoretical predictions for both standard and non-standard cosmological models. These predictions are especially vital given the high-precision data that we will generate from surveys like DES, DESI, LSST, SKA, EUCLID, and others.

In this thesis, we worked in this direction to stress-test two alternate non-standard scenarios: $f(R)$ and nDGP gravity models. We show how these models impact LSS properties, and proposed theoretical modelling of their differences with the standard ΛCDM paradigm. We hope that this thesis facilitates the potential for refining our understanding of these models, and, in the long run, ultimately aiming to unveil the underlying physics responsible for the accelerated expansion of our Universe.

Bibliography

[1] B. P. Abbott et al. "Observation of Gravitational Waves from a Binary Black Hole Merger". Phys. Rev. Lett. 116.6, 061102 (Feb. 2016), p. 061102. DOI: 10.1103/PhysRevLett.116.061102. arXiv: 1602.03837 [gr-qc].

[2] B. P. Abbott et al. "GW170817: Observation of Gravitational Waves from a Binary Neutron Star Inspiral". Phys. Rev. Lett. 119.16, 161101 (Oct. 2017), p. 161101. DOI: 10.1103/PhysRevLett.119.161101. arXiv: 1710.05832 [gr-qc].

[3] T. M. C. Abbott et al. "Dark Energy Survey year 1 results: Cosmological constraints from galaxy clustering and weak lensing". Phys. Rev. D 98.4, 043526 (Aug. 2018), p. 043526. DOI: 10.1103/PhysRevD.98.043526. arXiv: 1708.01530 [astro-ph.CO].

[4] T. M. C. Abbott et al. "Cosmological Constraints from Multiple Probes in the Dark Energy Survey". Phys. Rev. Lett. 122.17, 171301 (May 2019), p. 171301. DOI: 10.1103/PhysRevLett.122.171301. arXiv: 1811.02375 [astro-ph.CO].

[5] T. M. C. Abbott et al. "Dark Energy Survey Year 3 results: Constraints on extensions to Λ CDM with weak lensing and galaxy clustering". Phys. Rev. D 107.8, 083504 (Apr. 2023), p. 083504. DOI: 10.1103/PhysRevD.107.083504. arXiv: 2207.05766 [astro-ph.CO].

[6] Ixandra Achitouv et al. "Imprint of f (R) gravity on nonlinear structure formation". Phys. Rev. D 93.10, 103522 (May 2016), p. 103522. DOI: 10.1103/PhysRevD.93.103522. arXiv: 1511.01494 [astro-ph.CO].

[7] Alberto Acuto et al. "The BAHAMAS project: evaluating the accuracy of the halo model in predicting the non-linear matter power spectrum". MNRAS 508.3 (Dec. 2021), pp. 3519–3534. DOI: 10.1093/mnras/stab2834. arXiv: 2109.11855 [astro-ph.CO].

[8] Virginia Ajani et al. "Constraining neutrino masses with weak-lensing multiscale peak counts". Phys. Rev. D 102.10, 103531 (Nov. 2020), p. 103531. DOI: 10.1103/PhysRevD.102.103531. arXiv: 2001.10993 [astro-ph.CO].

[9] Shadab Alam, Aseem Paranjape, and John A. Peacock. "Impact of tidal environment on galaxy populations using GAMA". *arXiv e-prints*, arXiv:2305.01266 (May 2023), arXiv:2305.01266. DOI: 10.48550/arXiv.2305.01266. arXiv: 2305.01266 [astro-ph.CO].

[10] Shadab Alam et al. "Completed SDSS-IV extended Baryon Oscillation Spectroscopic Survey: Cosmological implications from two decades of spectroscopic surveys at the Apache Point Observatory". Phys. Rev. D 103.8, 083533 (Apr. 2021), p. 083533. DOI: 10.1103/PhysRevD.103.083533. arXiv: 2007.08991 [astro-ph.CO].

[11] Shadab Alam et al. "Towards testing the theory of gravity with DESI: summary statistics, model predictions and future simulation requirements". J. Cosmology Astropart. Phys. 2021.11, 050 (Nov. 2021), p. 050. DOI: 10.1088/1475-7516/2021/11/050. arXiv: 2011.05771 [astro-ph.CO].

[12] D. Alonso, E. Eardley, and J. A. Peacock. "Halo abundances within the cosmic web". MNRAS 447.3 (Mar. 2015), pp. 2683–2695. DOI: 10.1093/mnras/stu2632. arXiv: 1406.4159 [astro-ph.CO].

[13] M. Alpaslan et al. "Galaxy and Mass Assembly (GAMA): fine filaments of galaxies detected within voids." MNRAS 440 (May 2014), pp. L106–L110. DOI: 10.1093/mnrasl/slu019. arXiv: 1401.7331 [astro-ph.CO].

[14] Luca Amendola, Martin Kunz, and Domenico Sapone. "Measuring the dark side (with weak lensing)". J. Cosmology Astropart. Phys. 2008.4, 013 (Apr. 2008), p. 013. DOI: 10.1088/1475-7516/2008/04/013. arXiv: 0704.2421 [astro-ph].

[15] R. E. Angulo et al. "Scaling relations for galaxy clusters in the Millennium-XXL simulation". MNRAS 426.3 (Nov. 2012), pp. 2046–2062. DOI: 10.1111/j.1365-2966.2012.21830.x. arXiv: 1203.3216 [astro-ph.CO].

[16] Raul E. Angulo et al. "The BACCO simulation project: exploiting the full power of large-scale structure for cosmology". MNRAS 507.4 (Nov. 2021), pp. 5869–5881. DOI: 10.1093/mnras/stab2018. arXiv: 2004.06245 [astro-ph.CO].

[17] M. A. Aragon-Calvo, Joseph Silk, and Mark Neyrinck. "The unusual Milky Way-local sheet system: implications for spin strength and alignment". MNRAS 520.1 (Mar. 2023), pp. L28–L32. DOI: 10.1093/mnrasl/slac161. arXiv: 2208.03338 [astro-ph.GA].

[18] Miguel A. Aragón-Calvo et al. "The Spine of the Cosmic Web". ApJL 723.1 (Nov. 2010), pp. 364–382. DOI: 10.1088/0004-637X/723/1/364. arXiv: 0809.5104 [astro-ph].

[19] Christian Arnold, Matteo Leo, and Baojiu Li. "Realistic simulations of galaxy formation in f(R) modified gravity". *Nature Astronomy* 3 (July 2019), pp. 945–954. DOI: 10.1038/s41550-019-0823-y. arXiv: 1907.02977 [astro-ph.CO].

[20] Christian Arnold et al. "The modified gravity light-cone simulation project - I. Statistics of matter and halo distributions". MNRAS 483.1 (Feb. 2019), pp. 790–805. DOI: 10.1093/mnras/sty3044. arXiv: 1805.09824 [astro-ph.CO].

[21] Christian Arnold et al. "FORGE: the f(R)-gravity cosmic emulator project - I. Introduction and matter power spectrum emulator". MNRAS 515.3 (Sept. 2022), pp. 4161–4175. DOI: 10.1093/mnras/stac1091. arXiv: 2109.04984 [astro-ph.CO].

[22] Marika Asgari, Alexander J. Mead, and Catherine Heymans. "The halo model for cosmology: a pedagogical review". *arXiv e-prints*, arXiv:2303.08752 (Mar. 2023), arXiv:2303.08752. arXiv: 2303.08752 [astro-ph.CO].

[23] Marika Asgari et al. "KiDS-1000 cosmology: Cosmic shear constraints and comparison between two point statistics". A&A 645, A104 (Jan. 2021), A104. DOI: 10.1051/0004-6361/202039070. arXiv: 2007.15633 [astro-ph.CO].

[24] J. S. Bagla, Nishikanta Khandai, and Girish Kulkarni. "Mass function of haloes: scale invariant models". *arXiv e-prints*, arXiv:0908.2702 (Aug. 2009), arXiv:0908.2702. DOI: 10.48550/arXiv.0908.2702. arXiv: 0908.2702 [astro-ph.CO].

[25] Tessa Baker, Dimitrios Psaltis, and Constantinos Skordis. "Linking Tests of Gravity on All Scales: from the Strong-field Regime to Cosmology". ApJL 802.1, 63 (Mar. 2015), p. 63. DOI: 10.1088/0004-637X/802/1/63. arXiv: 1412.3455 [astro-ph.CO].

[26] Tessa Baker et al. "Novel Probes Project: Tests of gravity on astrophysical scales". *Reviews of Modern Physics* 93.1, 015003 (Jan. 2021), p. 015003. DOI: 10.1103/RevModPhys.93.015003.

[27] J. M. Bardeen et al. "The Statistics of Peaks of Gaussian Random Fields". ApJL 304 (May 1986), p. 15. DOI: 10.1086/164143.

[28] James M. Bardeen. "Gauge-invariant cosmological perturbations". *Phys. Rev. D* 22 (8 Oct. 1980), pp. 1882–1905. DOI: 10.1103/PhysRevD.22.1882. URL: https://link.aps.org/doi/10.1103/PhysRevD.22.1882.

[29] Alexandre Barreira, Sownak Bose, and Baojiu Li. "Speeding up N-body simulations of modified gravity: Vainshtein screening models". J. Cosmology Astropart. Phys. 2015.12 (Dec. 2015), pp. 059–059. DOI: 10.1088/1475-7516/2015/12/059. arXiv: 1511.08200 [astro-ph.CO].

[30] Alexandre Barreira, Sownak Bose, and Baojiu Li. "Speeding up N-body simulations of modified gravity: Vainshtein screening models". J. Cosmology Astropart. Phys. 2015.12, 059 (Dec. 2015), p. 059. DOI: 10.1088/1475-7516/2015/12/059. arXiv: 1511.08200 [astro-ph.CO].

[31] Alexandre Barreira, Ariel G. Sánchez, and Fabian Schmidt. "Validating estimates of the growth rate of structure with modified gravity simulations". Phys. Rev. D 94.8, 084022 (Oct. 2016), p. 084022. DOI: 10.1103/PhysRevD.94.084022. arXiv: 1605.03965 [astro-ph.CO].

[32] Alexandre Barreira et al. "Halo model and halo properties in Galileon gravity cosmologies". *JCAP* 04 (2014), p. 029. DOI: 10.1088/1475-7516/2014/04/029. arXiv: 1401.1497 [astro-ph.CO].

[33] Alexandre Barreira et al. "Nonlinear structure formation in nonlocal gravity". J. Cosmology Astropart. Phys. 2014.9, 031 (Sept. 2014), p. 031. DOI: 10.1088/1475-7516/2014/09/031. arXiv: 1408.1084 [astro-ph.CO].

[34] Matthias Bartelmann and Matteo Maturi. "Weak gravitational lensing". *Scholarpedia* 12.1 (Jan. 2017), p. 32440. DOI: 10.4249/scholarpedia.32440. arXiv: 1612.06535 [astro-ph.CO].

[35] Adrian E. Bayer et al. "Detecting Neutrino Mass by Combining Matter Clustering, Halos, and Voids". ApJL 919.1, 24 (Sept. 2021), p. 24. DOI: 10.3847/1538-4357/ac0e91. arXiv: 2102.05049 [astro-ph.CO].

[36] Peter S. Behroozi, Risa H. Wechsler, and Hao-Yi Wu. "The ROCKSTAR Phase-space Temporal Halo Finder and the Velocity Offsets of Cluster Cores". ApJL 762.2, 109 (Jan. 2013), p. 109. DOI: 10.1088/0004-637X/762/2/109. arXiv: 1110.4372 [astro-ph.CO].

[37] M.J. Berger and P. Colella. "Local adaptive mesh refinement for shock hydrodynamics". *Journal of Computational Physics* 82.1 (1989), pp. 64–84. ISSN: 0021-9991. DOI: https://doi.org/10.1016/0021-9991(89)90035-1. URL: https://www.sciencedirect.com/science/article/pii/0021999189900351.

[38] F. Bernardeau. "The effects of smoothing on the statistical properties of large-scale cosmic fields." A&A 291 (Nov. 1994), pp. 697–712. DOI: 10.48550/arXiv.astro-ph/9403020. arXiv: astro-ph/9403020 [astro-ph].

[39] F. Bernardeau et al. "Large-scale structure of the Universe and cosmological perturbation theory". Phys. Rep. 367.1-3 (Sept. 2002), pp. 1–248. DOI: 10.1016/S0370-1573(02)00135-7. arXiv: astro-ph/0112551 [astro-ph].

[40] M. Betoule et al. "Improved cosmological constraints from a joint analysis of the SDSS-II and SNLS supernova samples". A&A 568, A22 (Aug. 2014), A22. DOI: 10.1051/0004-6361/201423413. arXiv: 1401.4064 [astro-ph.CO].

[41] Philip Bett et al. "The spin and shape of dark matter haloes in the Millennium simulation of a Λ cold dark matter universe". MNRAS 376.1 (Mar. 2007), pp. 215–232. DOI: 10.1111/j.1365-2966.2007.11432.x. arXiv: astro-ph/0608607 [astro-ph].

[42] Philip Bett et al. "The spin and shape of dark matter haloes in the Millennium simulation of a Λ cold dark matter universe". MNRAS 376.1 (Mar. 2007), pp. 215–232. DOI: 10.1111/j.1365-2966.2007.11432.x. arXiv: astro-ph/0608607 [astro-ph].

[43] J. R. Bond and S. T. Myers. "The Peak-Patch Picture of Cosmic Catalogs. I. Algorithms". ApJS 103 (Mar. 1996), p. 1. DOI: 10.1086/192267.

[44] J. R. Bond et al. "Excursion Set Mass Functions for Hierarchical Gaussian Fluctuations". ApJL 379 (Oct. 1991), p. 440. DOI: 10.1086/170520.

[45] J. Richard Bond, Lev Kofman, and Dmitry Pogosyan. "How filaments of galaxies are woven into the cosmic web". Nature 380.6575 (Apr. 1996), pp. 603–606. DOI: 10.1038/380603a0. arXiv: astro-ph/9512141 [astro-ph].

[46] J. Richard Bond, Lev Kofman, and Dmitry Pogosyan. "How filaments of galaxies are woven into the cosmic web". Nature 380.6575 (Apr. 1996), pp. 603–606. DOI: 10.1038/380603a0. arXiv: astro-ph/9512141 [astro-ph].

[47] Tony Bonnaire et al. "Cosmology with cosmic web environments. I. Real-space power spectra". A&A 661, A146 (May 2022), A146. DOI: 10.1051/0004-6361/202142852. arXiv: 2112.03926 [astro-ph.CO].

[48] Tony Bonnaire et al. "Cosmology with cosmic web environments. II. Redshift-space auto and cross-power spectra". A&A 674, A150 (June 2023), A150. DOI: 10.1051/0004-6361/202245626. arXiv: 2212.06838 [astro-ph.CO].

[49] Sownak Bose, Wojciech A. Hellwing, and Baojiu Li. "Testing the quasi-static approximation in f(R) gravity simulations". J. Cosmology Astropart. Phys. 2015.2, 034 (Feb. 2015), p. 034. DOI: 10.1088/1475-7516/2015/02/034. arXiv: 1411.6128 [astro-ph.CO].

[50] Sownak Bose et al. "Speeding up N-body simulations of modified gravity: chameleon screening models". J. Cosmology Astropart. Phys. 2017.2, 050 (Feb. 2017), p. 050. DOI: 10.1088/1475-7516/2017/02/050. arXiv: 1611.09375 [astro-ph.CO].

[51] Michael Boylan-Kolchin et al. "Resolving cosmic structure formation with the Millennium-II Simulation". MNRAS 398.3 (Sept. 2009), pp. 1150–1164. DOI: 10.1111/j.1365-2966.2009.15191.x. arXiv: 0903.3041 [astro-ph.CO].

[52] Philip Bull et al. "Beyond Λ CDM: Problems, solutions, and the road ahead". *Physics of the Dark Universe* 12 (June 2016), pp. 56–99. DOI: 10.1016/j.dark.2016.02.001. arXiv: 1512.05356 [astro-ph.CO].

[53] J. S. Bullock et al. "A Universal Angular Momentum Profile for Galactic Halos". ApJL 555.1 (July 2001), pp. 240–257. DOI: 10.1086/321477. arXiv: astro-ph/0011001 [astro-ph].

[54] James S. Bullock and Michael Boylan-Kolchin. "Small-Scale Challenges to the ΛCDM Paradigm". ARA&A 55.1 (Aug. 2017), pp. 343–387. DOI: 10.1146/annurev-astro-091916-055313. arXiv: 1707.04256 [astro-ph.CO].

[55] M. Cataneo et al. "On the road to percent accuracy: non-linear reaction of the matter power spectrum to dark energy and modified gravity". MNRAS 488.2 (Sept. 2019), pp. 2121–2142. DOI: 10.1093/mnras/stz1836. arXiv: 1812.05594 [astro-ph.CO].

[56] Matteo Cataneo et al. "New constraints on f(R) gravity from clusters of galaxies". Phys. Rev. D 92.4, 044009 (Aug. 2015), p. 044009. DOI: 10.1103/PhysRevD.92.044009. arXiv: 1412.0133 [astro-ph.CO].

[57] Matteo Cataneo et al. "Cluster abundance in chameleon f(R) gravity I: toward an accurate halo mass function prediction". J. Cosmology Astropart. Phys. 2016.12, 024 (Dec. 2016), p. 024. DOI: 10.1088/1475-7516/2016/12/024. arXiv: 1607.08788 [astro-ph.CO].

[58] Marius Cautun, Rien van de Weygaert, and Bernard J. T. Jones. "NEXUS: tracing the cosmic web connection". MNRAS 429.2 (Feb. 2013), pp. 1286–1308. DOI: 10.1093/mnras/sts416. arXiv: 1209.2043 [astro-ph.CO].

[59] Marius Cautun et al. "Evolution of the cosmic web". MNRAS 441.4 (July 2014), pp. 2923–2973. DOI: 10.1093/mnras/stu768. arXiv: 1401.7866 [astro-ph.CO].

[60] Marius Cautun et al. "The Santiago-Harvard-Edinburgh-Durham void comparison-I. SHEDding light on chameleon gravity tests". MNRAS 476.3 (May 2018), pp. 3195–3217. DOI: 10.1093/mnras/sty463. arXiv: 1710.01730 [astro-ph.CO].

[61] S. Chandrasekhar. "Stochastic problems in physics and astronomy". *Reviews of modern physics* 15.1 (1943).

[62] Jonás Chaves-Montero et al. "Subhalo abundance matching and assembly bias in the EAGLE simulation". MNRAS 460.3 (Aug. 2016), pp. 3100–3118. DOI: 10.1093/mnras/stw1225. arXiv: 1507.01948 [astro-ph.GA].

[63] Nora Elisa Chisari et al. "Modelling baryonic feedback for survey cosmology". *The Open Journal of Astrophysics* 2.1, 4 (June 2019), p. 4. DOI: 10.21105/astro.1905.06082. arXiv: 1905.06082 [astro-ph.CO].

[64] Timothy Clifton et al. "Modified gravity and cosmology". Phys. Rep. 513.1 (Mar. 2012), pp. 1–189. DOI: 10.1016/j.physrep.2012.01.001. arXiv: 1106.2476 [astro-ph.CO].

[65] Shaun Cole and Nick Kaiser. "Biased clustering in the cold dark matter cosmogony." MNRAS 237 (Apr. 1989), pp. 1127–1146. DOI: 10.1093/mnras/237.4.1127.

[66] Peter Coles and Bernard Jones. "A lognormal model for the cosmological mass distribution." MNRAS 248 (Jan. 1991), pp. 1–13. DOI: 10.1093/mnras/248.1.1.

[67] Planck Collaboration. "Planck 2015 results. XIII. Cosmological parameters". A&A 594, A13 (Sept. 2016), A13. DOI: 10.1051/0004-6361/201525830. arXiv: 1502.01589 [astro-ph.CO].

[68] Planck Collaboration. "Planck 2018 results. VI. Cosmological parameters". A&A 641, A6 (Sept. 2020), A6. DOI: 10.1051/0004-6361/201833910. arXiv: 1807.06209 [astro-ph.CO].

[69] S. Contreras, R. E. Angulo, and M. Zennaro. "A flexible subhalo abundance matching model for galaxy clustering in redshift space". MNRAS 508.1 (Nov. 2021), pp. 175–189. DOI: 10.1093/mnras/stab2560. arXiv: 2012.06596 [astro-ph.CO].

[70] S. Contreras et al. "The evolution of the galaxy content of dark matter haloes". MNRAS 465.3 (Mar. 2017), pp. 2833–2848. DOI: 10.1093/mnras/stw2826. arXiv: 1607.06154 [astro-ph.GA].

[71] S. Contreras et al. "The cosmological dependence of halo and galaxy assembly bias". MNRAS 507.3 (Nov. 2021), pp. 3412–3422. DOI: 10.1093/mnras/stab2367. arXiv: 2105.05854 [astro-ph.CO].

[72] Sergio Contreras et al. "The MillenniumTNG Project: inferring cosmology from galaxy clustering with accelerated N-body scaling and subhalo abundance matching". MNRAS 524.2 (Sept. 2023), pp. 2489–2506. DOI: 10.1093/mnras/stac3699. arXiv: 2210.10075 [astro-ph.GA].

[73] Asantha Cooray and Ravi Sheth. "Halo models of large scale structure". Phys. Rep. 372.1 (Dec. 2002), pp. 1–129. DOI: 10.1016/S0370-1573(02)00276-4. arXiv: astro-ph/0206508 [astro-ph].

[74] Matteo Costanzi et al. "Cosmology with massive neutrinos III: the halo mass function and an application to galaxy clusters". J. Cosmology Astropart. Phys. 2013.12, 012 (Dec. 2013), p. 012. DOI: 10.1088/1475-7516/2013/12/012. arXiv: 1311.1514 [astro-ph.CO].

[75] J. Courtin et al. "Imprints of dark energy on cosmic structure formation - II. Non-universality of the halo mass function". MNRAS 410.3 (Jan. 2011), pp. 1911–1931. DOI: 10.1111/j.1365-2966.2010.17573.x. arXiv: 1001.3425 [astro-ph.CO].

[76] Martın Crocce, Sebastián Pueblas, and Román Scoccimarro. "Transients from initial conditions in cosmological simulations". MNRAS 373.1 (Nov. 2006), pp. 369–381. DOI: 10.1111/j.1365-2966.2006.11040.x. arXiv: astro-ph/0606505 [astro-ph].

[77] Martın Crocce et al. "Simulating the Universe with MICE: the abundance of massive clusters". MNRAS 403.3 (Apr. 2010), pp. 1353–1367. DOI: 10.1111/j.1365-2966.2009.16194.x. arXiv: 0907.0019 [astro-ph.CO].

[78] Richard H. Cyburt et al. "Big bang nucleosynthesis: Present status". *Reviews of Modern Physics* 88.1, 015004 (Jan. 2016), p. 015004. DOI: 10.1103/RevModPhys.88.015004. arXiv: 1505.01076 [astro-ph.CO].

[79] Cédric Deffayet et al. "Nonperturbative continuity in graviton mass versus perturbative discontinuity". Phys. Rev. D 65 (4 Jan. 2002), p. 044026. DOI: 10.1103/PhysRevD.65.044026. URL: https://link.aps.org/doi/10.1103/PhysRevD.65.044026.

[80] DESI Collaboration. "The DESI Experiment Part I: Science,Targeting, and Survey Design". *arXiv e-prints*, arXiv:1611.00036 (Oct. 2016), arXiv:1611.00036. DOI: 10.48550/arXiv.1611.00036. arXiv: 1611.00036 [astro-ph.IM].

[81] Vincent Desjacques. "Environmental dependence in the ellipsoidal collapse model". MNRAS 388.2 (Aug. 2008), pp. 638–658. DOI: 10.1111/j.1365-2966.2008.13420.x. arXiv: 0707.4670 [astro-ph].

[82] Vincent Desjacques, Donghui Jeong, and Fabian Schmidt. "Large-scale galaxy bias". Phys. Rep. 733 (Feb. 2018), pp. 1–193. DOI: 10.1016/j.physrep.2017.12.002. arXiv: 1611.09787 [astro-ph.CO].

[83] Giulia Despali et al. "The universality of the virial halo mass function and models for non-universality of other halo definitions". MNRAS 456.3 (Mar. 2016), pp. 2486–2504. DOI: 10.1093/mnras/stv2842. arXiv: 1507.05627 [astro-ph.CO].

[84] Benedikt Diemer. "Universal at Last? The Splashback Mass Function of Dark Matter Halos". ApJL 903.2, 87 (Nov. 2020), p. 87. DOI: 10.3847/1538-4357/abbf52. arXiv: 2007.10346 [astro-ph.CO].

[85] Benedikt Diemer and Andrey V. Kravtsov. "A Universal Model for Halo Concentrations". ApJL 799.1, 108 (Jan. 2015), p. 108. DOI: 10.1088/0004-637X/799/1/108. arXiv: 1407.4730 [astro-ph.CO].

[86] Scott Dodelson and Fabian Schmidt. *Modern Cosmology*. 2020. DOI: 10.1016/C2017-0-01943-2.

[87] Tibor Dome et al. "Cosmic web dissection in fuzzy dark matter cosmologies". MNRAS 525.1 (Oct. 2023), pp. 348–363. DOI: 10.1093/mnras/stad2276. arXiv: 2301.09762 [astro-ph.CO].

[88] Paweł Drozda, Wojciech A. Hellwing, and Maciej Bilicki. "Galaxy and halo angular clustering in Λ CDM and modified gravity cosmologies". Phys. Rev. D 106.4, 043513 (Aug. 2022), p. 043513. DOI: 10.1103/PhysRevD.106.043513. arXiv: 2204.05305 [astro-ph.CO].

[89] Alan R. Duffy et al. "Dark matter halo concentrations in the Wilkinson Microwave Anisotropy Probe year 5 cosmology". MNRAS 390.1 (Oct. 2008), pp. L64–L68. DOI: 10.1111/j.1745-3933.2008.00537.x. arXiv: 0804.2486 [astro-ph].

[90] G. Dvali, G. Gabadadze, and M. Porrati. "4D gravity on a brane in 5D Minkowski space". *Physics Letters B* 485.1-3 (July 2000), pp. 208–214. DOI: 10.1016/S0370-2693(00)00669-9. arXiv: hep-th/0005016 [hep-th].

[91] Jaan Einasto et al. "Evolution of skewness and kurtosis of cosmic density fields". A&A 652, A94 (Aug. 2021), A94. DOI: 10.1051/0004-6361/202039999. arXiv: 2011.13292 [astro-ph.CO].

[92] Daniel J. Eisenstein et al. "Detection of the Baryon Acoustic Peak in the Large-Scale Correlation Function of SDSS Luminous Red Galaxies". ApJL 633.2 (Nov. 2005), pp. 560–574. DOI: 10.1086/466512. arXiv: astro-ph/0501171 [astro-ph].

[93] Bridget Falck et al. "The Vainshtein mechanism in the cosmic web". J. Cosmology Astropart. Phys. 2014.7, 058 (July 2014), p. 058. DOI: 10.1088/1475-7516/2014/07/058. arXiv: 1404.2206 [astro-ph.CO].

[94] S. M. Fall and G. Efstathiou. "Formation and rotation of disc galaxies with haloes." MNRAS 193 (Oct. 1980), pp. 189–206. DOI: 10.1093/mnras/193.2.189.

[95] Andreas Faltenbacher and Simon D. M. White. "Assembly Bias and the Dynamical Structure of Dark Matter Halos". ApJL 708.1 (Jan. 2010), pp. 469–473. DOI: 10.1088/0004-637X/708/1/469. arXiv: 0909.4302 [astro-ph.CO].

[96] Simone Ferraro, Fabian Schmidt, and Wayne Hu. "Cluster abundance in f(R) gravity models". Phys. Rev. D 83.6, 063503 (Mar. 2011), p. 063503. DOI: 10.1103/PhysRevD.83.063503. arXiv: 1011.0992 [astro-ph.CO].

[97] Pedro G. Ferreira. "Cosmological Tests of Gravity". ARA&A 57 (Aug. 2019), pp. 335–374. DOI: 10.1146/annurev-astro-091918-104423. arXiv: 1902.10503 [astro-ph.CO].

[98] Bartolomeo Fiorini, Kazuya Koyama, and Tessa Baker. "Fast production of cosmological emulators in modified gravity: the matter power spectrum". *arXiv e-prints*, arXiv:2310.05786 (Oct. 2023), arXiv:2310.05786. DOI: 10.48550/arXiv.2310.05786. arXiv: 2310.05786 [astro-ph.CO].

[99] Bartolomeo Fiorini et al. "Fast generation of mock galaxy catalogues in modified gravity models with COLA". J. Cosmology Astropart. Phys. 2021.9, 021 (Sept. 2021), p. 021. DOI: 10.1088/1475-7516/2021/09/021. arXiv: 2106.05197 [astro-ph.CO].

[100] J. E. Forero-Romero et al. "A dynamical classification of the cosmic web". MNRAS 396.3 (July 2009), pp. 1815–1824. DOI: 10.1111/j.1365-2966.2009.14885.x. arXiv: 0809.4135 [astro-ph].

[101] Punyakoti Ganeshaiah Veena et al. "The Cosmic Ballet: spin and shape alignments of haloes in the cosmic web". MNRAS 481.1 (Nov. 2018), pp. 414–438. DOI: 10.1093/mnras/sty2270. arXiv: 1805.00033 [astro-ph.CO].

[102] Punyakoti Ganeshaiah Veena et al. "The Cosmic Ballet II: spin alignment of galaxies and haloes with large-scale filaments in the EAGLE simulation". MNRAS 487.2 (Aug. 2019), pp. 1607–1625. DOI: 10.1093/mnras/stz1343. arXiv: 1903.06716 [astro-ph.CO].

[103] Punyakoti Ganeshaiah Veena et al. "Cosmic Ballet III: Halo spin evolution in the cosmic web". MNRAS 503.2 (May 2021), pp. 2280–2299. DOI: 10.1093/mnras/stab411. arXiv: 2007.10365 [astro-ph.CO].

[104] Liang Gao, Volker Springel, and Simon D. M. White. "The age dependence of halo clustering". MNRAS 363.1 (Oct. 2005), pp. L66–L70. DOI: 10.1111/j.1745-3933.2005.00084.x. arXiv: astro-ph/0506510 [astro-ph].

[105] Liang Gao and Simon D. M. White. "Assembly bias in the clustering of dark matter haloes". MNRAS 377.1 (Apr. 2007), pp. L5–L9. DOI: 10.1111/j.1745-3933.2007.00292.x. arXiv: astro-ph/0611921 [astro-ph].

[106] Jorge Enrique Garcıa-Farieta, Héctor J Hortúa, and Francisco-Shu Kitaura. "Bayesian deep learning for cosmic volumes with modified gravity". *arXiv e-prints*, arXiv:2309.00612 (Sept. 2023), arXiv:2309.00612. DOI: 10.48550/arXiv.2309.00612. arXiv: 2309.00612 [astro-ph.CO].

[107] Jorge Enrique Garcıa-Farieta et al. "Probing gravity with redshift-space distortions: Effects of tracer bias and sample selection". Phys. Rev. D 103.10, 103524 (May 2021), p. 103524. DOI: 10.1103/PhysRevD.103.103524. arXiv: 2103.14019 [astro-ph.CO].

[108] Shiming Gu et al. "A non-standard Halo Mass Function as a solution to the structure-growth tension, application to KiDS-1000 and DES-y3". *arXiv e-prints*, arXiv:2302.00780 (Feb. 2023), arXiv:2302.00780. DOI: 10.48550/arXiv.2302.00780. arXiv: 2302.00780 [astro-ph.CO].

[109] James E. Gunn and III Gott J. Richard. "On the Infall of Matter Into Clusters of Galaxies and Some Effects on Their Evolution". ApJL 176 (Aug. 1972), p. 1. DOI: 10.1086/151605.

[110] Suhani Gupta, Wojciech A. Hellwing, and Maciej Bilicki. "Improved analytical modeling of the nonlinear power spectrum in modified gravity cosmologies". Phys. Rev. D 107.8, 083525 (Apr. 2023), p. 083525. DOI: 10.1103/PhysRevD.107.083525. arXiv: 2301.12016 [astro-ph.CO].

[111] Suhani Gupta et al. "Halo Mass Function as a Probe of Gravity". *XL Polish Astronomical Society Meeting*. Ed. by Ewa Szuszkiewicz et al. Vol. 12. Oct. 2022, pp. 95–98.

[112] Suhani Gupta et al. "Universality of the halo mass function in modified gravity cosmologies". Phys. Rev. D 105.4, 043538 (Feb. 2022), p. 043538. DOI: 10.1103/PhysRevD.105.043538. arXiv: 2112.03699 [astro-ph.CO].

[113] Oliver Hahn et al. "Properties of dark matter haloes in clusters, filaments, sheets and voids". MNRAS 375.2 (Feb. 2007), pp. 489–499. DOI: 10.1111/j.1365-2966.2006.11318.x. arXiv: astro-ph/0610280 [astro-ph].

[114] Oliver Hahn et al. "Tidal effects and the environment dependence of halo assembly". MNRAS 398.4 (Oct. 2009), pp. 1742–1756. DOI: 10.1111/j.1365-2966.2009.15271.x. arXiv: 0803.4211 [astro-ph].

[115] Takashi Hamana et al. "Cosmological constraints from cosmic shear two-point correlation functions with HSC survey first-year data". PASJ 72.1, 16 (Feb. 2020), p. 16. DOI: 10.1093/pasj/psz138. arXiv: 1906.06041 [astro-ph.CO].

[116] A. J. S. Hamilton et al. "Reconstructing the Primordial Spectrum of Fluctuations of the Universe from the Observed Nonlinear Clustering of Galaxies". ApJ 374 (June 1991), p. L1. DOI: 10.1086/186057.

[117] Andrew P. Hearin et al. "Introducing decorated HODs: modelling assembly bias in the galaxy-halo connection". MNRAS 460.3 (Aug. 2016), pp. 2552–2570. DOI: 10.1093/mnras/stw840. arXiv: 1512.03050 [astro-ph.CO].

[118] Katrin Heitmann et al. "The Last Journey. I. An Extreme-scale Simulation on the Mira Supercomputer". ApJS 252.2, 19 (Feb. 2021), p. 19. DOI: 10.3847/1538-4365/abcc67. arXiv: 2006.01697 [astro-ph.CO].

[119] Wojciech A. Hellwing and Roman Juszkiewicz. "Dark matter gravitational clustering with a long-range scalar interaction". Phys. Rev. D 80.8, 083522 (Oct. 2009), p. 083522. DOI: 10.1103/PhysRevD.80.083522. arXiv: 0809.1976 [astro-ph].

[120] Wojciech A. Hellwing, Roman Juszkiewicz, and Rien van de Weygaert. "Hierarchy of N-point functions in the ΛCDM and ReBEL cosmologies". Phys. Rev. D 82.10, 103536 (Nov. 2010), p. 103536. DOI: 10.1103/PhysRevD.82.103536. arXiv: 1008.3930 [astro-ph.CO].

[121] Wojciech A. Hellwing et al. "DM haloes in the fifth-force cosmology". J. Cosmology Astropart. Phys. 2013.10, 012 (Oct. 2013), p. 012. DOI: 10.1088/1475-7516/2013/10/012. arXiv: 1111.7257 [astro-ph.CO].

[122] Wojciech A. Hellwing et al. "Hierarchical clustering in chameleon f(R) gravity". MNRAS 435.4 (Sept. 2013), pp. 2806–2821. ISSN: 0035-8711. DOI: 10.1093/mnras/stt1430. eprint: https://academic.oup.com/mnras/article-pdf/435/4/2806/3367715/stt1430.pdf. URL: https://doi.org/10.1093/mnras/stt1430.

[123] Wojciech A. Hellwing et al. "Clear and Measurable Signature of Modified Gravity in the Galaxy Velocity Field". Phys. Rev. Lett. 112.22, 221102 (June 2014), p. 221102. DOI: 10.1103/PhysRevLett.112.221102. arXiv: 1401.0706 [astro-ph.CO].

[124] Wojciech A. Hellwing et al. "The Copernicus Complexio: a high-resolution view of the small-scale Universe". MNRAS 457.4 (Apr. 2016), pp. 3492–3509. DOI: 10.1093/mnras/stw214. arXiv: 1505.06436 [astro-ph.CO].

[125] Wojciech A. Hellwing et al. "Revealing modified gravity signals in matter and halo hierarchical clustering". Phys. Rev. D 96.2, 023515 (July 2017), p. 023515. DOI: 10.1103/PhysRevD.96.023515. arXiv: 1703.03395 [astro-ph.CO].

[126] Wojciech A. Hellwing et al. "Caught in the cosmic web: Environmental effect on halo concentrations, shape, and spin". Phys. Rev. D 103.6, 063517 (Mar. 2021), p. 063517. DOI: 10.1103/PhysRevD.103.063517. arXiv: 2011.08840 [astro-ph.CO].

[127] César Hernández-Aguayo et al. "Galaxy formation in the brane world I: overview and first results". MNRAS 503.3 (May 2021), pp. 3867–3885. DOI: 10.1093/mnras/stab694. arXiv: 2006.15467 [astro-ph.CO].

[128] Catherine Heymans et al. "CFHTLenS tomographic weak lensing cosmological parameter constraints: Mitigating the impact of intrinsic galaxy alignments". MNRAS 432.3 (July 2013), pp. 2433–2453. DOI: 10.1093/mnras/stt601. arXiv: 1303.1808 [astro-ph.CO].

[129] Chiaki Hikage et al. "Cosmology from cosmic shear power spectra with Subaru Hyper Suprime-Cam first-year data". PASJ 71.2, 43 (Apr. 2019), p. 43. DOI: 10.1093/pasj/psz010. arXiv: 1809.09148 [astro-ph.CO].

[130] G. Hinshaw et al. "Nine-year Wilkinson Microwave Anisotropy Probe (WMAP) Observations: Cosmological Parameter Results". ApJS 208.2, 19 (Oct. 2013), p. 19. DOI: 10.1088/0067-0049/208/2/19. arXiv: 1212.5226 [astro-ph.CO].

[131] Yehuda Hoffman et al. "A kinematic classification of the cosmic web". MNRAS 425.3 (Sept. 2012), pp. 2049–2057. DOI: 10.1111/j.1365-2966.2012.21553.x. arXiv: 1201.3367 [astro-ph.CO].

[132] F. Hoyle. "The Origin of the Rotations of the Galaxies". *Problems of Cosmical Aerodynamics*. Jan. 1951, p. 195.

[133] Wayne Hu and Ignacy Sawicki. "Models of f(R) cosmic acceleration that evade solar system tests". Phys. Rev. D 76.6, 064004 (Sept. 2007), p. 064004. DOI: 10.1103/PhysRevD.76.064004. arXiv: 0705.1158 [astro-ph].

[134] Wayne Hu and Ignacy Sawicki. "Parametrized post-Friedmann framework for modified gravity". Phys. Rev. D 76.10, 104043 (Nov. 2007), p. 104043. DOI: 10.1103/PhysRevD.76.104043. arXiv: 0708.1190 [astro-ph].

[135] Mariana Jaber et al. "Hierarchical structure of the cosmic web and galaxy properties". MNRAS (Nov. 2023). DOI: 10.1093/mnras/stad3347. arXiv: 2304.14387 [astro-ph.GA].

[136] Bhuvnesh Jain, Uroš Seljak, and Simon White. "Ray-tracing Simulations of Weak Lensing by Large-Scale Structure". ApJL 530.2 (Feb. 2000), pp. 547–577. DOI: 10.1086/308384. arXiv: astro-ph/9901191 [astro-ph].

[137] A. Jenkins et al. "The mass function of dark matter haloes". MNRAS 321.2 (Feb. 2001), pp. 372–384. DOI: 10.1046/j.1365-8711.2001.04029.x. arXiv: astro-ph/0005260 [astro-ph].

[138] Austin Joyce, Lucas Lombriser, and Fabian Schmidt. "Dark Energy Versus Modified Gravity". *Annual Review of Nuclear and Particle Science* 66.1 (Oct. 2016), pp. 95–122. DOI: 10.1146/annurev-nucl-102115-044553. arXiv: 1601.06133 [astro-ph.CO].

[139] Gabriel Jung et al. "Quijote-PNG: Quasi-maximum Likelihood Estimation of Primordial Non-Gaussianity in the Nonlinear Dark Matter Density Field". ApJL 940.1, 71 (Nov. 2022), p. 71. DOI: 10.3847/1538-4357/ac9837. arXiv: 2206.01624 [astro-ph.CO].

[140] R. Juszkiewicz, F. R. Bouchet, and S. Colombi. "Skewness Induced by Gravity". ApJ 412 (July 1993), p. L9. DOI: 10.1086/186927. arXiv: astro-ph/9306003 [astro-ph].

[141] Roman Juszkiewicz, Wojciech A. Hellwing, and Rien van de Weygaert. "Skewness as a probe of baryon acoustic oscillations". MNRAS 429.2 (Feb. 2013), pp. 1206–1212. DOI: 10.1093/mnras/sts409. arXiv: 1205.6163 [astro-ph.CO].

[142] Roman Juszkiewicz, Volker Springel, and Ruth Durrer. "Dynamics of Pairwise Motions". ApJ 518.1 (June 1999), pp. L25–L28. DOI: 10.1086/312055. arXiv: astro-ph/9812387 [astro-ph].

[143] N. Kaiser. "On the spatial correlations of Abell clusters." ApJ 284 (Sept. 1984), pp. L9–L12. DOI: 10.1086/184341.

[144] G. Kauffmann, S. D. M. White, and B. Guiderdoni. "The formation and evolution of galaxies within merging dark matter haloes." MNRAS 264 (Sept. 1993), pp. 201–218. DOI: 10.1093/mnras/264.1.201.

[145] Guinevere Kauffmann, Adi Nusser, and Matthias Steinmetz. "Galaxy formation and large-scale bias". MNRAS 286.4 (Apr. 1997), pp. 795–811. DOI: 10.1093/mnras/286.4.795. arXiv: astro-ph/9512009 [astro-ph].

[146] Justin Khoury and Amanda Weltman. "Chameleon cosmology". Phys. Rev. D 69.4, 044026 (Feb. 2004), p. 044026. DOI: 10.1103/PhysRevD.69.044026. arXiv: astro-ph/0309411 [astro-ph].

[147] Martin Kilbinger. "Cosmology with cosmic shear observations: a review". *Reports on Progress in Physics* 78.8, 086901 (July 2015), p. 086901. DOI: 10.1088/0034-4885/78/8/086901. arXiv: 1411.0115 [astro-ph.CO].

[148] Martin Kilbinger et al. "CFHTLenS: combined probe cosmological model comparison using 2D weak gravitational lensing". MNRAS 430.3 (Apr. 2013), pp. 2200–2220. DOI: 10.1093/mnras/stt041. arXiv: 1212.3338 [astro-ph.CO].

[149] Anatoly A. Klypin, Sebastian Trujillo-Gomez, and Joel Primack. "Dark Matter Halos in the Standard Cosmological Model: Results from the Bolshoi Simulation". ApJL 740.2, 102 (Oct. 2011), p. 102. DOI: 10.1088/0004-637X/740/2/102. arXiv: 1002.3660 [astro-ph.CO].

[150] Alexander Knebe and Chris Power. "On the Correlation between Spin Parameter and Halo Mass". ApJL 678.2 (May 2008), pp. 621–626. DOI: 10.1086/586702. arXiv: 0801.4453 [astro-ph].

[151] Alexander Knebe et al. "Structure finding in cosmological simulations: the state of affairs". MNRAS 435.2 (Oct. 2013), pp. 1618–1658. DOI: 10.1093/mnras/stt1403. arXiv: 1304.0585 [astro-ph.CO].

[152] Michael Kopp et al. "Spherical collapse and halo mass function in f(R) theories". Phys. Rev. D 88.8, 084015 (Oct. 2013), p. 084015. DOI: 10.1103/PhysRevD.88.084015. arXiv: 1306.3233 [astro-ph.CO].

[153] Kazuya Koyama. "Cosmological tests of modified gravity". *Reports on Progress in Physics* 79.4, 046902 (Apr. 2016), p. 046902. DOI: 10.1088/0034-4885/79/4/046902. arXiv: 1504.04623 [astro-ph.CO].

[154] Kazuya Koyama. "Gravity beyond general relativity". *International Journal of Modern Physics D* 27.15, 1848001 (Jan. 2018), p. 1848001. DOI: 10.1142/S0218271818480012.

[155] Kazuya Koyama and Fabio P. Silva. "Nonlinear interactions in a cosmological background in the Dvali-Gabadadze-Porrati braneworld". Phys. Rev. D 75.8, 084040 (Apr. 2007), p. 084040. DOI: 10.1103/PhysRevD.75.084040. arXiv: hep-th/0702169 [hep-th].

[156] Kazuya Koyama, Atsushi Taruya, and Takashi Hiramatsu. "Nonlinear evolution of the matter power spectrum in modified theories of gravity". Phys. Rev. D 79.12, 123512 (June 2009), p. 123512. DOI: 10.1103/PhysRevD.79.123512. arXiv: 0902.0618 [astro-ph.CO].

[157] Andrey V. Kravtsov and Stefano Borgani. "Formation of Galaxy Clusters". ARA&A 50 (Sept. 2012), pp. 353–409. DOI: 10.1146/annurev-astro-081811-125502. arXiv: 1205.5556 [astro-ph.CO].

[158] Christina D. Kreisch et al. "The GIGANTES Data Set: Precision Cosmology from Voids in the Machine-learning Era". ApJL 935.2, 100 (Aug. 2022), p. 100. DOI: 10.3847/1538-4357/ac7d4b. arXiv: 2107.02304 [astro-ph.CO].

[159] Benjamin L'Huillier et al. "Dark matter haloes in modified gravity and dark energy: interaction rate, small- and large-scale alignment". MNRAS 468.3 (July 2017), pp. 3174–3183. DOI: 10.1093/mnras/stx700. arXiv: 1703.07357 [astro-ph.CO].

[160] Ivan Lacerna and Nelson Padilla. "The nature of assembly bias - II. Halo spin". MNRAS 426.1 (Oct. 2012), pp. L26–L30. DOI: 10.1111/j.1745-3933.2012.01316.x. arXiv: 1207.4476 [astro-ph.CO].

[161] Cedric Lacey and Shaun Cole. "Merger rates in hierarchical models of galaxy formation". MNRAS 262.3 (June 1993), pp. 627–649. DOI: 10.1093/mnras/262.3.627.

[162] Tsz Yan Lam and Baojiu Li. "Excursion set theory for modified gravity: correlated steps, mass functions and halo bias". MNRAS 426.4 (Nov. 2012), pp. 3260–3270. DOI: 10.1111/j.1365-2966.2012.21746.x. arXiv: 1205.0059 [astro-ph.CO].

[163] R. Laureijs et al. "Euclid Definition Study Report". *arXiv e-prints*, arXiv:1110.3193 (Oct. 2011), arXiv:1110.3193. arXiv: 1110.3193 [astro-ph.CO].

[164] Earl Lawrence et al. "The Coyote Universe. III. Simulation Suite and Precision Emulator for the Nonlinear Matter Power Spectrum". ApJL 713.2 (Apr. 2010), pp. 1322–1331. DOI: 10.1088/0004-637X/713/2/1322. arXiv: 0912.4490 [astro-ph.CO].

[165] Titouan Lazeyras, Marcello Musso, and Fabian Schmidt. "Large-scale assembly bias of dark matter halos". J. Cosmology Astropart. Phys. 2017.3, 059 (Mar. 2017), p. 059. DOI: 10.1088/1475-7516/2017/03/059. arXiv: 1612.04360 [astro-ph.CO].

[166] Titouan Lazeyras, Francisco Villaescusa-Navarro, and Matteo Viel. "The impact of massive neutrinos on halo assembly bias". J. Cosmology Astropart. Phys. 2021.3, 022 (Mar. 2021), p. 022. DOI: 10.1088/1475-7516/2021/03/022. arXiv: 2008.12265 [astro-ph.CO].

[167] Florent Leclercq, Jens Jasche, and Benjamin Wandelt. "Bayesian analysis of the dynamic cosmic web in the SDSS galaxy survey". J. Cosmology Astropart. Phys. 2015.6 (June 2015), pp. 015–015. DOI: 10.1088/1475-7516/2015/06/015. arXiv: 1502.02690 [astro-ph.CO].

[168] Jounghun Lee et al. "Modified Gravity Spins up Galactic Halos". ApJL 763.1, 28 (Jan. 2013), p. 28. DOI: 10.1088/0004-637X/763/1/28. arXiv: 1204.6608 [astro-ph.CO].

[169] Benjamin V. Lehmann et al. "The Concentration Dependence of the Galaxy-Halo Connection: Modeling Assembly Bias with Abundance Matching". ApJL 834.1, 37 (Jan. 2017), p. 37. DOI: 10.3847/1538-4357/834/1/37. arXiv: 1510.05651 [astro-ph.CO].

[170] Gerard Lemson and Guinevere Kauffmann. "Environmental influences on dark matter haloes and consequences for the galaxies within them". MNRAS 302.1 (Jan. 1999), pp. 111–117. DOI: 10.1046/j.1365-8711.1999.02090.x.

[171] Antony Lewis, Anthony Challinor, and Anthony Lasenby. *Efficient Computation of Cosmic Microwave Background Anisotropies in Closed Friedmann-Robertson-Walker Models*. Aug. 2000. DOI: 10.1086/309179. arXiv: astro-ph/9911177 [astro-ph].

[172] Baojiu Li and George Efstathiou. "An extended excursion set approach to structure formation in chameleon models". MNRAS 421.2 (Apr. 2012), pp. 1431–1442. DOI: 10.1111/j.1365-2966.2011.20404.x. arXiv: 1110.6440 [astro-ph.CO].

[173] Baojiu Li, Gong-Bo Zhao, and Kazuya Koyama. "Exploring Vainshtein mechanism on adaptively refined meshes". J. Cosmology Astropart. Phys. 2013.5, 023 (May 2013), p. 023. DOI: 10.1088/1475-7516/2013/05/023. arXiv: 1303.0008 [astro-ph.CO].

[174] Baojiu Li and Hongsheng Zhao. "Structure formation by the fifth force: Segregation of baryons and dark matter". Phys. Rev. D 81.10, 104047 (May 2010), p. 104047. DOI: 10.1103/PhysRevD.81.104047. arXiv: 1001.3152 [astro-ph.CO].

[175] Baojiu Li et al. "ECOSMOG: an Efficient COde for Simulating MOdified Gravity". J. Cosmology Astropart. Phys. 2012.1, 051 (Jan. 2012), p. 051. DOI: 10.1088/1475-7516/2012/01/051. arXiv: 1110.1379 [astro-ph.CO].

[176] Noam I. Libeskind et al. "Tracing the cosmic web". MNRAS 473.1 (Jan. 2018), pp. 1195–1217. DOI: 10.1093/mnras/stx1976. arXiv: 1705.03021 [astro-ph.CO].

[177] D. Nelson Limber. "The Analysis of Counts of the Extragalactic Nebulae in Terms of a Fluctuating Density Field." ApJL 117 (Jan. 1953), p. 134. DOI: 10.1086/145672.

[178] Hengjie Lin et al. "Forecast of neutrino cosmology from the CSST photometric galaxy clustering and cosmic shear surveys". MNRAS 515.4 (Oct. 2022), pp. 5743–5757. DOI: 10.1093/mnras/stac2126. arXiv: 2203.11429 [astro-ph.CO].

[179] Yun Liu et al. "Dark matter haloes in interacting dark energy models: formation history, density profile, spin, and shape". MNRAS 511.2 (Apr. 2022), pp. 3076–3088. DOI: 10.1093/mnras/stac229. arXiv: 2201.09817 [astro-ph.CO].

[180] Lucas Lombriser, Kazuya Koyama, and Baojiu Li. "Halo modelling in chameleon theories". J. Cosmology Astropart. Phys. 2014.3, 021 (Mar. 2014), p. 021. DOI: 10.1088/1475-7516/2014/03/021. arXiv: 1312.1292 [astro-ph.CO].

[181] Lucas Lombriser et al. "Modeling halo mass functions in chameleon f(R) gravity". Phys. Rev. D 87.12, 123511 (June 2013), p. 123511. DOI: 10.1103/PhysRevD.87.123511. arXiv: 1304.6395 [astro-ph.CO].

[182] LSST Science Collaboration. "LSST Science Book, Version 2.0". *arXiv e-prints*, arXiv:0912.0201 (Dec. 2009), arXiv:0912.0201. arXiv: 0912.0201 [astro-ph.IM].

[183] Aaron D. Ludlow et al. "The mass-concentration-redshift relation of cold and warm dark matter haloes". MNRAS 460.2 (Aug. 2016), pp. 1214–1232. DOI: 10.1093/mnras/stw1046. arXiv: 1601.02624 [astro-ph.CO].

[184] Arthur Lue, Román Scoccimarro, and Glenn D. Starkman. "Probing Newton's constant on vast scales: Dvali-Gabadadze-Porrati gravity, cosmic acceleration, and large scale structure". *Phys. Rev. D* 69 (12 June 2004), p. 124015. DOI: 10.1103/PhysRevD.69.124015. URL: https://link.aps.org/doi/10.1103/PhysRevD.69.124015.

[185] Zarija Lukić et al. "The Halo Mass Function: High-Redshift Evolution and Universality". ApJL 671.2 (Dec. 2007), pp. 1160–1181. DOI: 10.1086/523083. arXiv: astro-ph/0702360 [astro-ph].

[186] E. Lusso et al. "Tension with the flat ΛCDM model from a high-redshift Hubble diagram of supernovae, quasars, and gamma-ray bursts". A&A 628, L4 (Aug. 2019), p. L4. DOI: 10.1051/0004-6361/201936223. arXiv: 1907.07692 [astro-ph.CO].

[187] Stuart Lyall et al. "Testing modified gravity scenarios with direct peculiar velocities". MNRAS 518.4 (Feb. 2023), pp. 5929–5941. DOI: 10.1093/mnras/stac3323. arXiv: 2211.07101 [astro-ph.CO].

[188] Andrea V. Macciò et al. "Concentration, spin and shape of dark matter haloes: scatter and the dependence on mass and environment". MNRAS 378.1 (June 2007), pp. 55–71. DOI: 10.1111/j.1365-2966.2007.11720.x. arXiv: astro-ph/0608157 [astro-ph].

[189] Sara Maleubre et al. "Convergence of halo statistics: code comparison between Rockstar and CompaSO using scale-free simulations". *arXiv e-prints*, arXiv:2308.00438 (Aug. 2023), arXiv:2308.00438. DOI: 10.48550/arXiv.2308.00438. arXiv: 2308.00438 [astro-ph.CO].

[190] R. N. Manchester. "Millisecond Pulsars, their Evolution and Applications". *Journal of Astrophysics and Astronomy* 38.3, 42 (Sept. 2017), p. 42. DOI: 10.1007/s12036-017-9469-2. arXiv: 1709.09434 [astro-ph.HE].

[191] Qingqing Mao et al. "Constraining primordial non-Gaussianity with moments of the large-scale density field". MNRAS 443.2 (Sept. 2014), pp. 1402–1415. DOI: 10.1093/mnras/stu1255. arXiv: 1404.3725 [astro-ph.CO].

[192] Yao-Yuan Mao, Andrew R. Zentner, and Risa H. Wechsler. "Beyond assembly bias: exploring secondary halo biases for cluster-size haloes". MNRAS 474.4 (Mar. 2018), pp. 5143–5157. DOI: 10.1093/mnras/stx3111. arXiv: 1705.03888 [astro-ph.CO].

[193] Gabriela A. Marques et al. "Cosmology from weak lensing peaks and minima with Subaru Hyper Suprime-Cam survey first-year data". *arXiv e-prints*, arXiv:2308.10866 (Aug. 2023), arXiv:2308.10866. DOI: 10.48550/arXiv.2308.10866. arXiv: 2308.10866 [astro-ph.CO].

[194] Davide Martizzi et al. "Baryons in the Cosmic Web of IllustrisTNG - I: gas in knots, filaments, sheets, and voids". MNRAS 486.3 (July 2019), pp. 3766–3787. DOI: 10.1093/mnras/stz1106. arXiv: 1810.01883 [astro-ph.CO].

[195] Renate Mauland, Hans A. Winther, and Cheng-Zong Ruan. "Sesame: A power spectrum emulator pipeline for beyond-ΛCDM models". *arXiv e-prints*, arXiv:2309.13295 (Sept. 2023), arXiv:2309.13295. DOI: 10.48550/arXiv.2309.13295. arXiv: 2309.13295 [astro-ph.CO].

[196] A. J. Mead and L. Verde. "Including beyond-linear halo bias in halo models". MNRAS 503.2 (May 2021), pp. 3095–3111. DOI: 10.1093/mnras/stab748. arXiv: 2011.08858 [astro-ph.CO].

[197] A. J. Mead et al. "An accurate halo model for fitting non-linear cosmological power spectra and baryonic feedback models". MNRAS 454.2 (Dec. 2015), pp. 1958–1975. DOI: 10.1093/mnras/stv2036. arXiv: 1505.07833 [astro-ph.CO].

[198] A. J. Mead et al. "Accurate halo-model matter power spectra with dark energy, massive neutrinos and modified gravitational forces". MNRAS 459.2 (June 2016), pp. 1468–1488. DOI: 10.1093/mnras/stw681. arXiv: 1602.02154 [astro-ph.CO].

[199] A. J. Mead et al. "A hydrodynamical halo model for weak-lensing cross correlations". A&A 641, A130 (Sept. 2020), A130. DOI: 10.1051/0004-6361/202038308. arXiv: 2005.00009 [astro-ph.CO].

[200] A. J. Mead et al. "HMCODE-2020: improved modelling of non-linear cosmological power spectra with baryonic feedback". MNRAS 502.1 (Mar. 2021), pp. 1401–1422. DOI: 10.1093/mnras/stab082. arXiv: 2009.01858 [astro-ph.CO].

[201] Ofer Metuki, Noam I. Libeskind, and Yehuda Hoffman. "The abundance and environment of dark matter haloes". MNRAS 460.1 (July 2016), pp. 297–303. DOI: 10.1093/mnras/stw979. arXiv: 1606.01514 [astro-ph.GA].

[202] Myles A. Mitchell et al. "A general framework to test gravity using galaxy clusters II: A universal model for the halo concentration in f(R) gravity". MNRAS 487.1 (July 2019), pp. 1410–1425. DOI: 10.1093/mnras/stz1389. arXiv: 1901.06392 [astro-ph.CO].

[203] Myles A. Mitchell et al. "A general framework to test gravity using galaxy clusters IV: cluster and halo properties in DGP gravity". MNRAS 508.3 (Dec. 2021), pp. 4140–4156. DOI: 10.1093/mnras/stab2817. arXiv: 2106.13815 [astro-ph.CO].

[204] Antonio D. Montero-Dorta and Facundo Rodriguez. "The dependence of assembly bias on the cosmic web". *arXiv e-prints*, arXiv:2309.12401 (Sept. 2023), arXiv:2309.12401. DOI: 10.48550/arXiv.2309.12401. arXiv: 2309.12401 [astro-ph.GA].

[205] Surhud More et al. "The Overdensity and Masses of the Friends-of-friends Halos and Universality of Halo Mass Function". ApJS 195.1, 4 (July 2011), p. 4. DOI: 10.1088/0067-0049/195/1/4. arXiv: 1103.0005 [astro-ph.CO].

[206] Krishna Naidoo et al. "Constrained simulations of the local Universe with modified gravity". Phys. Rev. D 107.4, 043533 (Feb. 2023), p. 043533. DOI: 10.1103/PhysRevD.107.043533. arXiv: 2209.14386 [astro-ph.CO].

[207] Vijay K. Narayanan et al. "Constraints on the Mass of Warm Dark Matter Particles and the Shape of the Linear Power Spectrum from the Lyα Forest". ApJ 543.2 (Nov. 2000), pp. L103–L106. DOI: 10.1086/317269. arXiv: astro-ph/0005095 [astro-ph].

[208] Julio F. Navarro, Carlos S. Frenk, and Simon D. M. White. "The Structure of Cold Dark Matter Halos". ApJL 462 (May 1996), p. 563. DOI: 10.1086/177173. arXiv: astro-ph/9508025 [astro-ph].

[209] Takahiro Nishimichi et al. "Dark Quest. I. Fast and Accurate Emulation of Halo Clustering Statistics and Its Application to Galaxy Clustering". ApJL 884.1, 29 (Oct. 2019), p. 29. DOI: 10.3847/1538-4357/ab3719. arXiv: 1811.09504 [astro-ph.CO].

[210] R. Nityananda and T. Padmanabhan. "Scaling Properties of Nonlinear Gravitational Clustering". MNRAS 271 (Dec. 1994), p. 976. DOI: 10.1093/mnras/271.4.976. arXiv: gr-qc/9304022 [gr-qc].

[211] S. Nojiri, S. D. Odintsov, and V. K. Oikonomou. "Modified Gravity Theories on a Nutshell: Inflation, Bounce and Late-time Evolution". *Phys. Rept.* 692 (2017), pp. 1–104. DOI: 10.1016/j.physrep.2017.06.001. arXiv: 1705.11098 [gr-qc].

[212] Hiroaki Oyaizu. "Non-linear evolution of f(R) cosmologies I: methodology". Phys. Rev. D 78 (2008), p. 123523. DOI: 10.1103/PhysRevD.78.123523. arXiv: 0807.2449 [astro-ph].

[213] Hiroaki Oyaizu, Marcos Lima, and Wayne Hu. "Nonlinear evolution of f(R) cosmologies. II. Power spectrum". Phys. Rev. D 78.12, 123524 (Dec. 2008), p. 123524. DOI: 10.1103/PhysRevD.78.123524. arXiv: 0807.2462 [astro-ph].

[214] Enrique Paillas et al. "The Santiago-Harvard-Edinburgh-Durham void comparison II: unveiling the Vainshtein screening using weak lensing". MNRAS 484.1 (Mar. 2019), pp. 1149–1165. DOI: 10.1093/mnras/stz022. arXiv: 1810.02864 [astro-ph.CO].

[215] Enrique Paillas et al. "Redshift-space distortions with split densities". MNRAS 505.4 (Aug. 2021), pp. 5731–5752. DOI: 10.1093/mnras/stab1654. arXiv: 2101.09854 [astro-ph.CO].

[216] Diego Pallero et al. "Galaxy evolution in modified gravity simulations: using passive galaxies to constrain gravity with upcoming surveys" (2023). arXiv: 2310.02333 [astro-ph.GA].

[217] Alexandros Papageorgiou et al. *The Cluster Mass Function and the σ_8-tension*. 2023. arXiv: 2311.09826 [astro-ph.CO].

[218] Aseem Paranjape. "Analytical halo models of cosmic tidal fields". MNRAS 502.4 (Apr. 2021), pp. 5210–5226. DOI: 10.1093/mnras/stab359. arXiv: 2006.13954 [astro-ph.CO].

[219] Aseem Paranjape, Oliver Hahn, and Ravi K. Sheth. "Halo assembly bias and the tidal anisotropy of the local halo environment". MNRAS 476.3 (May 2018), pp. 3631–3647. DOI: 10.1093/mnras/sty496. arXiv: 1706.09906 [astro-ph.CO].

[220] J. A. Peacock and R. E. Smith. "Halo occupation numbers and galaxy bias". MNRAS 318.4 (Nov. 2000), pp. 1144–1156. DOI: 10.1046/j.1365-8711.2000.03779.x. arXiv: astro-ph/0005010 [astro-ph].

[221] Alan N. Pearl et al. "The DESI One-Percent Survey: Evidence for Assembly Bias from Low-Redshift Counts-in-Cylinders Measurements". *arXiv e-prints*, arXiv:2309.08675 (Sept. 2023), arXiv:2309.08675. DOI: 10.48550/arXiv.2309.08675. arXiv: 2309.08675 [astro-ph.CO].

[222] P. J. E. Peebles. "Origin of the Angular Momentum of Galaxies". ApJL 155 (Feb. 1969), p. 393. DOI: 10.1086/149876.

[223] P. J. E. Peebles. *The large-scale structure of the universe*. Princeton University Press, 1980.

[224] Leandros Perivolaropoulos and Foteini Skara. "Challenges for ΛCDM: An update". *arXiv e-prints*, arXiv:2105.05208 (May 2021), arXiv:2105.05208. arXiv: 2105.05208 [astro-ph.CO].

[225] A. Pezzotta et al. "The VIMOS Public Extragalactic Redshift Survey (VIPERS). The growth of structure at $0.5 < z < 1.2$ from redshift-space distortions in the clustering of the PDR-2 final sample". A&A 604, A33 (July 2017), A33. DOI: 10.1051/0004-6361/201630295. arXiv: 1612.05645 [astro-ph.CO].

[226] Annalisa Pillepich, Cristiano Porciani, and Oliver Hahn. "Halo mass function and scale-dependent bias from N-body simulations with non-Gaussian initial conditions". MNRAS 402.1 (Feb. 2010), pp. 191–206. DOI: 10.1111/j.1365-2966.2009.15914.x. arXiv: 0811.4176 [astro-ph].

[227] Planck Collaboration. "Planck 2013 results. XX. Cosmology from Sunyaev-Zeldovich cluster counts". A&A 571, A20 (Nov. 2014), A20. DOI: 10.1051/0004-6361/201321521. arXiv: 1303.5080 [astro-ph.CO].

[228] Cristiano Porciani, Avishai Dekel, and Yehuda Hoffman. "Testing tidal-torque theory - I. Spin amplitude and direction". MNRAS 332.2 (May 2002), pp. 325–338. DOI: 10.1046/j.1365-8711.2002.05305.x. arXiv: astro-ph/0105123 [astro-ph].

[229] C. Power et al. "The inner structure of ΛCDM haloes - I. A numerical convergence study". MNRAS 338.1 (Jan. 2003), pp. 14–34. DOI: 10.1046/j.1365-8711.2003.05925.x. arXiv: astro-ph/0201544 [astro-ph].

[230] Francisco Prada et al. "Halo concentrations in the standard Λ cold dark matter cosmology". MNRAS 423.4 (July 2012), pp. 3018–3030. DOI: 10.1111/j.1365-2966.2012.21007.x. arXiv: 1104.5130 [astro-ph.CO].

[231] William H. Press and Paul Schechter. "Formation of Galaxies and Clusters of Galaxies by Self-Similar Gravitational Condensation". ApJL 187 (Feb. 1974), pp. 425–438. DOI: 10.1086/152650.

[232] S. Prunet et al. "Initial Conditions For Large Cosmological Simulations". ApJS 178.2 (Oct. 2008), pp. 179–188. DOI: 10.1086/590370. arXiv: 0804.3536 [astro-ph].

[233] Sujatha Ramakrishnan et al. "Cosmic web anisotropy is the primary indicator of halo assembly bias". MNRAS 489.3 (Nov. 2019), pp. 2977–2996. DOI: 10.1093/mnras/stz2344. arXiv: 1903.02007 [astro-ph.CO].

[234] Darren S. Reed et al. "Towards an accurate mass function for precision cosmology". MNRAS 431.2 (May 2013), pp. 1866–1882. DOI: 10.1093/mnras/stt301. arXiv: 1206.5302 [astro-ph.CO].

[235] Adam G. Riess et al. "A 2.4% Determination of the Local Value of the Hubble Constant". ApJL 826.1, 56 (July 2016), p. 56. DOI: 10.3847/0004-637X/826/1/56. arXiv: 1604.01424 [astro-ph.CO].

[236] Cheng-Zong Ruan, Tong-Jie Zhang, and Bin Hu. "Non-linear matter power spectrum without screening dynamics modelling in f(R) gravity". MNRAS 492.3 (Mar. 2020), pp. 4235–4245. DOI: 10.1093/mnras/staa006. arXiv: 2001.09229 [astro-ph.CO].

[237] Cheng-Zong Ruan et al. "An emulator-based halo model in modified gravity – I. The halo concentration-mass relation and density profile". *arXiv e-prints*, arXiv:2301.02970 (Jan. 2023), arXiv:2301.02970. arXiv: 2301.02970 [astro-ph.CO].

[238] Jeremy Sakstein. "Astrophysical tests of screened modified gravity". *International Journal of Modern Physics D* 27.15, 1848008-228 (Jan. 2018), pp. 1848008–228. DOI: 10.1142/S0218271818480085.

[239] Gabriela Sato-Polito et al. "The dependence of halo bias on age, concentration, and spin". MNRAS 487.2 (Aug. 2019), pp. 1570–1579. DOI: 10.1093/mnras/stz1338. arXiv: 1810.02375 [astro-ph.GA].

[240] Brian P. Schmidt et al. "The High-Z Supernova Search: Measuring Cosmic Deceleration and Global Curvature of the Universe Using Type IA Supernovae". ApJL 507.1 (Nov. 1998), pp. 46–63. DOI: 10.1086/306308. arXiv: astro-ph/9805200 [astro-ph].

[241] Fabian Schmidt. "Weak lensing probes of modified gravity". Phys. Rev. D 78.4, 043002 (Aug. 2008), p. 043002. DOI: 10.1103/PhysRevD.78.043002. arXiv: 0805.4812 [astro-ph].

[242] Fabian Schmidt. "Cosmological simulations of normal-branch braneworld gravity". Phys. Rev. D 80.12, 123003 (Dec. 2009), p. 123003. DOI: 10.1103/PhysRevD.80.123003. arXiv: 0910.0235 [astro-ph.CO].

[243] Fabian Schmidt. "Dynamical masses in modified gravity". Phys. Rev. D 81.10, 103002 (May 2010), p. 103002. DOI: 10.1103/PhysRevD.81.103002. arXiv: 1003.0409 [astro-ph.CO].

[244] Fabian Schmidt, Wayne Hu, and Marcos Lima. "Spherical collapse and the halo model in braneworld gravity". Phys. Rev. D 81.6, 063005 (Mar. 2010), p. 063005. DOI: 10.1103/PhysRevD.81.063005. arXiv: 0911.5178 [astro-ph.CO].

[245] Fabian Schmidt, Alexey Vikhlinin, and Wayne Hu. "Cluster constraints on f(R) gravity". Phys. Rev. D 80.8, 083505 (Oct. 2009), p. 083505. DOI: 10.1103/PhysRevD.80.083505. arXiv: 0908.2457 [astro-ph.CO].

[246] Fabian Schmidt et al. "Nonlinear evolution of f(R) cosmologies. III. Halo statistics". Phys. Rev. D 79.8, 083518 (Apr. 2009), p. 083518. DOI: 10.1103/PhysRevD.79.083518. arXiv: 0812.0545 [astro-ph].

[247] T. Schrabback et al. "Evidence of the accelerated expansion of the Universe from weak lensing tomography with COSMOS". A&A 516, A63 (June 2010), A63. DOI: 10.1051/0004-6361/200913577. arXiv: 0911.0053 [astro-ph.CO].

[248] Uroš Seljak. "Analytic model for galaxy and dark matter clustering". MNRAS 318.1 (Oct. 2000), pp. 203–213. DOI: 10.1046/j.1365-8711.2000.03715.x. arXiv: astro-ph/0001493 [astro-ph].

[249] Uroš Seljak and Michael S. Warren. "Large-scale bias and stochasticity of haloes and dark matter". MNRAS 355.1 (Nov. 2004), pp. 129–136. DOI: 10.1111/j.1365-2966.2004.08297.x. arXiv: astro-ph/0403698 [astro-ph].

[250] Irwin I. Shapiro. "Fourth Test of General Relativity". *Phys. Rev. Lett.* 13 (26 Dec. 1964), pp. 789–791. DOI: 10.1103/PhysRevLett.13.789. URL: https://link.aps.org/doi/10.1103/PhysRevLett.13.789.

[251] Ravi K. Sheth, H. J. Mo, and Giuseppe Tormen. "Ellipsoidal collapse and an improved model for the number and spatial distribution of dark matter haloes". MNRAS 323.1 (May 2001), pp. 1–12. DOI: 10.1046/j.1365-8711.2001.04006.x. arXiv: astro-ph/9907024 [astro-ph].

[252] Ravi K. Sheth and Giuseppe Tormen. "Large-scale bias and the peak background split". MNRAS 308.1 (Sept. 1999), pp. 119–126. DOI: 10.1046/j.1365-8711.1999.02692.x. arXiv: astro-ph/9901122 [astro-ph].

[253] Ravi K. Sheth et al. "On the streaming motions of haloes and galaxies". MNRAS 326.2 (Sept. 2001), pp. 463–472. DOI: 10.1046/j.1365-8711.2001.04457.x. arXiv: astro-ph/0010137 [astro-ph].

[254] Difu Shi et al. "Exploring the liminality: properties of haloes and subhaloes in borderline f(R) gravity". MNRAS 452.3 (Sept. 2015), pp. 3179–3191. DOI: 10.1093/mnras/stv1549. arXiv: 1503.01109 [astro-ph.CO].

[255] Junsup Shim, Jounghun Lee, and Baojiu Li. "Massive Gravity Wrapped in the Cosmic Web". ApJL 784.1, 84 (Mar. 2014), p. 84. DOI: 10.1088/0004-637X/784/1/84. arXiv: 1311.7187 [astro-ph.CO].

[256] R. E. Smith et al. "Stable clustering, the halo model and non-linear cosmological power spectra". MNRAS 341.4 (June 2003), pp. 1311–1332. DOI: 10.1046/j.1365-8711.2003.06503.x. arXiv: astro-ph/0207664 [astro-ph].

[257] George F. Smoot. "COBE observations and results". *3K cosmology*. Ed. by Luciano Maiani, Francesco Melchiorri, and Nicola Vittorio. Vol. 476. American Institute of Physics Conference Series. May 1999, pp. 1–10. DOI: 10.1063/1.59326. arXiv: astro-ph/9902027 [astro-ph].

[258] Yunjia Song and Ying Zu. "Elucidating the impact of massive neutrinos on halo assembly bias". *arXiv e-prints*, arXiv:2311.07650 (Nov. 2023), arXiv:2311.07650. arXiv: 2311.07650 [astro-ph.CO].

[259] Thomas P. Sotiriou and Valerio Faraoni. "f(R) theories of gravity". *Reviews of Modern Physics* 82.1 (Jan. 2010), pp. 451–497. DOI: 10.1103/RevModPhys.82.451. arXiv: 0805.1726 [gr-qc].

[260] Volker Springel. "High Performance Computing and Numerical Modelling". *Saas-Fee Advanced Course*. Ed. by Yves Revaz et al. Vol. 43. Saas-Fee Advanced Course. Jan. 2016, p. 251. DOI: 10.1007/978-3-662-47890-5_3. arXiv: 1412.5187 [astro-ph.GA].

[261] Volker Springel et al. "Simulations of the formation, evolution and clustering of galaxies and quasars". Nature 435.7042 (June 2005), pp. 629–636. DOI: 10.1038/nature03597. arXiv: astro-ph/0504097 [astro-ph].

[262] Square Kilometre Array Cosmology Science Working Group et al. "Cosmology with Phase 1 of the Square Kilometre Array Red Book 2018: Technical specifications and performance forecasts". PASA 37, e007 (Mar. 2020), e007. DOI: 10.1017/pasa.2019.51. arXiv: 1811.02743 [astro-ph.CO].

[263] Ryuichi Takahashi et al. "Revising the Halofit Model for the Nonlinear Matter Power Spectrum". ApJL 761.2, 152 (Dec. 2012), p. 152. DOI: 10.1088/0004-637X/761/2/152. arXiv: 1208.2701 [astro-ph.CO].

[264] Andrius Tamosiunas et al. "Chameleon screening in cosmic voids". J. Cosmology Astropart. Phys. 2022.11, 056 (Nov. 2022), p. 056. DOI: 10.1088/1475-7516/2022/11/056. arXiv: 2206.06480 [gr-qc].

[265] J. H. Taylor and J. M. Weisberg. "A new test of general relativity - Gravitational radiation and the binary pulsar PSR 1913+16". ApJL 253 (Feb. 1982), pp. 908–920. DOI: 10.1086/159690.

[266] R. Teyssier. "Cosmological hydrodynamics with adaptive mesh refinement. A new high resolution code called RAMSES". A&A 385 (Apr. 2002), pp. 337–364. DOI: 10.1051/0004-6361:20011817. arXiv: astro-ph/0111367 [astro-ph].

[267] Jeremy Tinker et al. "Toward a Halo Mass Function for Precision Cosmology: The Limits of Universality". ApJL 688.2 (Dec. 2008), pp. 709–728. DOI: 10.1086/591439. arXiv: 0803.2706 [astro-ph].

[268] Jeremy L. Tinker et al. "The Large-scale Bias of Dark Matter Halos: Numerical Calibration and Model Tests". ApJL 724.2 (Dec. 2010), pp. 878–886. DOI: 10.1088/0004-637X/724/2/878. arXiv: 1001.3162 [astro-ph.CO].

[269] C. To et al. "Dark Energy Survey Year 1 Results: Cosmological Constraints from Cluster Abundances, Weak Lensing, and Galaxy Correlations". Phys. Rev. Lett. 126.14, 141301 (Apr. 2021), p. 141301. DOI: 10.1103/PhysRevLett.126.141301. arXiv: 2010.01138 [astro-ph.CO].

[270] Ryan J. Turner, Chris Blake, and Rossana Ruggeri. "A local measurement of the growth rate from peculiar velocities and galaxy clustering correlations in the 6dF Galaxy Survey". MNRAS 518.2 (Jan. 2023), pp. 2436–2452. DOI: 10.1093/mnras/stac3256. arXiv: 2207.03707 [astro-ph.CO].

[271] A. I. Vainshtein. "To the problem of nonvanishing gravitation mass". *Physics Letters B* 39.3 (May 1972), pp. 393–394. DOI: 10.1016/0370-2693(72)90147-5.

[272] A. Vale and J. P. Ostriker. "The non-parametric model for linking galaxy luminosity with halo/subhalo mass". MNRAS 371.3 (Sept. 2006), pp. 1173–1187. DOI: 10.1111/j.1365-2966.2006.10605.x. arXiv: astro-ph/0511816 [astro-ph].

[273] R. van de Weygaert and J. R. Bond. "Clusters and the Theory of the Cosmic Web". In: *A Pan-Chromatic View of Clusters of Galaxies and the Large-Scale Structure*. Ed. by M. Plionis, O. López-Cruz, and D. Hughes. Vol. 740. 2008, p. 335. DOI: 10.1007/978-1-4020-6941-3_10.

[274] J. L. van den Busch et al. "KiDS-1000: Cosmic shear with enhanced redshift calibration". A&A 664, A170 (Aug. 2022), A170. DOI: 10.1051/0004-6361/202142083. arXiv: 2204.02396 [astro-ph.CO].

[275] Antonia Sierra Villarreal et al. "The immitigable nature of assembly bias: the impact of halo definition on assembly bias". MNRAS 472.1 (Nov. 2017), pp. 1088–1105. DOI: 10.1093/mnras/stx2045. arXiv: 1705.04327 [astro-ph.CO].

[276] F. von Braun-Bates et al. "The $f(R)$ halo mass function in the cosmic web". J. Cosmology Astropart. Phys. 2017.3, 012 (Mar. 2017), p. 012. DOI: 10.1088/1475-7516/2017/03/012. arXiv: 1702.06817 [astro-ph.CO].

[277] Michael S. Warren et al. "Precision Determination of the Mass Function of Dark Matter Halos". ApJL 646.2 (Aug. 2006), pp. 881–885. DOI: 10.1086/504962. arXiv: astro-ph/0506395 [astro-ph].

[278] William A. Watson et al. "The halo mass function through the cosmic ages". MNRAS 433.2 (Aug. 2013), pp. 1230–1245. DOI: 10.1093/mnras/stt791. arXiv: 1212.0095 [astro-ph.CO].

[279] Risa H. Wechsler et al. "The Dependence of Halo Clustering on Halo Formation History, Concentration, and Occupation". ApJL 652.1 (Nov. 2006), pp. 71–84. DOI: 10.1086/507120. arXiv: astro-ph/0512416 [astro-ph].

[280] Steven Weinberg. "The cosmological constant problem". *Rev. Mod. Phys.* 61 (1 Jan. 1989), pp. 1–23. DOI: 10.1103/RevModPhys.61.1. URL: https://link.aps.org/doi/10.1103/RevModPhys.61.1.

[281] M. White. "The mass of a halo". A&A 367 (Feb. 2001), pp. 27–32. DOI: 10.1051/0004-6361:20000357. arXiv: astro-ph/0011495 [astro-ph].

[282] Martin White. "The Mass Function". ApJS 143.2 (Dec. 2002), pp. 241–255. DOI: 10.1086/342752. arXiv: astro-ph/0207185 [astro-ph].

[283] S. D. M. White. "Angular momentum growth in protogalaxies". ApJL 286 (Nov. 1984), pp. 38–41. DOI: 10.1086/162573.

[284] Abbé M. Whitford, Cullan Howlett, and Tamara M. Davis. "Using peculiar velocity surveys to constrain neutrino masses". MNRAS 513.1 (June 2022), pp. 345–362. DOI: 10.1093/mnras/stac783. arXiv: 2112.10302 [astro-ph.CO].

[285] Clifford M. Will. "The Confrontation between General Relativity and Experiment". *Living Reviews in Relativity* 17.1, 4 (Dec. 2014), p. 4. DOI: 10.12942/lrr-2014-4. arXiv: 1403.7377 [gr-qc].

[286] Hans A. Winther et al. "Modified gravity N-body code comparison project". MNRAS 454.4 (Dec. 2015), pp. 4208–4234. DOI: 10.1093/mnras/stv2253. arXiv: 1506.06384 [astro-ph.CO].

[287] Hans A. Winther et al. "Emulators for the nonlinear matter power spectrum beyond Λ CDM". Phys. Rev. D 100.12, 123540 (Dec. 2019), p. 123540. DOI: 10.1103/PhysRevD.100.123540. arXiv: 1903.08798 [astro-ph.CO].

[288] Wenxiao Xu et al. "Galaxy properties in the cosmic web of EAGLE simulation". MNRAS 498.2 (Oct. 2020), pp. 1839–1851. DOI: 10.1093/mnras/staa2497. arXiv: 2009.07394 [astro-ph.GA].

[289] Xiaohu Yang, H. J. Mo, and Frank C. van den Bosch. "Constraining galaxy formation and cosmology with the conditional luminosity function of galaxies". MNRAS 339.4 (Mar. 2003), pp. 1057–1080. DOI: 10.1046/j.1365-8711.2003.06254.x. arXiv: astro-ph/0207019 [astro-ph].

[290] Xiaohu Yang et al. "Revealing the Cosmic Web-dependent Halo Bias". ApJL 848.1, 60 (Oct. 2017), p. 60. DOI: 10.3847/1538-4357/aa8c7a. arXiv: 1704.02451 [astro-ph.GA].

[291] Y. B. Zel'Dovich. "Reprint of 1970A&A.....5...84Z. Gravitational instability: an approximate theory for large density perturbations." A&A 500 (Mar. 1970), pp. 13–18.

[292] Andrew R. Zentner, Andrew P. Hearin, and Frank C. van den Bosch. "Galaxy assembly bias: a significant source of systematic error in the galaxy-halo relationship". MNRAS 443.4 (Oct. 2014), pp. 3044–3067. DOI: 10.1093/mnras/stu1383. arXiv: 1311.1818 [astro-ph.CO].

[293] D. H. Zhao et al. "Accurate Universal Models for the Mass Accretion Histories and Concentrations of Dark Matter Halos". ApJL 707.1 (Dec. 2009), pp. 354–369. DOI: 10.1088/0004-637X/707/1/354. arXiv: 0811.0828 [astro-ph].